PSU CGTP 9701

Center for Gas Turbine and Power
The Pennsylvania State University
153 Hammond Building
University Park, PA 16802

UNSTEADY FLOW FIELD IN A MULTISTAGE AXIAL FLOW COMPRESSOR

N. Suryavamshi
B. Lakshminarayana
J. Prato
Department of Aerospace Engineering

January 1997

Research Sponsored by
Allison Engine Company (R. Fagan and E. Hall)
NASA Lewis Research Center
(NAG 3-1745 and NAG 3-1222 — A. J. Strazisar)
Rolls-Royce, Inc. (R. Moritz and M. Howard)

TABLE OF CONTENTS

ABSTRACT

The flow field in a multistage compressor is three-dimensional, unsteady, and turbulent with substantial viscous effects. Some of the specific phenomena that has eluded designers include the effects of rotor-stator and rotor-rotor interactions and the physics of mixing of velocity, pressure, temperature and velocity fields. An attempt was made, to resolve experimentally, the unsteady pressure and temperature fields downstream of the second stator of a multistage axial flow compressor which will provide information on rotor-stator interaction effects and the nature of the unsteadiness in an embedded stator of a three stage axial flow compressor.

Detailed area traverse measurements using pneumatic five hole probe, thermocouple probe, semi-conductor total pressure probe (Kulite) and an aspirating probe downstream of the second stator were conducted at the peak efficiency operating condition. The unsteady data was then reduced through an ensemble averaging technique which splits the signal into deterministic and unresolved components. Auto and cross correlation techniques were used to correlate the deterministic total temperature and velocity components (acquired using a slanted hot-film probe at the same measurement locations) and the gradients, distributions and relative weights of each of the terms of the average passage equation were then determined.

Based on these measurements it was observed that the stator wakes, hub leakage flow region, casing endwall suction surface corner region, and the casing endwall region away from the blade surfaces were the regions of highest losses in total pressure, lowest efficiency and highest levels of unresolved unsteadiness. The deterministic unsteadiness was found to be high in the hub and casing endwall regions as well as on the pressure side of the stator wake. The spectral distribution of hot-wire and kulite voltages shows

that at least eight harmonics of all three rotor blade passing frequencies are present at this measurement location. In addition to the basic three rotor blade passing frequencies (R1, R2 and R3) and their harmonics, various difference frequencies such as (2R1-R2) and (2R3-R2) and their harmonics are also observed. These difference frequencies are due to viscous and potential interactions between rotors 1, 2 and 3 which are sensed by both the total pressure and aspirating probes at this location.

Significant changes occur to the stator exit flow features with passage of the rotor upstream of the stator. Because of higher convection speeds of the rotor wake on the suction surface of the downstream stator than on the pressure side, the chopped rotor wake was found to be arriving at different times on either side of the stator wake. As the rotor passes across the stator leading edge, the wakes start increasing in size and the corner region starts reducing in size. The hub leakage flow region starts contracting in the circumferential direction and starts moving radially. Some of the stator hub wall flow is then transported across the stator passage and deposited on the pressure surface of the stator.

By correlating the deterministic total temperature and the velocity components an attempt was made to evaluate the deterministic heat-flux distribution and the levels of each of the terms of the average passage equation system. The deterministic heat-flux terms were seen to be most significant in the stator wakes away from the endwall regions. The dominant terms in the average-passage equation system away from the endwalls were due to the tangential gradient compared to the radial gradient terms and both the terms were found to be of equal importance in the hub and casing endwall regions. Gradients due to the revolution aperiodic terms was found to be the smallest at all locations downstream of the stator.

LIST OF FIGURES

LIST OF TABLES

NOMENCLATURE

a	Coefficient of the Collis-Williamson formulation (equation 3.7)
A_c	Area of the choked orifice of the aspirating probe
$ADPAC$	Denotes results from the Advanced Ducted Propfan Analysis Code (proprietary of Allison Engine Company)
AP	Denotes Aspirating Probe
$ASDF$	Auto spectral density function (equation 2.22)
AT	Denotes area traverse mechanism
b	Coefficient of the Collis-Williamson formulation (equation 3.7)
B	Bias
BPF	Blade passing frequency
C	Aspirating probe hot-wire calibration constant
c	Chord length (m)
CCW	Counter clockwise direction of rotation
c_p	Coefficient of specific heat at constant pressure
C_{pt}	Total pressure rise coefficient $C_{pt} = \frac{(P_o - \overline{P}_{s1})}{(\overline{P}_{o1} - \overline{P}_{s1})}$
$C_{pt_{ijk}}$	Instantaneous total pressure rise coefficient (equation 3.14)
CW	Clockwise direction of rotation
d	Diameter of the hot-wire
$DS2$	Downstream of stator 2
$DS3$	Downstream of stator 3
E	Hot-wire output voltage
f	Frequency bin width for spectral distribution
F	Clock frequency of data acquisition (Equation 2.1); Body force terms

FFT	Fast Fourier transform of a function
FFU	Flow function used to evaluate performance pressure losses (equation 2.9)
FHP	Denotes five hole probe
$H(t)$	Gate function used in ensemble averaging
H_o	Stagnation Enthalpy
IGV	Inlet guide vane
k	Thermal conductivity of the fluid
KUL	Denotes Kulite Probe
l	Hot-wire length
LE	Leading edge
m	Coefficient of the Collis-Williamson formulation (equation 3.7)
M	Mach number at the wire plane
m_{cor}	Corrected weight flow through the compressor (kg/s) (equation 2.3)
m_{uncor}	Uncorrected weight flow through the compressor (kg/s)
n	Aspirating probe hot-wire calibration constant
N	Shaft rotational speed (RPM); Number of measurements
N_b	Number of blades per rotor
N_{cor}	Corrected rotor rotational speed (RPM) (equation 2.2)
N_{pb}	Discretization of a blade passage
N_{rev}	Number of revolutions of data acquired
N_s	Shaft Rotational Speed (RPS) ($N_s = N/60.0$)
N_{uncor}	Uncorrected rotor rotational speed (RPM)
Nu	Nusselt number
p	Static pressure
P	Pressure

PS	Pressure side
r	Recovery factor for hot-wire
R	Universal gas constant; Correlation function (with appropriate subscripts); Mixing stress (equation 6.6)
R_s	Hot-wire anemometer bridge series resistance
R_w	Hot-wire resistance at the operating temperature
Re_d	Reynolds number based on the hot-wire diameter
$R1$	Denotes Rotor 1
$R2$	Denotes Rotor 2
$R3$	Denotes Rotor 3
RMS	Root mean square value
s	Blade spacing
S	Precision error
$S_{\overline{x}}$	Precision index
$S1$	Denotes Stator 1
$S2$	Denotes Stator 2
$S3$	Denotes Stator 3
SS	Suction side
T	Temperature; Rotor blade passing period; Torque
TE	Trailing edge
TR	Total temperature rise coefficient $TR = \frac{(T_o - \overline{T_{o\,1}})}{(\overline{T_{o\,10}} - \overline{T_{o\,1}})}$
Tu	Turbulent Intensity based on overall unsteadiness (equation 2.20)
U	Total uncertainty
u'	Turbulent fluctuations in velocity in the axial direction
U_t	Rotor blade tip speed

v'	Turbulent fluctuations in velocity in the tangential direction
V	Absolute velocity (m/s)
w'	Turbulent fluctuations in velocity in the radial direction
W_i	Incremental weight flow (equation 2.6 and 2.14)
X	Value of measurement variable

Greek Letters:

α	Absolute flow angle measured from the axial direction
β	Absolute flow pitch angle; bias error
γ	Ratio of specific heats
δ	Ratio of the absolute total pressure at the inlet to compressor and the static pressure at sea level conditions (14.69 psia); total measurement error
ΔA_i	Incremental area used in performance calculation
Δk	Time shift used in cross correlation of signals
ΔT_o	Total Temperature Rise
ϵ	Precision error
ϵ_D	Deterministic eddy diffusivity of heat
ϵ_H	Eddy diffusivity of heat
ζ	Total pressure loss (equation 4.5)
η_{isen}	Isentropic efficiency
η_{temp}	Temperature based isentropic efficiency (equation 2.17)
η_{torque}	Torque based efficiency (equation 2.18)
θ	Ratio of the absolute total temperature at the inlet to compressor and the static temperature at sea level conditions (288.15 K)
λ	Blockage factor (with subscripts)
Λ	Mixing heat-flux (equation 6.7)

μ	Absolute viscosity of the fluid; Average value
ν_T	Eddy diffusivity for momentum transfer
ρ	Fluid (air) density; Cross-correlation function (with subscripts) (equation 3.30)
τ	Clearance height (rotor tip or stator hub); Fraction of rotor blade passing period; Shear stress (with subscripts)
ω	Vorticity
Ω	Rotation rate

Subscripts:

1	Inlet to IGV
1.....10	Indicates stations on the compressor (Figure 2.2)
BA	Denotes blade aperiodic component
BP	Denotes blade periodic component
cor	Indicates corrected condition
i	Indicates number of hot-wire; Ensemble averaging index indicating rotor revolution; Also indicates the radial location of pressure and temperature measurement for mass flow calculation (equations 2.6 and 2.14)
IGV	Indicates Inlet Guide Vane
in	Denotes inlet to compressor
IN	Indicates Inviscid
j	Ensemble averaging index indicating rotor blade count
k	Ensemble averaging index indicating position in rotor blade passage
l	Indicates local value
m	Indicates mean value
net	Indicates net value

o	Indicates total or stagnation value
or	Rise in stagnation value
$pole$	Indicates pole rakes
r	Denotes radial component or coordinate direction; Indicates ratio
RA	Denotes revolution aperiodic component
RP	Denotes revolution periodic component
s	Indicates static value; Indicates shaft resolved component
$strut$	Indicates struts
$uncor$	Indicates uncorrected condition
V	Indicates viscous
wi	Indicates related to wire
z	Denotes axial component or coordinate direction
θ	Denotes tangential or circumferential component or coordinate direction
τ	Denotes time delay for cross correlation
∞	Indicates free-stream value

Superscripts:

$'$	Denotes unresolved component
$-$	Denotes area/mass/time/passage average
$*$	Denotes conditions at the sonic orifice
$\tilde{}$	Denotes ensemble average

ACKNOWLEDGMENT

This work was sponsored by Allison Engine Company, NASA Lewis Research Center (NAG 3-1745, NAG 3-1222), and Rolls Royce Inc. We would like to thank the technical monitors and other individuals in these organizations who provided technical assistance and comments in all phases of this work, including the installation of the facility and performance evaluation, development of instrumentation, data acquisition and interpretation. These individuals are as follows:

R. Fagan, E. Hall, and P. Tramm of Allison Engine Company

R. Strazisar, J. Adamczyk, K. L. Suder, D. Van Zante, and M. Hathaway of NASA Lewis Research Center

R. Moritz and M. Howard of Rolls-Royce, Inc.

The authors also wish to acknowledge United Technologies Research Center (UTRC) / Pratt and Whitney (P&W) Aircraft Division of United Technologies Corporation for donating the multistage compressor facility and to H. Weingold, E. Canal and M. Christianson of UTRC/P&W Aircraft for providing valuable advice, help in installing the facility, in shakedown testing, and in performance evaluation. Installation of such a major research facility could not have been completed without funding from The Pennsylvania State University and help from many individuals, notably; G. Sayers, H. Houtz, B. Dillon, J. Fetterolf, G. Gurney, and R. Auhl.

Chapter 1

INTRODUCTION

Knowledge of both steady and unsteady flow in turbomachinery is essential for accurate assessment, analysis, and design. With increasing emphasis placed on improving performance, increasing efficiency, reducing weight and increasing life cycles of engines, prime importance is placed on the compressor. As higher cycle pressure ratios are achieved, importance is placed on reducing losses. This presents compressor design engineers with the dual requirements for high pressure ratios and high compression efficiency, while maintaining adequate surge margin for safe, transient operation. As the cycle pressure and temperature ratios are increased, the optimum bypass ratio increases, so the core engine size reduces and deleterious viscous flow and blade-row interaction effects make the achievement of high efficiency more difficult, particularly in the aft stages of the high pressure core compressors. Even though present day compressor design has reached polytropic efficiency levels of around 90%, it is felt that there is potentially reducible inefficiency levels associated with the interaction between the blades and the near end-wall flow phenomena.

Unsteady interactions are known to affect various aspects of turbomachinery performance, including: (1) blade loading, (2) stage efficiency, (3) heat transfer, (4) noise generation and (5) energy transfer. In fact, the fundamental mechanism of energy transfer in turbomachines is the unsteady throughflow. However, virtually all existing turbomachine design systems are based on the assumption that the flow is steady in time. While the importance of including unsteady effects in the turbomachinery design process is generally accepted, the specific influence of unsteady interactions on the time averaged flow is not well understood. Consequently, it is not obvious how these effects should

be integrated into turbomachinery component design systems. A more complete understanding of the unsteady flow in turbomachinery components is required to integrate these effects in current and next generation design and analysis tools and may, therefore lead to an improvement in our ability to predict the performance of turbomachines and to corresponding improvements in turbomachinery design practice.

The unsteadiness resulting from the relative motion of neighboring blade rows cause various interactions between the blade rows that may influence both the aerodynamic and structural behavior as well as noise emission of the rotor and stator blades of the turbomachine. The potential flow fields about a blade extend both upstream and downstream of the blade, and decay exponentially with a length scale of the order of a chord. The wake interaction refers to the unsteadiness induced at a blade row by the wakes shed by the blades of an upstream blade row and convected downstream. Owing to the slow decay of the wakes, the wake interaction persists significantly farther downstream than the potential flow interaction. In the endwall, the unsteadiness caused by the secondary and leakage flows and associated vortices also contribute to the blade row interactions. All earlier investigations in a multistage compressor, with the exception of Falchetti (1992) and Cherrett and Bryce (1992) were carried out in either low speed compressors or compressors having the same number of rotor and stator blades in every blade row. Hence, there is a need for detailed understanding of the physics of the flow in a high speed multistage compressor. This is one of the goals of the Penn State program.

The consistency between test and prediction data for multistage compressors is generally markedly worse near the endwalls, particularly near the blade tip. In fact, in many cases, due to this type of discrepancy, the computational fluid dynamics (CFD) results may be misleading in terms of the appropriate design changes for embedded blade rows in a multistage turbomachine. Unfortunately, these shortcomings may not be realized until after expensive rig testing and reblading have been performed. The conclusion is

that deviations between prediction and test data near the endwalls results from unmodeled mixing phenomena resulting from aerodynamic mechanisms which are introduced in the multistage environment. If suitable modeling procedures for these processes were available, then it is likely that significant improvements in multistage compressor (and turbine) performance and design cycle cost and time could be achieved. Given the ability to accurately account for these multistage mixing effects, an estimated 2-3% improvement in compressor adiabatic efficiency and 5% or greater improvement in compressor surge margin over current compressor designs might be achieved. Perhaps of greater importance is that the ability to rapidly analyze and alter compressor design with confidence using multistage CFD tools would result in a significant reduction in development time and expenses.

A systematic approach is essential in understanding the various flow phenomena, and their relative order of magnitude and interaction effects. It is only through this understanding that improvements can be made in performance and design of blading. The main approaches used to resolve this problem are either experimental or computational in nature. However, computational tools have not yet reached the stage where a successful analysis of a core compressor can be carried out. This is because, of limitations to the equation system, modeling of the various terms and the excessive computational time required by computers. So experimental investigations are very essential to acquire the basic knowledge of the various flow features and to develop models for the various correlation terms. Much of the present information is based on research carried out in cascades and single stage rig configurations (eg., Raj and Lakshminarayana (1973), Ravindranath and Lakshminarayana (1980), Suder et al. (1987) in transonic compressors etc). Very few investigations exist in multistage compressors (Dring et al. (1986), Cherrett et al. (1992) etc). A review of the work done in multistage compressors will be conducted in the next section. The design of these compressors is still based on empirical

correlations derived from single stage and cascade testing. The Penn State multistage compressor facility research program which is representative of the aft stages of a high pressure core compressor hopes to address the above mentioned issues through detailed experimental studies.

1.1 Literature Review

Further improvements in the design, leading to improvements in efficiency, stage loading, life, compactness and stability rely heavily upon developing improved understanding of the flow field and in addition, the improvements in computational methods require detailed measurements to be taken in representative high speed multistage compressors to create data bases for both the design and the development purposes. Very few investigations have been carried out in multistage axial flow compressors to date. Some of the work done in the field of multistage axial flow compressors is reviewed below. The review is divided into four subsections: (1) Steady flow in multistage compressors , (2) Unsteady flow investigations in multistage compressors including blade-row interaction phenomena (3) Spanwise mixing phenomena and (4) Computational and analysis methods.

1.1.1 Steady flow in multistage compressors

Robinson (1992) has provided a critical review of the recent advances in understanding the nature of the flow in multistage compressors. One of the earliest investigation of the flow field in a multistage environment was reported by Smith (1970), who measured the annulus wall boundary layer growth and the velocity profiles at the exit of each of the stages. Wisler (1984) describes the results of the NASA sponsored programs on the GE 4-stage low speed compressor rig studying multistage compressor exit flow phenomena.

This study had the objective of reducing the losses associated with endwall phenomena through modifications to baseline velocity triangles and by tailoring airfoil shapes. Dring and Joslyn (1986) provided an assessment on the through flow analysis of a low speed two stage axial flow compressor by making detailed comparisons between computed and experimental results. Recent aerodynamic studies include area traverses of a total pressure probe at the exit of stator 2 in a highly loaded compressor (Calvert et al. (1989)) and radial traverses of total pressure and total temperature at the exit of each blade row of a high speed multistage compressor (Falchetti (1992)). Robinson (1992) describes the results of detailed experimental investigations carried out in the Cranfield low speed compressor test rig using various types of stator blading to study the effects of end-bend on stator exit flow properties.

1.1.2 Unsteady flow investigations in multistage compressors and measurement limitations

Almost all of the above investigations were conducted with steady state instrumentation (wedge probes, pitot tubes, thermocouples etc). However, flow in a turbomachine is inherently unsteady. The unsteadiness resulting from the relative motion of neighboring blade rows cause various interactions between the blade rows that may influence both the aerodynamic and structural behavior as well as the noise emission from the rotor and stator blades of turbomachines. The potential flow interaction between the 2 blade rows moving relative to each other arises because of the circulation about the blades and the potential field. The potential flow fields about a blade extend both upstream and downstream of the blade, and decay exponentially with a length scale of the order of a chord. The wake interaction refers to the unsteadiness induced at a blade row by the wakes shed by the blades of an upstream blade row and thence convected downstream (Binder et al. (1985)). Owing to the slow decay of the wakes, the wake interaction persists significantly farther

downstream than the potential flow interaction. In the endwall region, the unsteadiness caused by the secondary flows and associated vortices also contribute to the blade row interactions.

Das and Jiang(1984) used three-hole cylindrical probes containing fast response pressure transducers in association with digital data acquisition system and ensemble averaging technique to study the flow field and distribution of the flow parameters in rotating stall regime in a three stage low speed axial flow compressor. Stauter et al. (1991) and Stauter (1992) provide details of unsteady flow field acquired from laser doppler velocimetry in a two-stage low speed axial flow compressor. The data reveal the complex motion associated with the wake transport and the leakage flow. Cherrett and Bryce (1992) conducted radial traverses of a high frequency pressure transducer behind the first three stages of a high speed multistage compressor operating at three different throttle settings. The analysis of the data revealed both periodic and random fluctuations in the flow field.

The above review shows that almost no measurements have been made of the unsteady temperature field in a multistage compressor. Time-resolved measurement of gas total temperature has always been a very difficult task. Conventional thermocouples lose frequency response above 1 kHz while compensated thermocouples are yet to be demonstrated. Constant current hot-wire techniques are also limited to low frequencies unless the fluctuations are small compared to the mean. Electronically compensated, thin-wire resistance thermometers operated at very low overheat ratios exhibit less sensitivity to velocity fluctuations than do conventional constant current hot-wires and have been used to measure temperature at 5 to 10 kHz. The electronic compensation is a function of free-stream conditions, however, requiring readjustment as the mean flow changes. More complex techniques using multiple constant temperature hot-wires have been demonstrated in low speed incompressible flow fields. However, these techniques are not easily extendable to high speed compressible flows with high dynamic pressure such as those

found in turbomachinery configurations.

Ng and Epstein (1983) reported the development of a piggy-backed high frequency total temperature probe (aspirating probe) for use in unsteady compressible flows. The aspirating probe has been used by Ng and Epstein (1985) to measure the time-resolved total temperature and pressure in a transonic compressor. Norton et al. (1989) used the combination probe to measure the total pressure fluctuations downstream of a high aspect ratio fan. Unfortunately they could not calibrate the wires, so they do not report any total temperature measurements. Kotidis and Epstein (1991) reported instantaneous total temperature measurements using the aspirating probe downstream of a transonic compressor rotor to resolve the issue of radial mixing.

Van Zante et al. (1994) improved the original design of the aspirating probe of Ng and Epstein (1983) by using platinum iridium alloy hot wires and measured instantaneous total temperature and total pressure downstream of a transonic axial flow compressor rotor. The main advantage of the NASA probe (Van Zante, 1994) over the earlier ones is the data from the 2 wires is used to obtain total pressure measurements which reduces the size of the probe and consequently the blockage. It is the NASA configuration that will be used in the present investigation.

Very little information is available on the three-dimensional unsteady velocity field in a multistage axial flow compressor. Only Capece and Fleeter (1987), Wisler et al. (1987), Stauter et al. (1991), Stauter (1992), Manwaring and Fleeter (1992) and Falchetti (1992) have reported unsteady velocity measurements using either cross wire probes or LDV/L2F methods. Except for the measurements by Falchetti (1992) using L2F, all other measurements were carried out in low speed compressors. Much of the unsteady velocity measurements are limited to single stage compressors and turbines. Kuroumaru et al. (1982) and Goto (1992) have measured unsteady velocity field as well as the Reynolds stress components in single stage compressors. Sharma et al. (1983) used a three sensor

hot-film probe to measure the unsteady three-dimensional velocity and Reynolds stress components in an axial flow turbine stage.

In spite of these advances, there is a lack of cohesive and detailed understanding of the flow features. Furthermore, most of the investigations reviewed earlier (with the exception of those due to Smith (1970), Calvert et al (1989), Falchetti (1992) and Cherrett and Bryce (1992)), were carried out in very low speed facilities, where there is no significant temperature rise. Hence, there is a need for detailed understanding of the multistage compressor flow phenomena, especially the role played by temperature fluctuations, in a high speed multistage compressor.

1.1.3 Spanwise mixing effects in multistage compressors

Flow mixing is an important aspect of compressor aerodynamic performance and has become a topic of increasing interest in recent years. Conventional turbomachinery design techniques normally idealize the flow as lying along surfaces of revolution in an axisymmetric frame of reference (a stream sheet). Blade designs are formulated based on the presumed velocity distributions at the blade passage inlet and exit for each stream sheet. The stream sheet approach, by itself, ignores mixing between stream sheets as this was originally considered a minor effect. Mixing, in this context, refers to exchanges of mass, momentum, and/or energy between stream sheets, and thus can imply either convection from secondary flows or diffusion, as well as the existence of shear stresses. The trend in gas turbine compressor designs towards higher stage loading and lower aspect ratios has caused mixing effects to be more easily detected and of noticeably greater importance.

Early measured data for highly loaded axial compressors indicated that high temperature endwall fluid was somehow being displaced to the blade midspan, thus dramatically affecting losses (real or apparent). These deviations were attributed to unmodeled mixing phenomena resulting in a redistribution of spanwise flow properties, and a considerable

that the inclusion of mixing was found to be crucial in accurately predicting spanwise variations of exit total temperatures in multistage machines.

Wisler et al. (1987) conducted detailed flow measurements in a large scale low speed four-stage axial flow compressor using ethylene gas tracer and hot-wire anemometry techniques. It was concluded that both secondary flow and turbulent diffusion were found to play important roles in the mixing process. Lakshminarayana (1987), indicated that the definition of turbulent diffusion used by Gallimore and Cumpsty (1986) and by Wisler et al. (1987) includes the periodic velocity components. He suggested that the velocity should be decomposed into a time mean averaged value, periodic component and random component. The periodic component is a velocity component and cannot be considered turbulence. Hence, the term "turbulent diffusion" should only be used to identify the diffusion caused by the random fluctuations and that it should not include the periodic fluctuations due to upstream wakes.

De Ruyck and Hirsch (1988) presented a radial mixing calculation method where both convective and turbulent mixing processes were included. They derived the secondary flows needed for convective mixing from pitch averaged vorticity equations combined with integral methods for 3-D endwall boundary layers, 3-D profile boundary layers and 3-D axisymmetric wakes and computed the convective transport due to secondary flows explicitly. The through flow program was applied to a cascade flow and 2 single stage rotor flows and they found that turbulent diffusion was the most important mixing mechanism.

Leylek and Wisler (1990) presented results from 3-D Navier-Stokes analyses and experiments to quantify the phenomena of spanwise mixing in compressors. A 3-D Navier Stokes solver with k-ϵ turbulence model was used in the investigation and the results were compared against the experimental data of Wisler et al. (1987). They concluded that both secondary flow and turbulent diffusion were shown to play important roles in the mixing process and can contribute to both spanwise and cross-passage mixing and the relative

departure from design expectations. In the rear stages of multistage machines, where blade aspect ratios are typically very low, this mixing can substantially influence the spanwise distributions of thermodynamic properties, making it difficult to pinpoint loss sources from measured data.

In the recent past a lot of attention has been focused on this aspect both from experimental and computational view points. Wennerstrom (1991) has provided an excellent review of the predictive efforts for transport phenomena in axial flow compressors. Adkins and Smith (1982) were the first to recognize the potential importance of mixing. They developed a model for calculating the magnitude and the effect of mixing on the multistage compressor performance. It was based on inviscid, small perturbation secondary flow theory and they concluded that secondary flows are responsible for deviation in blade row turning from 2-D cascade theory. Spanwise mixing was modeled as a diffusion process determining local values of mixing coefficients from the calculated secondary flow radial velocities. The model includes the secondary flow due to main-stream non free-vortex flow, end-wall boundary layers, blade end clearances, blade end shrouding, and blade boundary layer and wake centrifugation. Whitfield and Keith (1985) improved the Adkins and Smith (1982) wake model to include the effect of blade loading. The radial transport was predicted using simplified momentum equations in the radial and streamwise directions.

Gallimore and Cumpsty (1986) argued that the spanwise mixing model based on convection by radial velocity was not a very realistic model describing spanwise mixing. They concluded from ethylene gas tracer measurements in two low-speed four stage compressors that the dominant mechanism causing spanwise mixing in the latter stages of multistage compressor was a random, turbulent type, diffusion process and the contribution from convection by deterministic radial secondary flows, was small. Gallimore (1986) incorporated the above model in an axisymmetric through flow program and showed

importance of each of these mechanisms was configuration and loading dependent.

It is not unreasonable to assume that individual airfoil designs could determine the dominant mechanism in any case. A detailed unified throughflow modeling formulation was subsequently presented by Li and Chen (1992) which mathematically dictated that spanwise mixing was the result of molecular motion (viscous stresses), turbulent diffusion, and circumferential non-uniformities (secondary flows) to varying degrees. Numerous throughflow calculation procedures have been developed (Howard and Gallimore (1992), Kiousis et al. (1992), Dunham (1992)) which include the effects of spanwise mixing demonstrating the improved modeling accuracy which is available when these effects are properly modeled.

1.1.4 Computational Efforts and Analysis

Computational fluid dynamics (CFD) techniques have rapidly gained popularity during the past decade as an inexpensive means of approximating blade passage flow behavior. CFD techniques are currently commonly used in the compressor blade design process not strictly as a design tool but as a design analysis tool. Much of the current practice in the analysis of multistage compressor flows is to use the system of the passage averaged equations (for a detailed description of this system please refer to Lakshminarayana (1996), Chapter 4, section 4.2.3). These equations are solved using streamline curvature techniques by assuming the flow field is axisymmetric at the inlet of each blade row (for example, the Allison Axisymmetric Design Code, Fagan (1991)). The next step is to extend the CFD techniques to non-isolated blade rows. Several researchers have developed multistage turbomachinery analysis techniques based on the concept of coupling multiple isolated blade row analyses through through specialized boundary conditions. These so-called "mixing-plane" approaches yield relatively rapid solutions for the complex multistage turbomachinery flow problems (Denton (1979), Dawes(1992) and Hall

(1996)).

Without the simplification of a circumferential averaging procedure (a mixing plane), CFD analyses based on the Reynolds-averaged Navier-Stokes equations must employ a time-accurate solution strategy to account for the aerodynamic interactions resulting from relative blade motion in multistage turbomachinery. Erdos et al. (1977) were the first to attempt to compute the time-dependent rotor/stator aerodynamic interaction in a compressor stage using sophisticated CFD boundary condition techniques. Dramatic increases in computational power and algorithmic efficiency have led to many more applications of this type of analysis (e.g. Rai (1987), Gundy-Burlet and Rai (1989), Hall et al. (1995)). Unfortunately, the designer has neither the time to perform such detailed analyses nor the understanding of the implications of unsteady flow phenomena to effectively modify a design based on data of this form.

A recent approach proposed by Adamczyk (1985) is the *average-passage* approach. In this approach, the actual flow through a blade row is approximated by a representative flow which is assumed to be steady (relative to the blade row), spatially periodic, and somehow representative of the "average" flow condition experienced by that particular blade row. Industry-wide observations of mixing in multistage turbomachines, and the desire for this averaged-passage flow description led to the development of the "average-passage" flow model by Adamczyk (1985). The average-passage flow model provides a rigorous mathematical framework for what every compressor designer understood - that deterministic flow mechanisms play an important role (contributions to mixing and influences of nearby blade rows) in multistage compressors.

In this method the instantaneous quantity (velocity component, pressure and temperature) is decomposed into deterministic (associated with shaft and blade frequency) and unresolved (not associated with shaft and blade frequency) components, and the unsteady Navier-Stokes equations are ensemble averaged and then time averaged to derive

the "average-passage" flow equations. The drawback to this approach is that the resulting equations contain more unknowns than there are equations, due to a number of terms which arise due to the nonlinearity of the governing equations, which must be modeled from experimental insight or empiricism. This is the so-called *closure* problem which results from the averaged form of the equations. In the case of the Reynolds-averaged Navier-Stokes equations, the closure problem is often remedied through the use of any of a wide variety of turbulence models which attempt to define the "average" influence of the turbulence through other known variables to close the system of equations. For the "average-passage" equations, closure schemes for the deterministic stress and heat-flux terms are necessary. One of the objectives of this research is to provide an understanding of the nature and magnitude of these terms aft of an embedded stator stage.

Even though there has been considerable research activity directed at understanding flow-field in multistage compressors and the phenomena of spanwise mixing and blade row interactions, there have been very few attempts to understand the physical nature of the unsteadiness. The information available for this research is scanty and major advances are needed to derive and improve the understanding and the data base in order to improve the overall design process and increase the efficiency, performance and stability of multistage axial flow compressors. This is a major objective of this thesis research.

1.2 Objectives

The flow field in a multistage compressor is three-dimensional, unsteady, and turbulent with substantial viscous effects. Some of the specific phenomena that has eluded designers include the effects of rotor-stator and rotor-rotor interactions and the physics of spanwise mixing of velocity, pressure, temperature and velocity fields. An attempt will be made, to resolve experimentally, the unsteady pressure, temperature and velocity fields

downstream of the second stator of a multistage axial flow compressor which will provide information on rotor-stator interaction effects and the nature of spanwise mixing in an embedded stator of a three stage axial flow compressor.

The major objectives of the thesis are:

1. To understand the nature of the unsteady three-dimensional pressure, temperature and velocity field in an embedded stator of a multi-stage axial flow compressor with a view of identifying sources and magnitudes of unsteadiness and losses.

2. To understand the physics of rotor-stator interaction and their effects on the unsteady total pressure and temperature field downstream of an embedded stator.

3. To study the influence of various components of the unsteadiness derived through the decomposition on the flow field, their gradients and levels.

4. To correlate the periodic, aperiodic and unresolved components of velocity and total temperature (velocity-temperature correlation) to understand the phenomena of thermal energy transport in a multistage compressor.

5. To evaluate the magnitude and nature of the various terms of the average-passage equation system, their gradients in the radial and circumferential direction and their relative weights so as to provide guidance to CFD specialists and compressor designers.

6. To evaluate the magnitude of the uncertainty in various measurement variables including velocity-temperature correlations.

7. To provide benchmark quality data to validate various flow models and solvers for multistage compressor flow field analysis and prediction.

1.3 Method of Approach

In order to accomplish the above objectives, an experimental investigation of the steady and the unsteady flow downstream of the second stator of a three stage axial flow compressor representative of the aft stages of a high pressure core compressor is undertaken. Detailed area traverse measurements using pneumatic five hole probe, thermocouple probe, semi-conductor total pressure probe (Kulite) and an aspirating probe downstream of the second stator were conducted at the peak efficiency operating condition. An area traverse mesh of 31 tangential by 25 radial nodes spanning two stator blade passages for the pneumatic and total pressure probes and 19 tangential by 17 radial nodes spanning one stator blade passage for the aspirating probe was used to discretize the flow field with clustering in the stator wake and in the endwall regions. Care was taken to ensure that the tangential and radial locations were the same for all the measurement instrumentation. The steady state data was acquired with adequate time averaging and the unsteady data was acquired using a high speed data acquisition system with rotor 2 based triggering and clocking. Once again care was taken to ensure that the trigger location stayed the same for all the measurements. In order to ensure quality of data, pre- and post-calibration of all the instrumentation was conducted. The unsteady data was then reduced through an ensemble averaging technique which splits the signal into deterministic and unresolved components. Various analysis methods like surface contour plots, passage average distributions, blade-to-blade distributions, temporal distribution and hub-to-tip distributions of the rotor exit flow along with spectral information is used to analyze the flow behaviour. Auto and cross correlation techniques are used to correlate the fluctuating total temperature and fluctuating velocity components (acquired using a slanted hot-film probe at the same measurement locations) and then determine the gradients, distributions and relative weights of each of the terms of the average passage equation. The flow chart

given in Table 1.1 gives an overall method of approach.

1.4 Organization of the Dissertation

This dissertation is organized into eight chapters including the present. The details of the test facility, control system, associated instrumentation, overall performance characteristics and blade row performance information are presented in Chapter 2. Chapter 3 gives full details of the high response instrumentation (aspirating and total pressure probes), their calibration and data reduction procedures and uncertainty analysis. Also covered in this chapter are the details of the data acquisition system and the complete methodology of data analysis including the ensemble averaging procedure and the average passage equation. Chapter 4 deals with the time-averaged results of the area traverse measurements at the exit of stator 2. Contour plots, blade-to-blade distributions, hub-to-tip distributions of passage averaged quantities of various time averaged quantities are used to qualitatively and quantitatively evaluate the stator exit flow. Chapter 5 deals exclusively with the unsteady total pressure and total temperature distribution. Contour and blade-to-blade distributions of RMS values of various unsteadiness in both temperature and pressure, temporal variations of stator exit flow, rotor 2 flow field at the stator 2 exit, spectral information and composite flow field descriptions are used to evaluate and interpret the unsteady flow field in the compressor. Use is made of the unsteady computations performed by Allison Engine Company on the Penn State compressor geometry. Chapter 6 evaluates the auto- and cross-correlations between the deterministic components of velocity and total temperature, their gradients, contour, blade-to-blade and hub-to-tip distributions of the various terms of the average passage equation system and their relative weights. This evaluation will result in identifying mechanisms of spanwise mixing and various loss and inefficiency generation sources identified in Chapters 4 and 5.

Table 1.1. Method of Approach

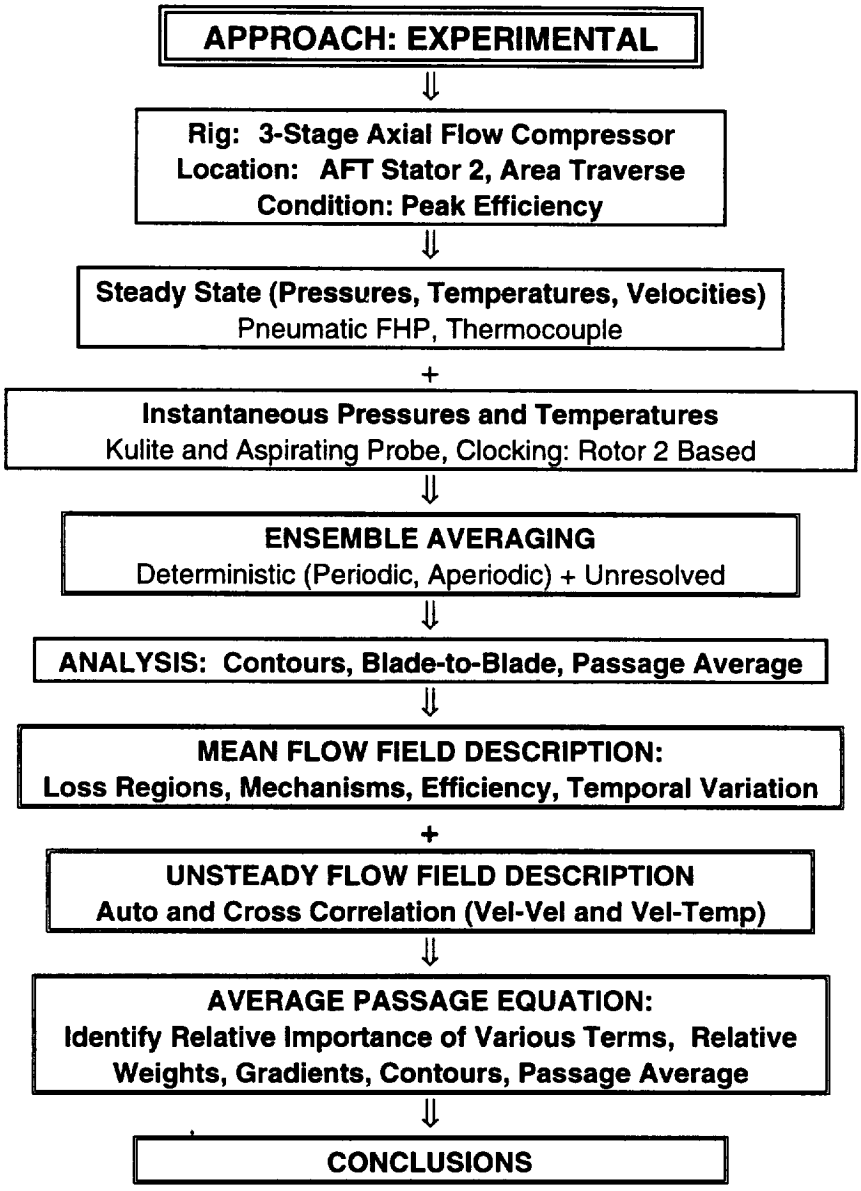

Summary and concluding remarks form the contents of Chapter 7 and the course of future work form the contents of Chapter 8. Several appendices have also been included in this thesis. Appendix A gives insight into uncertainty in scientific measurement and details of a general uncertainty analysis. Appendix B details the uncertainties of performance measurement, Appendix C deals with the uncertainties of unsteady total temperature and other measurement variables including the velocity-temperature correlations and the various terms of the "average-passage" equation system. Chapters 4, 5 and 6 list a table of uncertainties of all the derived quantities discussed in that chapter as well. Appendix D gives the development of the "average-passage" equation system itself.

Chapter 2

EXPERIMENTAL FACILITY AND PERFORMANCE CHARACTERISTICS

The measurements reported in this thesis were acquired using the Penn State Multi-stage Compressor Facility (PSU-MSCF). The compressor was donated to The Pennsylvania State University by Pratt and Whitney Aircraft of United Technologies Corporation. This compressor is similar in geometrical, aerodynamic and performance characteristics to the parametric series 3S1 and 3S2 compressors built by the Pratt and Whitney Compressor Group (Behlke et al. , 1979). This chapter details the description of the test rig, design parameters of the compressor including the blading, instrumentation, control and data acquisition systems. Results of the overall performance characteristics at various operating speeds, the inlet and exit flow fields, and the inter-stage and intra-stage performance maps are evaluated and discussed.

2.1 Test Facility Description

The test compressor is a three stage axial flow compressor consisting of an inlet guide vane row and three stages of rotor and cantilevered stator blading with a rotating hub. At the design operating point the compressor pumps a corrected mass flow of 9.448 kg/s at a total pressure ratio of 1.354, total temperature ratio of 1.10 and at a corrected torque based efficiency of 90.65%. Table 2.1 gives the general specifications of the compressor. The outer annulus wall has a constant diameter of 0.6096 m (24.0 in). The hub wall diameter varies from 0.5075 m (19.98 in) at the inlet to 0.5232 m (20.6 in) at the exit. All the stators are cantilevered from the outer annulus wall with a rotating hub drum. Rotor end seals are provided to control leakage flows at the rotor inlet and exit hub surfaces. All the blades are high quality airfoils, precision cast from high strength aluminum alloy.

Table 2.1. General Specifications of Test Compressor

Parameter	Value
Number of Stages	3
Design Corrected Rotor Speed	5410 rpm
Design Corrected Mass Flow	8.609 Kg/s
Design Overall Total Pressure Ration	1.354
Mass Averaged Peak Efficiency at 100% Corrected Speed (Torque Based)	90.65%
Tip Diameter	0.6096 m
Hub Diameter at inlet	0.5075 m
Hub Diameter at exit	0.5232 m
Blade Count (rotor)	70, 72, 74
Blade Count (stator)	71, 73, 75
Blade Tip Mach Number	0.5
Average Reynolds Number (Based on Stator 3 Chord Length and Axial Velocity)	244800
Average Hub to Tip Ratio	0.843
Average Diffusion Factor	0.438
Average Stage Flow Coefficient (V_z/U_t)	0.509
Average Reaction	0.570
Average Space Chord Ratio	0.780
Average Rotor Tip Clearance (static)	1.328 mm
Average Rotor Tip Clearance (dynamic)	0.667 mm
Average Stator Hub Clearance (static)	0.686 mm

The blades have circular shanks to provide rigid attachment to the ring and wheel carriers and accurate staggering capability. The mean-line blading design specifications are given in Table 2.2 and the representative profiles at hub, midspan and tip locations of all the rotors and stators are shown in Figure 2.1. All rotor and stator sections are NACA 65/CA airfoils (i.e., NACA Series 65 thickness distribution symmetrically distributed around a circular arc mean camber line). Minor modifications were made to the thickness distribution near the trailing edge to eliminate Series 65 hook. The inlet guide vane (IGV) is a NACA 400 series airfoil. Figure 2.2 shows all the representative airfoils at mid-span with the respective axial spacings and also the measurement locations. The variation of average dynamic tip clearances normalized by the local rotor span, as measured by UTRC for the three rotors as a function of speed is shown in Figure 2.3. The clearance is an algebraic average calculated from measurements at various circumferential locations. The compressor is supported in the test stand from the compressor inlet and exit flanges. Mounting is provided by an 0.875" diameter journal located low on each side of the inlet end flange and by a slot located low on each side of the exit end flange.

The compressor located on the test stand (Figure 2.4) consists of the following major components: drive assembly, compressor, inlet and exhaust ducting and the control and data acquisition system. The drive motor is a variable speed Siemens 500 H.P A.C. induction motor with a Siemens Simovert frequency controlled Inverter. The inverter is 3-phase, 460-volts, 6-60 Hz AC adjustable speed drive. The speed is changed through a speed control potentiometer on the main control system. The potentiometer can set the speed to within 1 RPM. The drive assembly comprises the induction motor coupled to the compressor via a 1:1.67 Philadelphia Gear speed increaser gear box and a Himmelstein MCRT 9-02T torque-meter. The cooling of the gear box is done with a water cooled heat exchanger and an oil pump. The torquemeter is of the non-contact shaft type with high static and dynamic accuracy. It has a full scale torque rating of 10,000 lb-in and

Table 2.2. PSU-MSCF Mean-Line Blading Design Specifications

Parameter	IGV	Rotor 1	Stator 1	Rotor 2	Stator 2	Rotor 3	Stator 3
No. of Blades	100	70	71	72	73	74	75
Dia. (m)	0.5569	0.5587	0.5603	0.5618	0.5632	0.5644	0.5659
Blade inlet mean camber angle (deg)	-6.40	52.97	46.48	53.72	48.91	52.45	47.01
Blade exit mean camber angle (deg)	26.60	27.50	14.53	27.38	16.49	27.59	21.33
Total Camber Angle (deg)	33.00	25.47	31.95	26.34	32.42	24.86	25.68
Chord Angle (deg)	13.50	-40.23	58.05	-40.55	32.70	-40.02	34.17
Chord (m)	0.01829	0.03218	0.03175	0.03132	0.03089	0.03089	0.03048
Space-chord Ratio	0.955	0.779	0.781	0.783	0.785	0.776	0.778
Thickness to Chord Ratio	0.060	0.065	0.085	0.065	0.085	0.065	0.085
Span (m)	0.05253	0.05093	0.04928	0.04783	0.04643	0.04516	0.04382
Ave. Tip Clearance (% Span)	—	1.423%	1.546% (hub)	1.330%	1.447% (hub)	1.463%	1.797% (hub)

All angles are measured with respect to axial direction. The tip clearances are dynamic for rotor (measured at 5500 rpm) and static for stator

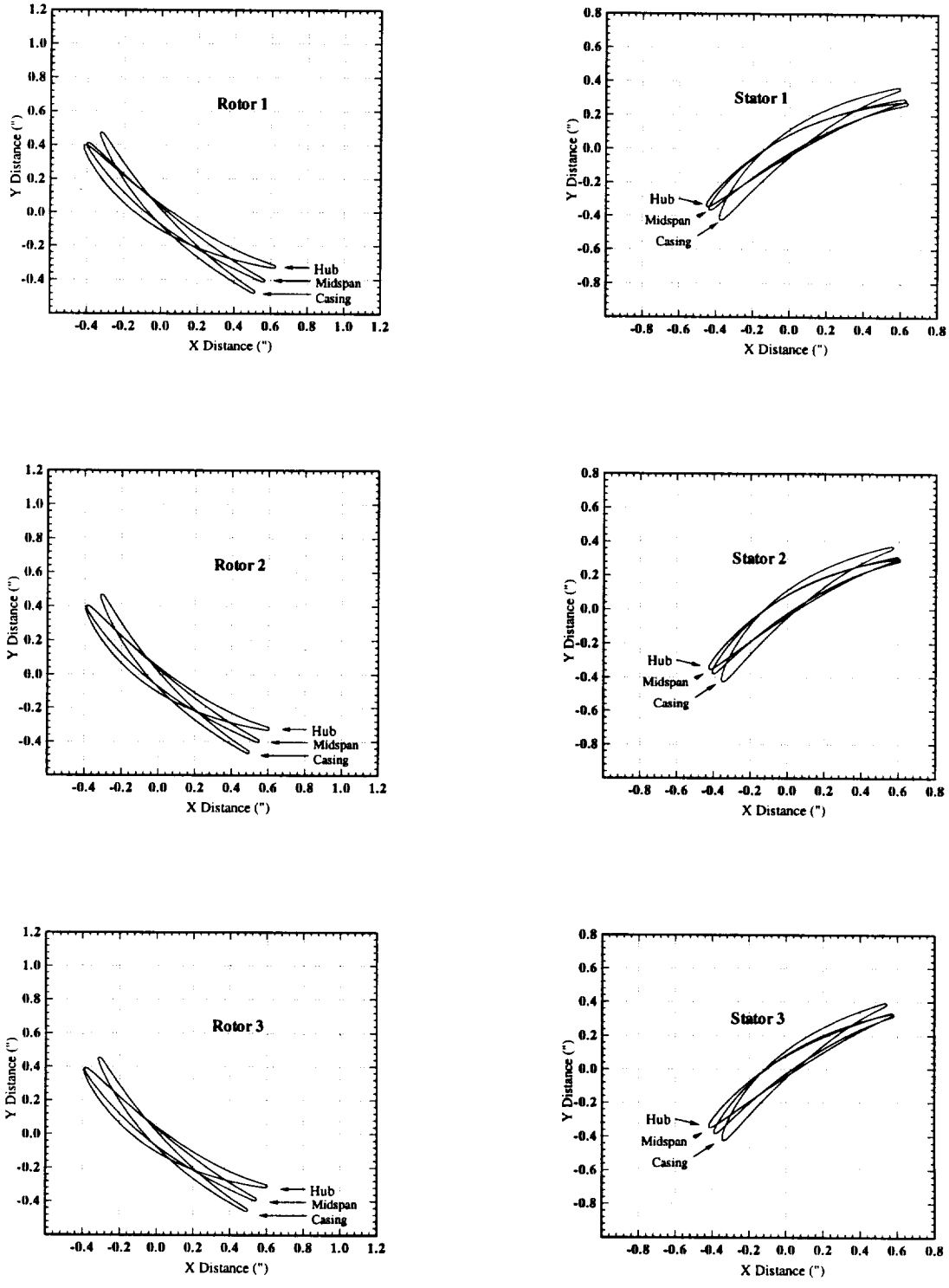

Figure 2.1. Representative Airfoil Profiles at Hub, Midspan and Tip

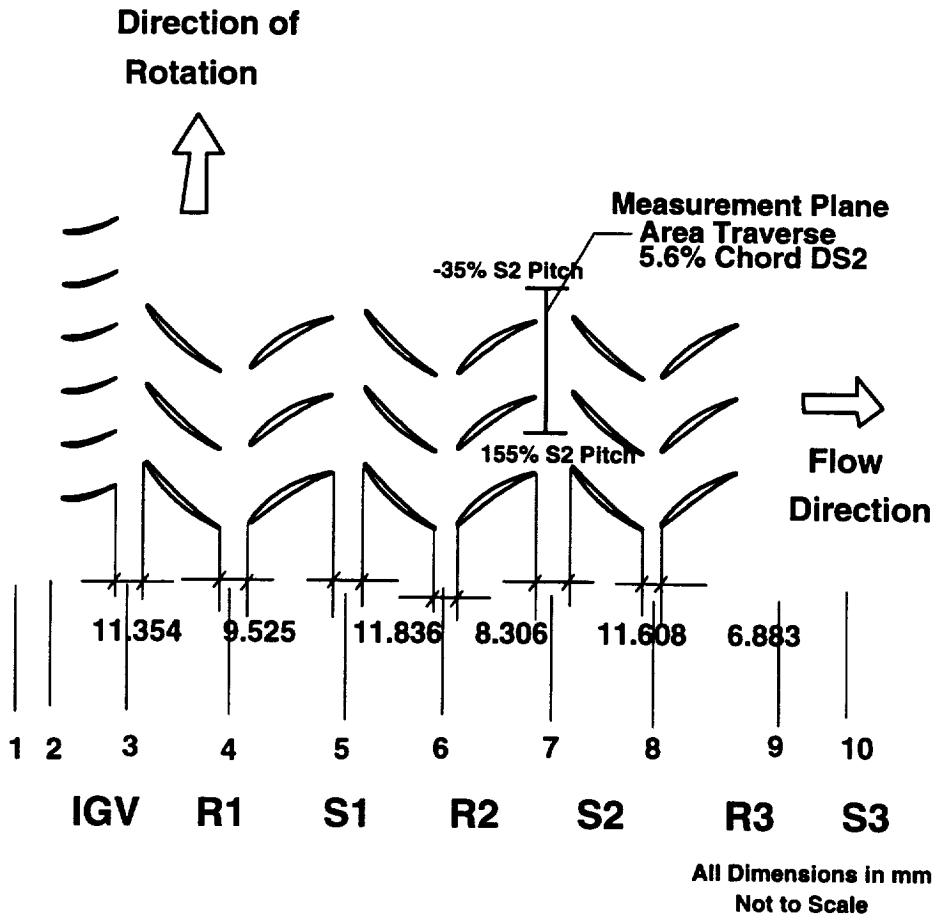

Figure 2.2. Unwrapped View of Test Compressor: Blade Profiles at Mid-Span

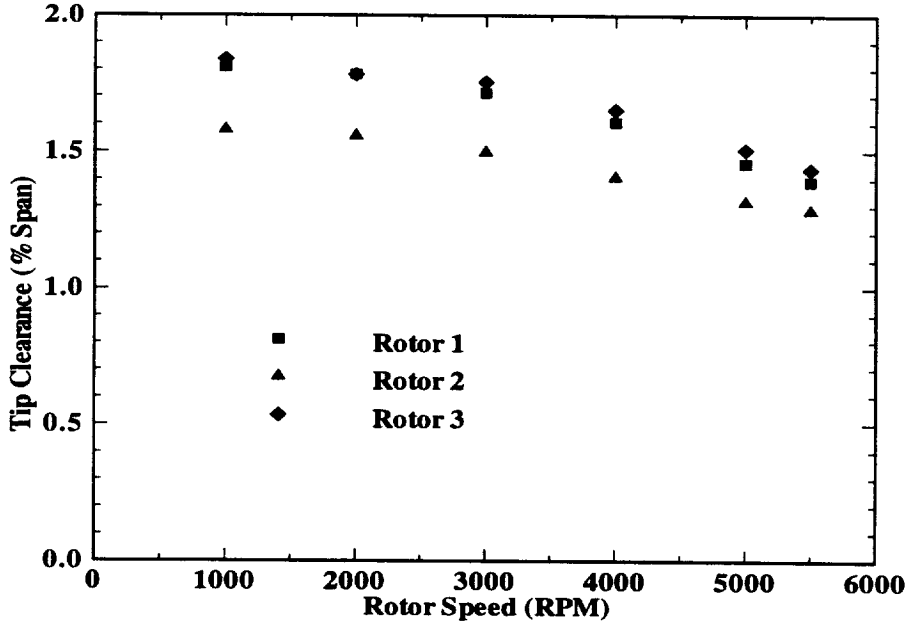

Figure 2.3. Variation of Average Dynamic Tip Clearance for all 3 Rotors at Different Speeds

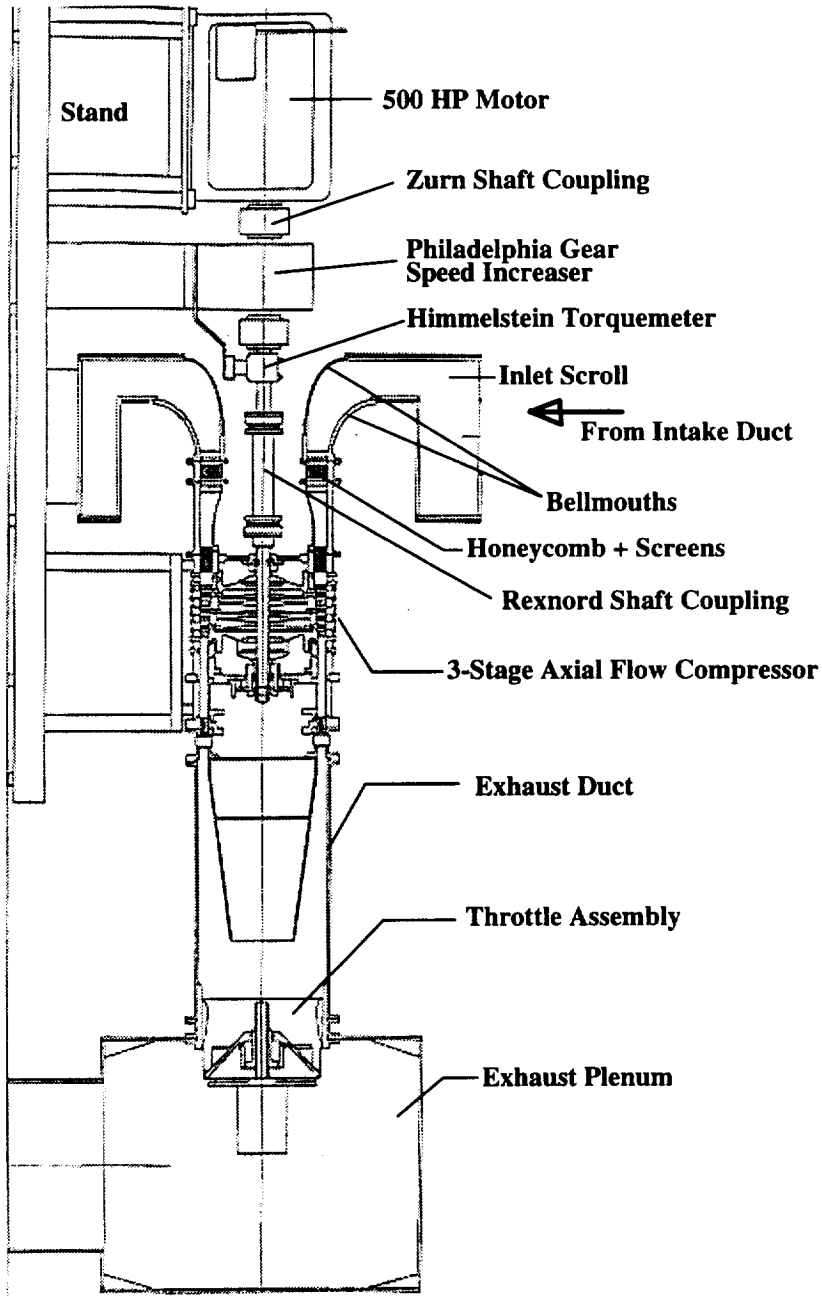

Figure 2.4. Test Stand Schematic Drawing of Compressor Rig

a speed rating of 0 to 7500 RPM. The non linearity is ±0.1% of full scale. It is also equipped with a standard type speed pickup (60 pulses per rev) that is used to determine the rotation speed of the compressor shaft. The torque is read on a 3kHz carrier amplifier (Himmelstein 61201 Universal Strain Gage Amplifier). The accuracy of the readout torque is ±0.05% full scale. A series of cloth and furnace filters are used at the inlet in conjunction with a Louver system to control the airflow into the compressor inlet duct. This filtered ambient air is ducted into the compressor inlet plenum via a silencer unit to reduce noise levels (the reduction is approximately 40 dB). The plenum (in the shape of a scroll) provides axisymmetric uniform velocity and temperature distributions at the inlet to the compressor. The flow path consists of a honeycomb section (0.25X2.0 inch cells) with screens (8 to 16 wires/inch) to assure a good flow distribution at inlet. A contraction section is also provided to accelerate the flow smoothly into the IGV section of the compressor. A throttle located downstream of the compressor is used to control the mass flow through the compressor. The throttle system includes a surge control device, which activates a quick release feature of the discharge throttle, for rapid stall recovery in the event of surge. The surge control system is explained in greater detail in a later section. The flow is exhausted through a duct into an exhaust anechoic chamber to reduce noise levels.

2.2 Control System

The safety and monitor control system for the compressor provides operational control of the facility at a central location. The panel display system provides continuous digital monitoring of all the critical operating parameters such as bearing temperatures, lubication oil temperatures, oil pressure etc. A 20 channel switch provides monitoring of non-critical temperatures. The schematic of the control system is given in Figure 2.5.

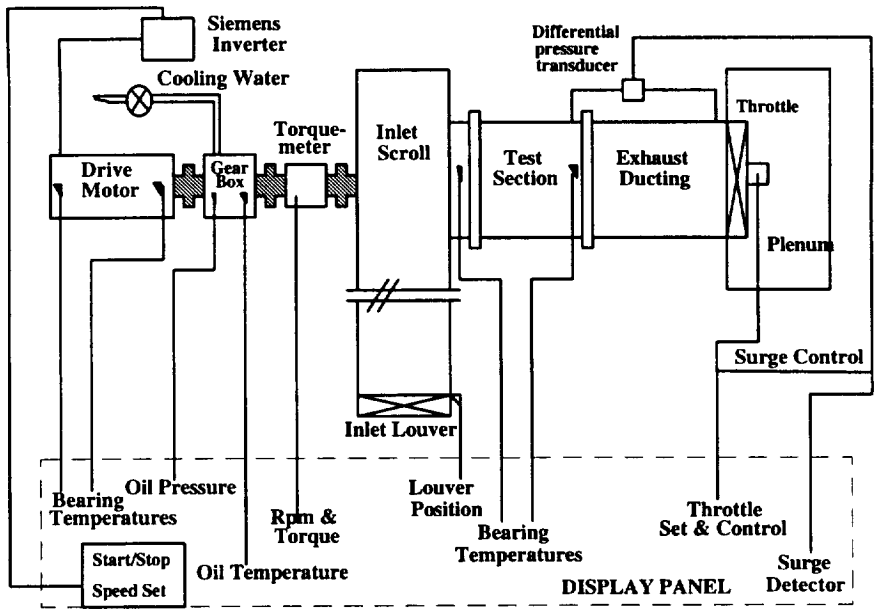

Figure 2.5. Schematic of the Safety and Monitor Control System of the Compressor

The control system includes an interlock system for safe operation of the facility. Devices that incorporate both display and interlock functions have been specified to provide the simplest and lowest cost system possible. Fourteen parameters have been identified as critical and these are listed in Table 2.3. All fourteen parameters will prevent startup of the facility if a system is not turned on or if a parameter is out of range. Four of the interlocked parameters are start permissive only. The other ten are run permissives and will provide a systematic shut-down of the facility if a critical parameter is out of range. The system was designed by Merl Christianson of Pratt and Whitney (1991) and installed and tested by L. P. Fetterolf at Penn State.

The surge control system is independent of the main control system. It is an electro-pneumatic device consisting of three major components: a surge sensor, a control unit and a vent solenoid valve. The schematic diagram of the surge sensor is shown in Figure 2.6. The sensor consists of a metal cylindrical container with a diaphragm unit attached onto top. An orifice in the diaphragm allows metered flow to occur either into

Table 2.3. List of Interlock Parameters and Devices for the Control System

Parameter	Monitor Device	Interlock Function	
		Start	end
GEARBOX			
Bearing 1	Digital Meter (Omega)	X	X
Bearing 2	Digital Meter (Omega)	X	X
Oil Temperature	Digital Meter (Omega)	X	X
Oil Pressure	Digital Meter (Sensotec)	X	X
Water Cooling	Gearbox Fault Light	X	X
TORQUEMETER			
Bearing 1	Digital Meter (Omega)	X	X
Bearing 2	Digital Meter (Omega)	X	X
COMPRESSOR			
Inlet Bearing	Digital Meter (Omega)	X	X
Exit Bearing	Digital Meter (Omega)	X	X
FACILITY			
Throttle Open	Throttle Fault Light	X	—
Throttle Reset	Throttle Fault Light	X	—
Throttle Air	Throttle Fault Light	X	—
Speed Pot. Down	Speed Fault Light	X	—
Inlet Louver	Inlet Fault Light	X	X

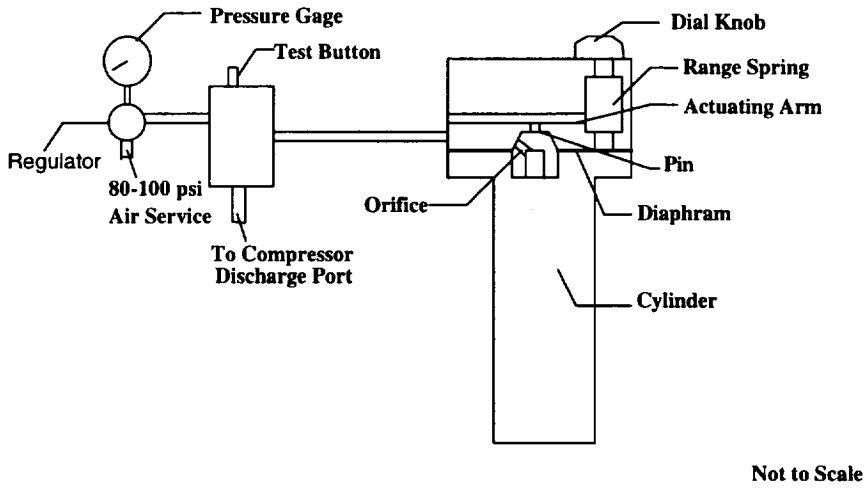

Figure 2.6. Schematic Drawing of the Surge Sensor

or from the cylinder whenever a pressure imbalance is present across the diaphragm. The time constant of the system is approximately 5 seconds. Compressor discharge and downstream plenum pressures are applied on either side of the diaphragm. When a surge occurs, the diaphragm moves upwards as there is a sudden lowering of pressure above the diaphragm. This upward motion of the diaphragm actuates an arm to activate a microswitch which then indicates surge on the control panel as well as performing a quick release of the throttle by cutting off the air supply that holds the throttle in place. Compression of the range spring of the actuator will set the pressure differential across the diaphragm at which the compressor will surge. Since this depends on the operating speeds of the compressor, the range spring setting has to be changed when operating at different speeds. For the 100% corrected speed, the setting is 2.5 psig. The vent solenoid is a standard all purpose three-way solenoid valve that interfaces with the surge detector and the compressor discharge throttle. The valve when energized, provides air pressure to the throttle actuating air cylinder for normal operation. When the valve is de-energized,

as would occur when the compressor surges, the valve will vent the cylinder pressure to atmosphere causing the compressor discharge pressure to push the throttle open for quick stall recovery. This system was also designed by Mr. M. B. Christianson of Pratt and Whitney and installed by Mr. L. P. Fetterolf of Penn State.

2.3 Instrumentation and Data Acquisition

The compressor supplied by Pratt and Whitney Aircraft was equipped with performance instrumentation and the research instrumentation was incorporated at Penn State. Total pressure and total temperature measurements were carried out using seven element kiel total pressure and temperature pole rakes, respectively. A schematic of the seven element total pressure rake is shown in Figure 2.7. These rakes were distributed across the circumference at inlet and exit in order to obtain a circumferential mean of the flow properties. They also serve to test the axi-symmetry of the flow. Wall static pressures were distributed throughout the casing of the compressor in order to evaluate individual stage behaviour. Stator leading edge kiels were used to evaluate the variation in total pressure throughout the compressor. Table 2.4 shows all the instrumentation that is used to measure performance and also to monitor the operating point of the compressor at all times. Four pressure and three temperature rakes were used at the inlet and three pressure and three temperature rakes were used at the exit. The casing pressure taps are distributed across the circumference of the compressor. Four casing pressure taps were used at all stations except at stations 1, 6, 7 and 10. Inlet mass flow measurement was made utilizing the total pressures and temperatures as measured by the inlet rakes and the casing wall static pressures at station 1. It was assumed that the static pressure distribution was constant from hub to tip at the inlet. This was verified by miniature five hole probe measurements at the inlet.

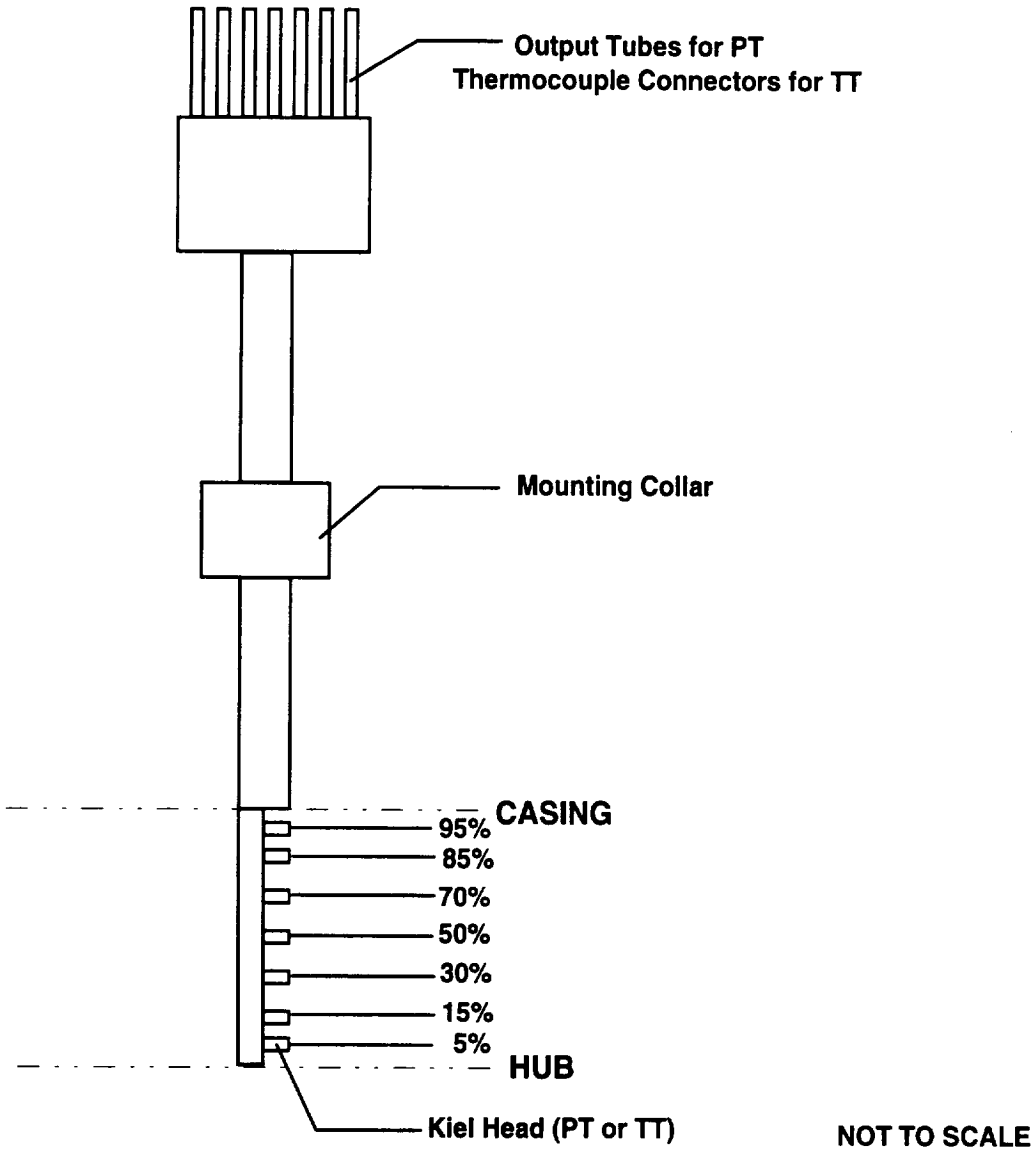

Figure 2.7. Schematic of the seven element total pressure rake

Table 2.4. List of Instrumentation for Performance Measurement

Location	Measurement	Type	Location (deg)
Station 1	Total Pressure	7-Element Rake	0, 90, 180, 240
	Total Temperature	7-Element Rake	3, 93, 285
	Static Pressure	Casing Static	38, 50, 56, 64, 103, 121, 159
			165, 214, 232, 240, 305, 323, 342
Station 2	Static Pressure	Casing Static	73, 160, 339
Station 3	Static Pressure	Casing Static	45, 180, 270
Station 4	Static Pressure	Casing Static	69, 73, 159, 278, 340
Station 5	Static Pressure	Casing Static	65, 159, 283, 336
Station 6	Static Pressure	Casing Static	78, 162, 339
Station 7	Static Pressure	Casing Static	10, 68, 99, 130, 158, 189, 321, 344
Station 8	Static Pressure	Casing Static	0, 72, 90, 163, 180, 345
Stator 1	Total Pressure	LE Kiel	Vanes: 4, 17, 24, 35, 43, 53, 63
Stator 2	Total Pressure	LE Kiel	Vanes: 5, 18, 26, 36, 45, 55, 65
Stator 3	Total Pressure	LE Kiel	Vanes: 4, 18, 26, 36, 46, 57, 67
Station 10	Total Pressure	7-Element Rake	94, 274, 356
	Total Temperature	7-Element Rake	4, 86, 240
	Static Pressure	Casing Static	0, 90, 120, 180, 245, 270

All angles are measured in CCW direction from the top dead center. Stator vanes are similarly numbered.

The pressure measurements were carried out using a 96 channel Scanivalve-10 psig Validyne pressure unit and Pressure System Inc., Model-780B pressure measurement system with dynamic calibration. It is a 2 range (0–$\pm$1.0 psi and 0–$\pm$7.5 psi) 64 channel system. It is controlled online by a PC-486 computer using the IEEE-488 interface board. The 780-B system is equipped with a pressure calibration unit (PCU) which automatically calibrates all 64 channels at once using a Digiquartz reference pressure transducer. The overall accuracies of the scanivalve-10psig validyne unit and the PSI system are $\pm$0.029 psia and $\pm$0.006 psia respectively. The temperatures were measured using an Omega Thermal Scanning System which consists of K-type thermocouples, a K-type CJ compensator and an signal amplifier. The overall accuracy of the temperature measurement is $\pm$1.0 Deg K. The compressor input torque and the rotor speed were measured using the torquemeter explained earlier. The accuracy of the torque measurement is $\pm$5 lb-in. The pressure and temperature data were acquired using the Metrabyte DAS-20 data acquisition system. To this system, a capability of stepping the scanivalve via computer to acquire all the pressure data was added.

In order to measure the performance of the compressor it is necessary to calibrate the various transducers used in the data acquisition mode. The validyne pressure transducers were calibrated in the laboratory before the start of the experiment using a standard AMTEK dead weight tester. It was calibrated from 0 to 1 psi in steps of 0.2 psi and from 1 to 10 psi in steps of 1 psi. Both upward and downward calibrations were conducted. The torquemeter was calibrated by the manufacturer using the standard load cell technique. All the calibration information was stored on the hard disk of the computer and a least square curve fit was used to obtain the data from these calibration curves.

2.4 Area Traverse Mechanism

In order to acquire instantaneous pressure, velocity and turbulence data in an embedded stage, an area traverse mechanism was designed and built at Penn State. The area traverse (AT) mechanism allows detailed area traverse of $1\frac{1}{2}$ blade passages upstream and downstream of rotor 3 and downstream of stator 3 (as shown in Figure 2.2). The schematic of the area traverse mechanism is shown in Figure 2.8. The AT allows for traversing of four different types of probes (five-hole probe, aspirating probe, single-sensor slanted hot-wire and the thermocouple probe). The AT is comprised of a traverse mechanism which allows for tangential and radial traverse and probe rotation about its axis (3 degrees of freedom). The mechanism is enclosed in a sealed chamber (A) which is mounted on the compressor outer casing. The probes (K) are encased in a teflon shoe (F) which is traversed in a slot (E), which ensures a smooth interface between the probe and the casing wall (G). The teflon shoes are designed to be at least three probe diameters wide on each side, to minimize local flow disturbances. The probes are traversed by stepper motors (B, C and H) driven by a IBM compatible 386 computer. The stepper motors are of 0.10565 Kg.m torque and are controlled by a MD-2B stepper motor controller. The stepper motor for tangential traverse (H) moves the chain driven sprocket which moves the traverse gear (I) using the chain (J). Radial motion is achieved by stepper motor (B) which moves the slide (D). Stepper motor C is utilized for rotating the probe about its own axis. Provisions are made for interfacing pneumatic and electrical lines through the side wall of chamber to provide both motion control and data acquisition. The area traverse can be driven by either a software driver (Q-Basic language) interfaced with the software to acquire pressure data from the PSI 780-B system or a command file format to acquire data with the DAS-50 system. The area traverse can be stepped in very fine increments; thereby very high accuracy can be maintained. The minimum step size is 0.000115 mm in the

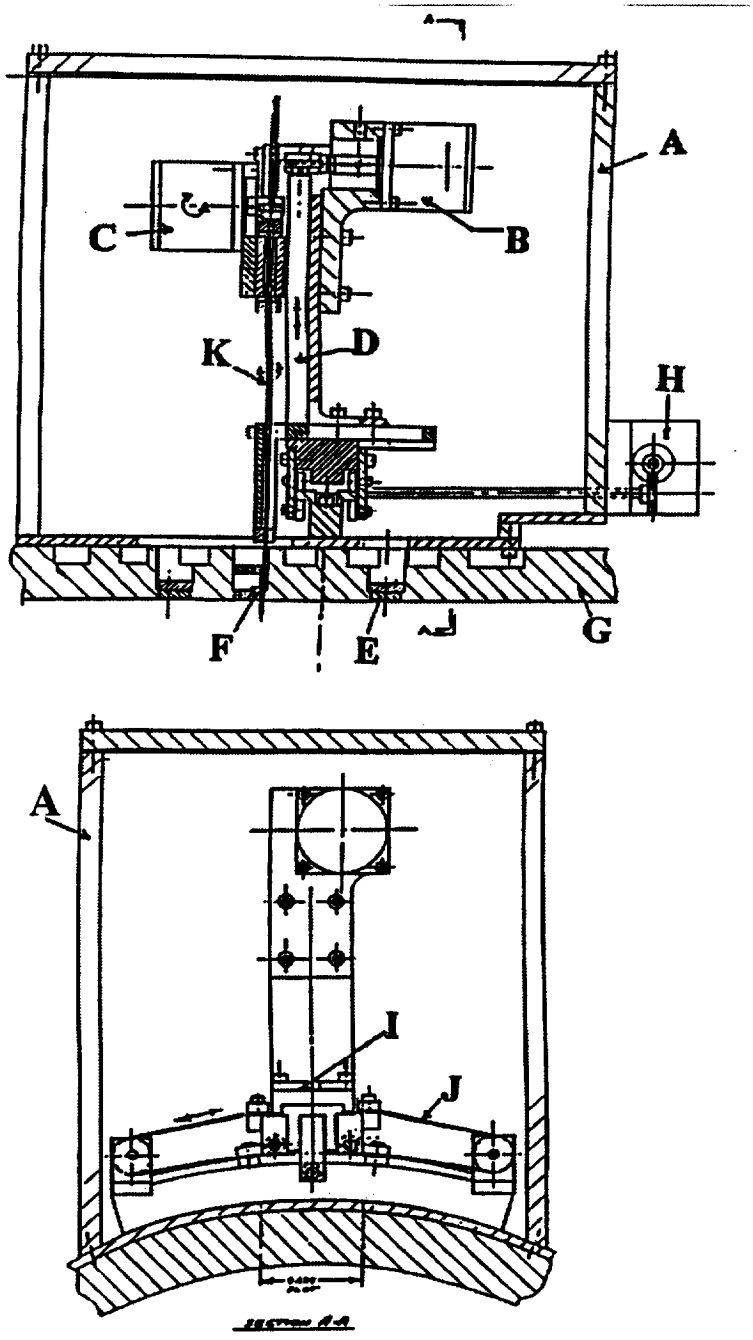

Figure 2.8. Schematic of the Area Traverse Mechanism

radial direction and 0.000454° in the tangential direction. The positioning is accurate to ± 0.05 mm in radial and tangential positioning and $\pm 0.1°$ in probe rotational positioning.

2.5 Data Acquisition System

All the data taken in this program was acquired through an IBM-PC compatible 486 computer using two types of data acquisition systems. Performance mapping, operating point setup, pneumatic five hole probe and thermocouple traverse data was acquired using the low speed data acquisition system. This system consists of a Metrabyte DAS-20 system which has eight differential channels for sampling data at speeds upto 100 kHz. This system also has capability to drive the scanivalve system and the PSI 780-B pressure system through an IEEE-488 interface board. Software to control the area traverse stepper motors were also interfaced with the PSI 780-B and DAS-20 systems to acquired pneumatic and thermocouple data respectively.

The high speed data acquisition system consists of the Metrabyte DAS-50 data acquisition system installed on a IBM compatible PC-486 machine. This has acquisition speeds upto 1MHz and up to 1 million samples can be acquired per second per channel. 3 such boards are used to acquire this data. The data acquisition can be triggered simultaneously using the once per revolution pulse from the BEI shaft encoder and the sampling clock frequency is also supplied by the shaft encoder. The frequency is calculated using the equation

$$F = \frac{N_b \, N_s \, N_{pb}}{60.0} \tag{2.1}$$

where F is the frequency in Hz, N_b is the number of blades on the rotor in question, N_s is the shaft rotational speed in RPM and N_{pb} is the number of points per blade pitch (resolution of the blade). The data was then downloaded on to the PC using DAS-50 software and then subject to analysis. The details of a typical data point for the aspirating

Table 2.5. Details of a Typical Unsteady Data Set

Parameter	Value
Compressor Speed	5410 RPM
No of Blades on Rotor 2	72
Blade Passing frequency	6492 Hz
For ensemble averaging	250 revolutions
Number of points per blade passage	20
No of channels of data	2
Sampling frequency per channel	129.840 Khz per channel
Total number of samples per channel	524,288 samples (4.037 s)

probe are given in Table 2.5. The schematic drawings of both the low and high speed data acquisition systems are given in Figure 2.9.

2.6 Overall Performance

The overall performance characteristics were measured and documented at three different rotor operating speeds (100, 85 and 105% of the design rotor speed) and at a set of operating throttle conditions. Two separate runs were conducted to establish repeatability and confidence in the compressor operating characteristics. The un-corrected rotor speed was calculated using the equation:

$$N_{uncor} = N_{cor}\sqrt{\theta} \tag{2.2}$$

where the corrected rotor speed (N_{cor}) is the design speed of the compressor (5410 rpm). The compressor was progressively loaded to establish the operating curve by incrementally closing the throttle. The compressor was loaded until surge occurred. Surge point was

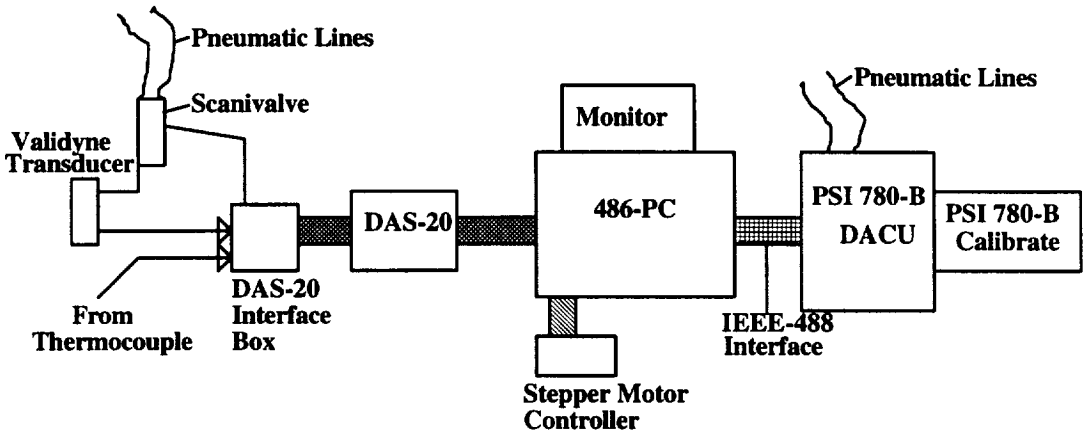

Low Speed Data Acquisition System

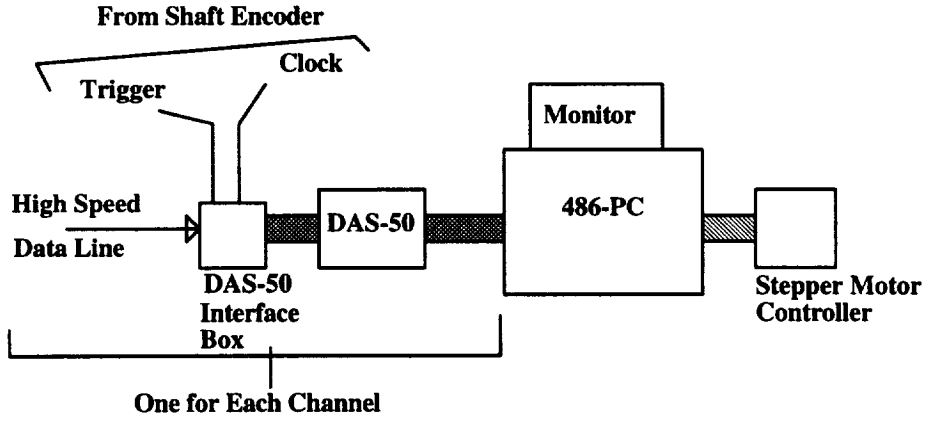

High Speed Data Acquisition System

Figure 2.9. Schematic of The Multistage Compressor Data Acquisition System

defined as the position at which the surge control system detects surge and opens the throttle valve. The data acquired for performance measurement consisted of inlet and exit total pressures, inlet and exit total temperatures, casing wall static pressures, drive torque and shaft speed. The ambient temperature and pressure was also recorded. The data acquisition was done by the DAS-20 system and later processed on the computer.

The test values for total temperature and pressure were circumferentially and radially mass averaged to produce average values for calculating overall performance. The static pressure distribution, assumed to be uniform from the hub to casing wall at the inlet, was used for the mass averaging. Compressible flow formulations were used in the calculations of the corrected weight flow.

The corrected weight flow, m_{cor}, is given by:

$$m_{cor} = m_{uncor}\frac{\sqrt{\theta}}{\delta} \tag{2.3}$$

where the uncorrected mass flow (true mass flow through the compressor) is calculated using:

$$m_{uncor} = \left[\sum_{i=1}^{7}\frac{W_i \Delta A_i}{C}\right] \tag{2.4}$$

where ΔA_i is the incremental area and C is defined by

$$C = \sqrt{\frac{R}{\gamma}\left(\frac{\gamma - 1}{2}\right)} \tag{2.5}$$

In this analysis values of γ and R are assumed to be 1.4 and 1716 ft.lb/slug.°R.

The segmental weight flow W_i is calculated using:

$$W_i = P_{s1}\sqrt{\frac{\left(\frac{P_{oli}}{P_{s1}}\right)^{\frac{\gamma-1}{\gamma}}\left[\left(\frac{P_{oli}}{P_{s1}}\right)^{\frac{\gamma-1}{\gamma}} - 1\right]}{T_{oli}}} \tag{2.6}$$

Since the tests were intended to reproduce conditions which would be present in the latter stages of a core compressor, the overall performance is presented from upstream of

the first rotor (Station 2) to the exit station (station 9). The overall pressure ratio based on the inlet to the first rotor was calculated using the procedure which includes losses due to IGV, pole rakes and the upstream struts (Behlke et al. , (1979)).

$$\overline{P}_r = \frac{\overline{P}_{10}}{\overline{P}_{02}} \tag{2.7}$$

where

$$\overline{P}_{02} = \overline{P}_{01} \times \overline{P}_{r,IGV} \times \overline{P}_{r,pole} \times \overline{P}_{r,strut} \tag{2.8}$$

where

$\overline{P}_{10}$ = exit station mass averaged total pressure

$\overline{P}_{02}$ = first rotor inlet mass averaged total pressure

$\overline{P}_{01}$ = inlet station mass averaged total pressure

$\overline{P}_{r,IGV}$ = total pressure ratio across the inlet guide vane

$\overline{P}_{r,pole}$ = total pressure ratio due to losses of flow station pole rakes

$\overline{P}_{r,strut}$ = total pressure ratio due to inlet strut losses

All the inlet loss pressures were calculated as a function of the inlet dynamic pressure calculated as a function of flow by:

$$\left(FFU\right) = 1.682842 \times 10^{-2} + m_{cor}(4.28655 \times 10^{-4} m_{cor} - 6.602824 \times 10^{-4}) \tag{2.9}$$

where m_{cor} is the corrected weight flow in lbm/s. The coefficients in the above correlation provided by P&W are dimensional.

$$\overline{P}_{r,IGV} = 1.0 - 0.0153400\left(FFU\right) \tag{2.10}$$

$$\overline{P}_{r,pole} = 1.0 - 0.0105285\left(FFU\right) \tag{2.11}$$

$$\overline{P}_{r,strut} = 1.0 - 0.0014550\left(FFU\right) \tag{2.12}$$

where the mass averaged total pressure is given by:

$$\overline{P}_o = \frac{\Sigma(W_i P_{oi} \Delta A_i)}{\Sigma(W_i \Delta A_i)} \tag{2.13}$$

where W_i is the incremental weight flow and ΔA_i is the incremental area. This procedure is used for deriving mass averaged values at inlet as well as at exit. For $\overline{P}_{01}$, W_i is based on P_{oi} and T_{oi} at inlet and P_s at the casing (equation 2.6). Likewise $\overline{P}_{10}$ is based on values at the exit (equation 2.14).

$$W_i = P_{s10}\sqrt{\frac{\left(\frac{P_{o10i}}{P_{s10}}\right)^{\frac{\gamma-1}{\gamma}}\left[\left(\frac{P_{o10i}}{P_{s10}}\right)^{\frac{\gamma-1}{\gamma}} - 1\right]}{T_{o10i}}} \tag{2.14}$$

Since no work is done ahead of the first rotor and heat loss through the casing is estimated to be negligible, the total temperature ratio from inlet of the strut to the exit of the IGV is assumed to be unchanged. Hence, $T_{o0} = T_{o1} = T_{o2}$.

$$\overline{T}_r = \frac{\overline{T}_{o10}}{\overline{T}_{o1}} \tag{2.15}$$

where the mass averaged total temperature is given by:

$$\overline{T}_o = \frac{\Sigma(W_i T_{oi} \Delta A_i)}{\Sigma(W_i \Delta A_i)} \tag{2.16}$$

The mass averaged adiabatic (temperature ratio based) and the torque based efficiencies are given by:

$$\eta_{temp} = \frac{\overline{P}_r^{\left(\frac{\gamma-1}{\gamma}\right)} - 1}{\overline{T}_r - 1} \tag{2.17}$$

$$\eta_{torque} = \frac{\overline{P}_r^{\left(\frac{\gamma-1}{\gamma}\right)} - 1}{(Net\ Energy)} \tag{2.18}$$

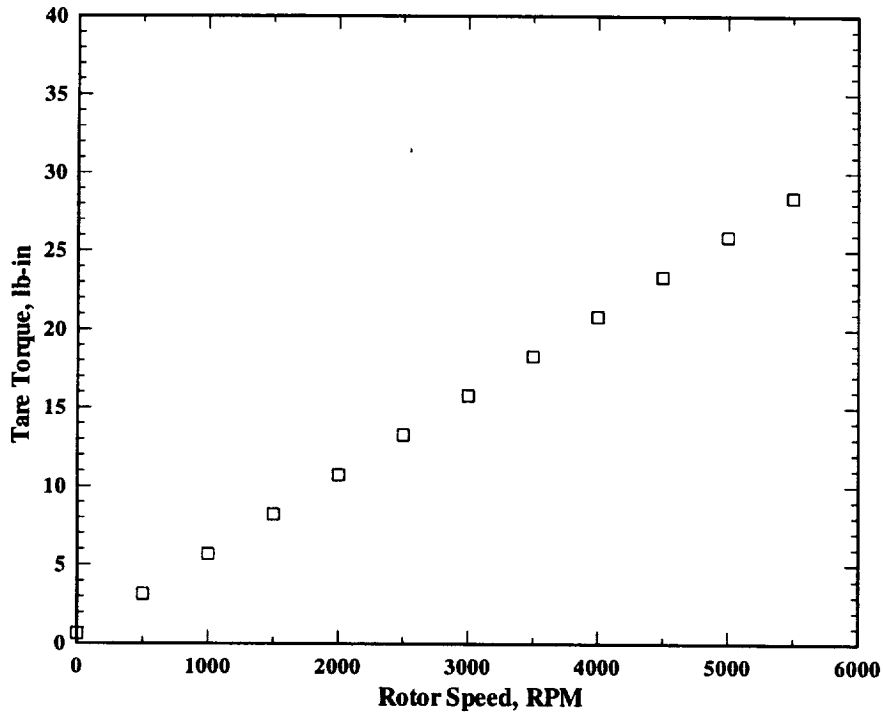

Figure 2.10. Tare Torque Calibration Data for PSU-MSCF

where net energy is:

$$Net\ Energy = \frac{2\pi N(Net\ Torque)}{(\overline{T_{o1}})(m_{uncor})(c_p)} \tag{2.19}$$

Here net torque (in N.m) is the difference between the true torque and the tare torque at the same rotor speed. The tare torque is the torque of the rotor drum with no blading on it. This was measured at Pratt and Whitney and the results are shown in Figure 2.10 as a function of the rotor speed.

In order to determine the error band in the performance measurement, a generalized uncertainty analysis was conducted on the various variables derived from the performance measurement. The analysis technique of Coleman and Steele (1989) was applied to the data reduction equations. The uncertainty in various measurement variables is detailed below: Overall uncertainty in pressure measurement was ± 0.0269 psi, in temperature was ± 1.6°F, in torque measurements it was estimated as ± 10 lb-in, and uncertainty in speed was estimated as ± 1 RPM.

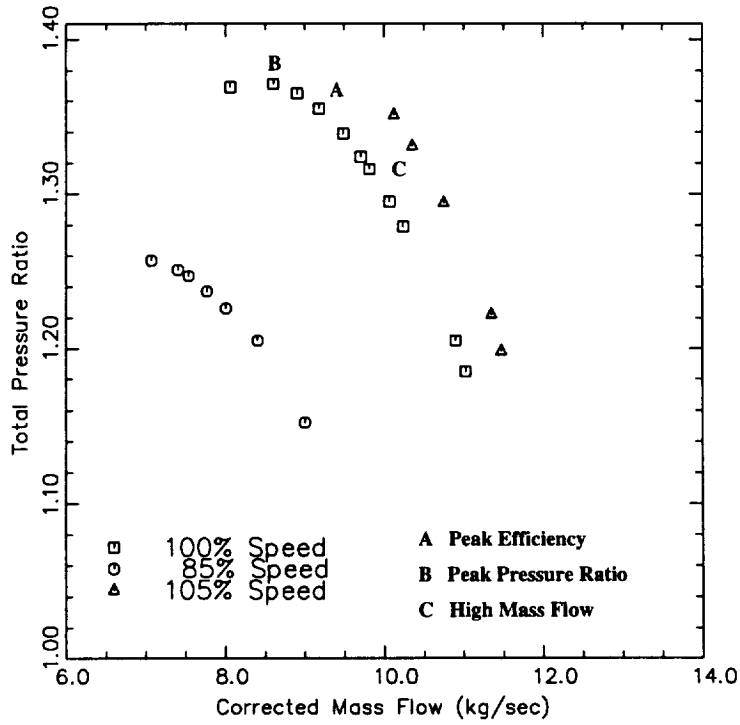

Figure 2.11. Total Pressure Ratio Characteristics at Three Rotor Speeds

Details of the uncertainty analysis are found in Appendix B. At the operating point of 20.67 lbm/s (corrected mass flow), 1.354 (total pressure ratio), 1.102 (total temperature ratio) and 90.512% (torque based efficiency),, the respective uncertainty bands are: ±0.091 lbm/s, ±0.003, ±0.005 and ±0.9069%. These numbers translate to uncertainty levels of ±0.44% in mass flow, ±0.22% in total pressure ratio, ±0.453% in total temperature ratio and ±1.0% in torque efficiency. However, based on the results of all the runs conducted at the peak efficiency point on the compressor, the repeatability of attaining the same mass flow, total pressure ratio and torque based efficiency are ±0.19%, ±0.22% and ±0.32% respectively.

The total pressure ratio characteristics at the three rotor speeds are shown in Figure 2.11. The pressure ratio increases with increase in rotor speed with the peak pressure ratio being 1.26 for 85% speed and 1.37 for 100% speed. For the 105% speed, the peak pressure ratio was not reached since the compressor input power and speed was limited. The torque based efficiency is shown in Figure 2.12. Since the error in temperature based

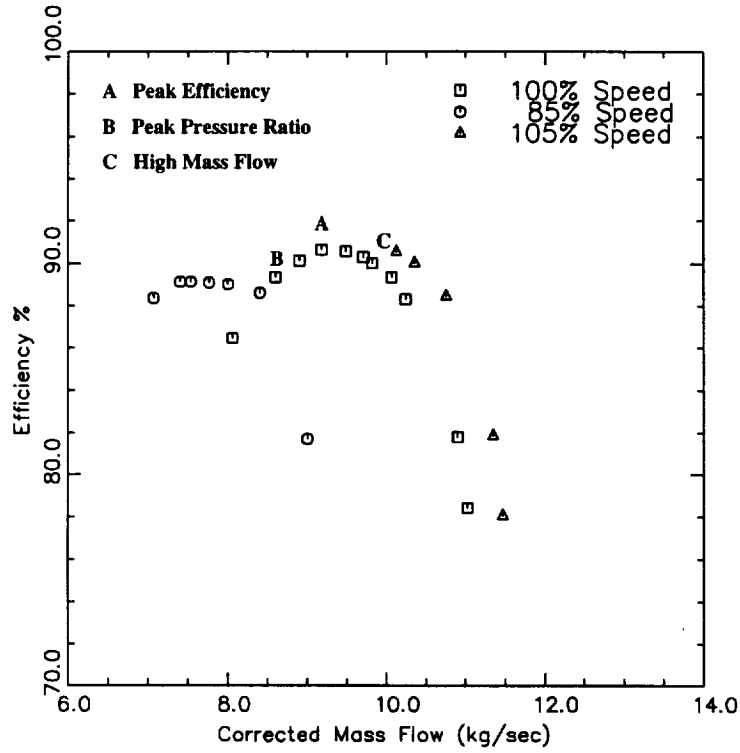

Figure 2.12. Torque Efficiency Characteristics at three rotor speeds

efficiency is high, the data is not included here. The performance of the compressor is similar to the P&W compressor 3S1 which is of similar design (Behlke et al. (1979)). The design speed has the highest peak efficiency of 90.65% achieved at 100% speed. Hence, design performance has been achieved. All of the data reported and interpreted in this thesis are taken at the peak efficiency point (A in Figures 2.11 and 2.12) and/or at the peak pressure ratio point (B in Figures 2.11 and 2.12). The casing static pressure data has been reported at 3 operating conditions (peak efficiency point A, peak pressure ratio point B and high mass flow point C (Figures 2.11 and 2.12).

In order to verify that the compressor is operating at the same operating condition for the entire period of this investigation, the variation of the corrected mass flow and efficiency based on the torque measurements with time over a four year period is shown in Figure 2.13 for the peak efficiency operating point. Figure 2.13(a) shows the mass flow variation and Figure 2.13(b) shows the torque efficiency variation. Also shown on these plots are the respective uncertainties of measurement. This shows that the compressor was

operating within the confines of the uncertainty imposed by the measurement techniques for the entire measurement period.

A basic procedure for the setup of the operating point of the compressor was developed. This procedure is:

1. The compressor is brought upto speed with the throttle in the fully open position and allowed to warm up.

2. Based on the inlet temperature, the corrected rotor speed is set.

3. The compressor is throttled upto an approximate operating point and the performance parameters are measured (corrected mass flow, total pressure ratio, total temperature ratio and torque efficiency).

4. Then depending on the location of these parameters with respect to the set-point, the compressor is either throttled up or down and the previous step repeated till the parameters of the operating point are reached within the set uncertainty levels.

5. Through out the experiment, the operating speed of the compressor is changed to reflect the changing inlet temperature, while keeping the throttle constant.

2.7 Inlet Flow Field

In order to characterize the axisymmetry in the inlet flow field, data was acquired at the peak efficiency point at 100% corrected speed. The data set consisted of radial distribution of inlet total pressure and temperature and casing pressure profiles at various circumferential locations on the compressor. In addition, the radial distribution of inlet velocity and pressures derived from the five hole probe at four circumferential locations are also available for comparison with the rake data. The radial distribution of turbulence intensity and the deterministic unsteadiness at the inlet were measured by a single sensor

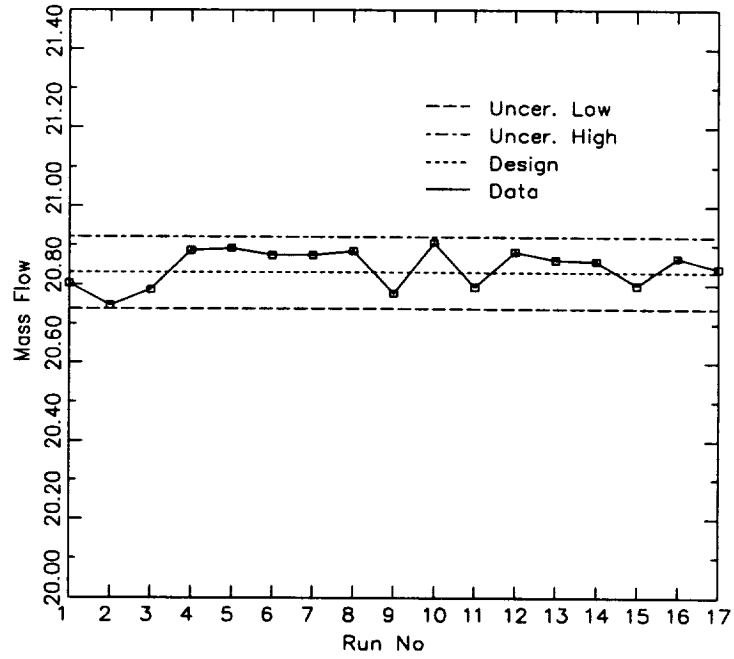

(a) Change in Corrected Mass Flow

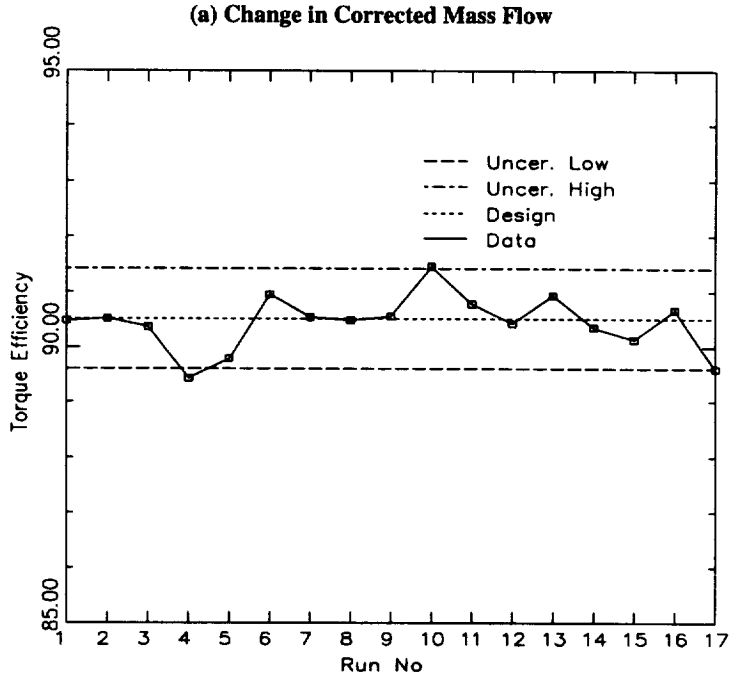

(b) Change in Torque Based Efficiency

Figure 2.13. Performance History of the Compressor Rig

hot-wire probe. The hot-wire was calibrated online in the compressor itself for the inlet data set and in a calibration jet for the exit data set. The data was acquired using a DISA-55M hot-wire anemometer and the DAS-50 data acquisition system. The radial profile was discretized into 31 points in the same manner as that of the five hole probe measurements.

Figure 2.14 shows the C_{pt} distribution for the circumferential locations $\theta = 0°, 90°, 240°,$ and 270°, the average inlet axial velocity profile derived form the five hole probe and turbulence intensity profiles from the hot-wire measurement. The presence of the potential core as well as the hub- and annulus-wall boundary layers is clearly visible from this figure for all four tangential locations (C_{pt}). The flow is nearly axisymmetric, except in the hub wall boundary layer regions. The annulus wall boundary layer is approximately 15% of the span and the hub wall boundary layer is approximately 10% of the span. The inlet tangential and radial velocities were found to be negligibly small at all circumferential locations across the span.

A single sensor hot-wire, placed normal to the axial flow direction measures the axial and the radial component. Hence, the single sensor data provides the turbulence intensity (based on overall unsteadiness) defined by

$$Tu = \frac{\sqrt{\overline{u'^2} + \overline{w'^2}}}{V_o} \tag{2.20}$$

where u' and w' are the fluctuations in the axial and the radial direction. The overall unsteadiness plotted in Figure 2.14 varies from 3% at mid-span to 9% and 14% at the hub and annulus walls respectively. The variation of unsteadiness is almost negligible in the core region as expected. Even though 3% intensity is considered rather high, it is believed that this is a combination of both random and periodic unsteadiness.

Power spectral energy distribution of the inlet hot-wire data is shown plotted in Figure 2.15 for three radial locations. The digitizing rate for data acquisition was 64 Khz

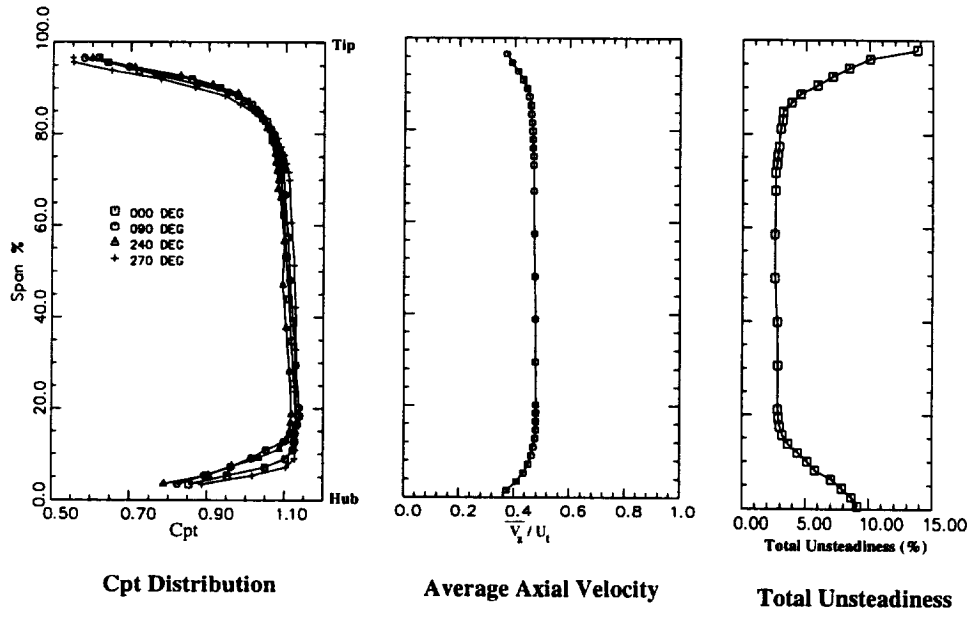

Figure 2.14. Inlet Flow Distribution: Total Pressure, Axial Velocity and Turbulence Intensity

(approximately 10 times the average blade passing frequency) and 131072 samples of data was acquired at each radial location. For a physical quantity $x(t)$ which is a function of time such as instantaneous velocity, the frequency domain can be expressed as

$$X(f) = \int_{-\infty}^{+\infty} x(t)e^{2\pi ift}dt \tag{2.21}$$

The auto-spectral density function (ASDF) of the time domain $x(t)$ is defined for $0 \leq f < \infty$ by

$$ASDF = \frac{2}{T}E\left[|X(f)|^2\right] \tag{2.22}$$

where $E[\ ]$ is an ensemble average, for fixed f, over the number of available sample records of $X(f)^2$. A fast Fourier transform (FFT) using the *Cooley-Tukey* algorithm was used to obtain the frequency domain and then this frequency domain was converted to the auto-spectral density function. The ordinate labeled ASDF (dB) is power level of the auto-spectral density function normalized by the square of the time average value of the

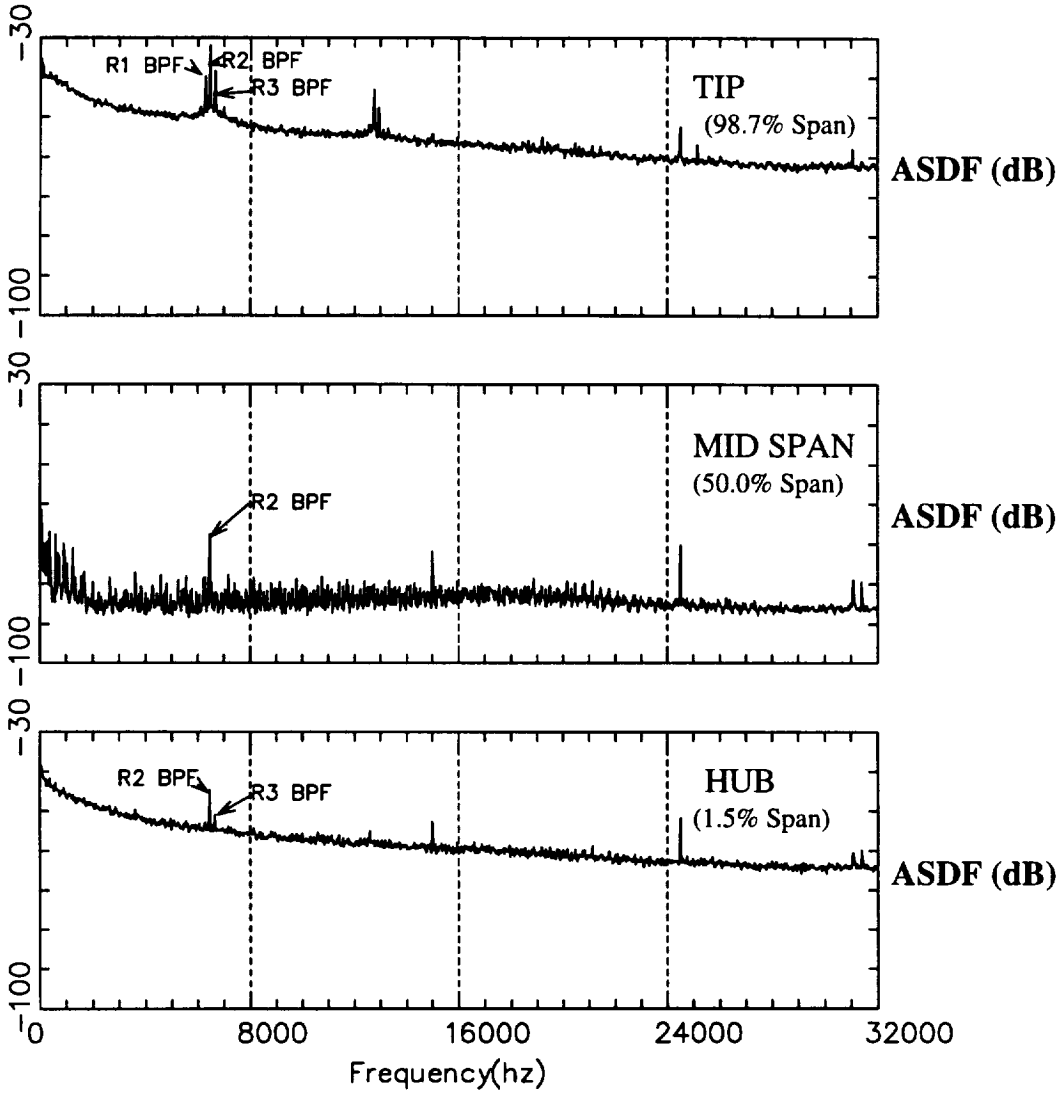

Figure 2.15. Inlet Flow Distribution: Power Spectral Energy Distribution

total velocity at that spanwise location. The turbulent energy at hub and tip is significantly higher than the energy at mid-span. The influence of all three rotors is felt upstream at the inlet, though at mid-span the effect of the third rotor is barely visible. The levels are higher at hub and tip than at mid-span. Rotor 2 exerts a larger influence on the upstream flow than the other rotors. This trend is seen all the way down to the third harmonic of the blade passing frequency at all the locations even though the levels are very low. This shows that the influence of the rotor blade passing frequency is felt upstream of the blade row as well.

The spectral energy distribution on a log-log scale (not shown) has overall shapes very similar to that presented by Goto (1992) at hub and tip. The spectrum at the hub has two distinct regions of slopes -1.125 and -1.78 departing from the characteristic -1.66 slope shown by homogeneous turbulence (Hinze, (1975)). The spectrum at the tip has three distinct regions with slopes changing from -1.092 to -1.267 to -1.98 as frequency increases from low to high. This is consistent with the measurements of Grant et al. (1968), who measured changes in slope of turbulence with wave number in a high Reynolds number flow in a tidal channel. At the mid-span region however, there is a very peculiar behaviour. At moderate frequency, there is very little drop in energy levels as the slope remains almost 0 and at high frequency, there is a sudden change in slope to -1.54. But a comparison with either the tip or the hub shows that the energy levels are very low.

2.8 Flow Field at the Exit of the Compressor

Detailed radial traverses of the five hole probe at three different circumferential positions and the single sensor hot-wire probe at one circumferential position were conducted to investigate the nature of the exit flow field. Since the exit measurement station (Station 10 in Figure 2.2) is 2.774 chords downstream of stator 3, the flow is expected to be

completely mixed up and to be axisymmetric in the circumferential direction. Figure 2.16 shows the spanwise distribution of total pressure coefficient, axial velocity, radial velocity and outlet flow angle at various circumferential locations at the exit of the compressor (Station 10 in Figure 2.2). These plots show that radial distribution of flow properties, even though similar, axial symmetry has not yet been achieved. This station is far downstream (2.774 chords) downstream of stator 3. The wakes, secondary flow and leakage flow effects still persist. The pressure and the axial velocity profile shows that the core region is small, the annulus wall boundary layer growth is substantial. The effect of rotor 3 flow - hub wall flow separation, reported later, can be still seen near the hub, as well as the influence of leakage flow. The radial velocities, however, are small at most locations. The outlet angle distribution shows underturning which indicates evidence of leakage flow near the hub (stator tip clearance).

2.9 Performance of Embedded Stages

The evaluation of casing pressures and stator leading edge kiel pressure data will be useful in determining whether the flow behaviour is as expected inside the stages. The surface static pressure distribution across the compressor will enable the detection of stall or abnormal behaviour in the flow field. The casing and kiel pressure data was acquired simultaneously with the performance data at the same operating points.

2.9.1 Casing Static Pressure:

The circumferential variation of casing static pressures at 3 operating conditions of peak efficiency, peak pressure ratio and high mass flow was analyzed at the 100% speed operating conditions and the results are shown in Figure 2.17. The static pressures were found to be nearly uniform circumferentially at all axial locations except those at the exit

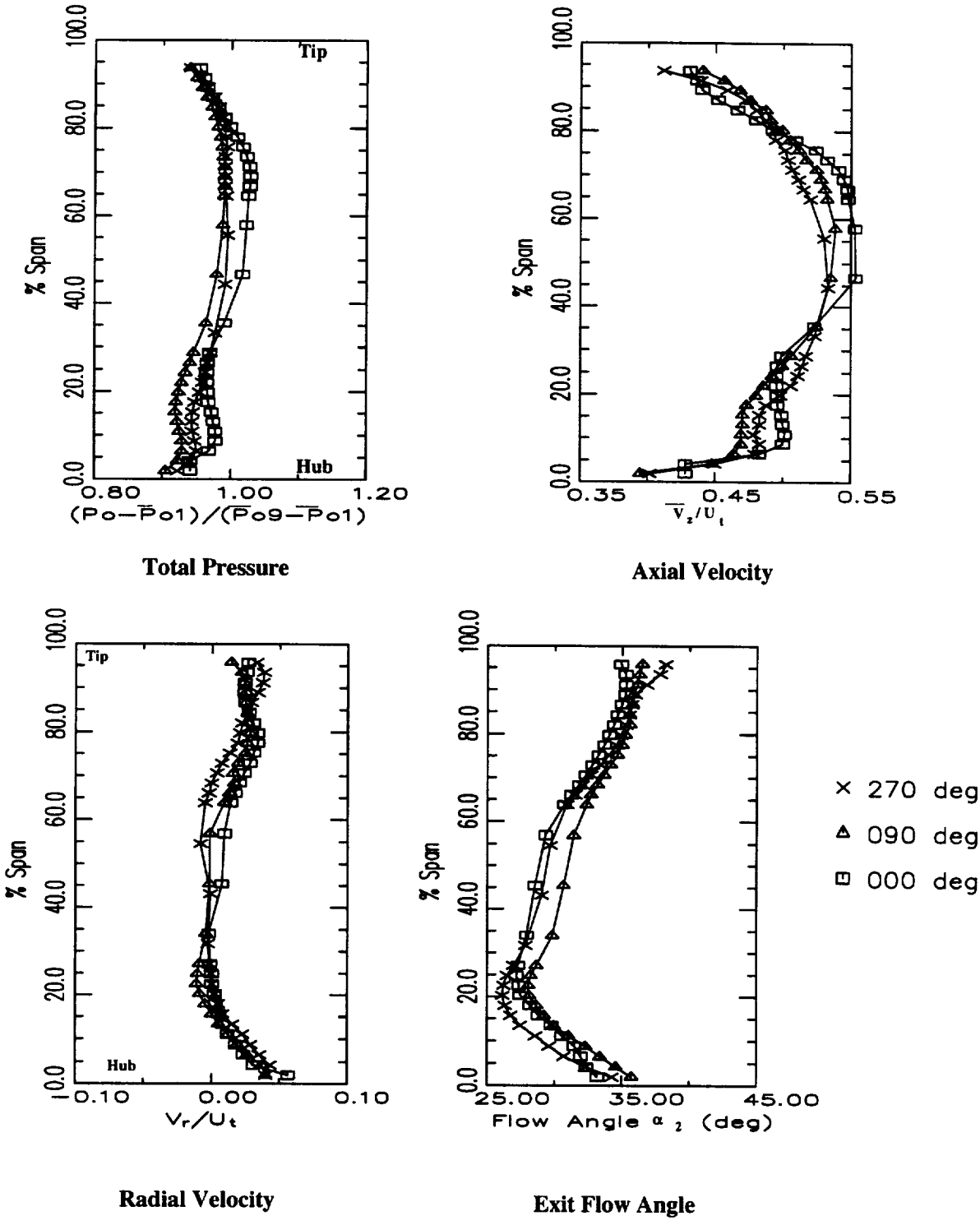

Figure 2.16. Compressor exit flow distribution: Five hole probe data (peak efficiency condition, 100% speed)

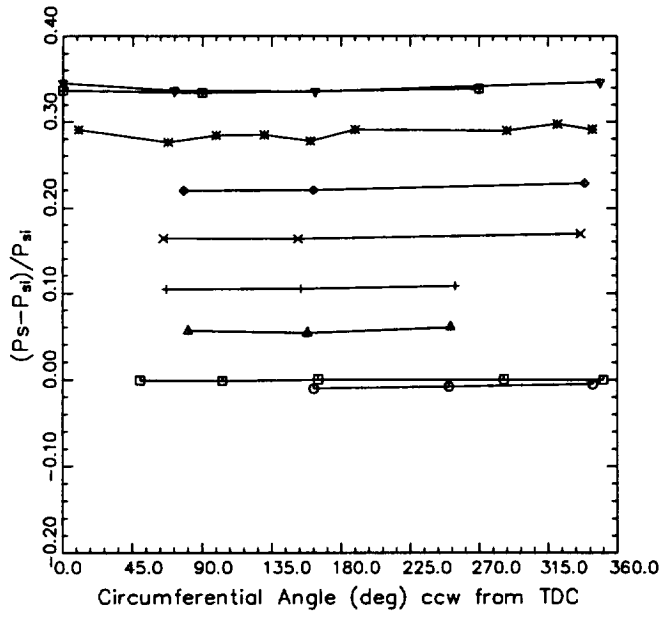

Peak Efficiency (Point A)

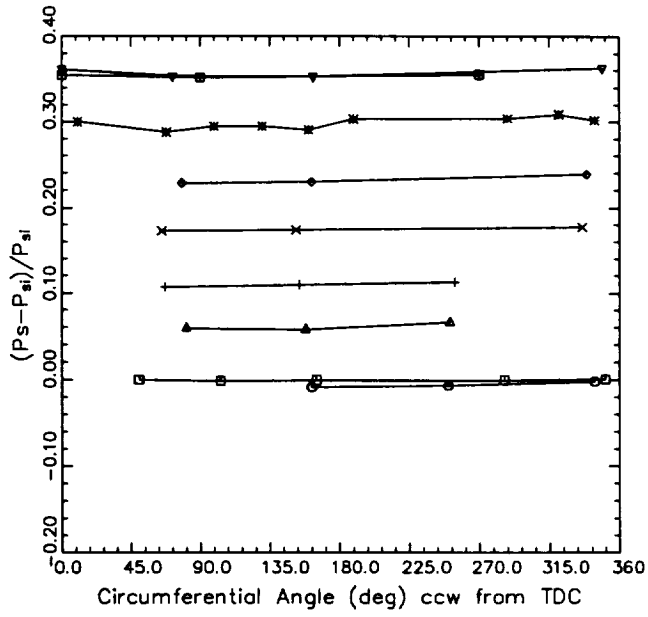

Peak Pressure Ratio (Point B)

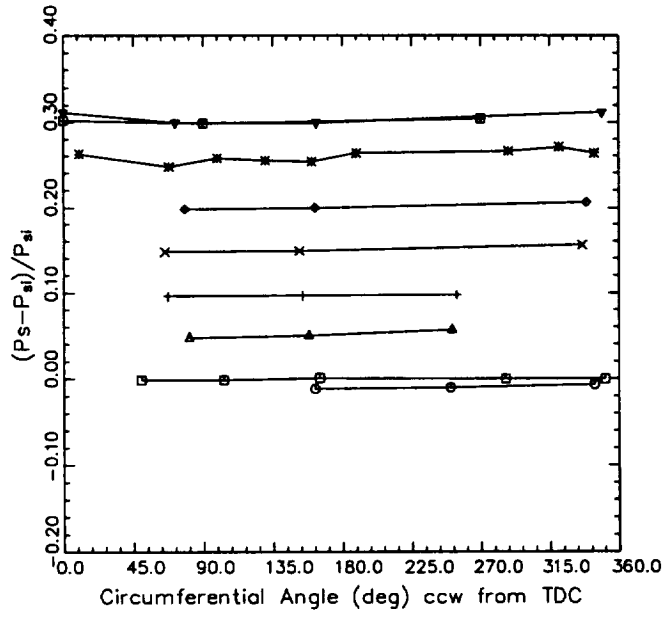

High Mass Flow (Point C)

Axial Distance From R1 Hub

−2.147	in	IGV up
−0.197	in	R1 up
1.380	in	R1 dn
2.705	in	S1 dn
4.145	in	R2 dn
5.550	in	S2 dn
6.662	in	R3 dn
8.927	in	S3 dn
11.304	in	Exit

Figure 2.17. Compressor casing static pressure distribution: 100% Speed

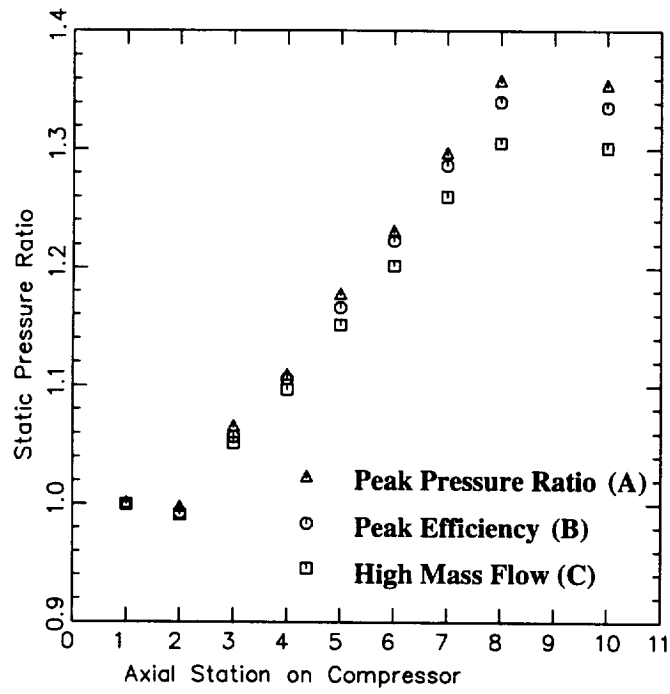

Figure 2.18. Compressor casing static pressure distribution: Average values, 100% speed conditions

of rotor 3. At the exit of rotor 3 the casing static taps are very close to the rotor 3 trailing edge, where the flow is highly unsteady and there is the added effect of the tip leakage flow giving rise to a circumferentially non-uniform pressure distribution at this location. There is not much change in the overall qualitative picture of the casing static pressures with change in loading condition. The variation of averaged casing static pressure ratio across the compressor at the 100% speed operating conditions is shown in Figure 2.18. The casing static pressure is normalized by the static pressure on the casing at the inlet (Station 1). There is a drop in static pressure across the IGV as the flow is accelerated as it flows through the guide vanes. There is a gradual static pressure rise through out the compressor at all three operating conditions. As the flow proceeds downstream of the first stator (Station 4), the static pressure ratio starts to deviate with change in operating conditions.

2.9.2 Total Pressure:

The spanwise variation of total pressures measured at various locations along the compressor using total pressure rakes and five hole probe is shown in Figure 2.19, at the peak efficiency point at 100% speed. The five hole probe data downstream of stator 2 has been mass averaged across one blade passage whereas the five hole probe data at inlet, exit and downstream of stator 3 has been circumferentially averaged. The flow is very well behaved at the inlet and through stage 1. The tip region at the exit of stators 2 and 3 has a conventional profile with monotonic increase in pressure from the endwall to freestream. The hub region, however, has a complex profile due to interaction of hub wall boundary layer and the leakage of the flow due to the cantilevered stator blade. Similar characteristics have been measured by Dransfield and Calvert (1976), Calvert et al. (1989) and Falchetti (1992). There is no deterioration of the flow as it passes through the compressor except for increased viscous layers in the endwall region. The flow downstream of the third stator is very similar to the flow downstream of the second stator.

The core flow region, which is approximately 75% of the span at inlet, reduces gradually to less than 30% of span at the exit of the compressor. Since the measurements shown in Figure 2.19 are at the exit of stators, the leakage effects due to rotor tip clearances are not observed. The data indicate that the leakage flow has mixed within the stator passage, resulting in a conventional viscous layer (monotonically decreasing towards the annulus wall). Whereas the flow near the hub shows the effect of leakage due to clearance between a stationary blade and a rotating hub, the values of Cpt increase from hub to about 10% of span, followed by a flat profile (and a wake type of region at exit). This is typical of profiles caused by the interaction of leakage flow with the primary flow (Lakshminarayana et al.(1995)).

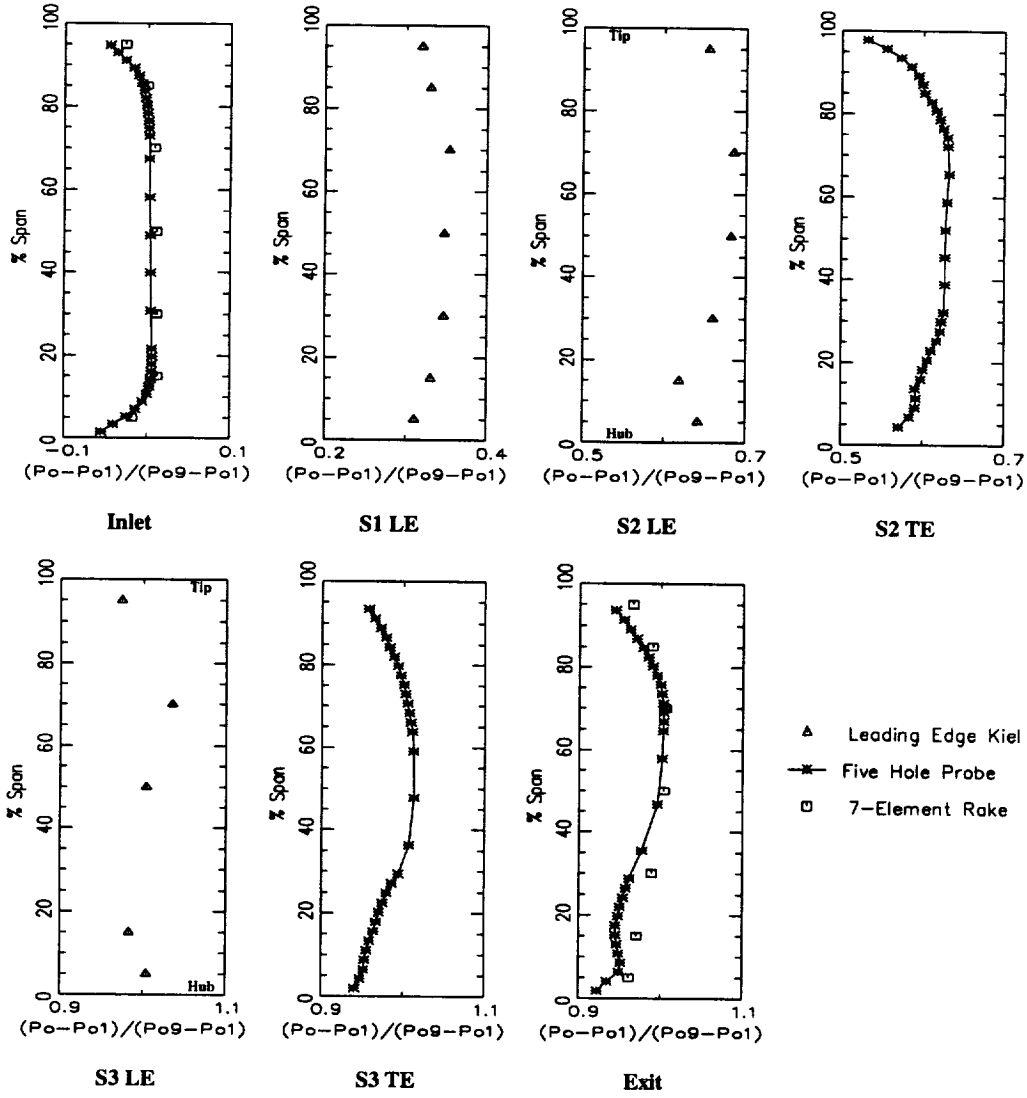

Figure 2.19. Spanwise variation of total pressure profiles across the compressor at the peak efficiency operating condition, 100% speed

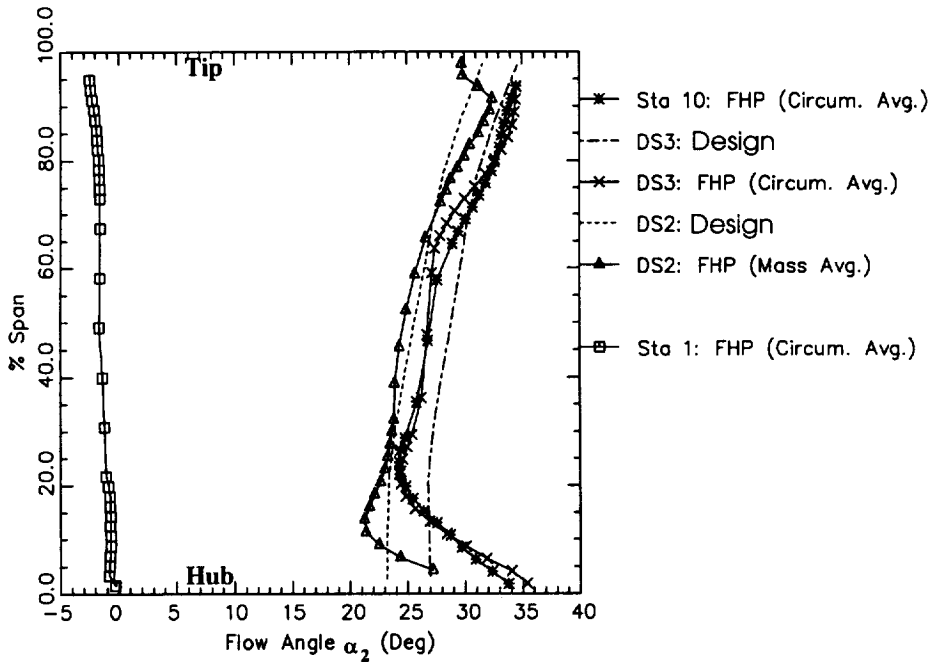

Figure 2.20. Spanwise variation of absolute flow angle across the compressor at the peak efficiency operating condition, 100% speed

2.9.3 Flow Angle and Axial Velocity

The absolute flow angle at the exit of stators 2 and 3 and at the exit of the compressor are shown in Figure 2.20. The inlet flow was axial. The design angles are also shown in this figure. Downstream of stator 2, beyond 70% span, the measured profiles show under-turning up to about 95% span. Over-turning is observed in the outer 5% of the stator blade span, caused by secondary flow. Both underturning and overturning are observed near the hub. Up to about 9% of the span from the hub, the flow is underturned. The overturning is confined to spanwise locations extending from 10% to 25% span. This is typical of the distribution observed in vortical motion. This may also have been caused by separated flow in the upstream rotor, (as explained earlier), and the associated shear gradient, resulting in secondary flow and overturning in this region. Downstream of stator 3, the radial distribution of exit flow angle is very similar to those observed at the exit of stator 2. The underturning region near the hub has increased. The passage averaged pitch

angle distribution were found to be small at all axial locations and were of the same order of magnitude as the measurement uncertainties.

The spanwise variation of average axial velocity at several axial locations along the compressor at the peak efficiency point, 100% speed is shown in Figure 2.21. The mass flow based on measured local axial velocity is found to be almost the same at all axial locations. The flow is uniform in the mid-span regions with variations occurring in the end-wall regions due to the effect of various flow mechanisms (hub clearance flow from stators, tip clearance flow from the rotors, annulus wall boundary layers and secondary flow).

The radial distribution of average axial velocity indicates substantial changes as the flow goes through several blade rows. The boundary layer thickness at the inlet is approximately 10% near the hub and 10-15% near the tip. This grows substantially as the flow progresses through the compressor. The hub wall flows show the same trend as Cpt where the stator-hub leakage flow interacts with the main flow to produce unconventional boundary layer wake type of profiles near the hub wall region. This may also have been caused by a scraping vortex and the upstream rotor hub separated flow. This region extends from 10% to 20% of the span from the hub.

The leakage flow tends to reduce the boundary layer growth, especially very near the wall. This is clearly seen from a comparison of the velocity profiles near the hub and the tip. The flat portion of the profile (from 10 to 20% span), which has higher than expected values (of the extrapolated boundary layer profile from 30 to 20%) may have been caused by either a scraping vortex or the upstream separated flow in the rotor. The separated flow at the exit of the rotor has higher absolute velocity than the un-separated flow. This hypothesis is supported by higher than expected temperature rise (see figure 9) in this region. This hypothesis is supported by the fact that the static pressure is nearly invariant across the span at this location.

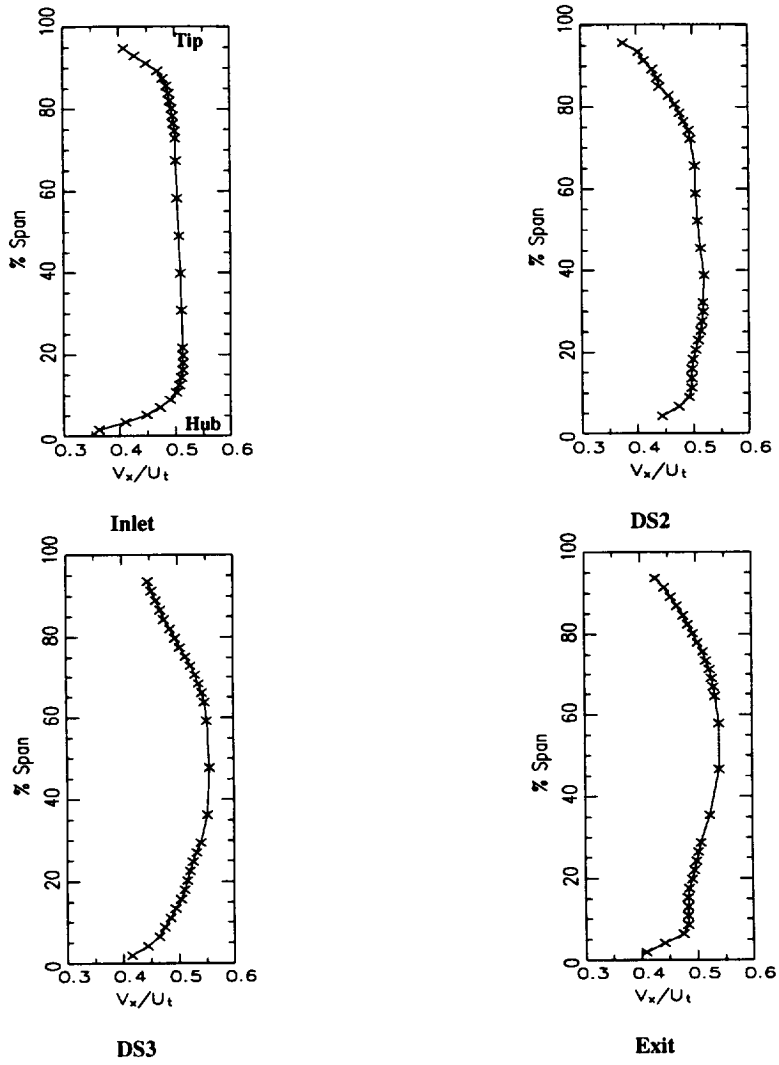

Figure 2.21. Spanwise variation of absolute axial velocity across the compressor at the peak efficiency operating condition, 100% speed

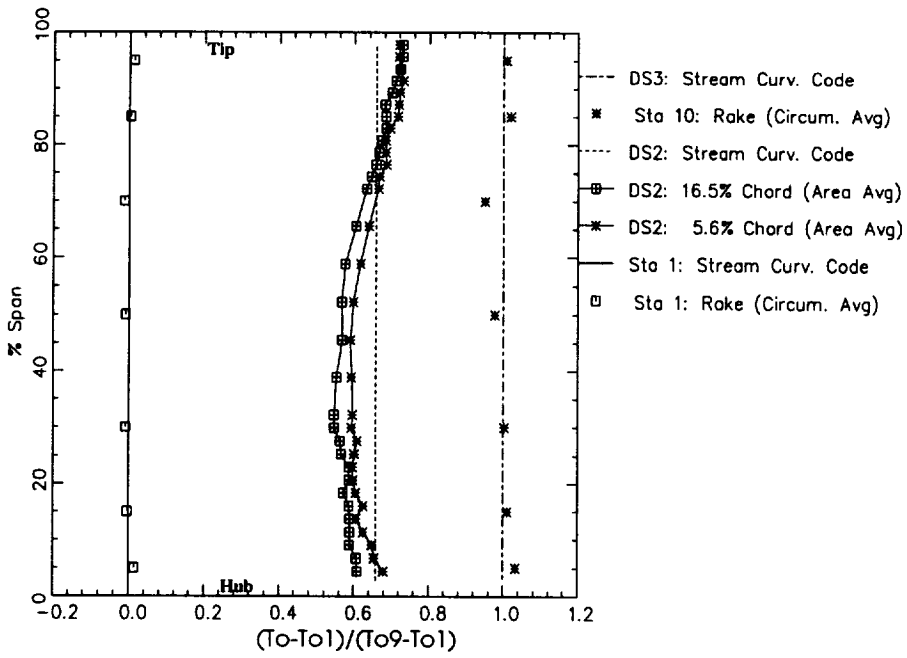

Figure 2.22. Spanwise variation of total temperature ratio across the compressor at the peak efficiency operating condition, 100% speed

2.9.4 Total Temperature

Detailed area traverses were conducted using a low frequency response thermocouple at 5.6% chord downstream of stator 2 trailing edge. The circumferentially area averaged total temperature ratios (based on mass averaged inlet total temperature) are plotted in Figure 2.22 for the peak efficiency condition. Also shown on these plots are the circumferentially averaged radial distributions of inlet and exit total temperature ratio. The temperature field is very well behaved at the inlet where the temperature distribution is almost uniform in the radial direction. Downstream of stator 2 the profiles already show evidence of higher temperatures at the end walls with the temperature near the tip higher than that at the hub. Similar behavior is reported by Smith (1970), Falchetti (1992) and Howard and Gallimore (1992). Higher stagnation temperatures near the endwalls are caused by viscous layers and the associated higher temperature rise across the rotors in these regions. At the compressor exit, the radial gradients in total temperature near the

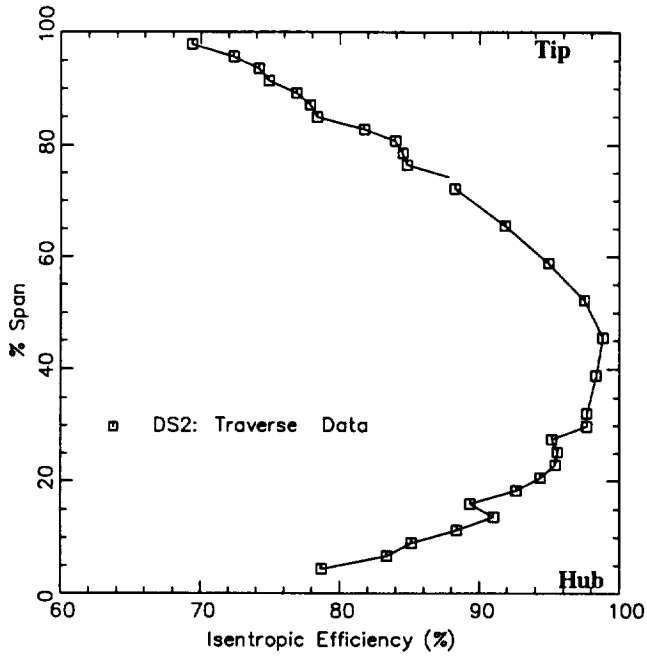

Figure 2.23. Spanwise variation of isentropic efficiency across the compressor at the peak efficiency operating condition, 100% speed

endwalls are much lower than the radial gradients at corresponding spanwise locations downstream of stator 2. This is due to increased spanwise mixing of the flow downstream of stator 3. Similar distributions were measured by Behlke et al. (1979) and computed by Adkins and Smith (1982) and Gallimore (1986). Calculations to predict the total temperatures at the exit of stators without mixing by both Adkins and Smith (1982) and Gallimore (1986) have shown high total temperature at the endwalls compared to the midspan region.

2.9.5 Isentropic Efficiency

Radial distributions of isentropic efficiency of the first two stages calculated downstream of stator 2 (based on the total pressure and total temperature traverses at this location) is shown in Figure 2.23. Isentropic efficiency (η_{isen}) is defined by:

$$\eta_{isen} = \frac{P_r^{\left(\frac{\gamma-1}{\gamma}\right)} - 1}{T_r - 1} \tag{2.23}$$

Measured isentropic efficiency downstream of stator 2 is the lowest at the hub and tip regions and highest in the midspan regions as is expected. With higher losses in the tip wall regions (lower total pressure ratios and higher total temperature ratios), the efficiencies are much lower than the efficiencies in the hub regions. The tip regions have the lowest efficiency indicating the rotor leakage flow and the stator annulus wall secondary flow are more severe than their counterpart near the hub. Similar distributions have been measured by Calvert et al. (1989).

Chapter 3

EXPERIMENTAL TECHNIQUES AND DATA PROCESSING

In order to achieve the objectives lined out in Chapter 1, it is necessary to measure the unsteady total pressure and total temperature aft of stator 2. The unsteady total pressure was measured using the semiconductor based Kulite total pressure probe and the unsteady total temperature was measured using a hot-wire based aspirating probe. Details of the design, operation, calibration, data reduction and uncertainty for both the probes are discussed in this chapter. Also discussed in this chapter are the details of data processing techniques (ensemble averaging), spectral methods and auto and cross correlation methods.

3.1 Semiconductor Pressure Transducer

Unsteady total pressure measurements in the Multistage Compressor Facility were obtained using a semi-conductor total pressure probe (Kulite XB-062 type). The probe has a tip diameter of 0.062 in and is shown in Figure 3.1. The transducer is of the XC-062-25A type. This is a 25 psia absolute pressure transducer with a natural frequency of 250 kHz and has an external temperature compensation module for temperature changes from 80 to 180 deg F. The design is of a solid state device with a diffused four arm Wheatstone bridge incorporated on the surface of a silicon diaphragm. An exitation voltage of 10V DC is used to activate the bridge circuit. The output is amplified by a low noise power amplifier with a frequency response of atleast 100 kHz. The transducer is calibrated in a pressure and temperature controlled tank. A steady state calibration is done at constant temperature for a range of pressures (consistent with the operating pressures in the compressor) and a linear least squares regression model is fitted to this data (since the response of the kulite

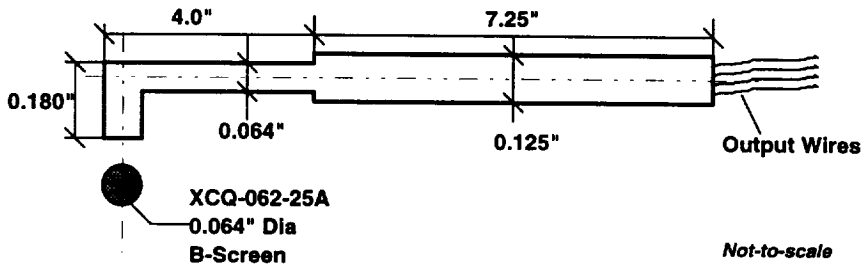

Figure 3.1. Schematic Drawing of Total Pressure Probe: Kulite XB-062-25A

probe is linear). Thermal drifts were the biggest problem with the Kulite probes (Cherrett and Bryce, 1992). In order to account for possible drifts in the transducer (even though the transducer was equipped with a temperature compensation device), the calibration was repeated at all the temperatures encountered in the compressor and a range of calibration curve fits were stored in the data base. When reducing compressor data, the appropriate temperature curve fit was selected to reduce the data. Both pre- and post-calibrations were conducted to limit the transducer drift during the compressor test run if any. It was found that the maximum drift in transducer voltage was around 2.5 mv, which is approximately equal to the least count of measurement (2.44 mv). This was within operational parameters of the transducer.

This transducer is provided with a "B" type screen which consists of a 0.005" thick plate with 0.006" dia. holes positioned on a circle. The diameter of the circle is greater than the active diameter of the diaphragm. This eliminates the possibility of a particle penetrating through the holes and hitting the unclamped portion of the diaphragm. The field frequency response of the entire assembly is approximately 60 kHz in the compressor facility (Figure 3.2). and the probe is sensitive to angles of attack of ± 30 degrees in both

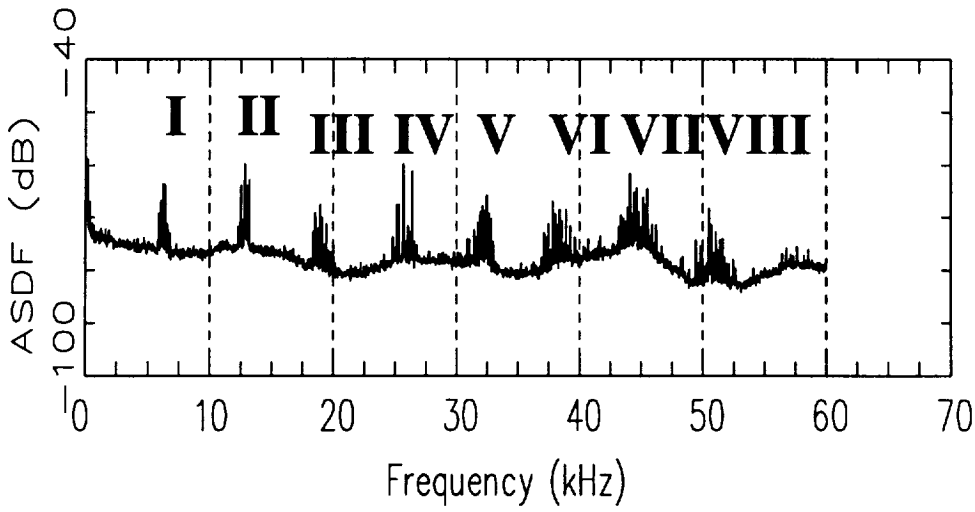

Figure 3.2. Field Frequency Response Curve of Kulite Total Pressure Probe: PSU-MSCF Midspan, Midpitch Data

yaw and pitch planes. Based on the ASME uncertainty analysis (Coleman and Steele, 1989), the uncertainty in the kulite total pressure measurement is ±0.0074 psia.

3.2 Aspirating Probe

Time-resolved measurement of gas total temperature has always been a very difficult task. Conventional thermocouples lose frequency response above 1 kHz while compensated thermocouples are yet to be demonstrated. Constant current hot-wire techniques are also limited to low frequencies unless the fluctuations are small compared to the mean. Electronically compensated, thin-wire resistance thermometers operated at very low overheat ratios exhibit less sensitivity to velocity fluctuations than do conventional constant current hot-wires and have been used to measure temperature at 5 to 10 kHz. The electronic compensation is a function of free-stream conditions, however, requiring

readjustment as the mean flow changes. More complex techniques using multiple constant temperature hot-wires have been demonstrated in low speed incompressible flow fields. However, these techniques are not easily extendable to high speed compressible flows with high dynamic pressure such as those found in turbomachinery configurations. Ng and Epstein (1983) reported the development of a piggy-backed high frequency total temperature probe (aspirating probe) for use in unsteady compressible flows. It is this probe that is used in the present study.

3.2.1 Design and Construction

Conventional hot-wires measure the thermal energy lost by convection to the fluid. Thus they are sensitive to the difference between the hot-wire temperature (T_w) and the fluid total temperature (T_o) and the mass flux (ρU) at the wire plane. For a constant temperature hot-wire in a flow of uniform composition, the square of the anemometer bridge voltage (V) is proportional to the power dissipated in the fluid.

$$V^2 = f(\rho U)(T_w - rT_o) \tag{3.1}$$

where r is the recovery factor of the hot-wire. In an unsteady compressible flow field, all the flow quantities fluctuate temporally. To overcome this problem, Ng and Epstein (1983) placed two co-planar hot-wires operating at different temperatures in the channel of an aspirating probe, the convergent exit of which was choked. The continuity equation for a one-dimensional channel flow can be written as:

$$\rho U = \left(\frac{P_o}{\sqrt{T_o}}\right)\sqrt{\frac{\gamma}{R}}M(1+\frac{\gamma-1}{2}M^2)^{\frac{-(\gamma+1)}{2(\gamma-1)}} \tag{3.2}$$

where P_o stands for the total pressure of the fluid, γ the ratio of specific heats of the fluid, R the universal gas constant and M the fluid Mach number. When the flow is choked at

the sonic exit, equation 3.2 reduces to:

$$(\rho U)^* = \left(\frac{P_o}{\sqrt{T_o}}\right)\sqrt{\frac{\gamma}{R}}\left(\frac{2}{\gamma+1}\right)^{\frac{(\gamma+1)}{2(\gamma-1)}} \tag{3.3}$$

where $*$ indicates the conditions at the sonic orifice. Therefore the mass flow at the wire plane can be written as:

$$\rho U = \left(\frac{P_o}{\sqrt{T_o}}\right)\frac{A^*}{A_c}\sqrt{\frac{\gamma}{R}}\left(\frac{2}{\gamma+1}\right)^{\frac{(\gamma+1)}{2(\gamma-1)}} \tag{3.4}$$

where A_c is the area of the orifice. For a fixed geometry, the ratio $\frac{A^*}{A_c}$ is a constant, and for a gas of fixed composition, γ and R are constant, so that the channel mass flow (ρU) is only a function of the system total pressure and temperature. Therefore, equation 3.1 can be rewritten as:

$$V^2 = f\left(\frac{P_o}{\sqrt{T_o}}\right)(T_w - rT_o) \tag{3.5}$$

with the assumption that the conductive heat losses at the wire ends are small compared to the convective heat loss. For a constant temperature hot-wire equation 3.5 can be written as:

$$V^2 = \frac{(R_s + R_w)^2}{R_w}\pi l k Nu(T_w - rT_o) \tag{3.6}$$

where R_s is the bridge resistance in series with the wire, R_w the resistance of the hot-wire at the operating temperature, l the wire length, k the thermal conductivity of the fluid, and Nu the Nusselt number. Ng and Epstein (1983) adopted the Collis and Williamson (1959) formulation of the Nusselt number - Reynolds number relationship:

$$Nu = \left(\frac{T_m}{T_\infty}\right)^{0.17}\left[\, a(Re_d)^m + b \,\right] \tag{3.7}$$

where Re_d is the Reynolds number based on the wire diameter, and a, b and m are empirically derived constants, approximately $a = 0.97$, $b = 0.02$ and $m = 0.41$. By substituting equation 3.7 into equation 3.6 and writing the Reynolds number based on the

wire diameter in terms of the compressible flow parameters of equation 3.4, we have

$$
\begin{aligned}
V^2 &= \frac{(R_s + R_w)^2}{R_w} \\
&\times \pi l k \left\{ a \left[\frac{d}{\mu} \frac{P_o}{\sqrt{T_o}} \frac{A^*}{A_c} \sqrt{\frac{\gamma}{R}} \left(\frac{2}{\gamma - 1} \right)^{\frac{-(\gamma+1)}{2(\gamma-1)}} \right]^m + b \right\} \\
&\times \left(\frac{T_m}{T_\infty} \right)^{0.17} (T_w - rT_o)
\end{aligned}
\tag{3.8}
$$

Equation 3.8 is used in the design of the aspirating probe to set the ratio of the throat to channel area for given operating conditions (Mach number, gas composition and free-stream conditions). Once these are fixed then a calibration equation incorporating the constant parameters of equation 3.8 can be written.

$$
\begin{aligned}
{V_1}^2 &= \left[C_1 \left(\frac{P_0}{\sqrt{T_0}} \right)^{n_1} \right] (T_{w1} - rT_0) \\
{V_2}^2 &= \left[C_2 \left(\frac{P_0}{\sqrt{T_0}} \right)^{n_2} \right] (T_{w2} - rT_0)
\end{aligned}
\tag{3.9}
$$

The constants (C and n) are determined by calibration. By operating the wires at different wire temperatures in separate constant temperature anemometer circuits, two simultaneous voltage measurements are made from which the two unknowns P_o and T_o are calculated. Ng and Epstein (1983) verified that the aspirating probe was responding to the temperature fluctuations in the flow as predicted by equation 3.9.

The independence of the two relations in the equation 3.9 will determine the probe sensitivity to total pressure and total temperature and thus the calibration space. The difference between the two hot-wire temperatures influences the independence of the two relations. The greater the separation in the wire temperatures, the more independent the two hot-wire equations will be with improved sensitivity to pressures and temperatures.

Given the concept of operating two hot-wires in a constant Mach number channel, the design of the aspirating probe is an engineering compromise between several constraints; spatial resolution (small size) versus hot-wire length to diameter ratio (l/d); and angular

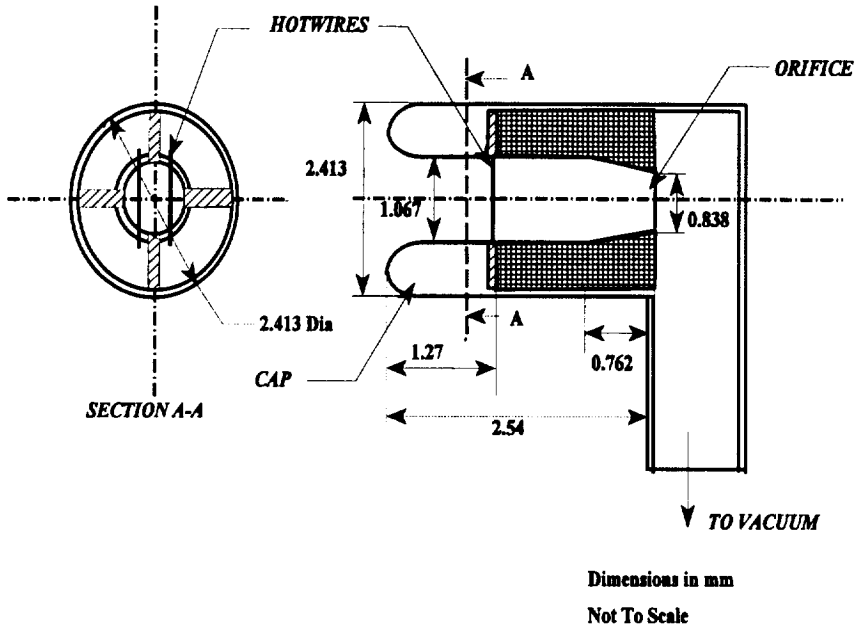

Figure 3.3. Scaled Drawing of the Aspirating Probe Geometry

acceptance versus frequency response. The hot-wire l/d must be large (above 200) in order for the end effects to be small. The channel diameter has to be as small as possible in order to keep the overall diameter of the probe small. Also manufacturing constraints limit the diameter of the channel. Based on this the channel diameter was chosen to be 0.042" (1.0668 mm). 5-μm tungsten wires were used giving an effective l/d of 214 which would eliminate the end effects. The choked orifice at the channel exit is 0.033" (0.8382 mm) so as to set the Mach number at the wire plane at 0.4. In order to maximize the high frequency sensitivity, the ends of the wires were copper plated through the thermal boundary layer (approximately 15% of channel diameter). The overall design of the aspirating probe was obtained from Dr. Ng of VPISU (1990). This was then scaled down to fit into the multistage compressor blade space row. The scaled drawing of the aspirating probe is shown in Figure 3.3 This probe was manufactured by Mr. H. Houtz at the GTWT, ARL, Penn State. A brief description of the manufacturing process is given below.

The tungsten wires (5μm dia) are soldered to four insulating brass supports which

make up the probe channel. A choked orifice is made out of machined epoxy. Two sleeves surround the brass conductors. These sleeves are bounded onto the brass conductors by epoxy which acts as an insulator for the probe supports. A probe cap is machined out of aluminum and screws onto the end of the channel. Since it is fat lipped, it gives good off axis performance. The RTV seal gives a smooth transition around the tungsten wires that are soldered to the support.

3.2.2 Calibration Procedure

A static calibration of the aspirating probe is considered adequate since the frequency response of the probe is high. The calibration requires measurement of the dc output voltage from each hot-wire for a range of pressures and temperatures of the tank. The calibration tank setup consists of a 10 gallon tank which is heated by a heating jacket and covered with heating blanket thermal insulation. The tank is connected to a source of compressed air supply in order to pressurize the tank. The pressure in the tank is measured by the validyne pressure transducer ($\pm$0.029 psia accuracy). The tank temperatures are recorded by 2 thermocouple probes in series with a cold junction compensating amplifier circuit ($\pm$1.0°K accuracy). The hot-wire anemometer voltages (DISA 55-M system) are recorded directly on digital voltmeters and on a Textronix storage scope. The kulite voltages are recorded via a signal conditioning unit on a digital voltmeter. The calibration procedure is computer controlled and the data is acquired using the DAS-50 system on the PC-486 computer. The calibration is performed at a constant temperature of the tank at various tank pressures and at each point recording the pressure, temperature, the 2 hot-wire voltages and the kulite voltage. The procedure is repeated for a set of temperatures and the calibration constants for each temperature are calculated. The sample calibration of the aspirating probe is shown in Figure 3.4.

Also plotted in this figure are the representative data at the mid-span mid-pitch

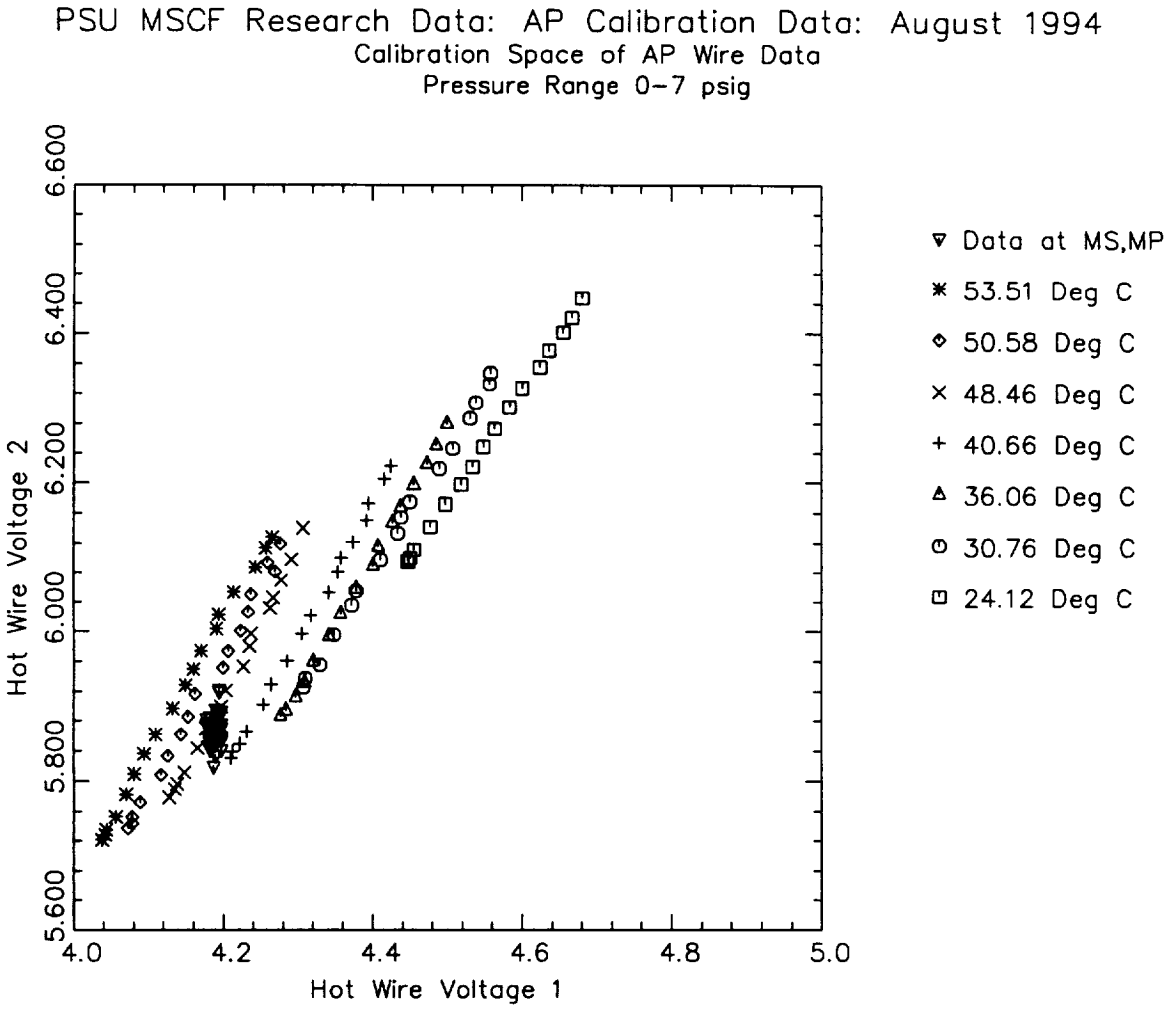

Figure 3.4. Calibration space of the original aspirating probe: Representative data taken in the compressor is also shown

location downstream of stator 2 at the peak efficiency operating condition. The calibration space is very narrow, and much of the data is in a very small band at the lower end of the calibration map. The wire overheat ratios were maintained at 1.3 and 1.5 resulting in wire temperatures of 367.4 and 415 Deg K respectively. It is clear that large changes in total temperature resulted in very small changes in the hot-wire voltages. This translated to very low sensitivities (Hot-wire: 15 mv/Deg C and 55 mv/psia). With an A/D resolution of 2.44 mv, the temperature and pressure resolution was found to be only 0.15 Deg C and 0.042 psia respectively. These numbers were not satisfactory since the unsteadiness levels especially in total temperature were found to be of the order of the temperature resolution. So an effort was made to improve the sensitivities and the overall calibration of the aspirating probe.

3.3 Improved Aspirating Probe

An effort was made to improve the sensitivities and increase the width of the calibration space. Firstly the 5μm tungsten wires were replaced by 5μm platinum coated tungsten (Wallaston) wires. This improved the overheat ratios the wire could be maintained at to 1.5 and 1.8. Consequently the wire temperatures increased to 434.9 and 518.18 Deg K respectively. This increased the temperature difference between the hot-wire and the fluid, thereby improving the heat transfer characteristics of the hot-wire. This also improved the pulse response of the probe (44 and 67 kHz for wire OHRs of 1.5 and 1.8 respectively). Nextly, the wire voltages were amplified by use of an A.C. instrumentation amplifier of high signal to noise ratio. An amplification gain of 4 was used as higher gains resulted in stability problems. The use of the amplifier improves the A/D resolution of the signal and increases the resolution of the total temperature signal.

This new probe was then recalibrated at various temperatures and pressures and a

calibration space was calculated. The calibration space of the improved aspirating probe (two hot-wire voltages) as a function of temperature and pressure is shown in Figure 3.5. The sensitivities of the two hot-wires to temperature and pressure are also given in the figure. This translates to a temperature resolution of 0.0049 Deg C and a pressure resolution of 0.0025 psia (both based on the A/D resolution of 2.44 mv). The sensitivity of the kulite probe is 0.0042 psia. Compared to the previous probe this was a tremendous improvement in the performance of the aspirating probe. With this successful step, we were able to acquire total temperature data from the rig.

3.4 Data Reduction Procedure

The standard data reduction procedure used by earlier investigators (Ng and Epstein (1983) etc.) involved the use of the total pressure measured by a piggybacked kulite probe and wire voltage measured by the aspirating probe to derive the total temperature. Later Van Zante et al. (1994) modified the operating characteristics of the aspirating probe to improve the sensitivities and used only the two hot-wire voltages to derive the total temperature. This eliminated the use of the kulite piggyback probe, thereby reducing blockage caused inside the compressor. As stated in an earlier section, this configuration, is used in the present investigation. The emphasis of the data reduction procedure will be on the 2-wire methodology, however, the wire and kulite method of data reduction is included for information purposes only.

3.4.1 Two wire method

In this method the total temperature of the flow is determined using the voltage signal from the two hot-wires. Since there are two measures of voltage, the total temperature of the fluid can be determined by solving the equation set 3.9. Equating the pressures from

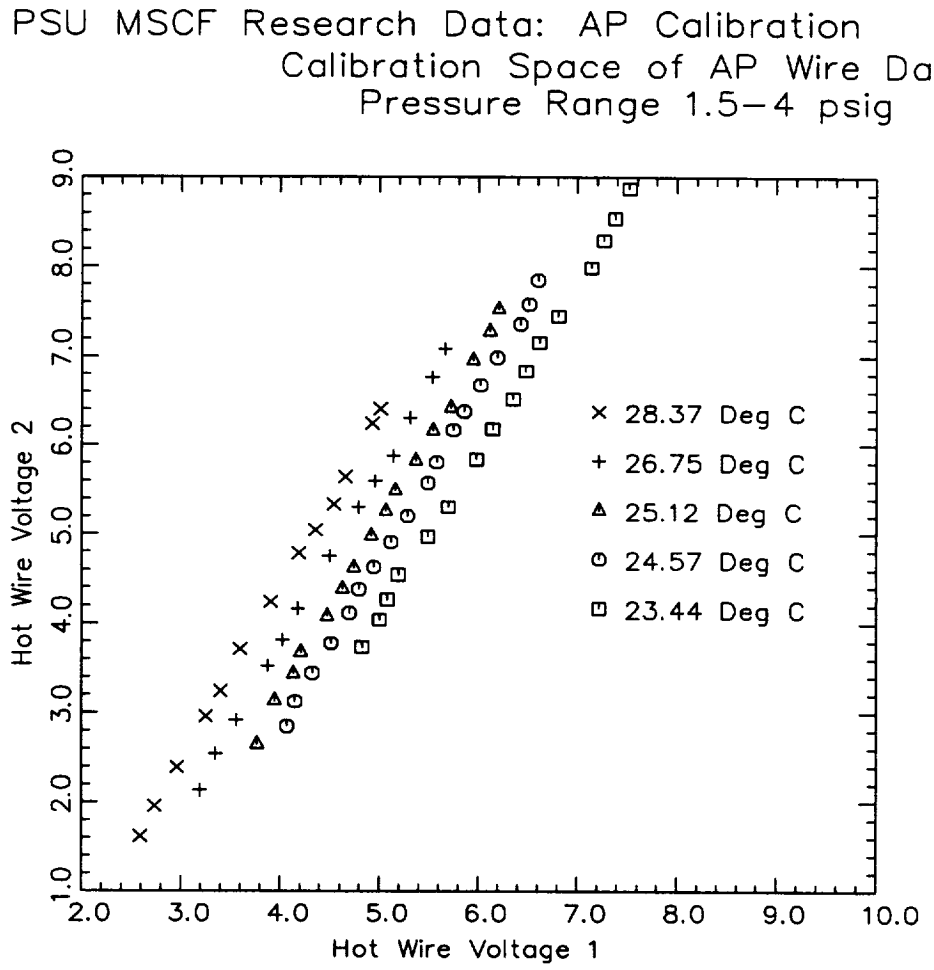

Both Hot-wires 5 μm Platinum Coated Tungsten wires
Wire 1 OHR: 1.5, Wire 2 OHR: 1.8
Sensitivities: Hot-wire: 496 mv/Deg C, 985 mv/psia
Kulite: 266 mv/psia

Figure 3.5. Calibration space of the improved aspirating probe. Wire sensitivities shown as marked

the two equations of 3.9 we get,

$$\left[\frac{V_1^2\, T_o^{\frac{n_{1,T}}{2}}}{C_{1,T}(T_{w1} - RT_o)}\right]^{\frac{1}{n_{1,T}}} = \left[\frac{V_2^2\, T_o^{\frac{n_{2,T}}{2}}}{C_{2,T}(T_{w2} - RT_o)}\right]^{\frac{1}{n_{2,T}}} \tag{3.10}$$

The equation 3.10 is solved using the Calibration Constants and Equation Method (CCEM). In this method the calibration constants derived from curve-fitting equation 3.9 for various temperatures were themselves curve-fit using a least squares procedure as a function of temperature. A Newton-Raphson iteration scheme is used to solve the equation. The iteration procedure proceeds as follows:

1. A least squares curve-fit for the calibration constants as a function of temperature is done.

2. An initial guess for the temperature is given. This step is very important, since the equations are not very robust, a bad initial guess can destroy the solution. For this guessed temperature, the values of the various constants are calculated using the curve-fit values.

3. Equation 3.10 is then solved to get the next temperature.

4. The above steps are repeated till convergence.

Once the temperature is calculated, pressure can then be found by substituting T into the equation below:

$$P = \frac{V_i^2\, T^{\frac{N_{i,T}}{2}}}{C_{i,T}(T_{wi} - RT)} \tag{3.11}$$

Either wire 1 or wire 2 can be used. Once again, the values of the constants are calculated from the curve-fit values for the temperature T.

3.4.2 Wire and Kulite method

When Ng and Epstein (1983) first proposed the aspirating probe, they concluded that the temperature calculated using the two wire method was not as accurate as that

calculated from a measurement of pressure from a piggybacked pressure transducer. Van Zante et al. (1994) proved that the piggybacked transducer was not needed and that temperature and pressure can be determined using the two wire method only. Both Ng and Epstein (1983) and Van Zante et al. (1994) based their conclusions on the results of experiments on transonic compressor flow fields (high pressure and temperature ratio). The present application is a low subsonic (Mach number of 0.4) compressor of very low temperature ratio. It was not clear if the aspirating probe had enough sensitivity to make total temperature measurements with just the two wires alone. So the piggyback configuration was retained, with the piggyback in the tangential direction to facilitate radial gradient measurements.

In this method the pressure from the piggybacked kulite transducer is used as an input into the data reduction scheme. The pressure is calculated from the voltages of the kulite transducer.

$$P = m \times Volt + b \tag{3.12}$$

where m and b are the least squares curve fit constants of the kulite transducer calibration. Since the kulite calibration has been found to be unchanged with changes in temperature, the calibration is conducted at room temperature only. Using this pressure, a Newton-Raphson iteration procedure is used to solve equation 3.13 to derive the temperature.

$$\frac{T_{wi} - RT}{T^{\frac{N_i}{2}}} = \frac{V_i^2}{C_i P^{N_i}} \tag{3.13}$$

The iteration procedure proceeds in a fashion similar to the one used to solve equation 3.10 as explained above.

In this method it is assumed that the pressure signal sensed by the kulite transducer is the same as that sensed by the aspirating probe. This is not true since the frequency responses of both instrumentation as well as the basic methodology of pressure measurement is not the same. Also due to the physical sizes of the two probes, there is a time lag

between the two signals. In order to account for this time lag a shift has to be applied to the kulite signal (in terms of encoder counts) relative to the hot-wire signal and then reduce the data. This shift is determined from a cross-correlation of the pressure signals determined from the kulite transducer and the two-wire method. This cross correlation was done for the mid-span mid-pitch location downstream of stator 2 and the same shift was used at all other locations. For example, if the shift is +2 encoder counts, the first point of the kulite signal is reduced with the third point of the hot-wire signal to get the first temperature point. Figure 3.6 illustrates this point. In this figure the ensemble averaged blade periodic component of total temperature at the mid-span, mid-pitch location downstream of stator 2 is shown. The location of the rotor wake as well as the variation across the pitch has been captured after the kulite data was shifted relative to the hot-wire signal.

3.5 Uncertainty Analysis

A detailed uncertainty analysis based on the ASME standard was conducted on the calibration and data reduction equations. RMS error estimates with 95% confidence intervals was used to quantify the uncertainty in measurement variables. The equations used in the uncertainty analysis as well the error estimate tables are given in Appendix C. Based on this uncertainty analysis, the overall uncertainty in instantaneous total temperature is $\pm 1.438\ Deg\ C$.

3.6 Unsteady Data Processing Methodology

The unsteadiness in turbomachines has been generally categorized as being either "periodic" or "random" ("turbulent"). Flow field fluctuations at discrete frequencies (e. g. blade passing frequency, shaft frequency etc.) are termed as "periodic" unsteadiness. "Random" unsteadiness has been used as a catch-all term which includes flow-field

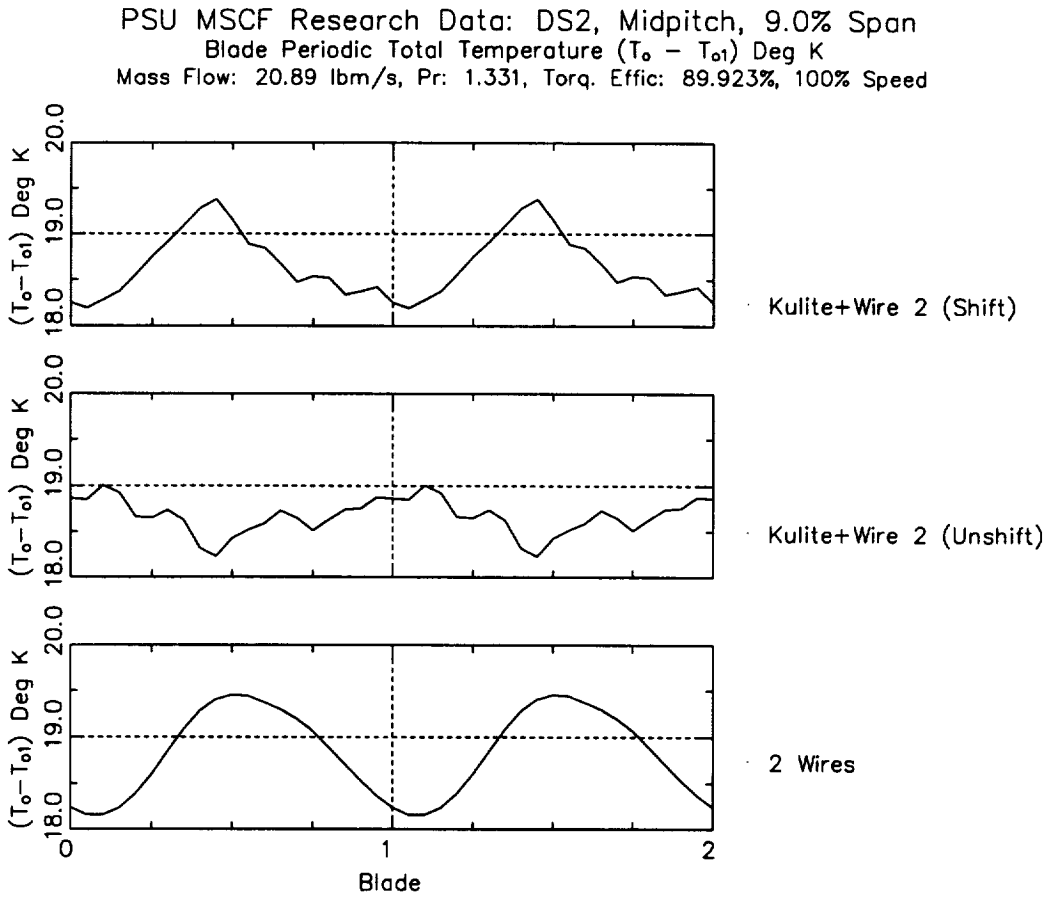

Figure 3.6. Variation of Ensemble averaged blade periodic component of Total temperature. Midspan, midpitch location downstream of stator 2: Comparison of shifted and unshifted signals.

fluctuations due to turbulence, vortex shedding, global flow-field fluctuations, random unsteadiness, and any other unsteadiness not correlated with the rotor speed. Therefore, in the absence of a more descriptive terminology for unsteady flow typical of turbomachines and to attempt to avoid confusion of terms, Suder et. al. (1987), used the terms *rotor-wake-generated* unsteadiness to describe the unsteadiness generated by the rotor wake deficit, and *unresolved* unsteadiness to refer to the remaining unsteadiness. Adamczyk (1985) used density weighted averaging (temporal and ensemble averaging) in the Navier-Stokes equations to derive the average passage equations. He decomposed instantaneous velocity and thermodynamic state variables into steady state component, revolution periodic, revolution aperiodic and unresolved components. These equations includes terms which account for the effects of the unsteady flows. A similar decomposition of the unsteady total pressure and temperature measured downstream of a second stage stator in a three stage compressor is carried out in this chapter.

3.6.1 Decomposition of Instantaneous Quantity

Each discrete measurement of total pressure is non-dimensionalized and presented as an instantaneous total pressure coefficient $C_{pt_{ijk}}$ and the total temperature as an instantaneous total temperature rise $T_{or_{ijk}}$.

$$C_{pt_{ijk}} = \frac{(P_{oijk} - \overline{P_{s1}})}{(\overline{P_{o1}} - \overline{P_{s1}})} \tag{3.14}$$

$$T_{or_{ijk}} = (T_{oijk} - \overline{T_{o1}}) \tag{3.15}$$

Here subscripts i,j, and k represent indices in ensemble averaging (i indicates the index of revolution, j the index of the blade in the row, and k the index of the point in the blade passage). Since the decomposition is the same for both total pressure and total temperature the decomposition of a general quantity ϕ_{ijk} is discussed in the following sections. The physical explanation for this type of averaging procedure is explained in detail in Chapter

5. The instantaneous quantity is decomposed into a shaft resolved (ensemble average) and an unresolved component.

$$\phi_{ijk} = (\phi_{jk})_s + \phi'_{ijk} \tag{3.16}$$

where

$$(\phi_{jk})_s = \frac{1}{N_{rev}} \sum_{i=1}^{N_{rev}} (\phi)_{ijk} \tag{3.17}$$

$$\phi'_{ijk} = \phi_{ijk} - (\phi_{jk})_s \tag{3.18}$$

This shaft resolved component has contributions from viscous and inviscid rotor-stator interaction effects which repeats every revolution. The shaft resolved component is further decomposed into a time average ($\overline{\phi}$), a revolution periodic ($(\phi_{jk})_{RP}$) and a revolution aperiodic ($(\phi_j)_{RA}$) component as shown in Fig. 3.7.

$$(\phi_{jk})_s = \overline{\phi} + (\phi_j)_{RA} + (\phi_{jk})_{RP} \tag{3.19}$$

where

$$\overline{\phi} = \frac{1}{N_{rev} \times N_b \times N_{pb}} \sum_{i=1}^{N_{rev}} \sum_{j=1}^{N_b} \sum_{k=1}^{N_{pb}} \phi_{ijk} \tag{3.20}$$

$$(\phi_j)_{RA} = \left\{ \frac{1}{N_{pb}} \sum_{k=1}^{N_{pb}} \left[(\phi_{jk})_s - \overline{\phi} \right] \right\}_j \tag{3.21}$$

$$(\phi_{jk})_{RP} = \left[(\phi_{jk})_s - \overline{\phi} - (\phi_j)_{RA} \right] \tag{3.22}$$

The time averaged component describes the steady state flow field which is the same in each blade passage of the blade row. The revolution periodic component describes the temporal fluctuations due to the relative motion between the blade rows and the revolution aperiodic component (which is a passage to passage average) arises from different blade count in successive stages (rotor or stator). For a single stage machine or a multistage machine with the same blade count in successive stages, the revolution aperiodic component identically goes to zero. The revolution aperiodic component generally represents the asymmetry

about the circumference in the rotor frame of reference with a time constant of one rotor 2 blade passing period. During analysis of the total pressure data acquired it was found that there are variations in the periodic fluctuations between blades in the same row due to various causes (geometrical, incidence variations, loading changes etc.). Since most of the design principles are based on solving the flow equations for one blade passage, it is essential to determine the periodic unsteadiness for the average rotor passage. This average passage is termed the "blade periodic unsteadiness" and the difference between the revolution periodic and the blade periodic is the "blade aperiodic unsteadiness".

$$(\phi_{jk})_{RP} = (\phi_k)_{BP} + (\phi_{jk})_{BA} \tag{3.23}$$

$$(\phi_k)_{BP} = \frac{1}{N_b} \sum_{j=1}^{N_b} \left[(\phi_{jk})_{RP}\right] \tag{3.24}$$

$$(\phi_{jk})_{BA} = \left[(\phi_{jk})_{RP} - (\phi_k)_{BP}\right] \tag{3.25}$$

The blade periodic component ($(\phi_k)_{BP}$) generally represents the fluctuations of the total pressure field over an "average" rotor 2 blade passing period. The blade aperiodic component ($(\phi_{jk})_{BA}$) generally represents the asymmetry about the circumference in the rotor frame of reference with a time constant of the sampling period. Since the decomposition of the original signal has already filtered the asymmetries with a time constant on the order of a rotor 2 revolution passing period (revolution aperiodic), this component includes short term asymmetries synchronized to the asymmetries synchronized to the passage of the individual rotor 2 blades. Figure 3.7 shows the detailed decomposition of an actual total pressure data set acquired at the mid-span mid-pitch location using the kulite total pressure probe.

While this decomposition is mathematically rigorous (i.e. the unsteady signal can be reconstructed by summing each of the components), it is premised upon the idealized assumption that all of the deterministic structure is synchronized to the shaft rotation. Measurement of the unsteady total temperature field resulting from some deterministic

physical phenomena, such as vortices originating in the stationary frame of reference, will be included in the unresolved component. Additionally, variations in the magnitude of the velocity deficit, width, and spatial positions of the rotor wakes between rotor revolutions, which are clearly shaft-synchronized physical phenomena, contribute to the unresolved component. As a consequence, the magnitude of the shaft-resolved and unresolved components of the unsteady temperature signals cannot be explicitly defined as the respective contributions to the total unsteadiness of the deterministic structures and random turbulence. However, this data can be used to identify in which regions of the flow field each of these components make significant contributions to the total unsteadiness and consequently mixing in the compressor.

3.6.2 Fourier and Spectral Analysis

Fourier and spectral methods of analysis are methods by which time series data is converted into frequency domains. This type of analysis is very useful in determining the levels of various unsteadiness associated with frequencies. The autospectral (also called power spectral) density function $G_{xx}(f)$ for a record represents the rate of change of mean square value with frequency. It is estimated by computing the mean square value in a narrow frequency band at various center frequencies, and then dividing by the frequency band.

For a physical quantity $x(t)$ which is a function of time such as instantaneous velocity, the frequency domain can be expressed as

$$X(f) = \int_{-\infty}^{+\infty} x(t) e^{2\pi i f t} dt \tag{3.26}$$

The auto-spectral density function (ASDF) $G_{xx}(f)$ of the time domain $x(t)$ is defined for $0 \leq f < \infty$ by

$$G_{xx}(f) = \frac{2}{T} E\left[|X(f)|^2\right] \tag{3.27}$$

Figure 3.7. Schematic of decomposition of instantaneous data: Actual total pressure data

where $E[\ ]$ is an ensemble average, for fixed f, over the number of available sample records of $X(f)^2$. A fast Fourier transform (FFT) using the *Cooley-Tukey* algorithm is used to obtain the frequency domain and then this frequency domain is converted to the auto-spectral density function.

3.6.3 Auto and Cross Correlation Methods

The autocorrelation function $R_{xx}(\tau)$ of a quantity $x(t)$ is the average of the product of the quantity at time t with the quantity at time $(t+\tau)$ for an appropriate averaging time T:

$$R_{xx}(\tau) = \frac{1}{T}\int_0^T x(t)x(t+\tau)dt \tag{3.28}$$

The delay τ can be either positive or negative. The time period T should approach infinity for an ergodic process, however, for the compressor data T is finite: For correlating the blade periodic components the averaging time is one blade passing period and for the ensemble average it is one rotor revolution period. The total mean square value (RMS) can be estimated from the above equation by setting the time delay to zero and taking the square root of the result.

The cross-correlation function $R_{xy}(\tau)$ of a quantity $x(t)$ is the average of the product of the quantity at time t with a quantity $y(t)$ at time $(t+\tau)$ for an appropriate averaging time T:

$$R_{xy}(\tau) = \frac{1}{T}\int_0^T x(t)y(t+\tau)dt \tag{3.29}$$

In this case as well, the averaging time T is the same as in the autocorrelation function defined above. The degree of correlation between the quantities $x(t)$ and $y(t)$ is given by the cross-correlation coefficient function $\rho_{xy}(\tau)$ of two quantities $x(t)$ and $y(t)$ is the ratio of the cross-correlation function $R_{xy}(\tau)$ to the square root of the product of the

autocorrelation functions of the two quantities at $\tau = 0$:

$$\rho_{xy}(\tau) = \frac{R_{xy}(\tau)}{\sqrt{R_{xx}(0)R_{yy}(0)}} \tag{3.30}$$

For all τ, the quantity $\rho_{xy}(\tau)$ satisfies $-1 \leq \rho_{xy}(\tau) \leq 1$.

Chapter 4

TIME AVERAGED FIELD DOWNSTREAM OF STATOR 2

The flow in a multistage compressor is highly unsteady. This unsteadiness is caused by the aerodynamic interaction of the rotor and stator flow fields and is called rotor-stator interaction. Rotor-stator interaction can affect the aerodynamic, structural and mechanical performance of a compressor. However, virtually all compressor design systems are based on the assumption that flow is steady in time. Thus, a better understanding of the unsteady flow interactions can lead to an improvement in the ability to predict the performance of compressors and to corresponding improvements in the actual performance of compressors.

In order to achieve the above objectives, detailed measurements of the steady and unsteady flow field (pressure, temperature and velocity components) downstream of an embedded stator stage is necessary. As explained in Chapters 1 and 3, unsteady total pressure data and unsteady total temperature data were acquired using a Kulite semi-conductor total pressure transducer and an aspirating probe respectively. Results from the traverse of a pneumatic five-hole probe and unsteady velocity measurements using a slanted hot-film probe (Prato (1996)) were also used to explain the various phenomena as well as to provide the temperature-velocity correlation terms for the mixing analysis. Chapter 3 explains in detail the calibration, data acquisition and data reduction procedures for pressure and temperature measurement techniques and Prato (1996) describes the unsteady velocity and pneumatic five hole probe measurement techniques. This chapter attempts to analyze the time averaged flow field downstream of the stator. Chapter 5 focuses on the unsteady flow field behavior and its mechanisms.

Area traverses were conducted at the peak efficiency operating condition (Point A

in Figures 2.11 and 2.12) at 5.6% chord axial location downstream of stator 2 (refer to Figure 2.2 for location) using a kulite total pressure probe for total pressure across two stator passages (25 radial and 31 tangential nodes) and an aspirating probe for the total temperature across one and a half stator passage (17 radial by 19 tangential locations) respectively. Care was taken to locate the probe at the same radial and tangential locations for both the pressure and temperature measurement. The measurement mesh is shown in Figure 4.1 for both the measurements. At each radial location both the probes were rotated to align them with the mean flow direction as measured by the pneumatic five hole probe.

Approximately 300 revolutions of rotor 2 synchronized data was acquired at each location from both the probes. 250 revolutions of each data set was used for ensemble averaging. The appropriate number of ensembles to process was determined by examining the differences between the mean and RMS values of the signals at the suction surface casing endwall corner region (the region of the highest levels of unsteadiness) averaged from 10, 20, 50, 100, 150, 200, 250 and 300 revolutions. Assuming exponential decay of difference as a function of number of ensembles, it was found that the bias introduced by averaging 250 ensembles was a small fraction of the measurement uncertainty. This data was then reduced to pressures and temperatures, ensemble averaged and then decomposed into time averaged pressure and temperature, RMS deterministic and unresolved unsteadiness distributions using the techniques described in chapter 3. At a few select locations, continuous stream of data was also acquired at a frequency of 200 kHz to conduct spectral analysis. The results of the spectral analysis are integrated with the ensemble averaged analysis to complete the flow field description downstream of an embedded stator. Use is also made of the steady state pneumatic five hole probe data as well as the time averaged results from the unsteady CFD simulation of this flow carried out by Dr. Ed Hall of Allison Engine Company to explain the various flow features seen in the pressure and temperature

data. The unsteady computations were conducted using the ADPAC analysis code.

Briefly, the ADPAC analysis solves a time-dependent form of the three-dimensional Reynolds-averaged Navier-Stokes equations using a time-marching numerical formulation. Solutions may be obtained using either a rotating cylindrical coordinate system for annular flows, or a stationary Cartesian coordinate frame for linear cascades or other non-cylindrical geometries. The numerical algorithm employs a finite volume explicit multigrid Runge-Kutta time-marching solution algorithm. Steady state flows are obtained as the time-independent limit of the time-marching procedure. Several steady state convergence acceleration techniques (local time stepping, implicit residual smoothing, and multigrid) are available to improve the overall computational efficiency of the analysis. A pseudo-time iterative implicit algorithm is employed to permit large time steps for time-accurate flow predictions. A relatively standard implementation of the Baldwin-Lomax turbulence model was employed to compute the turbulent shear stresses and turbulent heat flux. A complex O-H mesh system (161x41x41 nodes for each blade row) was used to grid the compressor geometry and 1:1:1 blade count (rotor 2:stator 2:rotor 3) was used to compute the flow. The full details of the simulation are given in Hall (1996).

The time averaged flow is equivalent to the the steady state flow field as explained in Chapter 3. Equation 3.20 is used to calculate the time averaged pressure and temperature. This is then presented as a total pressure rise coefficient ($\overline{C_{pt}}$) and a total temperature rise ($\overline{T_{or}}$) respectively.

$$\overline{C_{pt}} = \frac{(\overline{P_{ol}} - \overline{P_{s1}})}{(\overline{P_{o1}} - \overline{P_{s1}})} \tag{4.1}$$

$$\overline{T_{or}} = (\overline{T_{ol}} - \overline{T_{o1}}) \tag{4.2}$$

where, $\overline{P_{ol}}$ is the local time averaged total pressure as measured by the kulite probe, $\overline{P_{s1}}$ is the mass averaged steady state casing static pressure measured at the inlet to the compressor, $\overline{P_{o1}}$ is the mass averaged steady state total pressure measured at the inlet

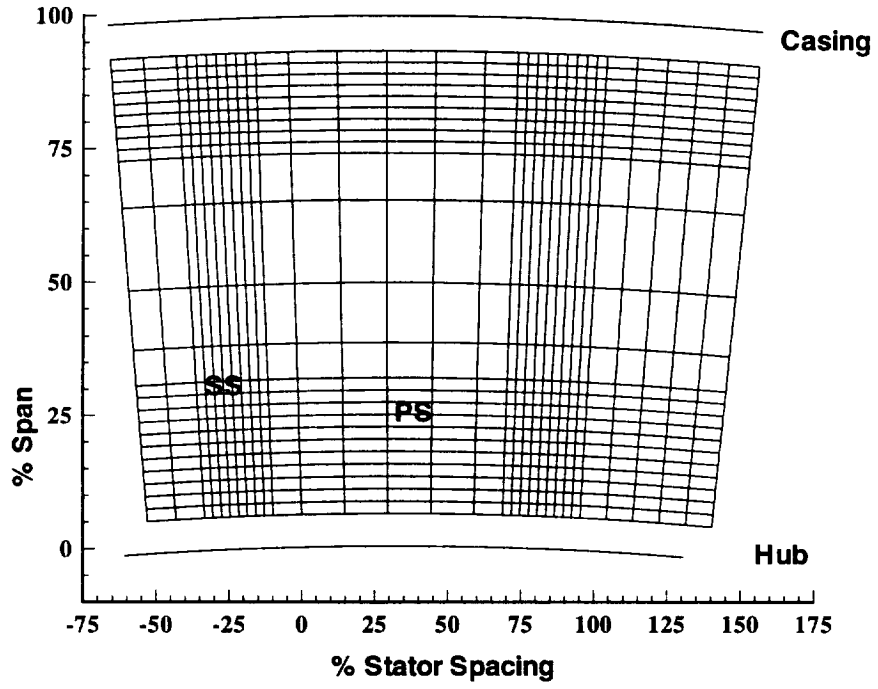

(a) Kulite Probe Mesh

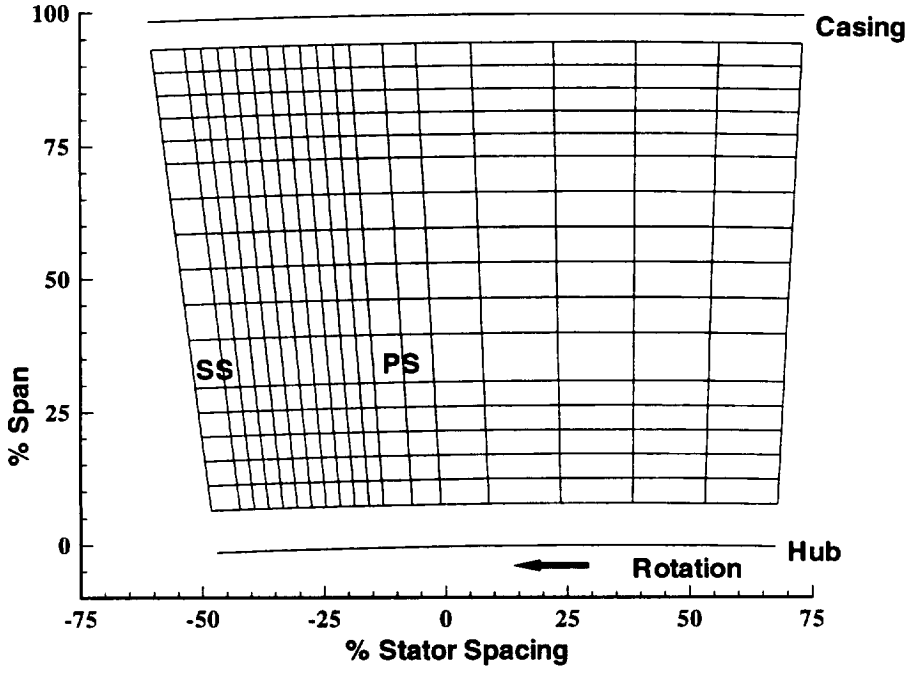

(b) Aspirating Probe Mesh

Figure 4.1. Area traverse mesh downstream of stator 2

to the compressor, $\overline{T_{ol}}$ is the local time averaged total temperature as measured by the aspirating probe and $\overline{T_{o1}}$ is the mass averaged steady state total pressure measured at the inlet to the compressor. Since, the time required to acquire each data point is quite long, the entire traverse was conducted over a period of a week for each measurement. Care was taken to maintain the compressor at the same operating point for the entire traverse and the inlet flow parameters (total pressure, total temperature and static pressure) are measured at the same time the unsteady data is acquired. In this way any errors that may enter the measurement due to operating point changes are taken care of. The setup of the compressor operating point is explained in detail in Chapter 2.

Blade-to-blade distribution at select radial locations, area contours and passage averaged hub-to-tip distributions of time averaged total and static pressure, total temperature, total velocity, isentropic efficiency, total pressure losses, secondary flow and axial component of vorticity are analyzed and discussed. The isentropic efficiency (η_{isen}) is calculated using the following equation:

$$\eta_{isen} = \frac{P_r^{\frac{\gamma-1}{\gamma}} - 1}{T_r - 1} \tag{4.3}$$

where P_r is the time averaged total pressure ratio and T_r is the time averaged total temperature ratio referred to conditions at the inlet to the compressor.

$$P_r = \frac{\overline{P_{ol}}}{\overline{P_{o1}}}, \; T_r = \frac{\overline{T_{ol}}}{\overline{T_{o1}}} \tag{4.4}$$

The total pressure loss (ζ) are calculated using:

$$\zeta = \frac{\overline{P_{o5}} - \overline{P_{ol}}}{0.5\rho U_t^2} \tag{4.5}$$

where $\overline{P_{o5}}$ is the passage averaged total pressure distribution upstream of the stator derived from the ADPAC solution. The hub-to-tip distribution was spline fit using cubic splines and interpolation was used to derive the upstream total pressure. The rotor exit data was adjusted to account for the changes in operating point between the experiment and

computation. The secondary flow is defined as the velocity vector whose components are the difference between the measured circumferential velocity and the design value and the radial velocity.

$$\vec{V}_{sec} = (V_\theta - V_{\theta_d})\hat{i} + V_r\hat{j} \tag{4.6}$$

The design value (V_{θ_d}) is obtained from a through flow analysis of the geometry with the design deviation correlations. The axial component of vorticity is calculated using

$$\omega_z = \frac{1}{r}\frac{\partial(rV_\theta)}{\partial r} - \frac{1}{r}\frac{\partial V_r}{\partial \theta} \tag{4.7}$$

The data was interpolated onto a very fine grid using standard parametric spline fits. Then a finite difference formulation using second order differencing is used to calculate the various gradients for calculating axial vorticity component. The velocities are normalized by the blade tip speed and the radius is normalized by the inner radius of the compressor casing and hence the vorticity is normalized by the rotation rate (Ω).

Hub-to-tip distributions of mass weighted passage averaged quantities are also used to explain some of the physical phenomena at the stator 2 exit. The passage average $\overline{\phi}$ of any quantity ϕ is given by:

$$\overline{\phi} = \frac{\int_{ss}^{ps}(\rho V_z \phi) r d\theta}{\int_{ss}^{ps}(\rho V_z) r d\theta} \tag{4.8}$$

where V_z is the axial velocity component derived from the pneumatic five hole probe data at that radial and tangential measurement location and the integration is done for one blade passage only.

Before discussing the results, it is useful to ascertain the relative uncertainties of each of the quantities. The uncertainties are given in Table 4.1. The uncertainties are calculated based on the concepts outlined in Appendix A and are expressed as a ratio of the uncertainty calculated and the actual value of the derived quantity in percent.

Figure 4.2 shows the comparison between the time averaged total pressure data and the data acquired from a tangential traverse of the pneumatic five hole probe (FHP) at

Table 4.1. Uncertainty of Various Derived Quantities: Time Averaged Data

Quantity	Uncertainty (%)	Figures
Total Temperature Rise ($\overline{T}_{or}$)	± 7%	4.3, 4.4(a), 4.5, 4.6(a), 4.9(a)
Total Temperature Ratio ($\overline{T}_r$)	± 0.453%	4.10, 4.12
Total Pressure Coefficient ($\overline{C}_{pt}$)	± 2.483%	4.2, 4.3, 4.4(a), 4.4(a), 4.5, 4.6(b), 4.9(b)
Total Pressure Ratio ($\overline{P}_r$)	± 0.22%	4.10, 4.11
Static Pressure Coefficient ($\overline{C}_{ps}$)	± 2.667%	4.4(c), 4.6(c), 4.9(c)
Total Velocity (V_{tot}/U_t)	±3.3%	4.4(d), 4.6(d), 4.9(d)
Axial Velocity (V_z/U_t)	±3.3%	4.10, 4.13
Tangential Velocity (V_θ)	±2.5%	4.4(i), 4.6(i), 4.9(i)
Radial Velocity (V_r)	±2.5%	4.4(j), 4.6(j), 4.9(j)
Yaw angle	±4.0%	4.10, 4.14
Isentropic Efficiency (η_{isen})	±4.043%	4.4(e), 4.6(e), 4.9(e)
Total Pressure Loss (ζ)	±3.33 %	4.4(f), 4.6(f), 4.9(f)
Secondary Velocity ($\vec{V}_{sec}$)	±4.5%	4.4(g), 4.6(g), 4.9(g)
Axial Vorticity (ω_z/Ω)	±10%	4.4(h), 4.6(h), 4.9(h)

the same axial location at midspan. There is very good comparison between the time averaged values and the FHP results. The pressure coefficients have been modified to account for the small changes in the operating condition. All the features of the flow captured by the FHP have been captured by the kulite probe measurement. It is absolutely essential to ensure that there is repeatability of results. A tangential traverse was repeated at midspan using both the kulite and aspirating probes. The results of this traverse are shown in Figure 4.3. There is very good repeatability for the kulite total pressure data set. However, the repeatability in the aspirating probe is not as good as that of total pressure but it is still acceptable as the variation is within the limits of the measurement uncertainty. The results presented in Figures 4.2 and 4.3 provide confidence in the data acquired from a high response probe.

In this chapter, focus is placed on the following important features of the flow: the stator wake regions, effect of the secondary flow and the thickening of the boundary layer near the suction surface corner in the casing region and the effect of secondary and leakage flows in the hub endwall region. Figure 4.4 shows the contours of the following time averaged quantities: total pressure coefficient, total temperature rise, static pressure rise, total velocity normalized by rotor blade tip speed, tangential velocity, radial velocity, isentropic efficiency of the first two stages, total pressure loss, secondary velocity vectors and the axial component of vorticity respectively. The static pressure, the velocity field, total pressure losses and the vorticity distributions are derived from the pneumatic five-hole probe (FHP) data. Figure 4.5 shows the blade-to-blade distribution of time averaged total pressure and total temperature at a few select radial locations (close to hub, 21.76% span, mid-span, 81.89% span and close to casing endwall).

The core region defined as the region away from the endwalls (approximately 60% of the span) and the stator wakes (approximately 80% of the pitch) has high levels of total pressure coefficient, low levels of total temperature rise, high levels of static pressure,

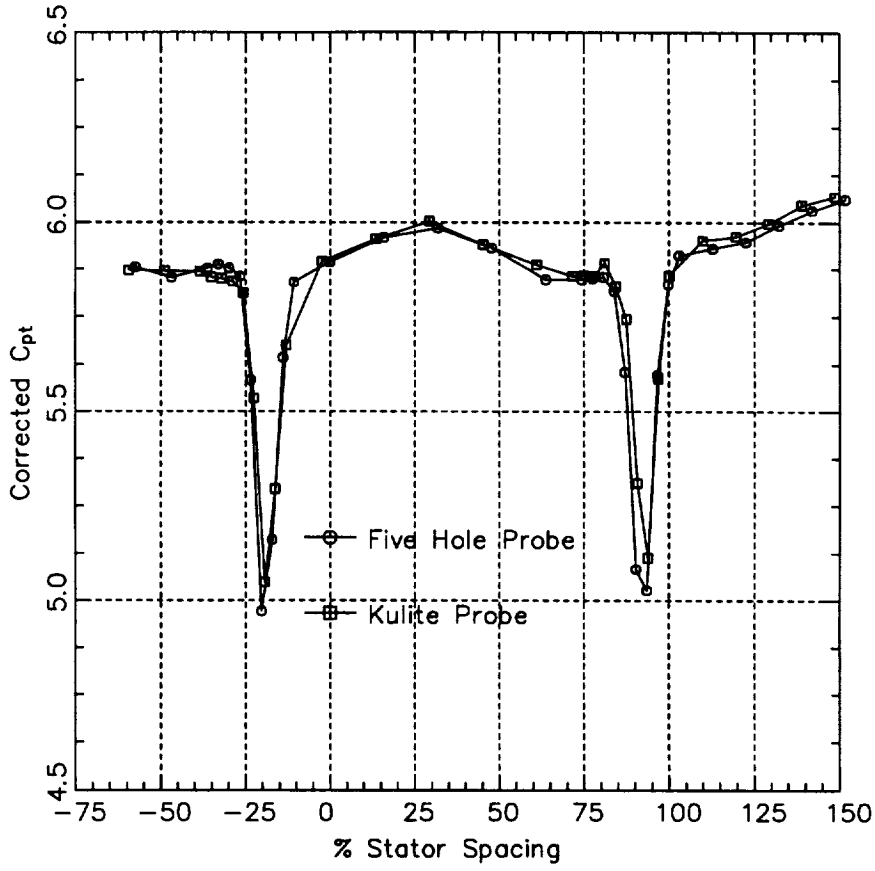

Figure 4.2. Comparison of Blade-to-blade Distribution of Time Averaged Total Pressure Coefficient and Total Pressure Derived from Pneumatic FHP Data at the Midspan Location

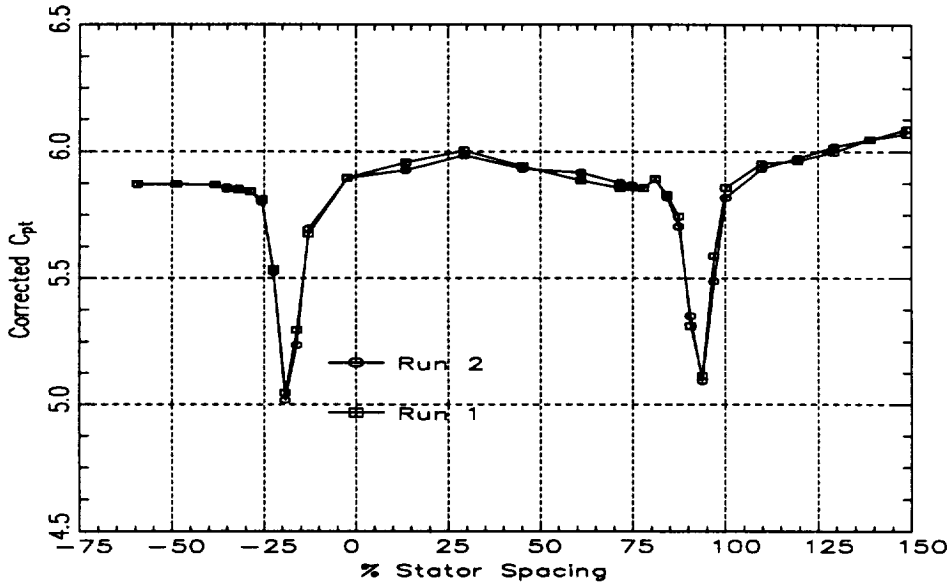

(a) Total Pressure: Kulite Probe

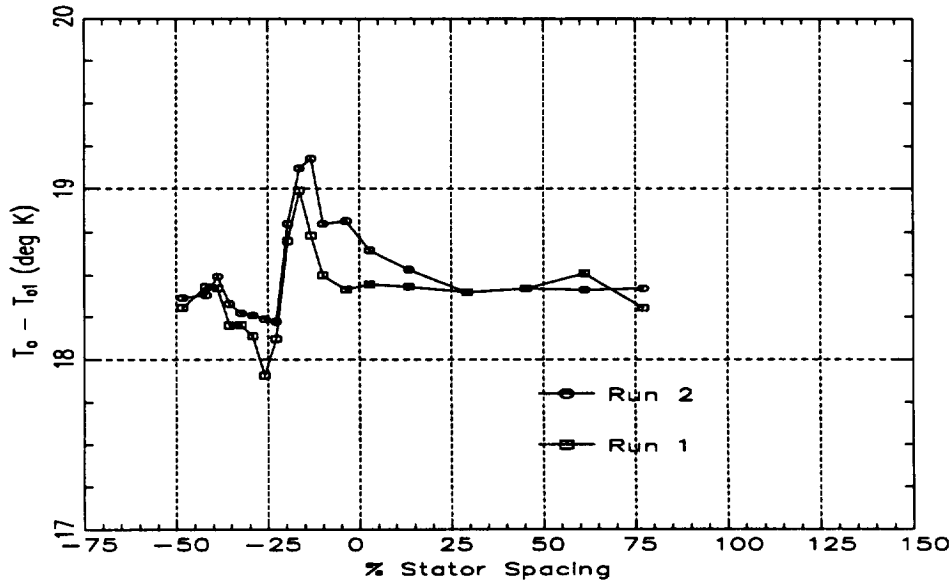

(b) Total Temperature: Aspirating Probe

Figure 4.3. Repeatability of Blade-to-blade Distribution of (a) Time Averaged Total Pressure Coefficient and (b) Time Averaged Total Temperature Rise: Midspan Location

high efficiency levels, low losses, negligible radial velocity, axial vorticity and secondary flow. There is consistency in the data acquired from the various probes (kulite, five hole probe and aspirating probe) with respect to the extent of the endwall region, presence of wakes and the resolution of the hub leakage and the casing corner regions of the flow. Detailed interpretation of the following important features of the flow: the stator wake regions, effect of the secondary flow and the thickening of the region near the suction surface corner in the casing region and the effect of secondary and leakage flows in the hub endwall region are given below.

4.1 Stator Wake Regions

Thin stator wakes are observed in the midspan regions at this axial location aft of the stator. This is consistently observed in all the data sets. The stator wake is characterized by high total temperature rise, low total pressure coefficients, higher static pressure, high vorticity, high levels of total pressure loss and high levels of radial inward velocity brought about by the radial inward pressure gradient. Widening of the stator wakes is seen in the endwall regions (both hub and casing endwall). In the hub endwall region the wake width increases both on the pressure side and on the suction side of the stator. However, in the casing endwall region, the thickening is mainly on the suction side. Due to interaction between the stator wake flow and the hub clearance flow as well as an increase in the blade loading brought about by high incidences from the rotor exit low momentum flow region upstream causes the thickening of the stator wakes in the hub endwall region. In the casing endwall region, the thickening is mainly due to the presence of a corner interaction with the endwall flow on the suction side.

The temperature wake (Figure 4.4(a)) is very thin in the midspan region and quite thick in the hub and casing endwall regions. The width of the temperature wake in the

midspan regions is almost the same as the total pressure wake. However, in the region from hub to midspan, the temperature wake on the pressure side of the stator is wider compared with the pressure (Figure 4.4(b)) and velocity wakes (Figure 4.4(d)) at the same location. This is probably due to increased mixing brought about by the interaction of the rotor wakes and rotor hub flow with the endwall flow on the hub and stator clearance flow. This would increase the amount of heat dissipated consequently increasing the temperature as well as the wake width on the pressure side. There is also accumulation of high temperature fluid from the upstream rotor wake on the pressure surface of the stator. This phenomena is consistent with the analysis of Kerrebrock and Mikolajczak (1970). This may also be due to radial outward transport of rotor hub flow on the pressure side of the stator (Figure 4.4(j)). The coupling between the velocity (Figure 4.4(d)) and pressure wakes (Figure 4.4(b)) is through the momentum equation whereas the coupling between the velocity and temperature (Figure 4.4(a)) is through the energy equation. Stronger coupling exists between stagnation pressure and total velocity than that exists between stagnation temperature and total velocity. Consequently the wake thickness correlation between stagnation pressure and velocity is much closer than that between total temperature and velocity.

The static pressure (Figure 4.4(c)) is found to increase slightly across the stator wake. The static pressure in the direction normal to the streamlines at the exit of the stator is given by:

$$\frac{1}{\rho}\frac{\partial p}{\partial n} = \frac{{W_s}^2}{R_c} + \frac{\partial}{\partial n}(\overline{{w_n'}^2}) + \frac{\partial}{\partial s}(\overline{w_n' w_s'}) \tag{4.9}$$

where s and n are the streamwise and normal directions respectively, R_c is the radius of curvature, $\overline{{w_n'}^2}$ is the turbulence intensity and $\overline{w_n' w_s'}$ is the turbulent shear stress. Presence of flow curvature, turbulence intensity and turbulent shear stress distribution contributes to an increase in the static pressure gradient.

Radial inward velocities and very low tangential and axial velocities in the wake

contribute to very high radial inward flow in the stator wakes. This is mainly due to the radial inward pressure gradient that exists in stators. In the endwall regions, the interaction of the stator wake flow with the endwall flow features causes intense mixing which results in much thicker wakes, higher losses, higher vorticity and very low efficiency compared with the midspan region.

Similar features have been documented by Howard et al. (1993) downstream of an embedded stator in a large scale low-speed compressor with repeating stage blading. Jung and Eikelmann (1995) also document very similar features to that observed both in the PSU data set as well as the Cranfield compressor (Howard et al. (1993)). The Jung and Eikelmann (1995) data is in a high speed industrial compressor.

The mass-averaged overall loss coefficient in total pressure (equation 4.5) for the entire stage is calculated to be 0.09802. The highest losses occur in the wakes and in the casing endwall corner region. The wake regions also have the lowest isentropic efficiency, however, these are mainly confined to the endwall region (Figure 4.4(e)). The efficiencies are lower on the pressure side of the stator wake than on the suction side due to higher temperatures observed at this location.

4.2 Hub Endwall Region

In order to examine the detailed structure of the flow field in the hub endwall region, the contours of various flow quantities (total temperature rise, total pressure coefficient, static pressure, total velocity, efficiency, loss, secondary flow vectors, axial vorticity, tangential and radial velocity close to the hub endwall (upto 25% span) are shown plotted in Figure 4.6. The regions of interest are: midpitch close to the hub and on the suction and pressure side of the stator wake close to the hub. The data near the midpitch location close to the hub indicates a region of low total pressure coefficient, low total velocity,

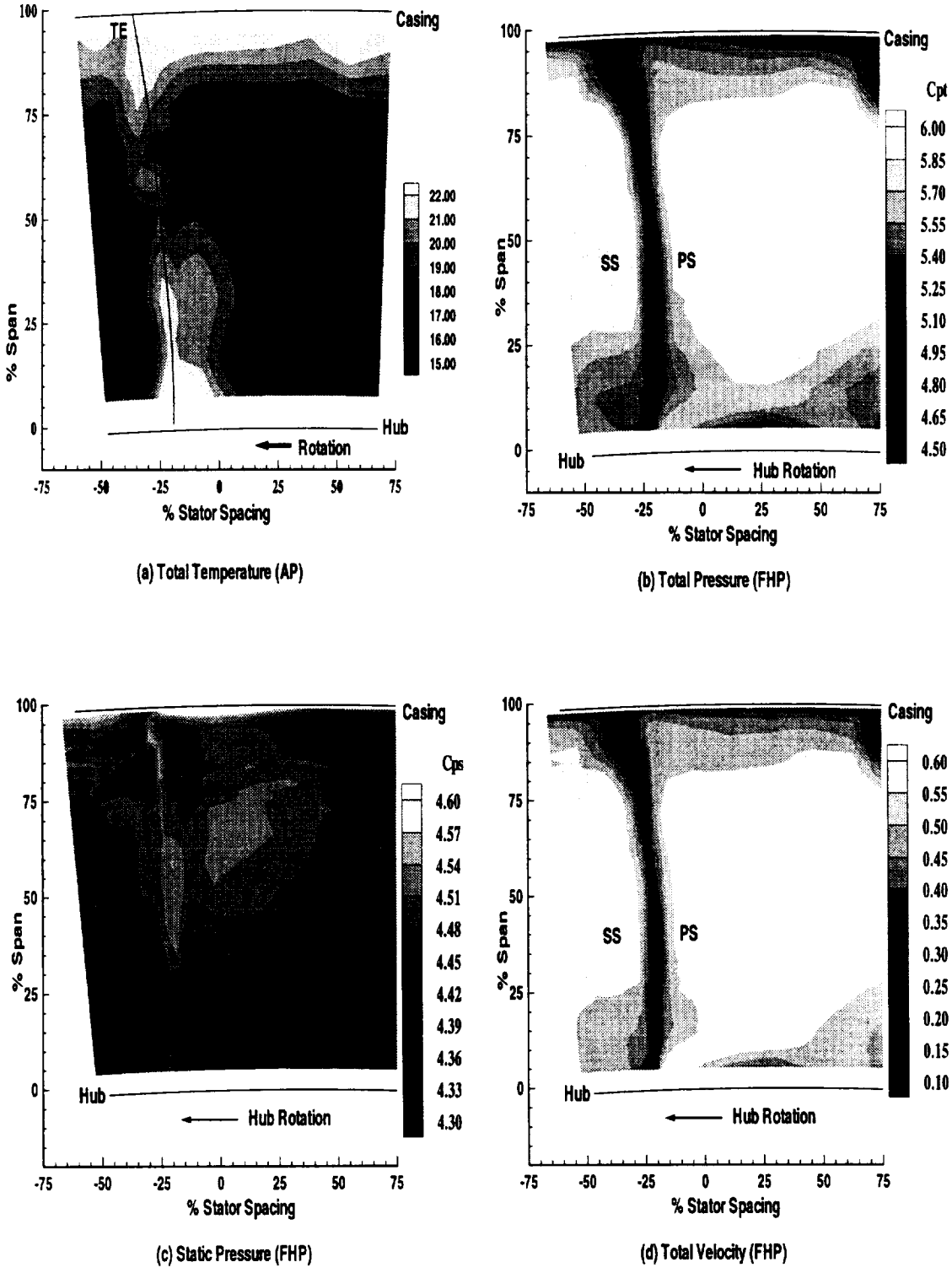

Figure 4.4. Contours of Time Averaged Quantities: (a) Total Temperature, (b) Total Pressure, (c) Static Pressure and (d) Total Velocity

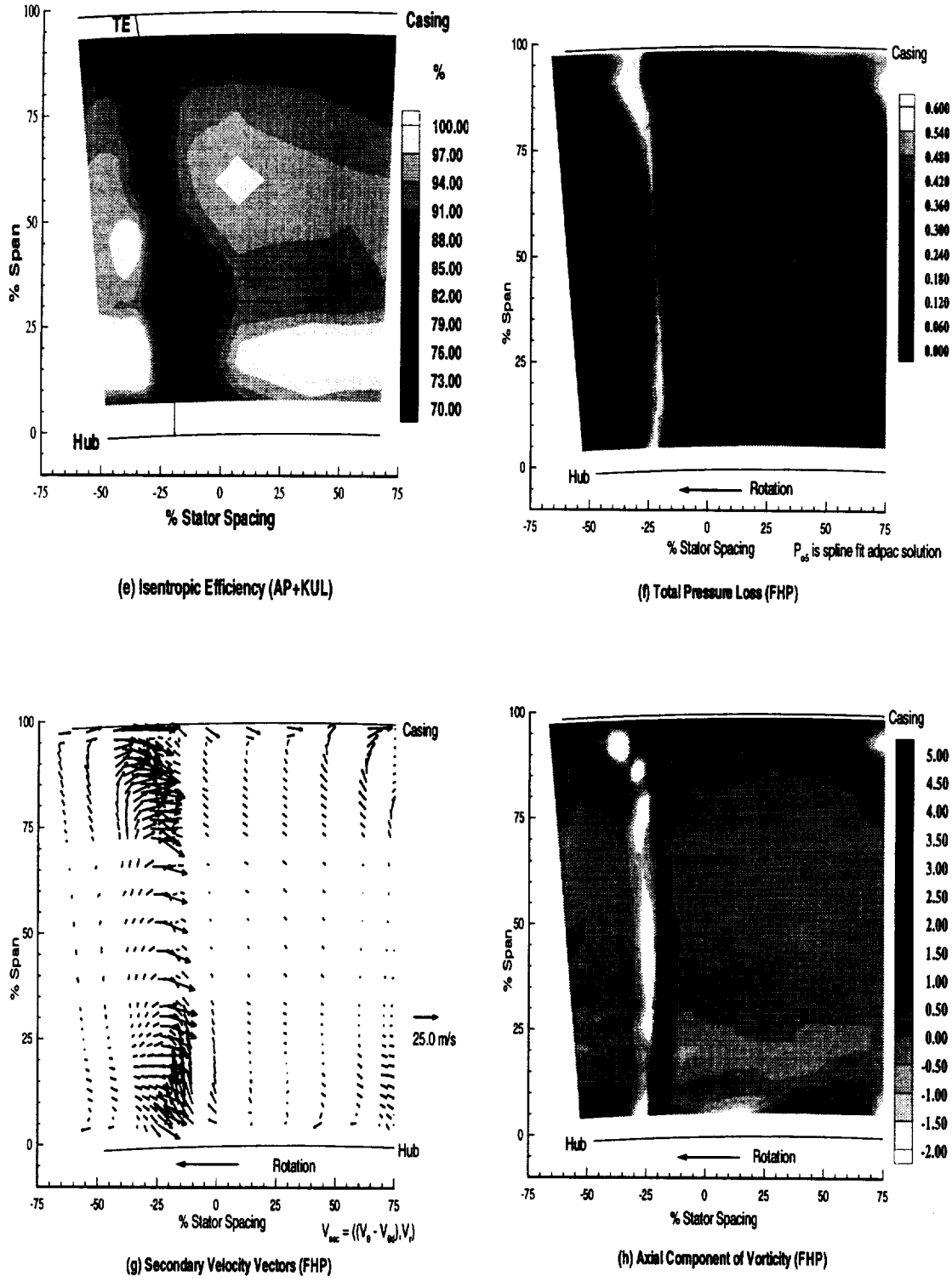

Figure 4.4 (Cont.). Contours of Time Averaged Quantities: (e) Isentropic Efficiency, (f) Total Pressure Loss, (g) Secondary Flow Vectors and (h) Axial Vorticity

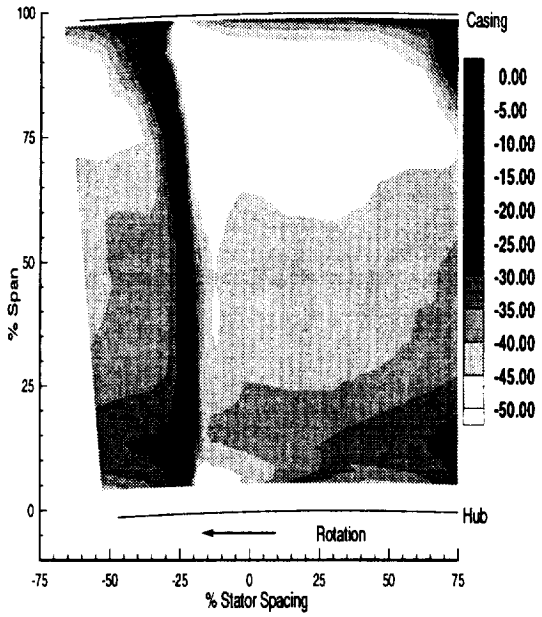

(i) Tangential Velocity, m/s (FHP)

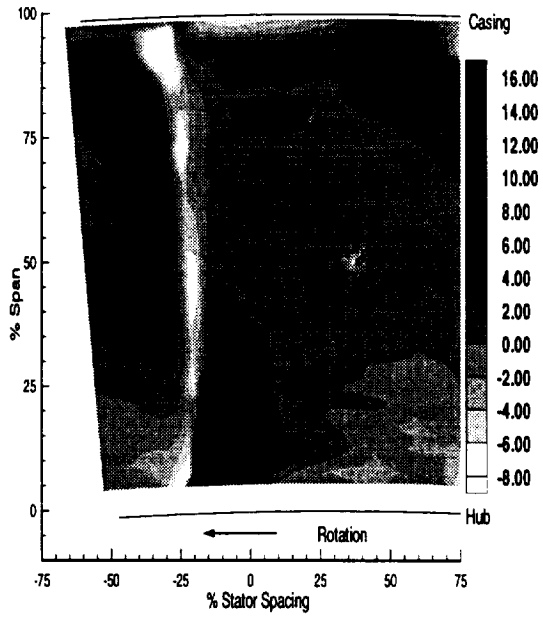

(j) Radial Velocity, m/s (FHP)

Figure 4.4 (Cont.). Contours of Time Averaged Quantities: (i) Tangential Velocity and (j) Radial Velocity

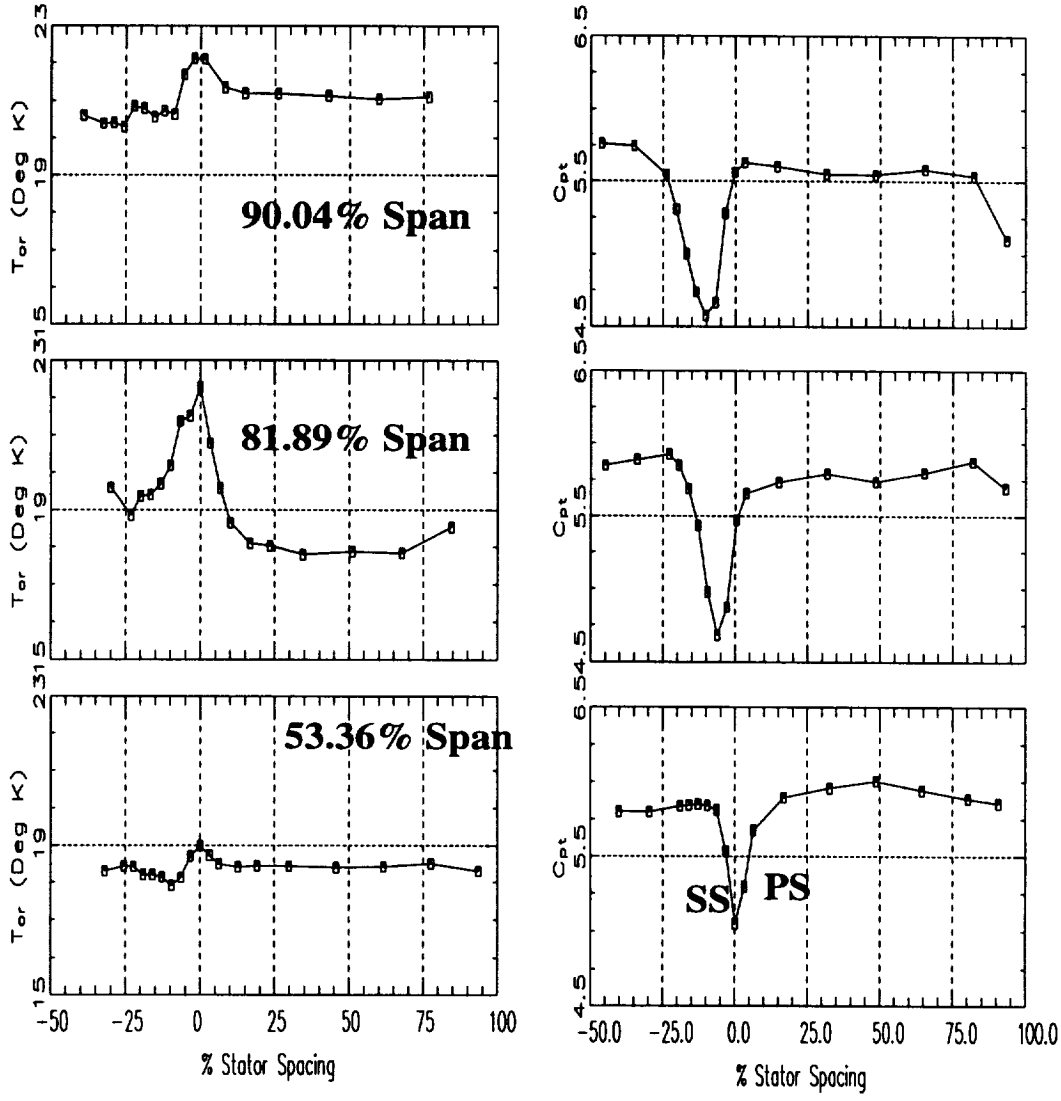

Figure 4.5. Blade-to-blade Distribution of Time Averaged Total Pressure Coefficient and Time Averaged Total Temperature Rise at Various Radial Locations

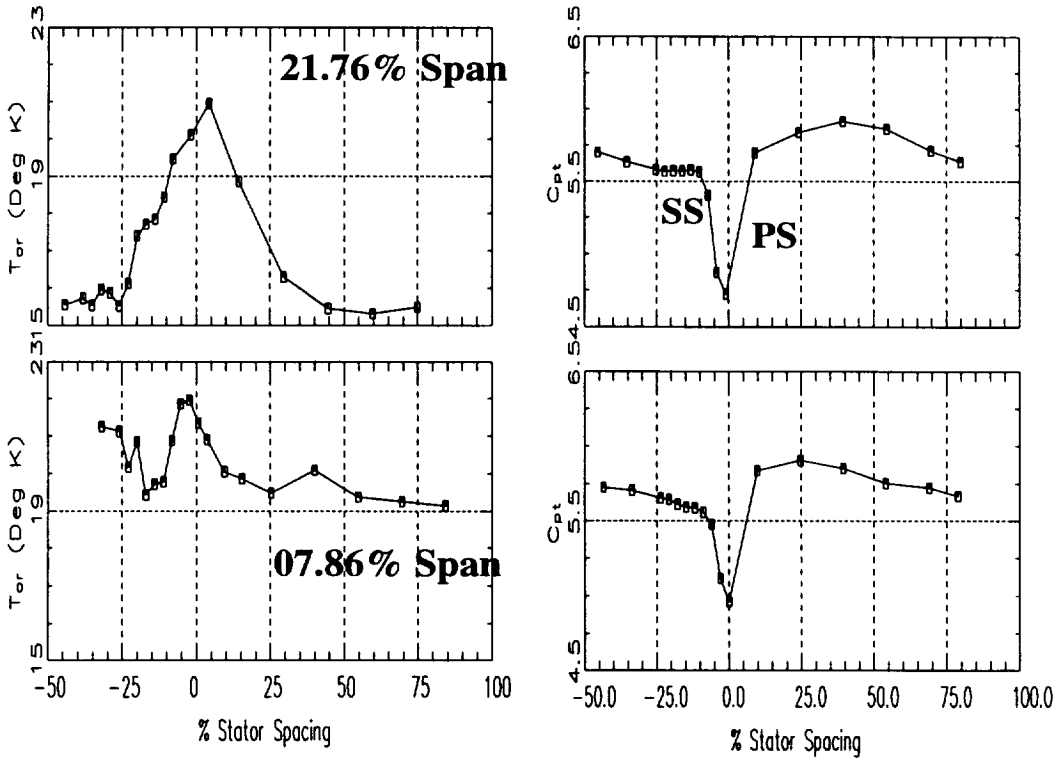

Figure 4.5 (Cont.). Blade-to-blade Distribution of Time Averaged Total Pressure Coefficient and Time Averaged Total Temperature Rise at Various Radial Locations

high losses, high tangential velocity (underturning) and a region of significant vorticity. The concentric loss patterns indicates that this region is possibly caused by the leakage flow generated due to the clearance between the stator tip and the rotating hub. From the vorticity distribution (Figure 4.6(h)), it can be seen that the direction of rotation of this structure is opposite to the direction of rotation of the hub. So this is most likely the leakage flow from the stator hub.

Figure 4.7 shows a schematic of the development of the leakage flow and its subsequent rollup into a vortex for an industrial compressor with cantilevered stator blading and a rotating hub (Jung and Eikelmann (1995)). Figure 4.8 shows a similar distribution for the Penn State data set. Comparing Figures 4.7 and 4.8, one can conclude that the low energy field on the stator hub is indeed the hub leakage flow. The leakage vortex originates near the leading edge of the blade and develops through the passage all the while increasing in strength through enrichment with the clearance fluid. This flow is then transported towards the suction surface by hub rotation. The Jung and Eikelmann (1995) data is from a high speed compressor at the peak efficiency condition and the present data is from a medium speed compressor at the peak efficiency condition. Similar distributions have been reported by Howard et al. (1993) in a large low speed multistage axial flow compressor with repeating stage blading. The extent of this leakage flow region is around 60% in the pitchwise and nearly 10% in the spanwise directions. As a result, this endwall phenomena generates more blockage than that generated by endwall viscous fluid on the hub endwall.

The temperature distribution is almost constant across the passage very close to the hub. This is very surprising considering that there is large mixing in this region due to the presence of a vortex which leads to viscous dissipation effects. This should result in production of heat and consequently a increase in temperature. A general increase in temperature is seen in the radial direction across this region consistent with the above

phenomena. Moreover very little experimental and computational information is available on the behavior of the total temperature field in a streamwise vorticity pattern. So at this time further speculation is just not justified. The efficiency distribution does not show any significant changes in the pitchwise direction, though there is a decrease in the passage averaged efficiency which is mainly due to the large deficit in total pressure both in the wake and the mid-passage leakage region as well as increase in the total temperature rise in the stator wakes.

The secondary flow vectors (Figure 4.6(g)) show a radially outward transport of flow on the pressure side of the stator from the hub upto 35% span. This is most likely brought about by scraping of the hub wall boundary layer as well as stator leakage flow. There is a high static pressure region near the pressure surface and a low pressure region near the suction surface of the hub (Figure 4.6(c)). The radial gradient in static pressure is observed to be negative on the pressure side and positive on the suction side. This is consistent with the secondary flow vector distribution shown in Figure 4.6(g). This radial outward transport caused by scraping probably accounts for higher temperatures observed on the pressure surface away from the hub.

Due to the presence of hub leakage flow vortex and its growth in the streamwise direction, the blockage increases thereby increasing the throughflow velocity of the fluid. This is very clearly seen in the higher levels of total velocity on the pressure side of the stator close to the hub (Figure 4.6(d)). This in turn increases the circumferential velocity which increases the stagnation enthalpy leading to an increase in the total temperature rise on the pressure side of the stator. Even though the stagnation pressure also increases in this region, the increase in entropy due to intense mixing results in decreased efficiency near the hub wall pressure surface corner. Near the suction side of the stator wake close to the hub, low temperatures, moderate pressure rise and high efficiency is observed. This is probably caused by leakage flow from the hub region augmented by hub rotation

washing away the corner separation region. This is also the region of intense flow mixing as observed by the band of negative vorticity spanning across almost the entire passage. This may account for high efficiency observed almost across the entire passage.

4.3 Suction Surface Casing Endwall Corner Region

The other region which has a complex flow and loss region that warrants interpretation is the suction surface casing endwall corner region. Figure 4.9(a)-(i) shows the contours of various flow quantities (total temperature rise, total pressure coefficient, static pressure, total velocity, efficiency, loss, secondary flow vectors, axial vorticity, tangential and radial velocity close to the casing endwall (from 70% span upto casing). This region is characterized by low values of stagnation pressure, axial velocity, static pressure, total velocity, efficiency as well as presence of large secondary flow, radial inward velocity and high vorticity. This is also a region of low efficiency and high unresolved unsteadiness (as will be observed later) as well as the high total pressure loss (almost 5% of upstream total pressure). The contour pattern generated by the radial velocity (Figure 4.9(j)) and the secondary flow pattern (Figure 4.9(g)) suggests a vortex type distribution, which is confirmed by the vorticity distribution (Figure 4.9(h)). Compared to the situation near the hub, the vortex center and the loss core are located at approximately in the same location with respect to the blade. This loss core is of a higher level than that seen at the hub region (5% compared to 2.5% at the hub).

This flow arises due to a combination of various phenomena: tendency for casing stall, high inlet skew and casing secondary flow. In this region, there is an intense secondary flow feature as evidenced by transverse flow and radial outward flow towards the low pressure region on the suction side of the stator (Figure 4.9(g)). The flow angle distribution shows that the flow is overturned on the suction side and underturned on the

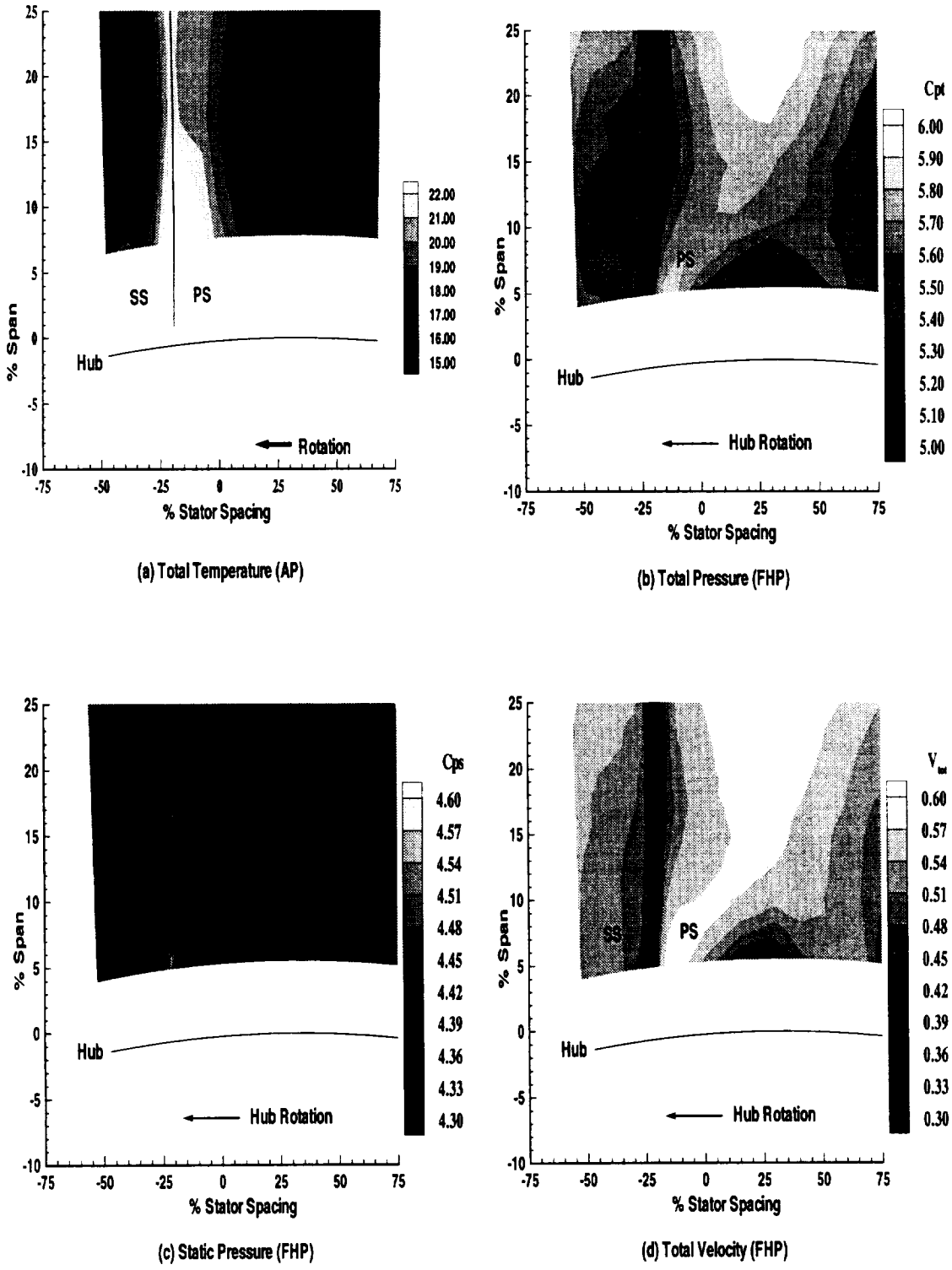

Figure 4.6. Contours of Time Averaged Quantities Near Hub: (a) Total Temperature, (b) Total Pressure, (c) Static Pressure and (d) Total Velocity

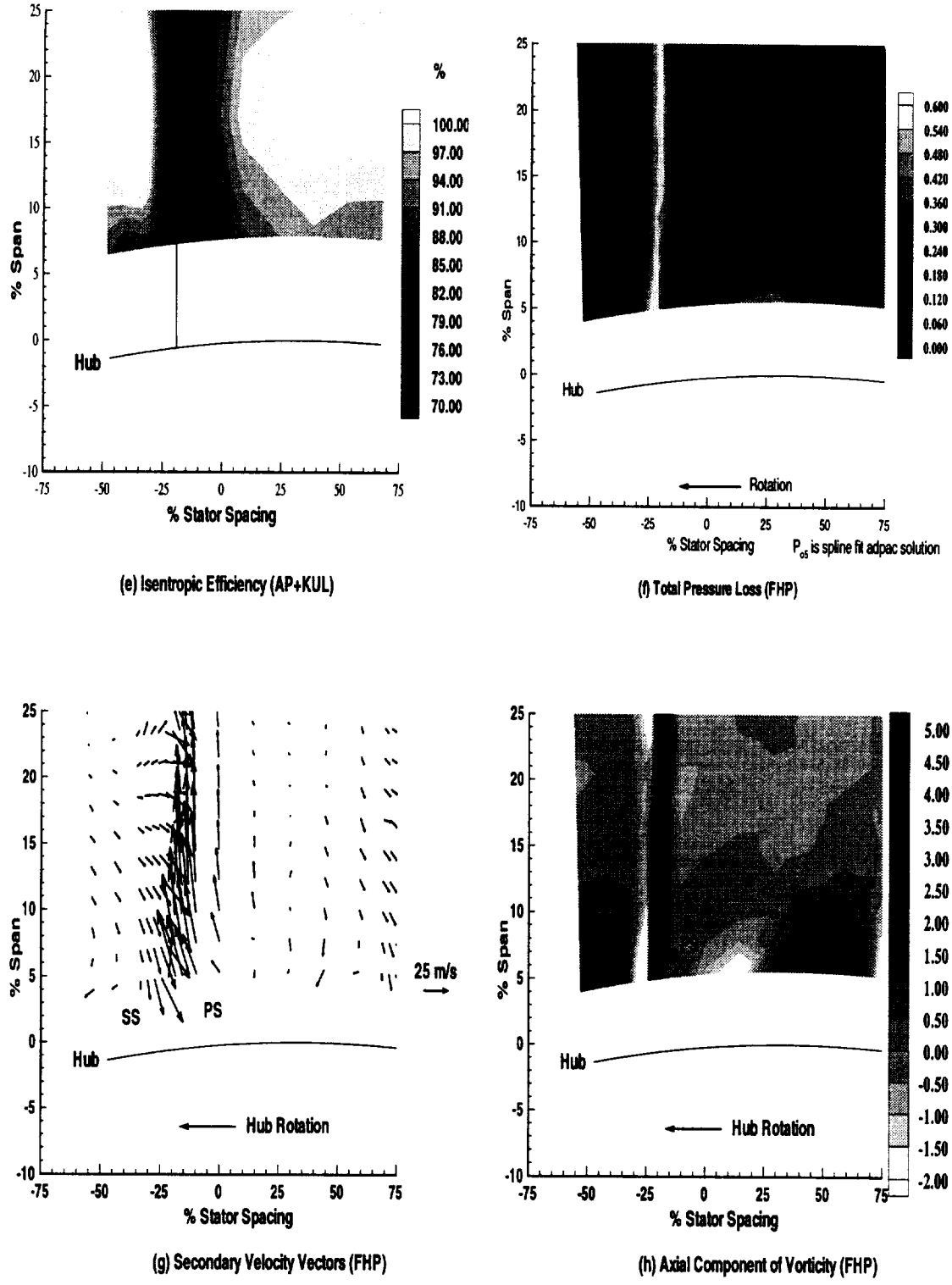

Figure 4.6 (Cont.). Contours of Time Averaged Quantities Near Hub: (e) Isentropic Efficiency, (f) Total Pressure Loss, (g) Secondary Flow Vectors and (h) Axial Vorticity

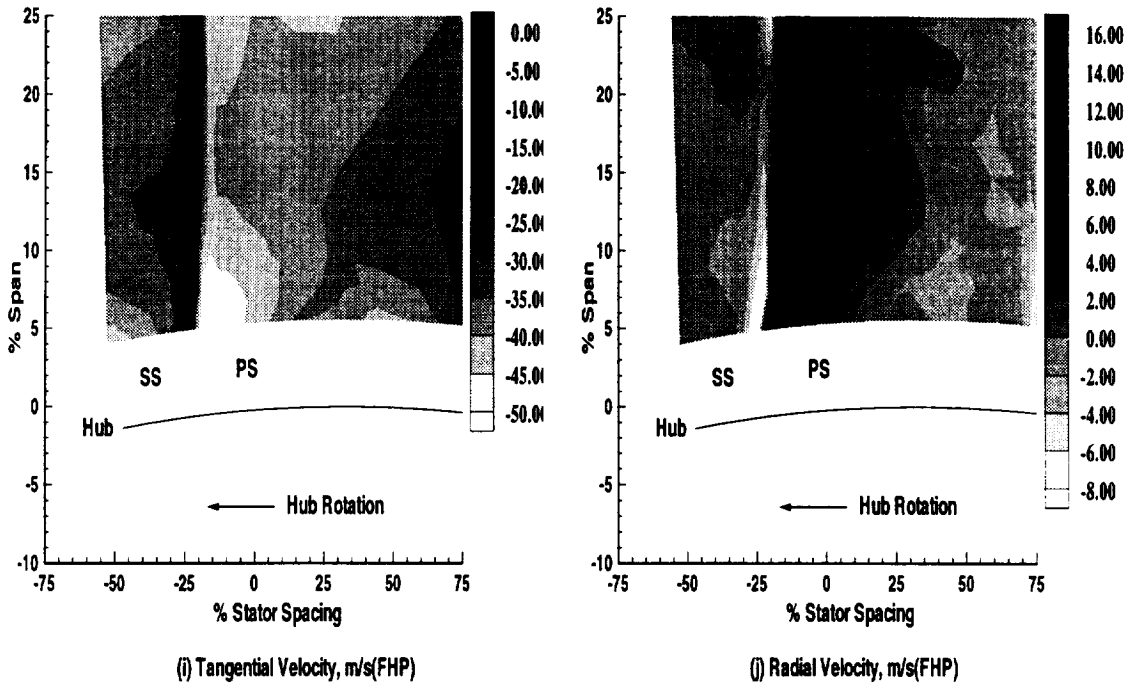

(i) Tangential Velocity, m/s(FHP)

(j) Radial Velocity, m/s(FHP)

Figure 4.6 (Cont.). Contours of Time Averaged Quantities Near Hub: (i) Tangential Velocity and (j) Radial Velocity

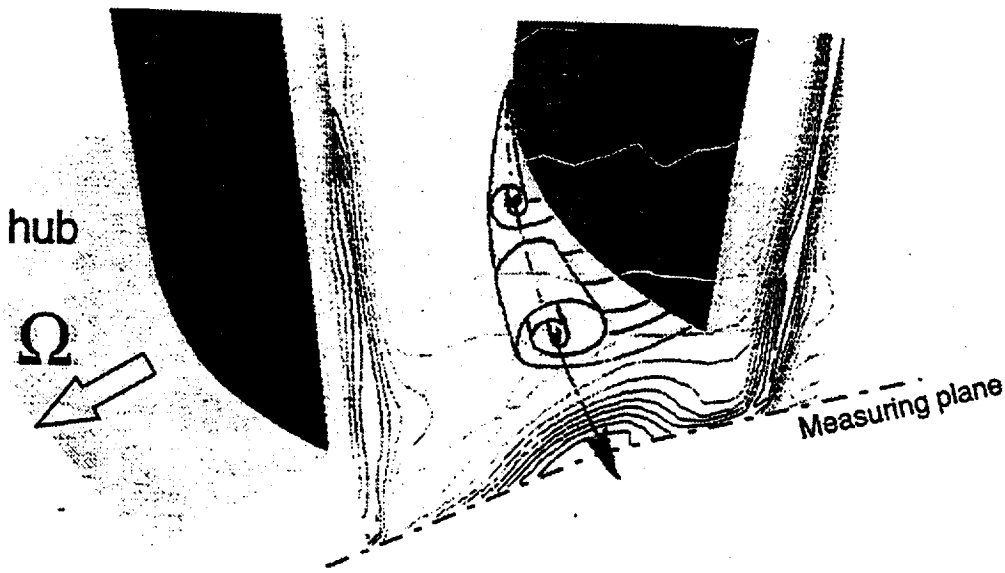

Figure 4.7. Schematic of the Development of the Hub Leakage Flow in the Stator Passage (Jung and Eikelmann (1995))

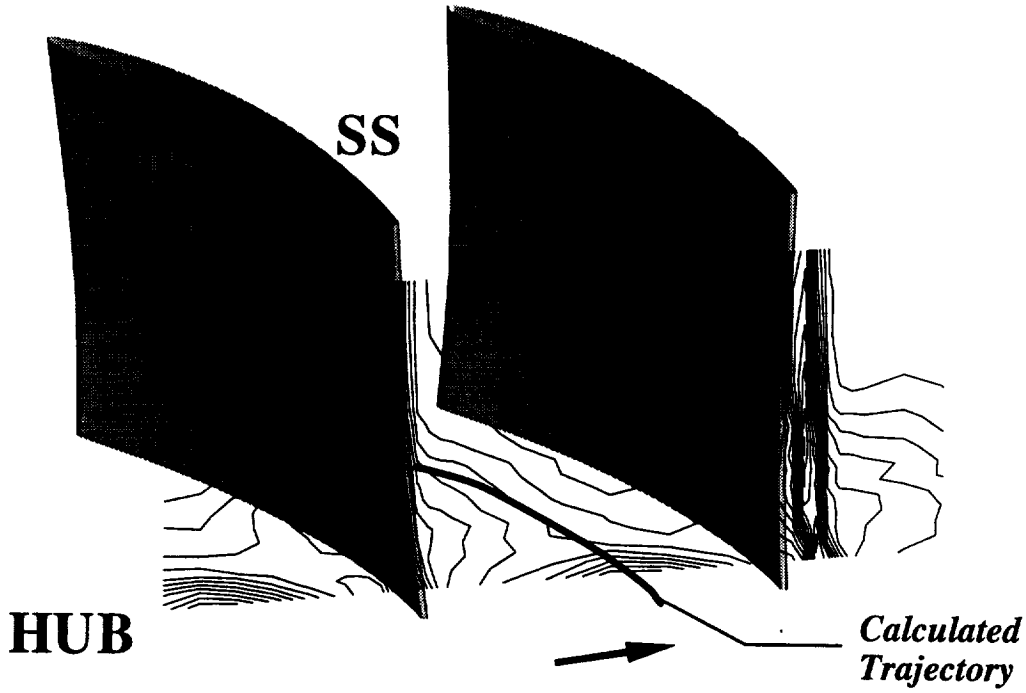

Figure 4.8. Trajectory of the Development of the Hub Leakage Flow in the Stator Passage

pressure side of the stator. The static pressure is quite low in the corner region confirming the presence of a vortex. The secondary velocity distribution shows an entrainment of flow into this region generating a large secondary vortex. There is also entrainment of flow into this region from the casing endwall corner region away from the blades. Radial outward flow seen in the secondary flow plot on the pressure side of the stator close to the casing is caused primarily by the static pressure gradient in the radial direction towards the hub (Figure 4.9(c)).

The total temperature rise distribution does not show any rise or fall in total temperature rise across the corner vortex region. This behavior is similar to that seen in the hub region across the hub leakage vortex. Away from the endwalls, the total temperature rise on the suction side is lower than that on the pressure side, primarily due to accumulation of higher temperature rotor wake fluid on the pressure side. Closer to the casing endwall, the temperature on the suction side is almost the same level as that on the pressure side. There is an increase in entropy production from the interaction and subsequent mixing of the corner vortex with the endwall flow facilitated by upstream rotor leakage flow. This results in an increased static temperature and thereby and increase in the total temperature of the flow.

The temperature wake width (Figure 4.9(a)) on the pressure side of the stator close to the casing endwall is larger than that observed from either total pressure or the total velocity (Figures 4.9(b) and (d) respectively). The rotor wake flow which is accumulating on the pressure side of the stator in the casing endwall region has a much higher temperature than the corresponding flow in the midspan regions. This increases the width of the total temperature wake but not the pressure wake. The other reason for the increase in wake width on the pressure side is probably due to the rapid decay of the total temperature wake compared to the total pressure wake. The mixing of corner flow with the wake leads to a rapid decay of the wake defect and rapid growth of the wake width. This is due

to an interaction of the secondary flow with the mainstream fluid. Two regions of high vorticity is seen in the casing endwall corner region (Figure 4.9(h)). The region with high levels of positive vorticity is close to the blade surface and this is caused by interaction between the wake and the secondary flow region. The other region which has high levels of negative vorticity is caused mainly by secondary flow features present at this location (Figure 4.9(g)).

In the casing endwall region away from the blade surfaces, intense mixing caused by interaction of the rotor tip leakage flow and the casing endwall boundary layer gives rise to almost uniform distribution of pressures, temperatures and consequently efficiency across the blade pitch from 85 to 95% span (last measurement location). Blade-to-blade non-uniformities are observed only near the stator wake regions.

4.4 Hub-to-tip Variation of Passage Averaged Flow Properties

The hub-to-tip distributions of passage averaged total pressure, total temperature, axial velocity, loss in total pressure, exit flow angle and isentropic efficiency is shown in Figure 4.10. Comparisons are made to the ADPAC solutions and design where available. The total pressure loss data has also been compared with the overall losses (profile+secondary flow loss+leakage flow loss) derived from cascade correlations described in chapter 6 of Lakshminarayana (1996). The differences between the ADPAC solution and the experimental data set is partly due to problems in matching the correct operating point for the computational data set. But the fact that a multistage calculation can capture the complex 3-D features is quite remarkable. Three distinct regions of the flow field can be observed from these distributions: hub endwall region, core flow region and casing endwall region.

The flow near the hub is mainly influenced by the stator clearance flow. The stator

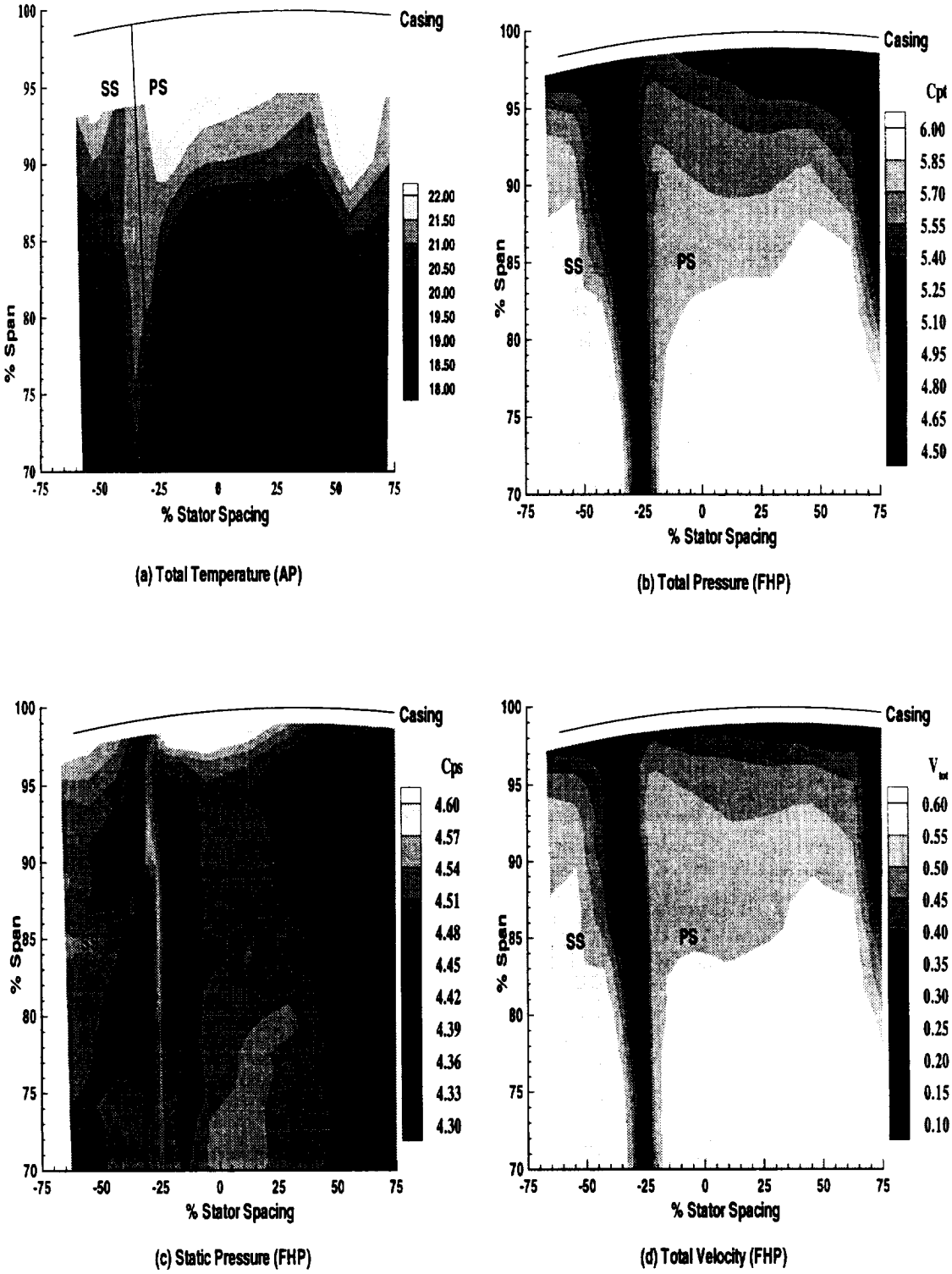

Figure 4.9. Contours of Time Averaged Quantities Near Casing: (a) Total Temperature, (b) Total Pressure, (c) Static Pressure and (d) Total Velocity

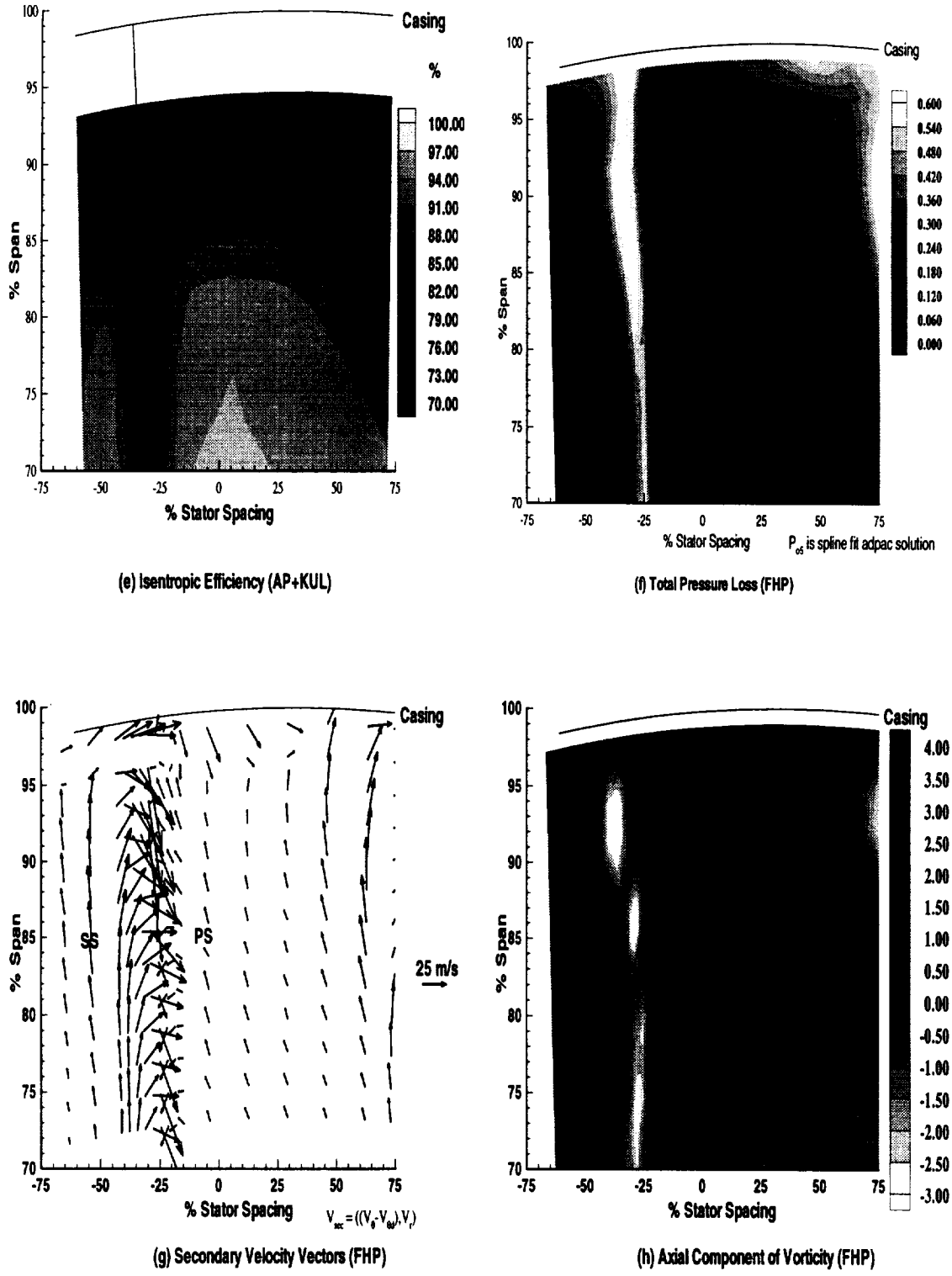

Figure 4.9 (Cont.). Contours of Time Averaged Quantities Near Casing: (e) Isentropic Efficiency, (f) Total Pressure Loss, (g) Secondary Flow Vectors and (h) Axial Vorticity

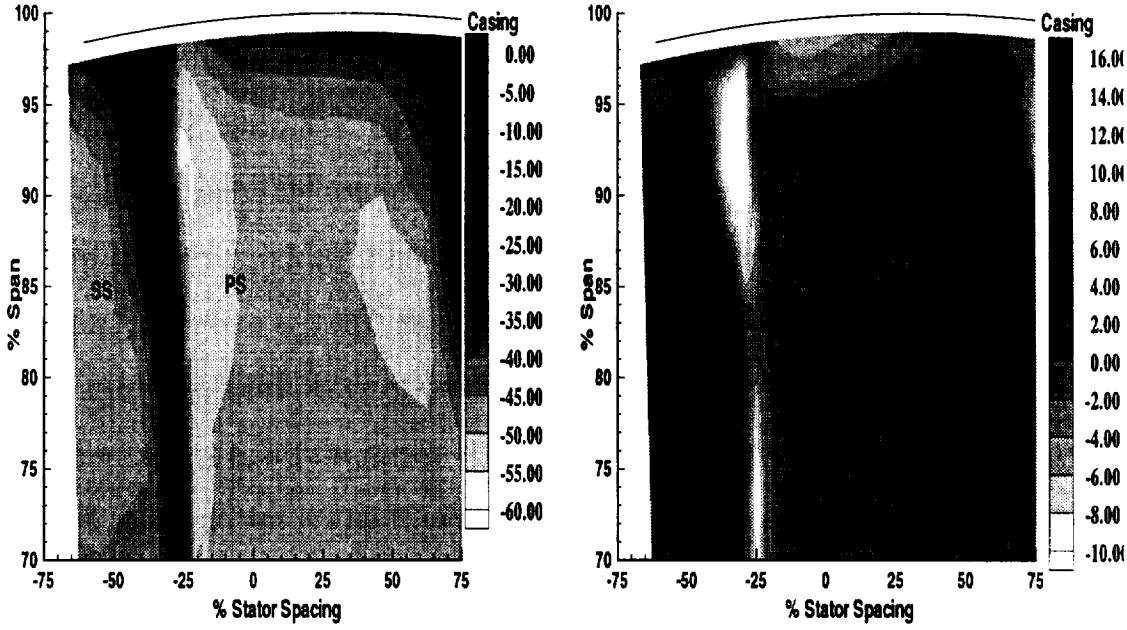

Figure 4.9 (Cont.). Contours of Time Averaged Quantities Near Casing: (i) Tangential Velocity and (j) Radial Velocity

leakage flow tends to reduce the tendency for the flow to separate in the hub endwall region, resulting in improved endwall flow (Figure 4.10(c)). This is clearly observed from a comparison of the flow profiles near the hub and the tip. The stator clearance flow has resulted in a smaller viscous region near the hub. The flat portion of the pressure profiles (from about 10% to 20% span), is due to the acceleration of the fluid brought about by the development of the leakage vortex through the passage. There is a complex profile seen in the total temperature rise distribution from the hub to about about 30% span. Higher temperatures are seen close to the hub and this is due to increased viscous dissipation generating heat brought about by the increased losses from the hub clearance flow. The increased losses leads to lower total pressures compared to the mid-span regions. A large drop in passage averaged temperature is observed between 10 and 20% span. Both underturning and overturning are observed near the hub. Up to about 9% of the span from the hub, the flow is underturned. The underturning of the fluid is caused by the presence of the leakage flow region. The overturning is confined to spanwise locations extending from about from 10% to about 30% span. This is typical of the distribution observed in vortical motion. Lower losses and higher efficiency levels are seen in the hub endwall region compared with the casing region. This is due to the presence of higher total pressures and lower temperatures compared with the casing region. If there was no hub clearance, the loss levels would be expected to be as high as that existing near the casing region. The presence of a hub clearance flow while detrimental somewhat improves the efficiency of the compressor.

In the core flow region (30% span to about 70% span), very little change in flow properties is observed. The total pressure loss levels compare very closely with the distributions measured by Wisler (1984) in a low speed model of a high speed core compressor. Only in the endwall regions do the distributions change. Higher losses are seen in the casing endwall in the present data set, whereas higher losses were seen in the

hub endwall region in the Wisler (1984) data. Cascade loss correlations (Lakshminarayana (1996)) which are mainly used in the preliminary design stages of compressor design tend to over-predict the overall loss coefficient by as much as 77% (ζ=0.1735 for the correlations compared with ζ=0.09802 for the experiment). It is clear that major improvements are required in the development of the loss correlations for multistage compressors. The overall efficiency upto stage 2 based on the experimental data is 89.5% and the overall efficiency of the compressor is 89.3% for this operating condition. The closeness of these numbers give added confidence to the experimental results.

The casing endwall flow region with lower pressures and higher temperature, near the casing extends to 75% span of the span. The total pressure, axial velocity, pressure loss and efficiency behavior is similar with momentum deficiency and increased losses from 75 to 100% span. The presence of stator endwall flow as well as interaction with the rotor leakage flow contributes to much lower efficiency in the casing endwall region. A large region of underturning is seen from the hub-to-tip distribution of the flow angle. This is mainly due to the secondary flow in the casing endwall region which has a higher radial extent than the region at the hub. This underturning also causes a drop in total pressure since secondary losses start dominating the flow. The extent of the underturned as well as the high loss region in the spanwise direction is nearly the same. The efficiencies and temperature distribution shows similar behavior. The stagnation temperature increases continuously from mid-span with larger gradients near the outer 20% span.

Close to the casing endwall very high levels of mixing and losses are found as evidenced by higher levels of unsteadiness in total pressure and total temperature. The presence of low momentum fluid in the casing region is due to the accumulation of endwall flow and losses through the consecutive stages of the machine. This is primarily caused by the losses due to the mixing of low momentum fluid with the leakage and secondary flow and the annulus wall boundary layer in the casing region of consecutive blade rows. This

increases viscous dissipation leads to increase in the entropy of the region consequently leading to a rise in total temperature. However, the increased entropy leads to a decrease in the total pressure. Consequently higher temperatures and lower pressures are recorded compared to the mid-span region. From the hub-to-tip variation of the loss distribution it can be seen that the losses in the casing endwall region are higher than that found in the hub region and this accounts for higher temperatures and lower pressures in the casing endwall region compared with the hub region.

4.5 Radial Distribution of Passage Averaged Flow Properties Across the Compressor

In this section, the radial distribution of passage averaged total pressure, total temperature, axial velocity and flow angle across the compressor are presented and discussed. Experimental data from kulite, pneumatic five hole and aspirating probes as well as computational data from the ADPAC solution are combined to interpret the flow field. Experimental data is available at the inlet, downstream of stators 2 and 3 and the exit of the compressor whereas the computational data is available at the exit of rotors 2 and 3 and stator 2 respectively. The data downstream of stator 2 along with the computational data at all axial locations have been mass weighted passage averaged across one blade passage whereas the five hole probe data at inlet, exit and downstream of stator 3 has been circumferentially averaged.

4.5.1 Total Pressure

The passage averaged total pressure distribution is shown in Figure 4.11. The tip region at the exit of stators 2 and 3 show a conventional profile with monotonic increase in total pressure from the endwall to freestream. The hub region, however, has a complex

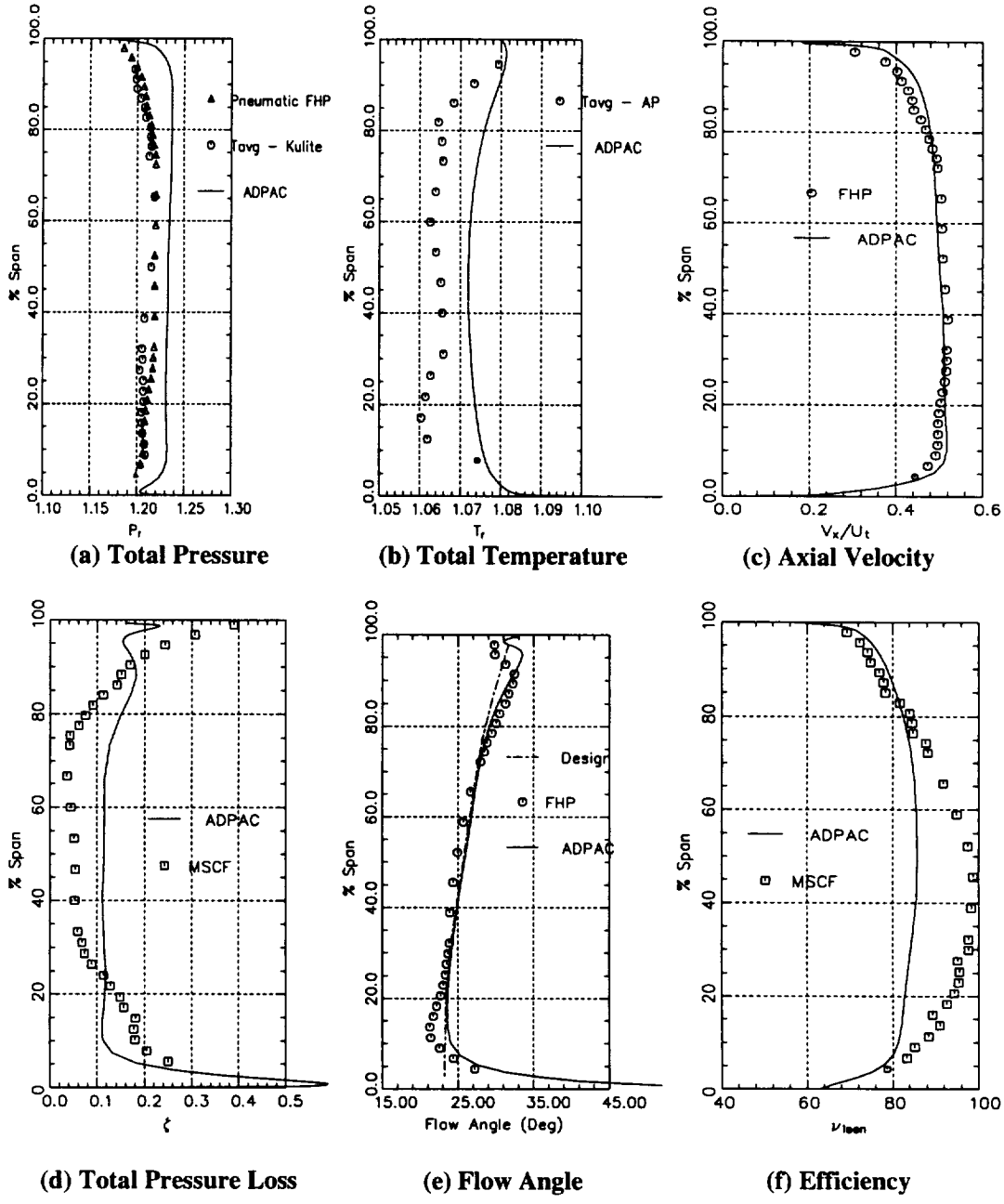

Figure 4.10. Radial Distribution of Passage Averaged Time Averaged Total Temperature, Total Pressure, Total Pressure Loss, Axial Velocity, Isentropic Efficiency and Exit Flow Angle Downstream of Stator 2

profile due to interaction of hub wall boundary layer and the leakage of the flow due to the cantilevered stator blade. Similar characteristics have been measured by Smith (1970), Dransfield and Calvert (1976), Calvert et al. (1989) and Falchetti (1992). There is no deterioration in the passage averaged profiles at the various downstream locations except for increased viscous layers in the endwall region. This is also observed in the computational results. The flow downstream of the third stator is very similar to the flow downstream of the second stator. The core flow region, which is approximately 75% of the span at inlet, reduces gradually to less than 30% of span at the exit of the compressor. Since the measurements shown in Figure 4.11 are at the exit of stators, the leakage effects due to rotor tip clearances are not observed directly. However, the computational results do show an influence of the rotor tip leakage flow downstream of both rotors 2 and 3 and their radial extent is far more pronounced downstream of rotor 2 than aft of rotor 3. The data indicates that the rotor tip leakage flow has mixed within the stator passage, resulting in a conventional viscous layer (monotonically decreasing towards the annulus wall). Whereas the flow near the hub of the stators show the effect of leakage due to clearance between a stationary blade and a rotating hub, the values of Cpt increase from hub to about 10% of span, followed by a flat profile (and a wake type of region at exit). This is typical of profiles caused by the interaction of leakage flow with the primary flow (Lakshminarayana et al.(1995)). The hub flow regions downstream of rotors do show a slight increase in total pressure possibly brought about by interaction between the rotating hub and the rotor suction side endwall corner flow which should have characteristics similar to that existing between the stator suction surface and casing endwall corner flow as observed earlier.

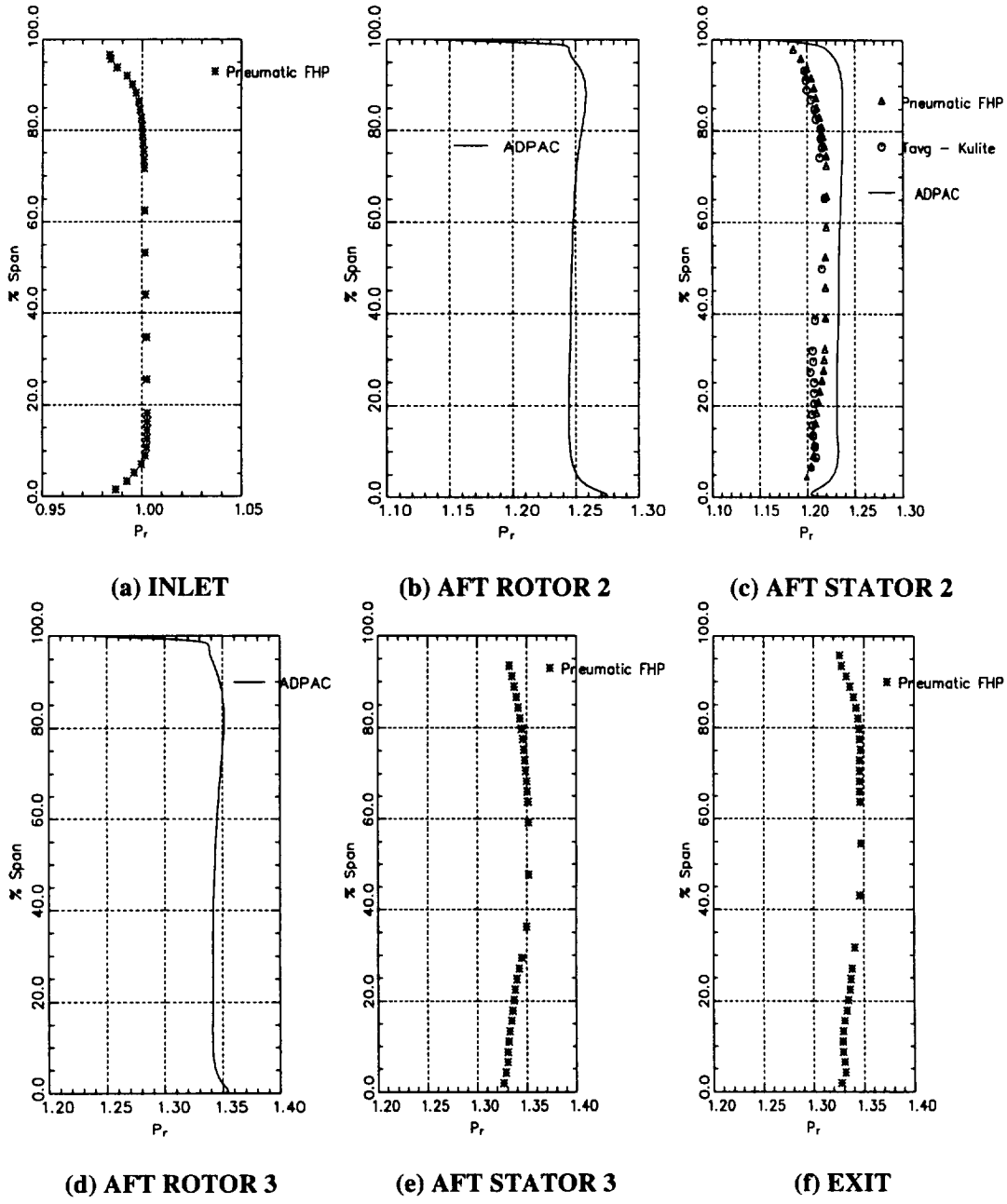

Figure 4.11. Radial Distribution of Passage Averaged Total Pressure Across the Compressor

4.5.2 Total Temperature

The temperature field (Figure 4.12 is very well behaved at the inlet where the temperature distribution is almost uniform in the radial direction. Downstream of rotor 2 the profile already show evidence of higher temperatures at the end walls with the temperature near the tip higher than that at the hub. Similar behavior is reported by Smith (1970), Falchetti (1992) and Howard and Gallimore (1992). Higher temperatures are seen close to the hub and this is due to increased viscous dissipation generating heat brought about by the increased losses from the hub clearance flow. The influence of the leakage flow with the temperature field is quite small in the hub region and this is seen in the conventional profiles of temperature compared to the pressure distribution. In the casing endwall region, very high levels of mixing and losses are found as evidenced by higher levels of unsteadiness in total pressure and total temperature. The presence of low momentum fluid in the casing region is due to the accumulation of endwall flow and losses through the consecutive stages of the machine. This is primarily caused by the losses due to the mixing of low momentum fluid with the leakage and secondary flow and the annulus wall boundary layer in the casing region of consecutive rotor stages. This increases the entropy of the region, consequently leading to increased viscous dissipation and a rise in total temperature. The ADPAC solution has predicted a drop in total pressure quite close to the endwall and similar measurements have been acquired by Smith (1970) and Falchetti (1992). Enough measurements were not acquired in the present situation to comment on this phenomena. The ADPAC solutions indicate that the stator exit profiles are flatter than that observed at the rotor exit. This is due to increased mixing of the flow as it passes through the stator passages. Similar distributions were measured by Behlke et al. (1979) and computed by Adkins and Smith (1982) and Gallimore (1986). Calculations to predict the total temperatures at the exit of stators without mixing by both Adkins and Smith

(1982) and Gallimore (1986) have shown very high total temperature at the endwalls compared to the midspan region.

4.5.3 Axial velocity

The radial distribution of average axial velocity (Figure 4.13) indicates substantial changes as the flow goes through several blade rows. The viscous layer thickness at the inlet is approximately 10% near the hub and 10-15% near the tip. This grows substantially as the flow progresses through the compressor. The hub wall flows show the same trend as total pressure where the stator-hub leakage flow interacts with the main flow to produce unconventional boundary layer wake type of profiles near the hub wall region. This may also have been caused by a scraping vortex and the upstream rotor hub separated flow. This region extends from 10% to 20% of the span from the hub. The leakage flow tends to reduce the boundary layer growth, especially very near the wall. This is clearly observed from a comparison of the velocity profiles near the hub and the tip. The flat portion of the profile (from 10 to 20% span), which has higher than expected values (of the extrapolated boundary layer profile from 30 to 20%) may have been caused by either a scraping vortex or the upstream separated flow in the rotor. The separated flow at the exit of the rotor has higher absolute velocity than the un-separated flow. This hypothesis is supported by higher than expected temperature rise in this region. This hypothesis is also supported by the fact that the static pressure is nearly invariant across the span at this location.

4.5.4 Flow Angle

The flow angle distributions are shown in Figure 4.14. Also shown on these figures are the design angles aft of stators 2 and 3. It is clear that downstream of stator 2, beyond 70% span, the measured profiles show under-turning up to about 95% span. Over-turning is observed in the outer 5% of the stator blade span, mainly caused by secondary flow.

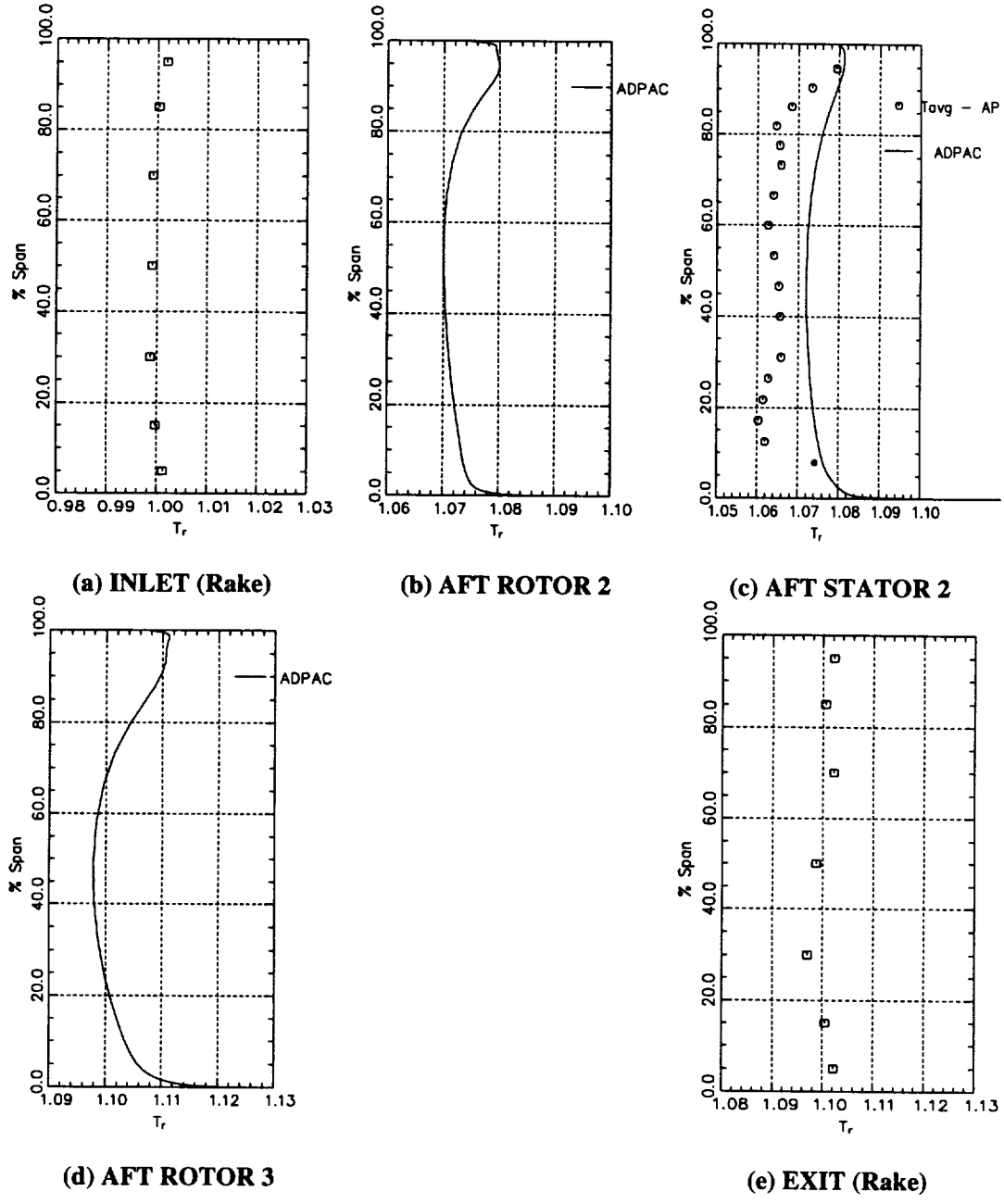

Figure 4.12. Radial Distribution of Passage Averaged Total Temperature Across the Compressor

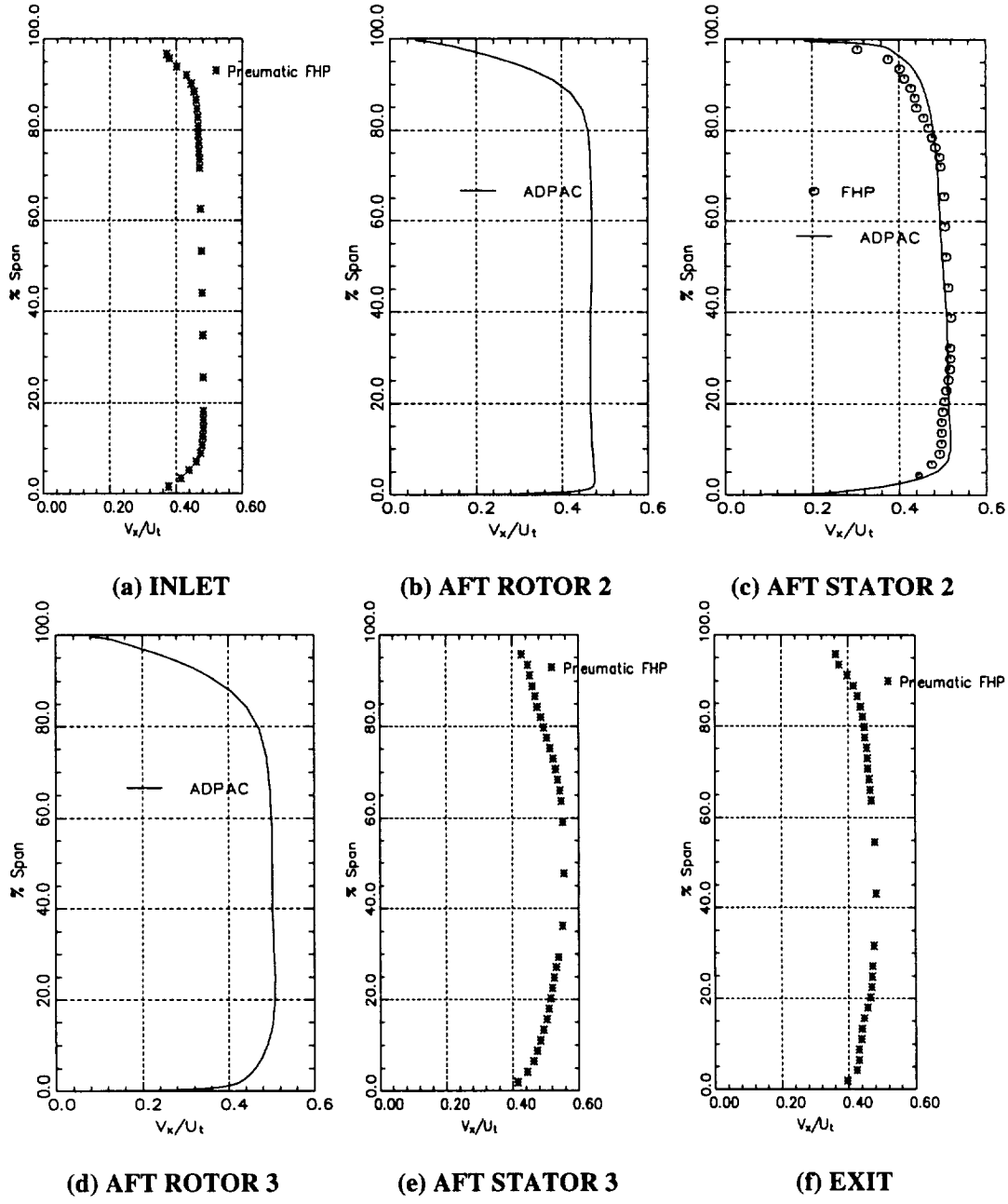

Figure 4.13. Radial Distribution of Passage Averaged Axial Velocity Across the Compressor

Both underturning and overturning are observed near the hub. Up to about 9% of the span from the hub, the flow is underturned. The overturning is confined to spanwise locations extending from 10% to 25% span. This is caused mainly by the leakage flow from the stator hub. This may also have been caused by separated flow in the upstream rotor, (as explained earlier), and the associated shear gradient, resulting in secondary flow and overturning in this region. Downstream of stator 3, the radial distribution of exit flow angle is very similar to those observed at the exit of stator 2. The underturning region near the hub has increased. The ADPAC solution has captured the phenomena of over- and under-turning quite well at the stator 2 exit. Away from the endwalls, the passage averaged flow angle is the same as that intended by the design which indicates that the flow is well behaved in the stator passage away from the endwalls.

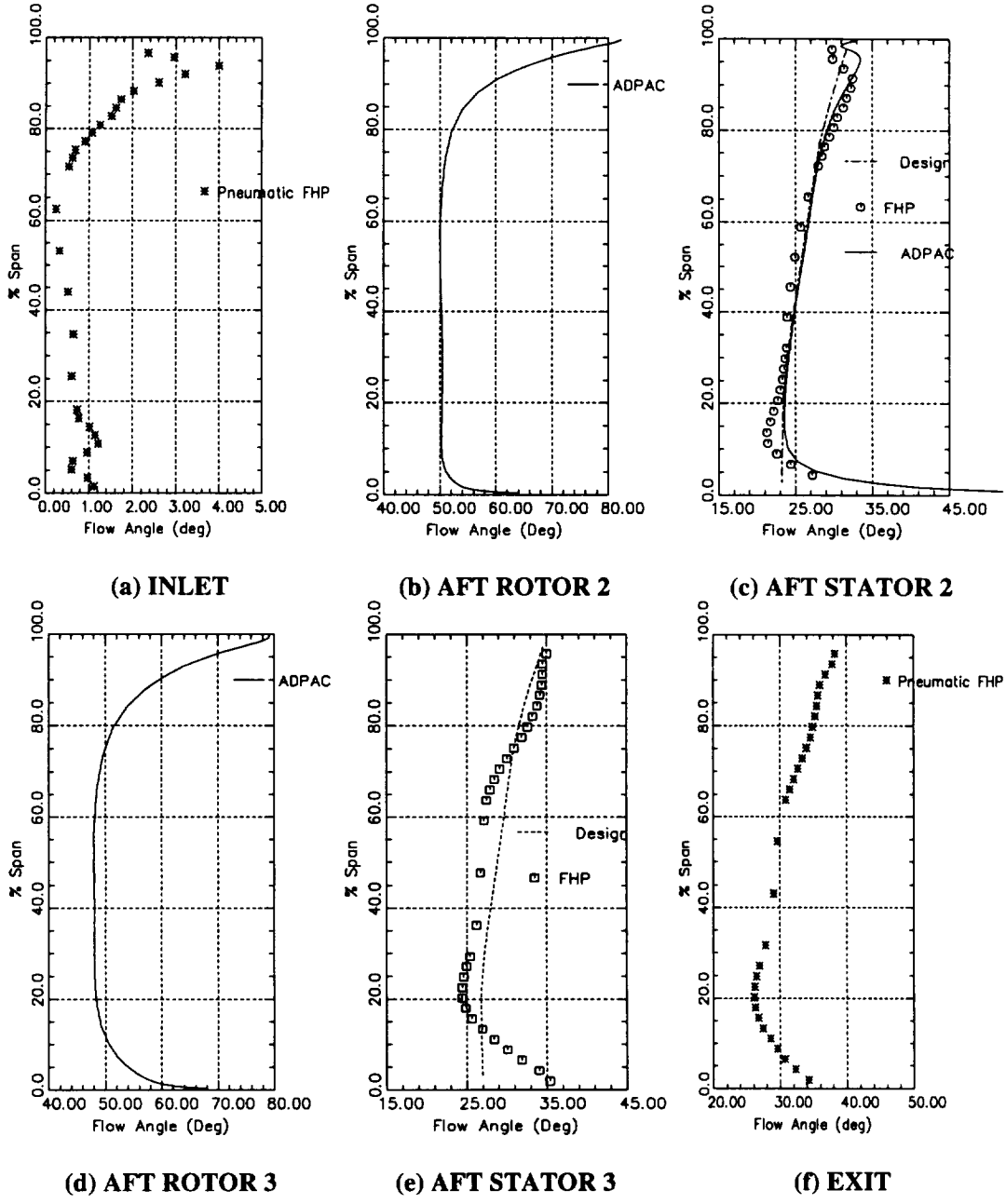

Figure 4.14. Radial Distribution of Passage Averaged Flow Angle Across the Compressor

Chapter 5

UNSTEADY FIELD DOWNSTREAM OF STATOR 2

In this chapter the unsteady total pressure and total temperature field is presented and analyzed. Unsteadiness at the exit of the stator arises due to interaction of at least three different mechanisms: the presence of rotor exit flow including wakes, secondary flow and leakage flow features being convected through the stator passage which have not fully mixed out, the shedding of vorticity from the stator trailing edge due to a time varying stator circulation or loading caused by the passage of the rotor flow over the stator surface, and the presence of a potential field due to upstream and downstream rotors. By analyzing the stator exit data, it is possible to determine which of these mechanisms are dominant contributors to the unsteadiness.

Figures 5.1, 5.2 and 5.3 show the spectral distribution of the hot-wire and kulite voltages at three radial locations (near hub, midspan and near tip) at the midpitch, pressure surface and suction surface locations. In all these figures, it can be observed that multiple frequencies and multiple harmonics of various frequencies exist. This is due to effects of potential and viscous interaction between the various rotors. R1, R2 and R3 marked in Figure 5.1 stand for blade passing frequencies of rotors 1, 2 and 3 (approximately 6.3 kHz, 6.5 kHz and 6.7 kHz respectively). Even though eight harmonics of rotor blade passing frequency (all three rotor frequencies are present as shown for the first harmonic), the combined frequency response is about 40 kHz. Figure 5.4 shows the spectral distribution of hot-wire 2 of the aspirating probe at the mid-span, mid-pitch location. In addition to the basic three rotor blade passing frequencies (R1, R2 and R3) and their harmonics, various difference frequencies such as (2R1-R2) and (2R3-R2) and their harmonics are also observed. These difference frequencies are due to viscous and potential interactions

between rotors 1, 2 and 3 which are sensed by both the kulite and aspirating probes at this location.

Care must be taken when interpreting the unsteady data because of the frequency response limitations of both the probes. The most apparent limitation of these measurements is the resolution of the random turbulent fluctuations which are included in the unresolved component of total temperature and pressure. Assuming a mean velocity of 100 m/s, the smallest length scale measured is given by $100/40000 = 2.5\times10^{-3}$m. Hence energy in turbulent eddies with length scales smaller than this are not measured. Therefore all the features associated with frequencies less than 40 kHz (blade passing, shaft frequency and substantial part of random turbulence) have been measured. For deterministic structure associated with the rotor blades (blade passing frequency of 6.5 kHz for the second rotor), this instrumentation can measure the first six harmonics. Although finer details of the structure may be contained in higher harmonics, beyond the measurement capability of the probe, the majority of the energy content is included in these lower harmonics.

The ensemble averaged flow is viewed from three different perspectives in this chapter. Firstly attention is focused on the RMS flow field. This provides the overall information of the unsteady flow field downstream of the stator. Blade-to-blade distributions at select radial locations and hub-to-tip contour plots of the various unsteadiness components are used. Attention is next focused on the temporal variation of the stator exit flow fluctuations at each instant of rotor passage time. This gives a complete perspective on how the flow field downstream of the stator is changing with passage of the rotor. For this perspective, 6 frames of ensemble averaged and RMS unresolved unsteadiness in total temperature and total pressure is used. Each frame represents one rotor 2 location with respect to the stator and 20 frames represent one blade passage (only six are shown for the sake of berivity and the explanation is based on all the frames). The shaft resolved and unresolved components of the total pressure coefficient are presented to illuminate flow

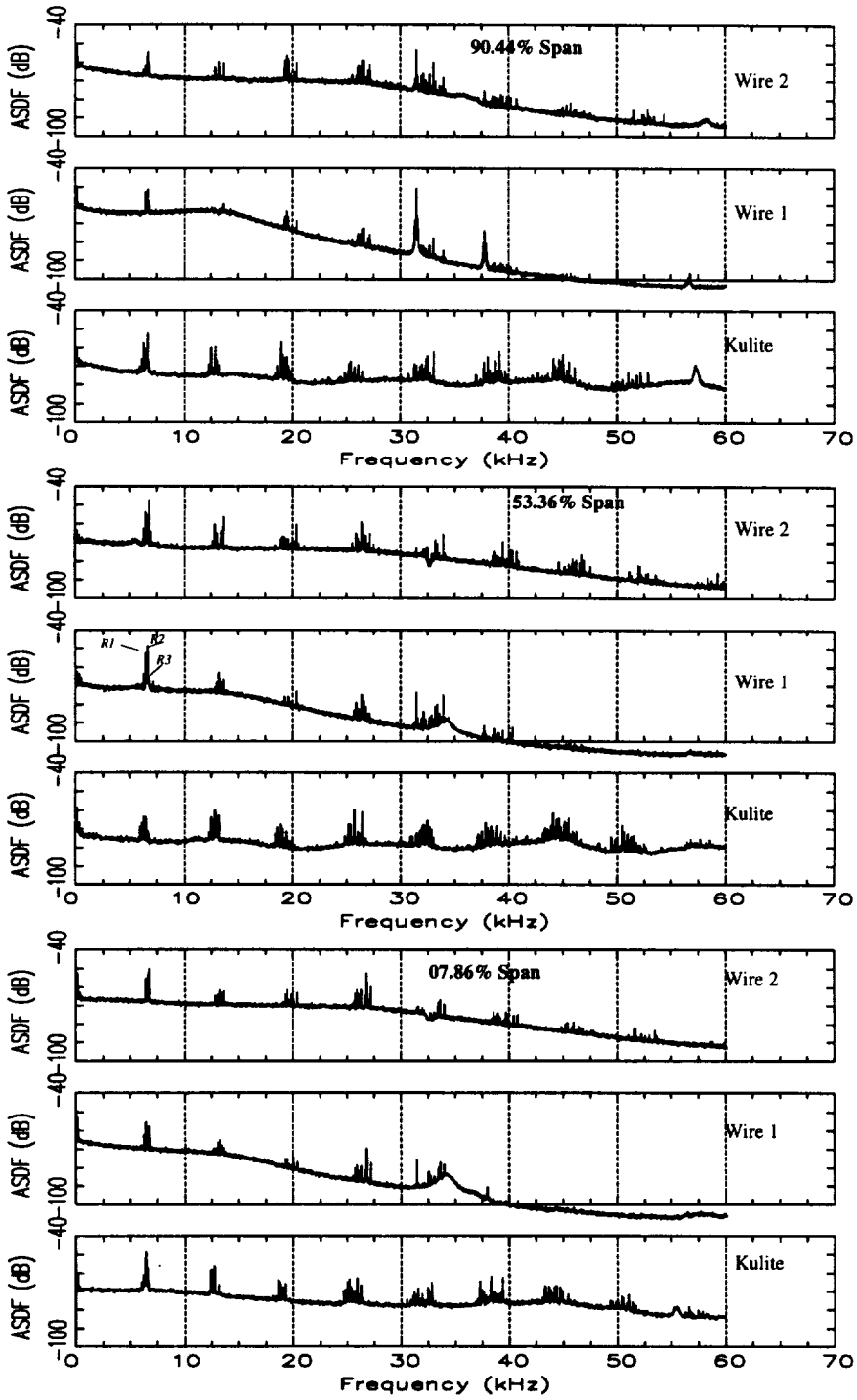

Figure 5.1. Power Spectral Distribution of Hot-wire and Kulite Voltages at Mid-Pitch Location: 3 Radii

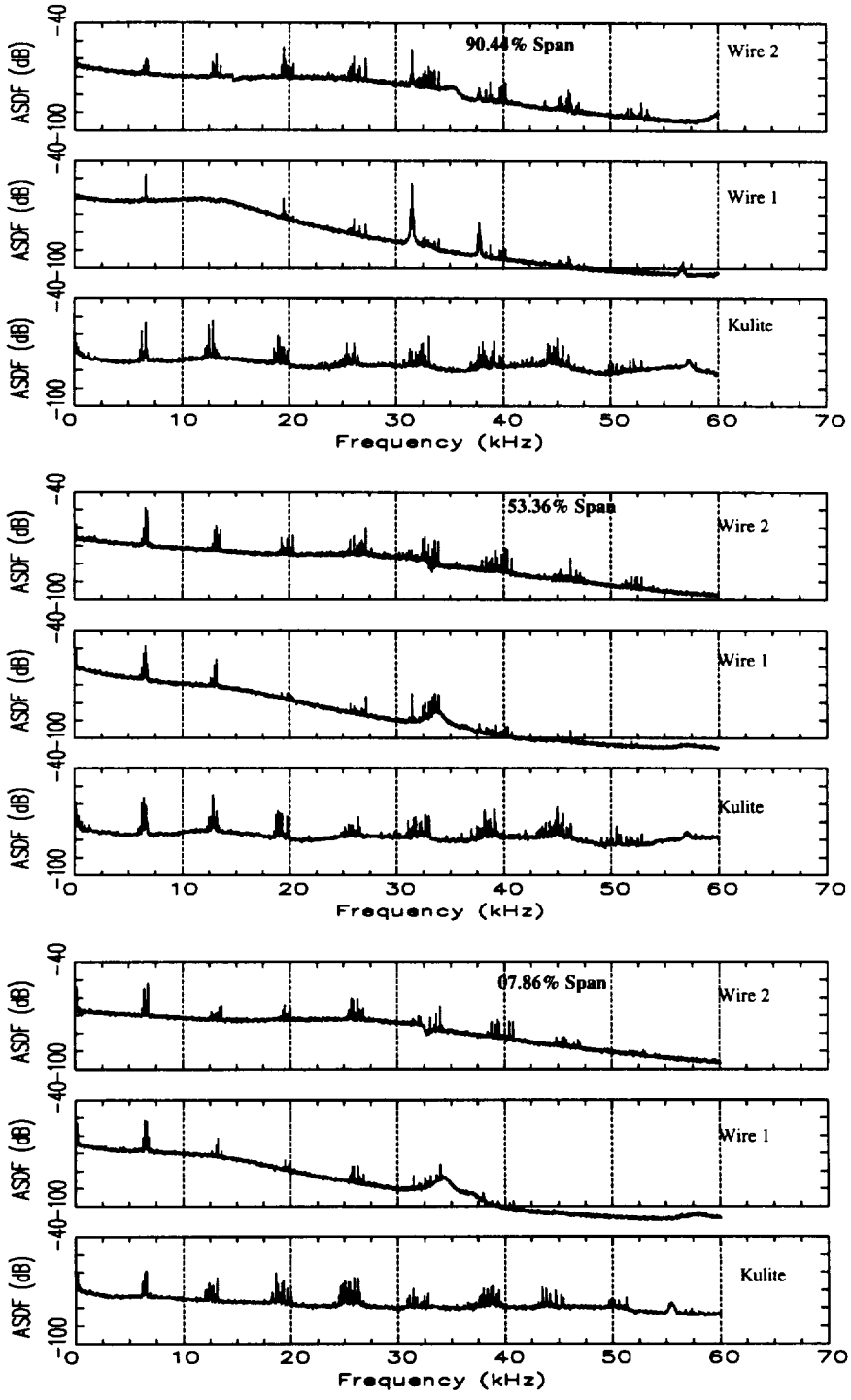

Figure 5.2. Power Spectral Distribution of Hot-wire and Kulite Voltages at Pressure Surface Location: 3 Radii

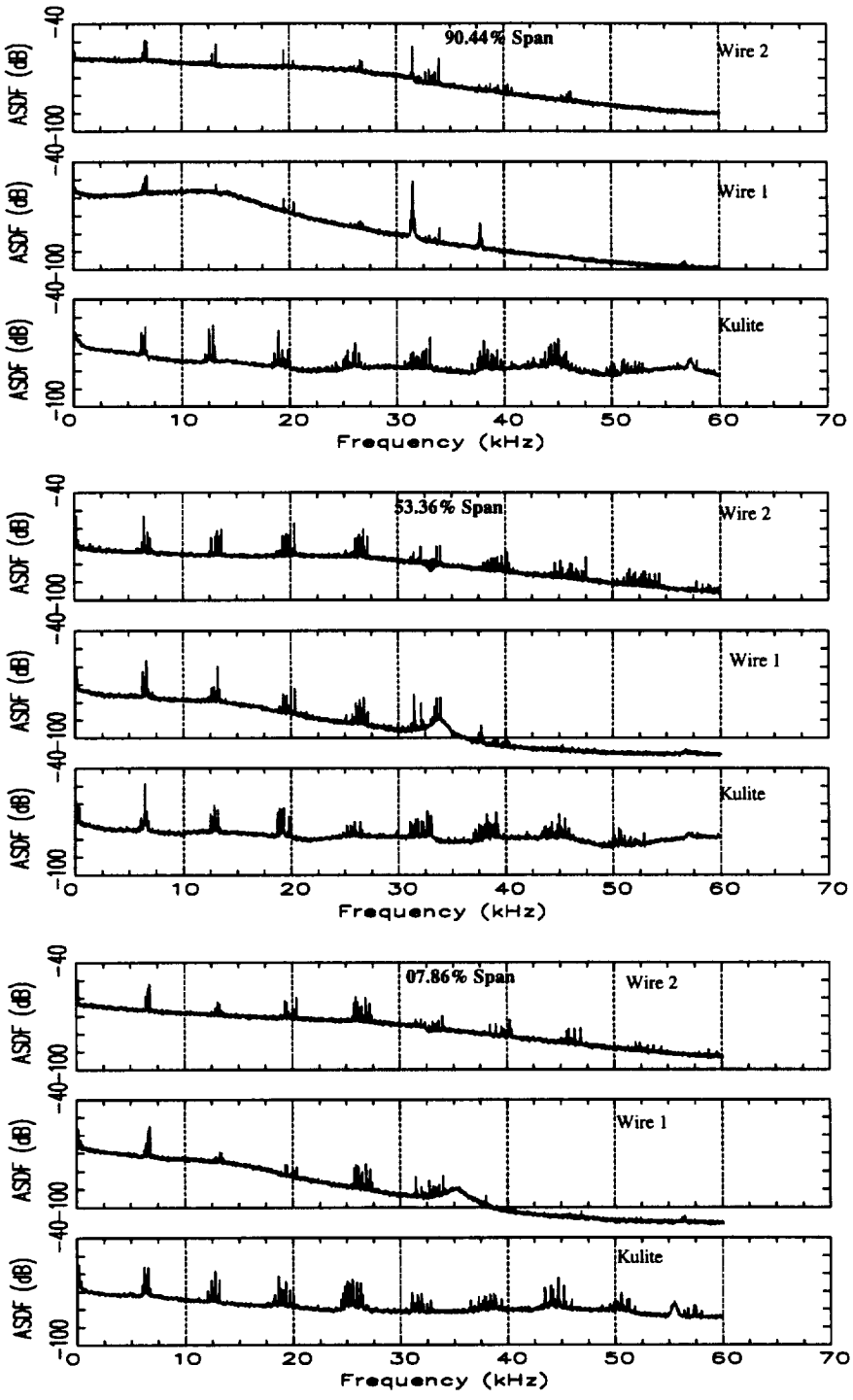

Figure 5.3. Power Spectral Distribution of Hot-wire and Kulite Voltages at Suction Surface Location: 3 Radii

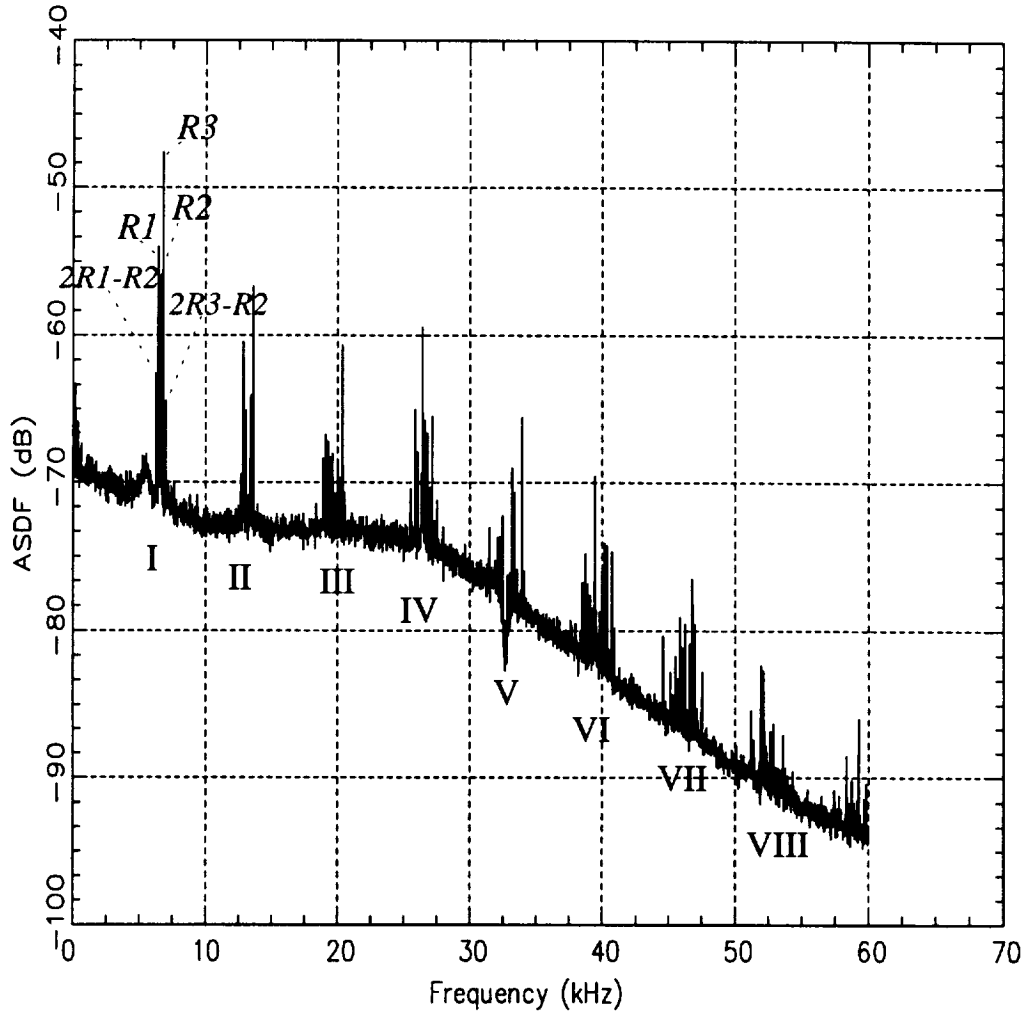

Figure 5.4. Power Spectral Distribution of Hot-wire 2 Voltages at Mid-span, Mid-pitch Location: Frequency Distribution

characteristics which are due to the relative motion between the rotor and stator. This represents the perspective of one rotor blade sweeping past the stator only. The results from this description are useful in determining the influence of the stator on the inlet flow to the downstream rotor. Thirdly, hub-to-tip contours of the ensemble averaged and unresolved unsteadiness in the rotor exit flow at three locations (suction side, pressure side and midpitch) are analyzed and discussed to determine the nature of the rotor flow as it passes through the stator passage.

The unsteadiness away from the endwalls is mainly caused by rotor wakes passing through the stator, as well as interaction of the rotor wakes with the blade boundary layers (and the resulting unsteadiness caused by both direct and indirect effects). It is well known that the rotor wake flow in a compressor migrates towards the pressure side of the downstream stator (Kerrebrock and Mikolajczak (1970). In the casing endwall region, the blade-to-blade variation of the annulus wall boundary layer as well as presence of leakage flow (and possibly tip vortex) induces unsteadiness. In addition "the corner stall region" which is nearly steady in cascades is unsteady due to rotor-stator interaction. Therefore in the casing endwall region, one can expect other sources (leakage flow, annulus wall boundary layer, secondary flow and corner stall) which are causes of higher unsteadiness levels. In the hubwall region, one can expect the interaction between the low momentum fluid or corner stall with the hubwall rotation. This rotation may transport this low momentum fluid away from the hub. Therefore the unsteadiness due to this interaction will show up away from the hub. The Penn State compressor has a cantilevered stator, hence the resulting leakage flow is possibly unsteady due to rotor-stator interaction. All these features are revealed in the data presented below.

The relative uncertainties of each of the unsteady quantities discussed in this chapter is given in Tables 5.1 and 5.2. The reader is referred to Table 4.1 for details on the uncertainty of the time averaged quantities. The uncertainties are calculated based on the

concepts outlined in Appendix A and are expressed as a ratio of the uncertainty calculated and the actual value of the derived quantity in percent.

Table 5.1. Uncertainty of Various Derived Quantities: Unsteady Data

Quantity	Uncertainty (%)	Figures
RMS Total Temperature Rise $RMS((\overline{T}_{or})_{tot})$, $RMS((\overline{T}_{or})_{unr})$ $RMS((\overline{T}_{or})_{RA})$, $RMS((\overline{T}_{or})_{RP})$ $RMS((\overline{T}_{or})_{BA})$, $RMS((\overline{T}_{or})_{BP})$	± 7%	5.5(a), 5.6(a), 5.7(a), 5.8(a),(c), 5.9(e),(g), 5.10, 5.12(a),(c), 5.13(e),(g), 5.14, 5.16(a),(c), 5.17(e),(g), 5.18 5.20, 5.21, 5.22, 5.23, 5.24, 5.25, 5.26, 5.28, 5.30, 5.32, 5.34 5.36(b),(d), 5.37(b), 5.38(b),(d), 5.39(b), 5.40(b),(d), 5.41(b) 5.42, 5.43, 5.44, 5.45
RMS Total Pressure Coefficient $RMS((\overline{C}_{pt})_{tot})$, $RMS((\overline{C}_{pt})_{unr})$ $RMS((\overline{C}_{pt})_{RA})$, $RMS((\overline{C}_{pt})_{RP})$ $RMS((\overline{C}_{pt})_{BA})$, $RMS((\overline{C}_{pt})_{BP})$	± 2.483%	5.5(b), 5.6(b), 5.7(b), 5.8(b),(d), 5.9(f),(h), 5.10, 5.12(b),(d), 5.13(f),(h), 5.15, 5.16(b),(d), 5.17(f),(h), 5.19 5.20, 5.21, 5.22, 5.23, 5.24, 5.25, 5.26, 5.27, 5.29, 5.31, 5.33
RMS Total Pressure	± 0.43%	5.36(a),(c), 5.37(a), 5.38(a),(c), 5.39(a), 5.40(a),(c), 5.41(a) 5.42, 5.43, 5.44, 5.45

Table 5.2. Uncertainty of Various Derived Quantities (Contd): Unsteady Data

Quantity	Uncertainty (%)	Figures
Total Velocity (V_{tot})	±2.5%	5.42, 5.43, 5.44, 5.45
Axial Velocity (V_z)	±2.5%	5.42, 5.43, 5.44, 5.45
Tangential Velocity (V_θ)	±2.5%	5.42, 5.43, 5.44, 5.45
Radial Velocity (V_r)	±2.5%	5.42, 5.43, 5.44, 5.45
Isentropic Efficiency (η_{isen})	±4.043%	5.46, 5.47

5.1 RMS Flow Field

In this section RMS values of the unsteady components of total pressure and temperature defined in Chapter 3 are presented and analyzed. For each of the unsteady components, the RMS values is calculated using the following equations (the equations are only shown for a general quantity ϕ but they are applicable to both total temperature and total pressure as well).

$$RMS((\phi)_{RP}) = 100\frac{\sqrt{\frac{1}{N_b \times N_{pb}}\sum_{j=1}^{N_b}\sum_{k=1}^{N_{pb}}(\phi_{jk})_{RP}{}^2}}{\overline{\phi}} \tag{5.1}$$

$$RMS((\phi)_{RA)} = 100\frac{\sqrt{\frac{1}{N_b}\sum_{j=1}^{N_b}(\phi_j)_{RA}{}^2}}{\overline{\phi}} \tag{5.2}$$

$$RMS((\phi)_{BP}) = 100\frac{\sqrt{\frac{1}{N_{pb}}\sum_{k=1}^{N_{pb}}(\phi_k)_{BP}{}^2}}{\overline{\phi}} \tag{5.3}$$

$$RMS((\phi)_{BA}) = 100\frac{\sqrt{\frac{1}{N_b \times N_{pb}}\sum_{j=1}^{N_b}\sum_{k=1}^{N_{pb}}(\phi_{jk})_{BA}{}^2}}{\overline{\phi}} \tag{5.4}$$

$$RMS(\phi') = 100\frac{\sqrt{\frac{\sum_{i=1}^{N_{rev}}\sum_{j=1}^{N_b}\sum_{k=1}^{N_{pb}}(\phi')_{ijk}^{\,2}}{N_b \times N_{pb} \times N_{rev}}}}{\bar{\phi}} \tag{5.5}$$

The RMS total unsteadiness is calculated by:

$$RMS((\phi)_{tot}) = \Big[RMS((\phi)_{RP})^2 + RMS((\phi)_{RA})^2 + RMS((\phi)_{BP})^2 + RMS((\phi)_{BA})^2 + RMS((\phi'))^2\Big]^{\frac{1}{2}} \tag{5.6}$$

Figure 5.5 shows the hub-to-tip contours of the RMS total unsteadiness in total temperature rise, total pressure coefficient and total velocity as well the hub-to-tip distributions of the passage averaged values. These plots provide regions where unsteadiness is large and facilitate development of models for the average passage equations. Very similar distributions are observed in both the velocity and pressure data in so far as the locations where high levels of unsteadiness are found. Four regions of the flow can be easily identified here: core flow, stator wake, hub endwall region and casing endwall region.

High levels of total unsteadiness are observed in the stator wake, and in the endwall regions especially the casing endwall corner region. Away from the endwalls, bulk of the unsteadiness is deterministic in nature. In the stator wake, significant levels of deterministic as well as unresolved unsteadiness is seen. On the pressure side of the wake away from the endwalls, the deterministic unsteadiness shows that the wake (based on pressure, temperature and velocity defects) is wider than that seen on the suction side. This is due to accumulation of the rotor exit flow on the pressure side of the stator. On the pressure side close to the hub, a region of high unsteadiness in total pressure rise coefficient and total velocity is observed. However, the unsteadiness in total velocity is lower than the unsteadiness in total pressure rise coefficient. No such distribution is seen in the total temperature rise data. This region warrants further investigation. The high

levels of total unsteadiness in the hub endwall region, possibly caused by the leakage flow interaction with the rotor hub endwall flow is observed very clearly in the total pressure coefficient distribution and to a lesser extent in the total temperature distribution but not in the velocity distribution. This could be due to a coarse grid used in the velocity measurement compared with the total pressure measurement.

In the casing endwall region on the suction side, a very distinct region of high unresolved unsteadiness is observed in all three plots (Figure 5.5). This is the same region, where high vorticity, a large secondary flow region, high losses and a low momentum region was observed in the time averaged data. The presence of high levels of unsteadiness in this region is indicative of intense mixing taking place. From the hub-to-tip distribution of the passage averaged values, it is clear that the highest contributions to the unsteadiness comes in the casing endwall region and the distribution is quite uniform from hub to about 70% span. This indicates that penalties in the efficiency arise from the casing endwall region and designers should pay closer attention to both steady viscous losses and unsteady effects in this region.

Blade-to-blade distributions as well as hub-to-tip contour plots of various RMS unsteadiness are used to explain and interpret the flow features in the flow regions identified above. Figures 5.6 and 5.7 show the blade-to-blade variation of RMS unsteadiness in total temperature and pressure across the stator pitch at five typical radial locations (close to the hub, 21.76% span, midspan, 81.89% span and close to the casing). Figures 5.8 and 5.9 show the hub-to-tip contours of the RMS total unsteadiness and its components (RMS unresolved, RMS revolution periodic and RMS revolution aperiodic unsteadiness for both total temperature and total pressure. Figures 5.10 and 5.11 show the hub-to-tip contours of the components of the RMS revolution periodic unsteadiness i.e. RMS blade periodic and RMS blade aperiodic unsteadiness in total temperature and total pressure respectively.

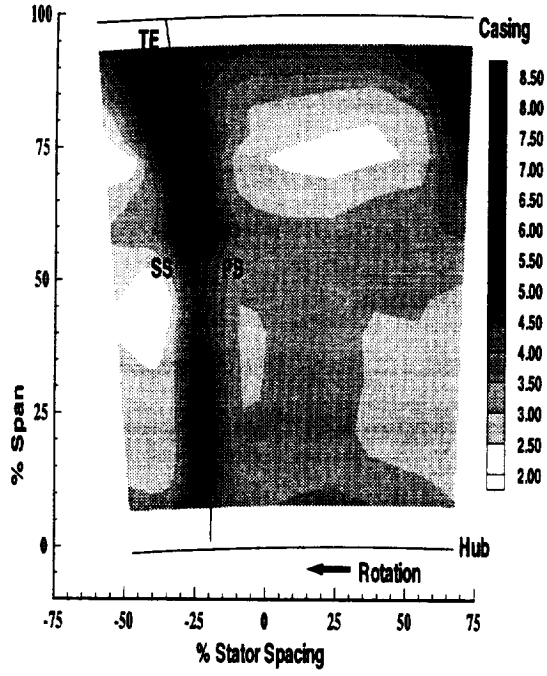

(a)RMS Total Unsteadiness (deg K)

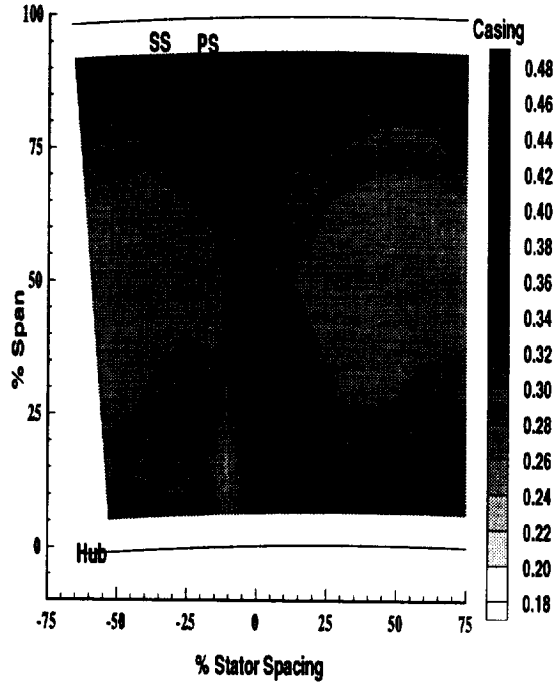

(b) RMS Total Unsteadiness (Cpt)

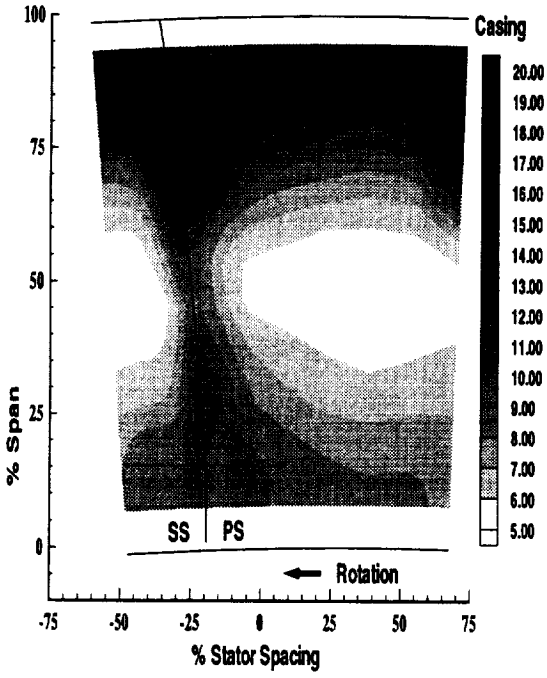

(c)RMS Total Unsteadiness in Velocity (Posn 1)

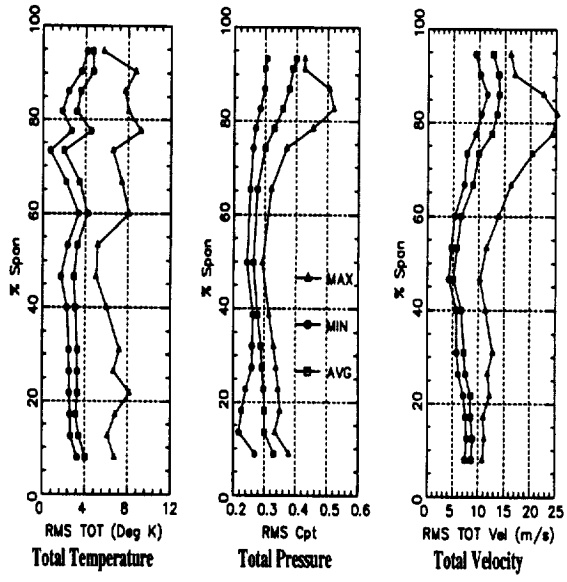

(d) Passage Average, Maximum and Minimum

Figure 5.5. RMS Total Unsteadiness Distribution: (a) Total Temperature (b) Total Pressure (c) Total Velocity (position 1) and (d) Passage Average, Minimum and Maximum

5.1.1 Core flow region

Appreciable levels of total unsteadiness in both pressure and temperature are observed in the core region (away from the blade surfaces and the hub and casing endwalls, approximately extending from 20% span to about 75% span and from -5% stator pitch to about 65% stator pitch in Figure 5.8). This is mainly caused by rotor wakes convecting through the stator blade row. In this region, the comparative levels of both deterministic (revolution periodic and revolution aperiodic) and unresolved unsteadiness in total pressure and total temperature are of similar magnitudes. The revolution aperiodic unsteadiness is quite small compared to the revolution periodic unsteadiness. Only in the endwall regions the influence of the revolution aperiodic unsteadiness is found on the flow. In the core flow levels of both blade periodic unsteadiness and blade aperiodic unsteadiness are almost the same. This indicates fairly good periodicity in the rotor wake flow away from the endwalls.

5.1.2 Stator wakes

The stator wake region has low total pressure and higher total temperature caused by upstream rotor wakes, vortices linked to the shedding of the unsteady blade boundary layers and turbulence in the stator wake. Hence, it is logical to expect both deterministic and unresolved unsteadiness levels to be higher than that in the free-stream or core flow. In the stator wake region, values of the shaft resolved unsteadiness (revolution periodic and revolution aperiodic) and unresolved unsteadiness are of the same order of magnitude in the mid-span regions and shaft resolved unsteadiness is much lower than the unresolved unsteadiness in both the hub and casing endwall regions. A clearer wake region is seen in the total temperature distribution than in the total pressure distribution. The thickness of the wake based on the RMS unsteadiness compares favorably with the thickness of

the wake based on the time averaged values. On the suction side of the wake away from the endwalls, levels of revolution periodic and unresolved unsteadiness are quite low and similar in magnitude. This could be due to transport of rotor exit flow to the pressure side of the downstream stator which would increase the levels of the deterministic as well as unresolved unsteadiness on the pressure side of the stator. The unsteady CFD simulations of this flow conducted by Hall (1996) very clearly show the migration of the shaft resolved rotor wake features to the pressure side of the downstream stator. It may be possible that the higher strain rates on the suction side may tend to smear out the unresolved fluctuations in total pressure associated with stator exit flow.

On the pressure side of the stator, away from the endwalls, the levels of both the revolution periodic and unresolved unsteadiness are higher than the corresponding values on the suction side of the stator. This is certainly due to the migration of stator exit flow to the pressure side. The revolution aperiodic unsteadiness which is mainly due to the viscous interaction between the upstream rotors (passage to passage geometry variations and to differences in blade count) does not show any changes in the stator wake regions away from the endwall and the magnitudes are very low indeed. This is to be expected in well designed compressors. Only in the endwall regions, where there are influences of tip clearance flow and possible separations on the rotor suction surface hub endwall region, do the revolution aperiodic unsteadiness change and this is explained in the next section. Since the blade count differences between rotors 1 and 2 is 2, a two node per revolution pattern is expected in a rotor revolution plot. The degree of amplitude of this node is a measure of the viscous interaction between rotors 1 and 2. This is expected to be different in various regions of the flow and Figure 5.9 seems to confirm this observation. Detailed explanations of these features are given in later sections dealing with the rotor exit flow features at this measurement location.

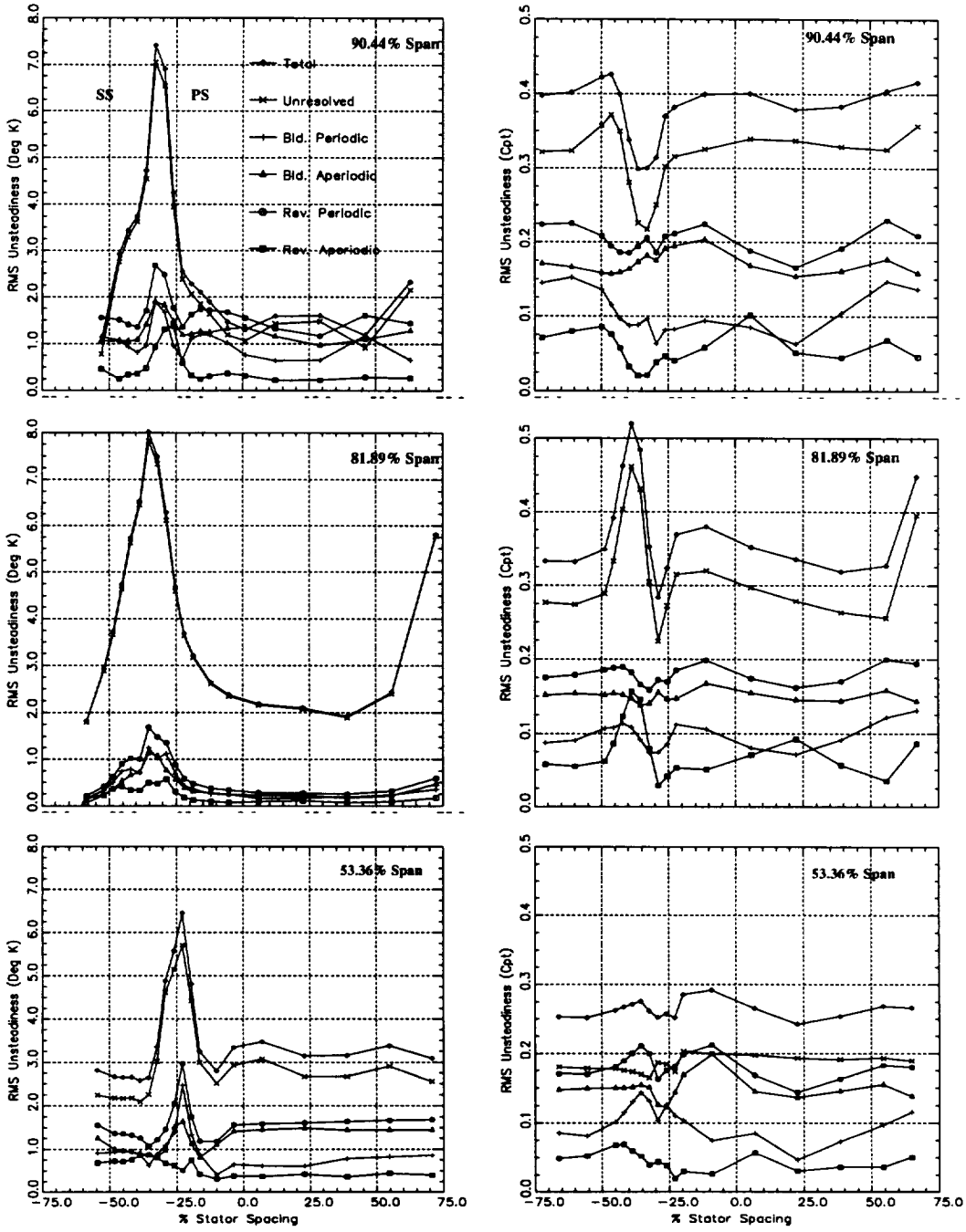

(a) Total Temperature (deg K) (b) Total Pressure (Cpt)

Figure 5.6. Blade-to-blade variation of time averaged RMS unsteadiness in total temperature rise and total pressure at various radii

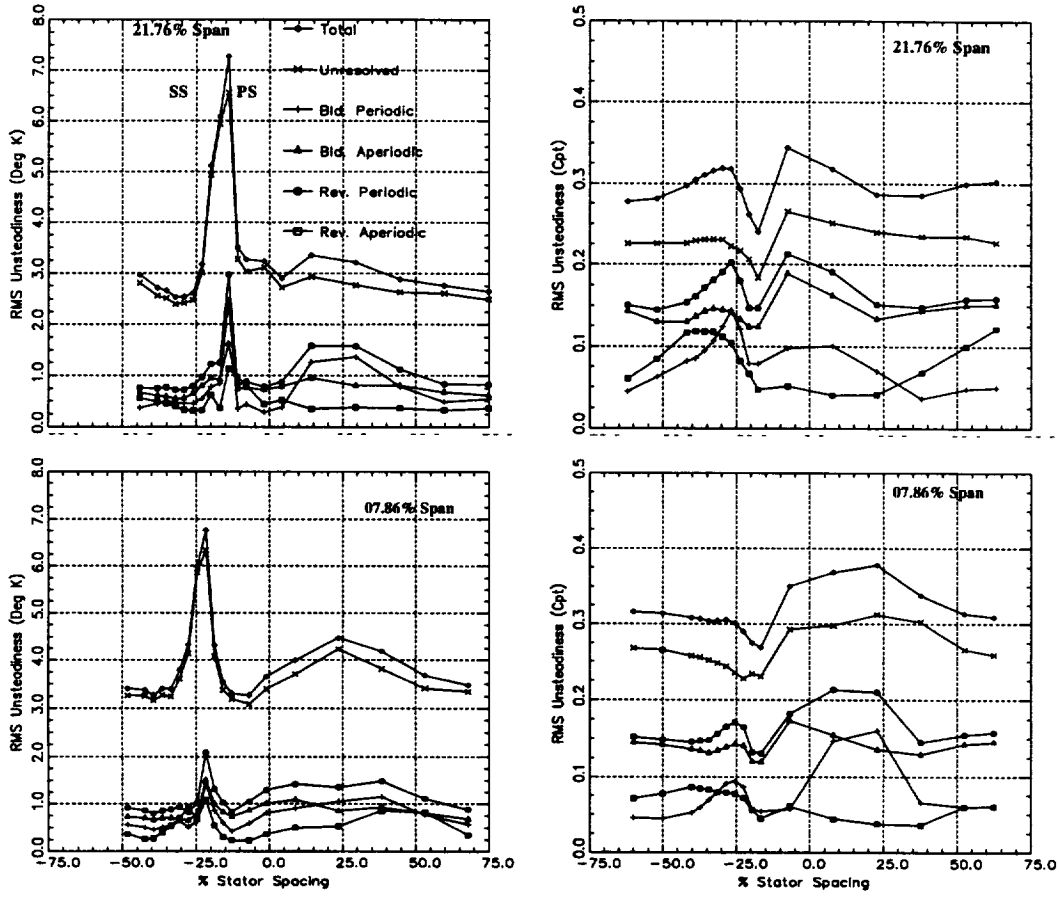

(a) Total Temperature (Deg K)

(b) Total Pressure (Cpt)

Figure 5.7. Blade-to-blade variation of time averaged RMS unsteadiness in total temperature rise and total pressure at various radii (cont'd)

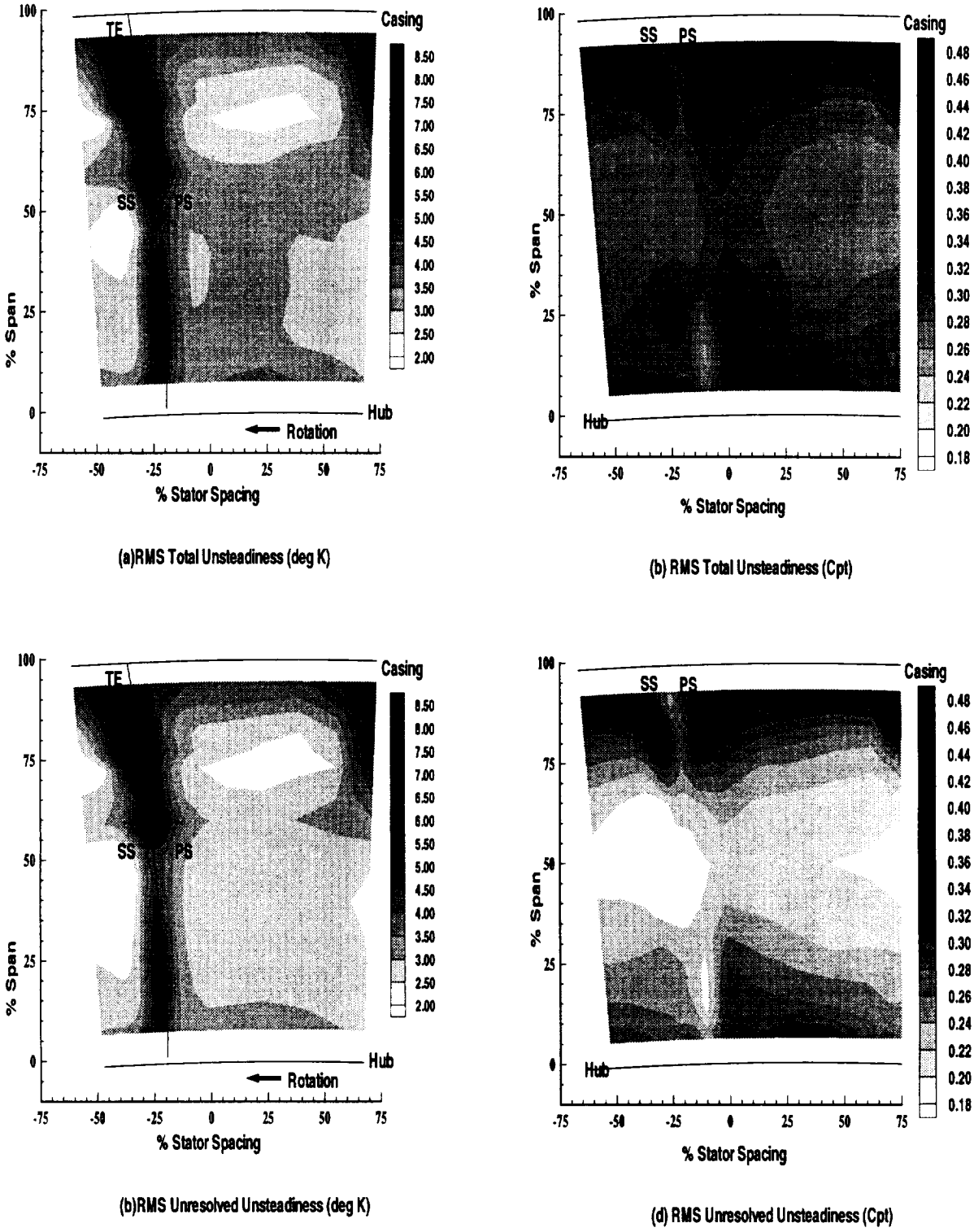

(a)RMS Total Unsteadiness (deg K)

(b) RMS Total Unsteadiness (Cpt)

(b)RMS Unresolved Unsteadiness (deg K)

(d) RMS Unresolved Unsteadiness (Cpt)

Figure 5.8. Contours of RMS unsteadiness in total temperature and total pressure

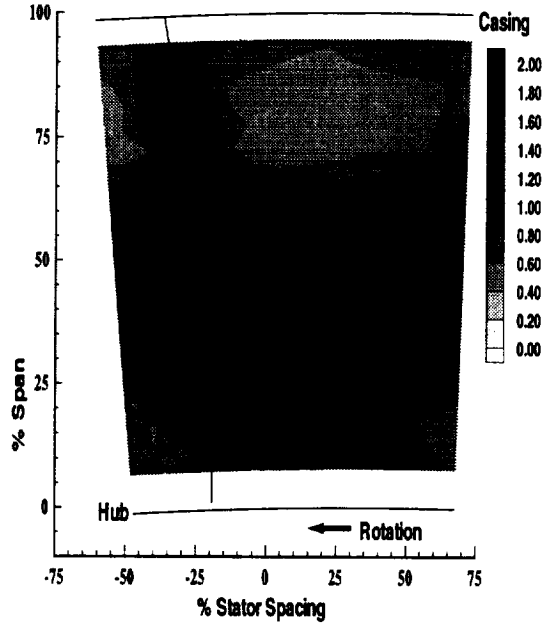

(e)RMS Revolution Periodic Unsteadiness (deg K)

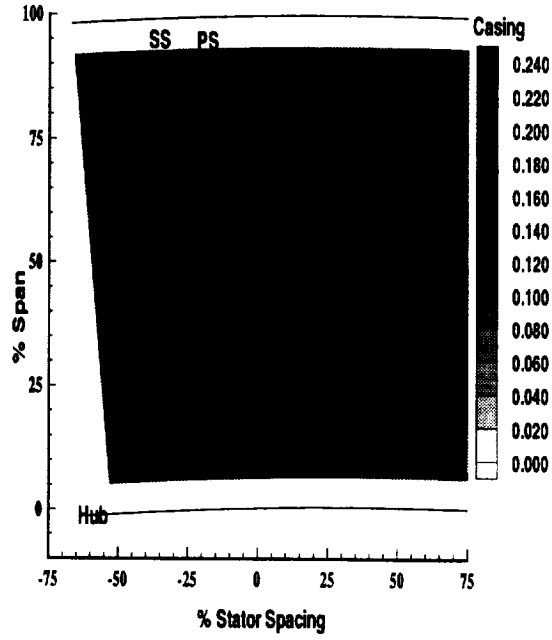

(c) RMS Revolution Periodic Unsteadiness (Cpt)

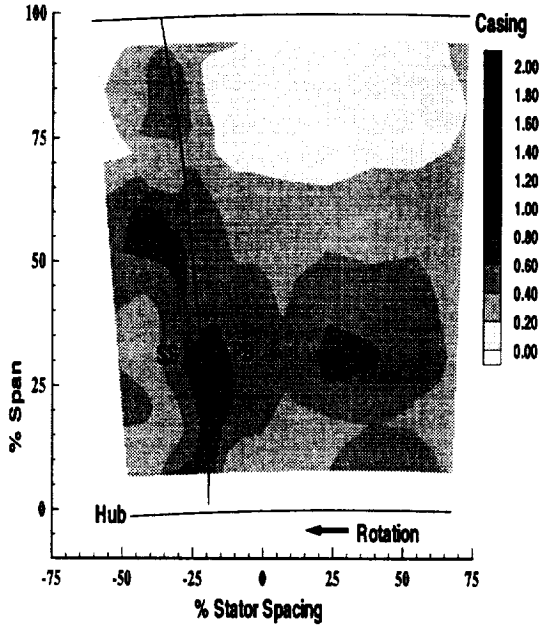

(g)RMS Revolution Aperiodic Unsteadiness (deg K)

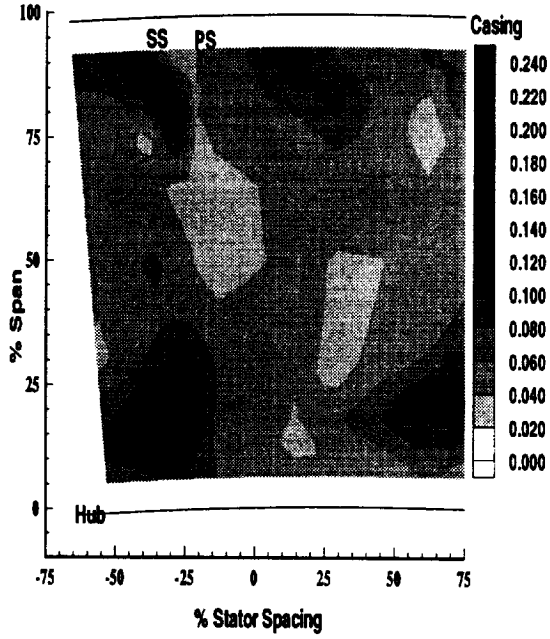

(h) RMS Revolution Aperiodic Unsteadiness (Cpt)

Figure 5.9. Contours of RMS unsteadiness in total temperature and total pressure (cont'd)

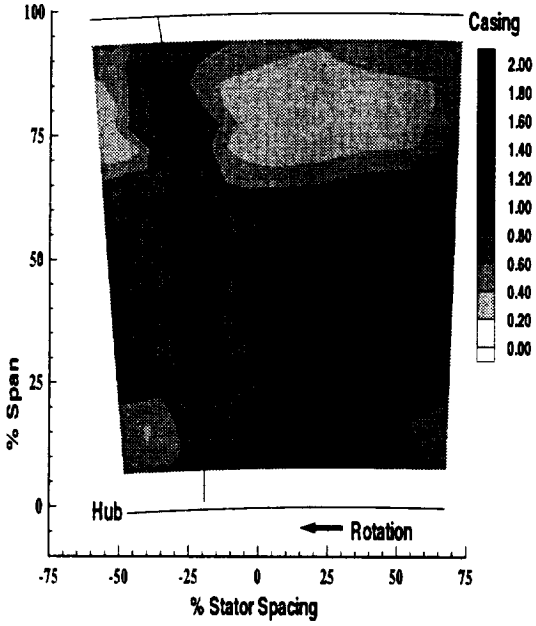

(a)RMS Revolution Periodic Unsteadiness (deg K)

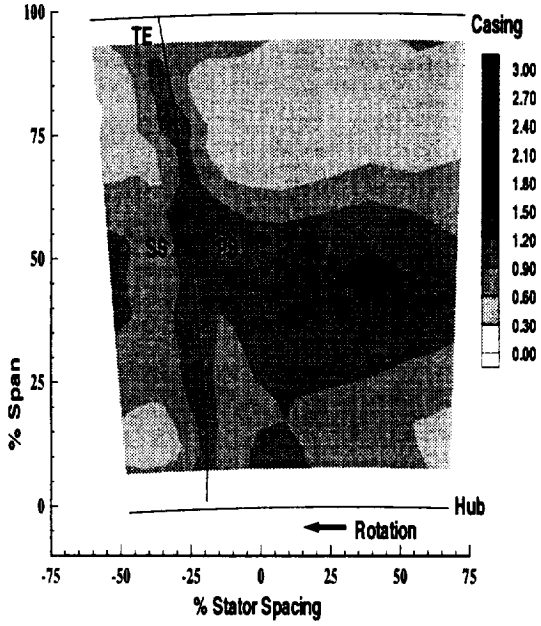

(b)RMS Blade Aperiodic Unsteadiness (deg K)

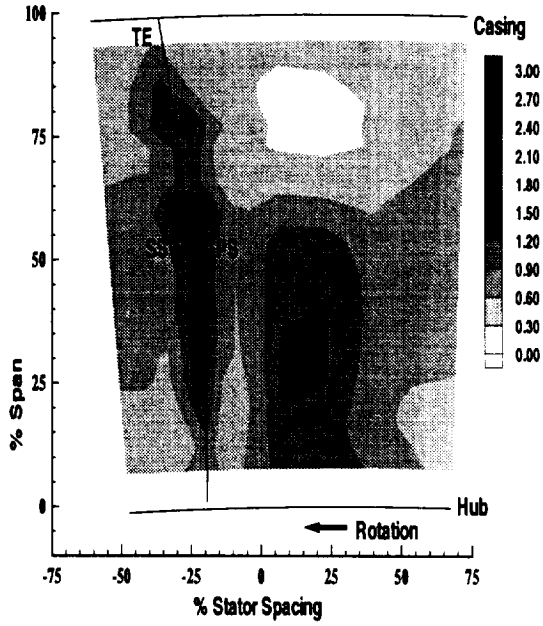

(c)RMS Blade Periodic Unsteadiness (deg K)

Figure 5.10. Contours of RMS Blade Aperiodic and Blade Periodic Unsteadiness in Total Temperature

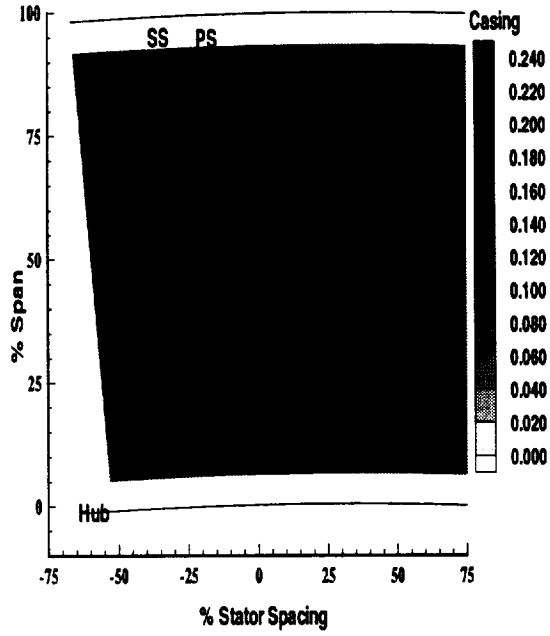

(a) RMS Revolution Periodic Unsteadiness (Cpt)

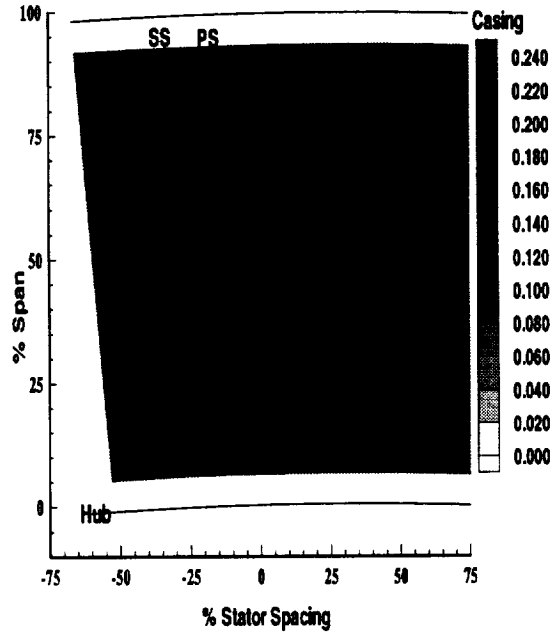

(b) RMS Blade Aperiodic Unsteadiness (Cpt)

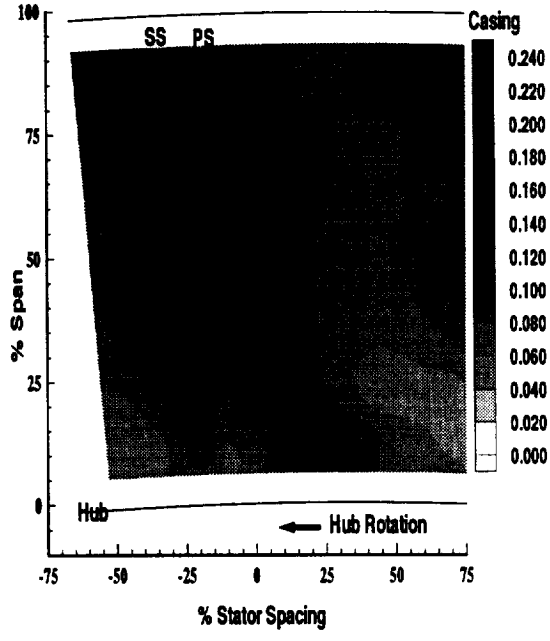

(c) RMS Blade Periodic Unsteadiness (Cpt)

Figure 5.11. Contours of RMS Blade Aperiodic and Blade Periodic Unsteadiness in Total Pressure

5.1.3 Hub endwall region

As was observed earlier, the hub endwall region is dominated by the clearance flow from the stator hub endwall and its interaction with the hub endwall fluid and the upstream rotor wakes. In order to explain the physics better a closeup view of the hub endwall region (all quantities) is plotted in Figures 5.12, 5.13, 5.14 and 5.15. The unsteadiness distributions does indicate that the this region has significant levels of both revolution periodic and unresolved unsteadiness in both total temperature and pressure. However, the levels of the unresolved unsteadiness is much higher than the revolution periodic unsteadiness. This is mainly due to the propagation and decay of the hub leakage vortex which may be unresolved in nature. The revolution periodic unsteadiness is the rotor hub wake fluid which is transported by the leakage flow and its subsequent interaction with the leakage flow. The radial and pitchwise extent of the unsteadiness is region is almost the same for both the data sets. It may be recalled here that the time averaged distributions of total temperature did not show any significant changes in total temperature in this region, even though significantly higher levels of unsteadiness are seen. Different behaviors are observed insofar as the distributions of the temperature and pressure unsteadiness are concerned. The total pressure unsteadiness distributions show much higher levels of unresolved unsteadiness in the clearance flow region compared with the wake at the same spanwise location, whereas the total temperature distribution shows higher levels of unresolved unsteadiness in the wake compared to the clearance flow region (Figure 5.7). This is true for the revolution periodic unsteadiness distribution as well. This is probably due to different behaviors of static pressure and static temperature distributions in a streamwise vortex. The revolution aperiodic unsteadiness is of very little significance in this region.

Slightly away from the leakage flow region, a region of comparable levels of revolu-

tion periodic and revolution aperiodic unsteadiness is observed on the suction side of the blade. It is surmised that this is due to the transport of possibly separated rotor boundary fluid on the suction side close to the hub. The CFD simulation was not able to shed any additional light on this phenomena other than indicate a slight thickening of the boundary layer on the suction side in the hub endwall region of the upstream rotor. A thickening of the pressure side of the hub wake is seen all the way upto 15% span in the total pressure distribution and about 12% in the total temperature distribution in total unsteadiness. This is mainly unresolved in nature both for the temperature and pressure. This is surmised to be due to accumulation of the hub leakage fluid on the pressure side of the stator due to the hub rotation.

5.1.4 Casing endwall region

In the casing endwall region, the dominant source of unsteadiness is in the suction surface corner region and bulk of this unsteadiness is unresolved in nature. In order to explain the physics better a closeup view of the casing endwall region (all quantities) is plotted in Figures 5.16, 5.17, 5.18 and 5.19. From the time averaged flow it was observed that this was due to intense secondary flow and interaction of the casing endwall fluid with the corner flow region. The presence of high levels of unresolved unsteadiness indicates a dominant source of mixing to be turbulent in nature. There is significant level of revolution periodic unsteadiness in the endwall region, but it is close to the blade on both sides of the stator whereas the unresolved unsteadiness is only on the suction side of the stator. The appearance of revolution periodic unsteadiness is probably due to the transport of the rotor tip leakage flow to the suction side of the stator passage. The center of the core of high unsteadiness is at approximately 80% span in the total temperature distribution and at 85% span in the total pressure distribution. From the time averaged data, the center of the low total pressure region is at 85% span, whereas the vortex core was at 90% span. This

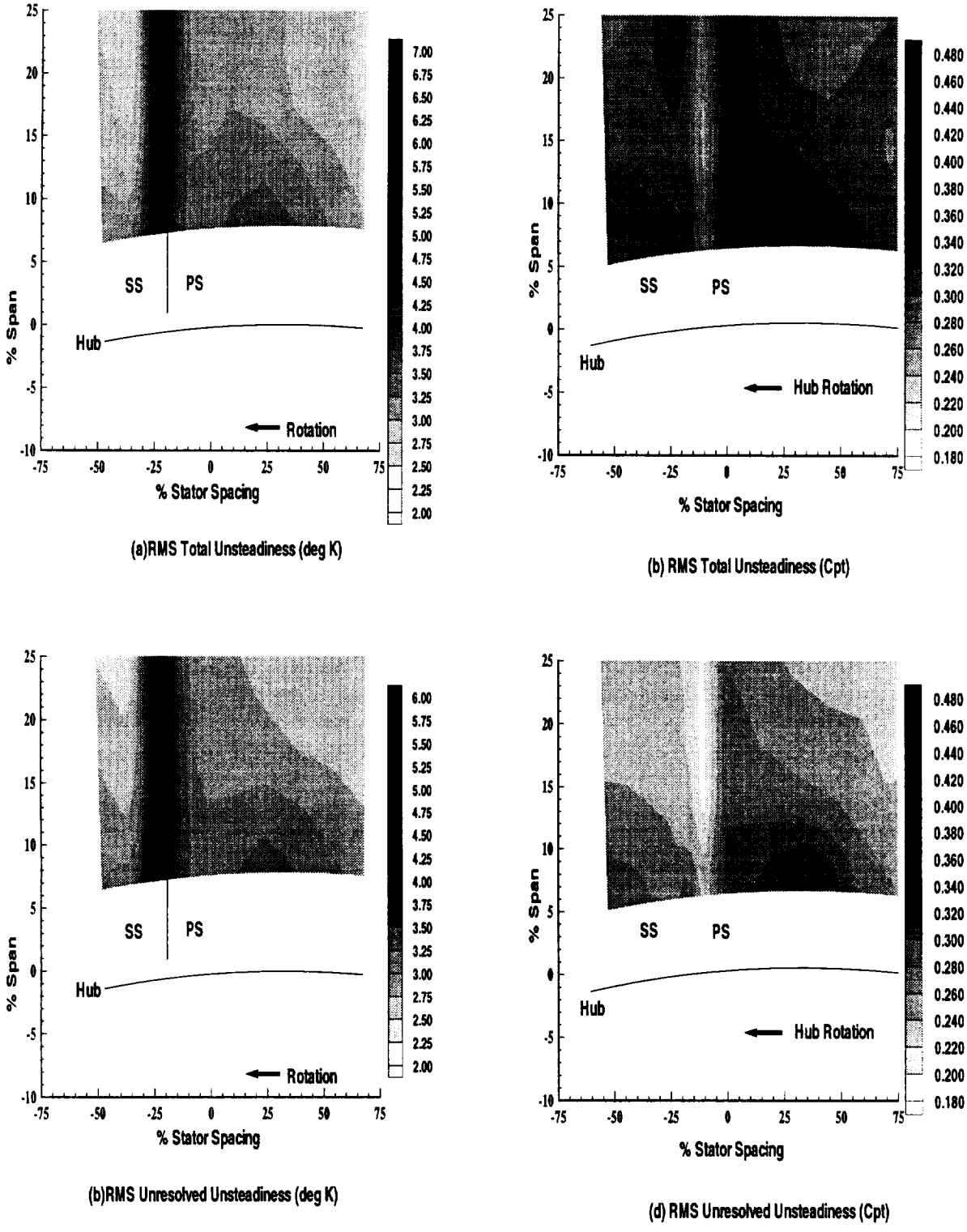

Figure 5.12. Contours of RMS unsteadiness in total temperature and total pressure near hub

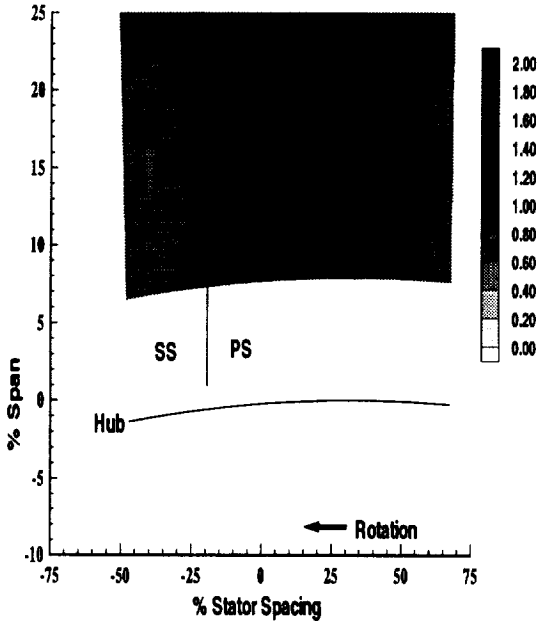

(e)RMS Revolution Periodic Unsteadiness (deg K)

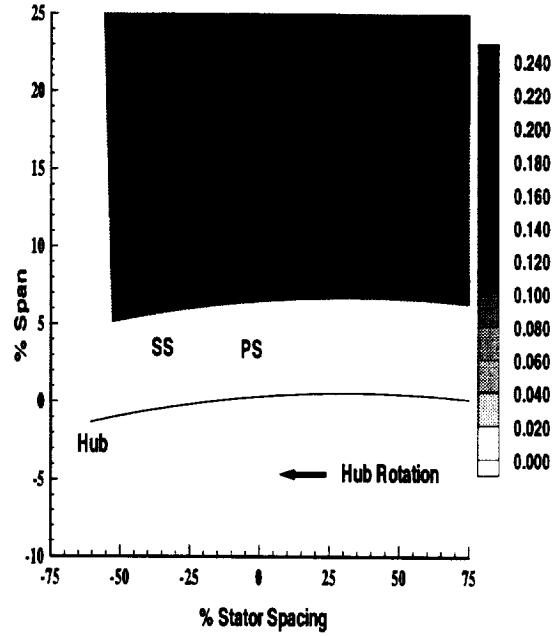

(f) RMS Revolution Periodic Unsteadiness (Cpt)

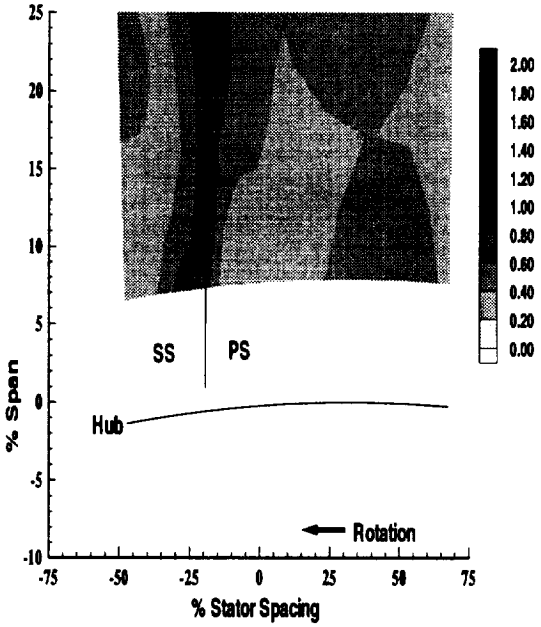

(g)RMS Revolution Aperiodic Unsteadiness (deg K)

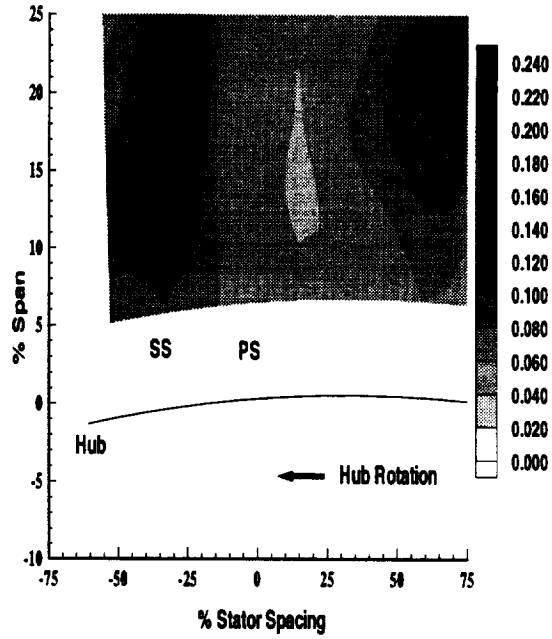

(h) RMS Revolution Aperiodic Unsteadiness (Cpt)

Figure 5.13. Contours of RMS unsteadiness in total temperature and total pressure near hub (cont'd)

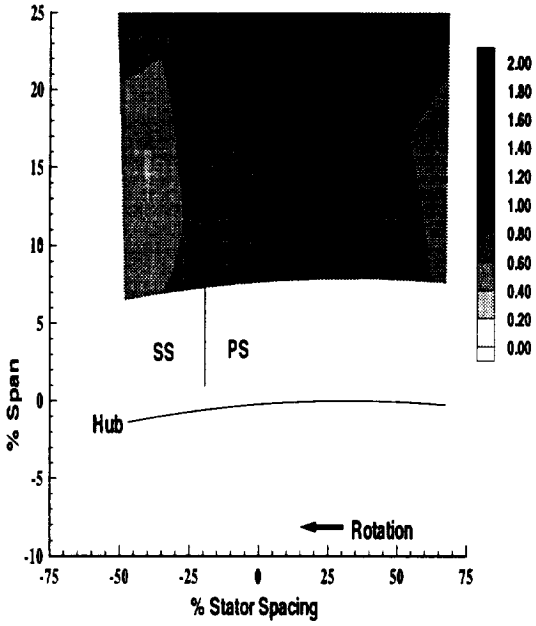

(a)RMS Revolution Periodic Unsteadiness (deg K)

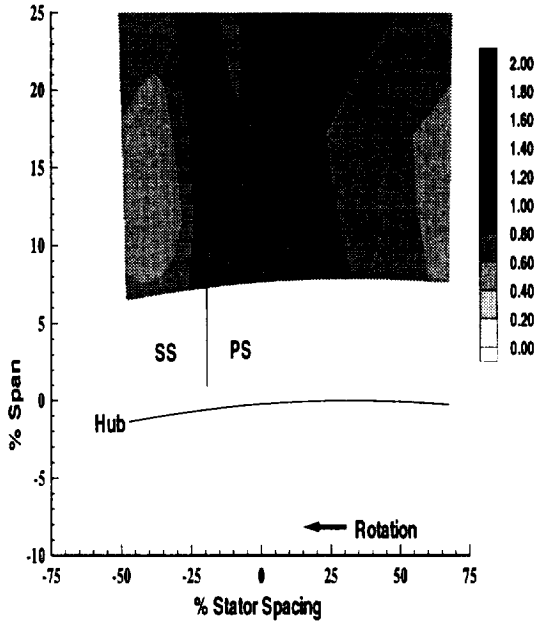

(b)RMS Blade Aperiodic Unsteadiness (deg K)

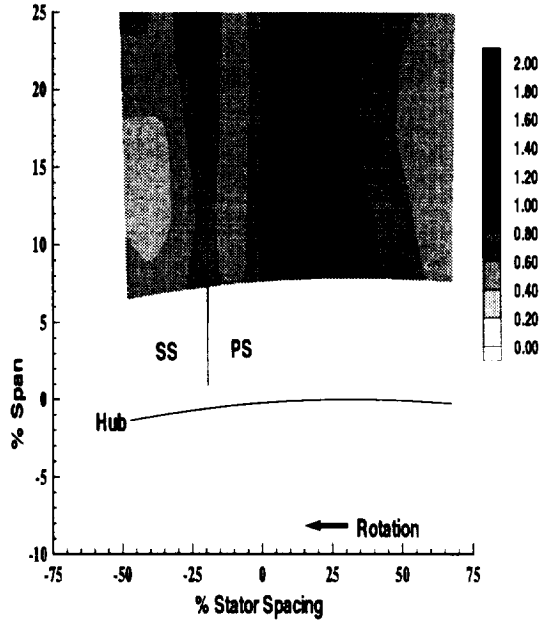

(c)RMS Blade Periodic Unsteadiness (deg K)

Figure 5.14. Contours of RMS Blade Aperiodic and Blade Periodic Unsteadiness in Total Temperature Near Hub

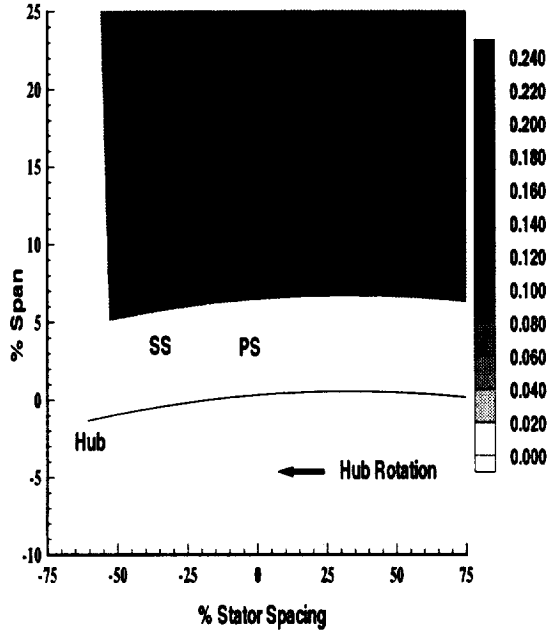

(a) RMS Revolution Periodic Unsteadiness (Cpt)

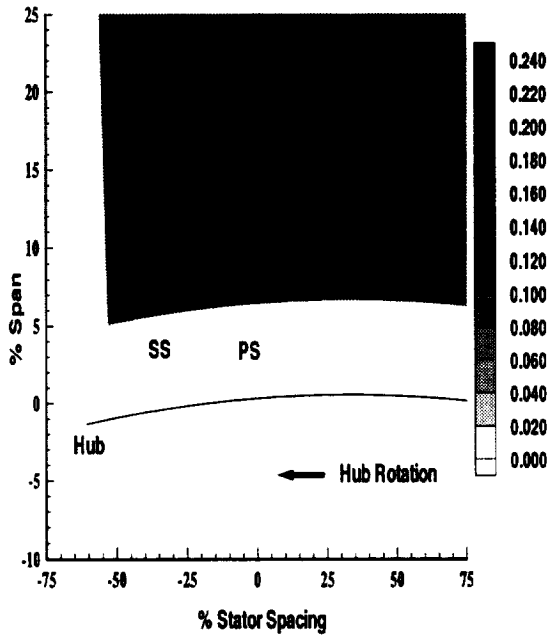

(b) RMS Blade Aperiodic Unsteadiness (Cpt)

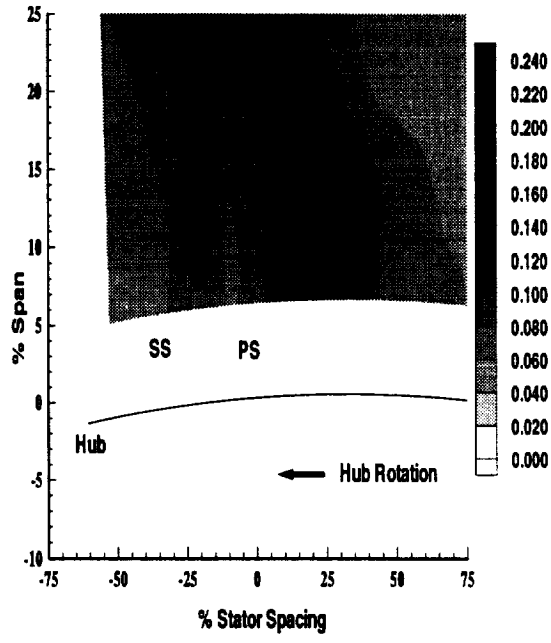

(c) RMS Blade Periodic Unsteadiness (Cpt)

Figure 5.15. Contours of RMS Blade Aperiodic and Blade Periodic Unsteadiness in Total Pressure Near Hub

change in the location of the time averaged and unsteady cores is probably due to radial inward transport brought about by secondary flows and the presence of radial inward static pressure gradient. The unsteady CFD simulation seems to qualify this hypothesis. The revolution aperiodic unsteadiness levels are high in these regions as well confirming the probable transport of the rotor tip leakage flow to the suction surface. Away from the blade surfaces, the levels of unresolved unsteadiness are higher than that observed in the core region, consistent with the increase in vorticity and associated turbulence production in the endwall viscous fluid. However, the periodic unsteadiness levels do not change significantly leading to speculation that possible rotor wake smearing may be taking place or that the decay rates of the rotor wake flow are much higher than that existing at other radial locations or possible transport away from the endwall. Detailed examination of the unsteady velocity distribution may shed light on this matter.

5.2 Temporal Variation of Stator Exit Flow

In this section, the temporal variation of the stator exit flow is discussed. Figures 5.20-5.26 show several perspectives of the stator exit flow (ensemble averaged and unresolved unsteadiness in total pressure and total temperature) "frozen" at the same instant in time within the rotor revolution, but derived by averaging over 250 consecutive rotor revolutions. Seven frames from the passage of the first rotor blade across the stator passage is shown but the interpretation is based on the analysis of 20 frames (the first blade passage in the revolution). A clock in the upper right hand corner of each perspective shows the passage of the rotor blade across the stator passage (from $\tau/T = 0.0$ to $\tau/T = 1.0$). Here τ represents the fraction of blade passing period T. These times are arbitrary as the location of the rotor blade with respect to stator is not known. The location of the trigger

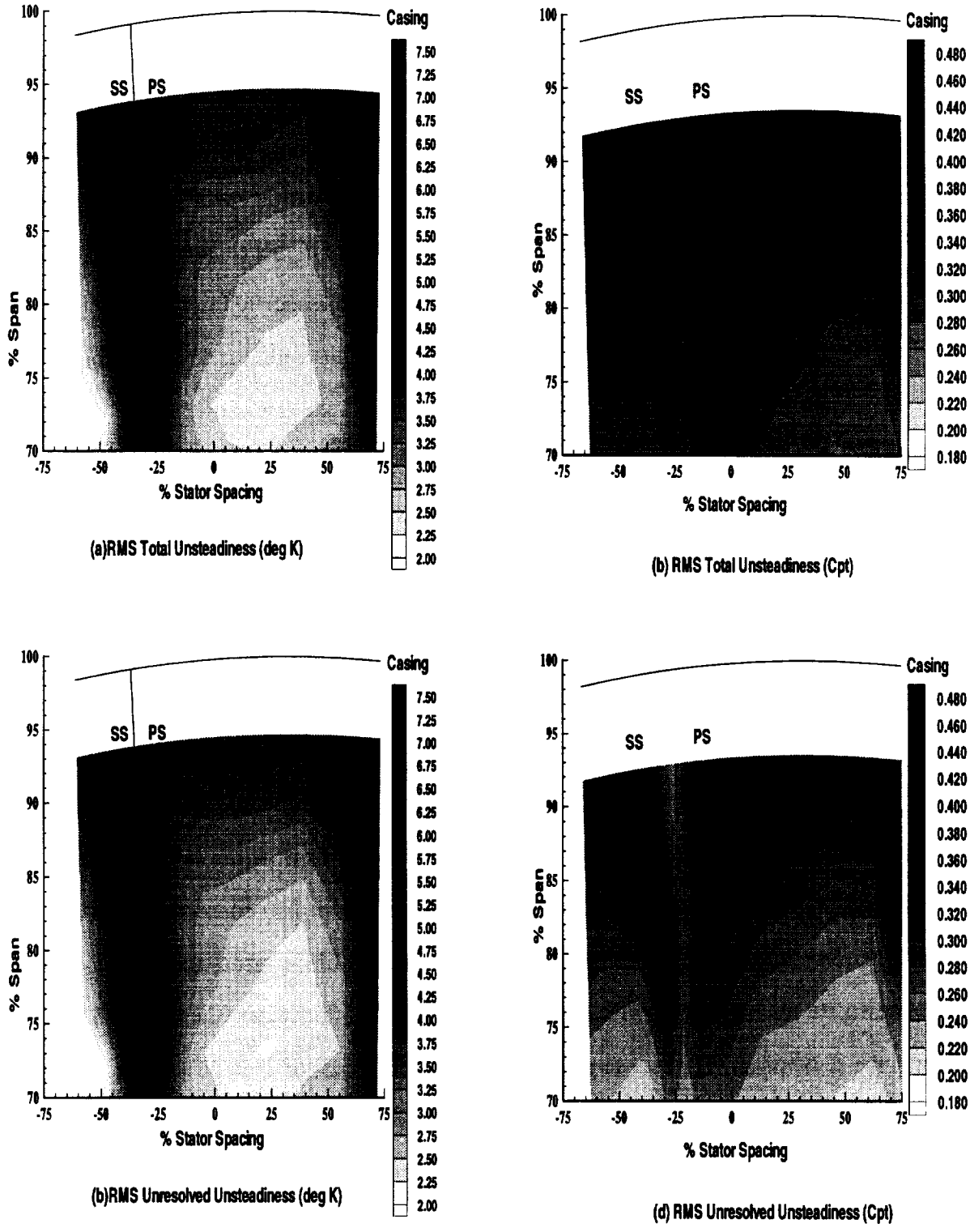

Figure 5.16. Contours of RMS unsteadiness in total temperature and total pressure near Tip

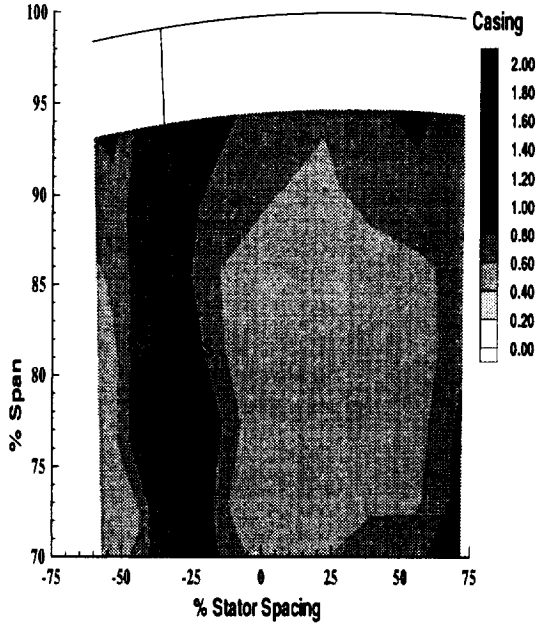

(e)RMS Revolution Periodic Unsteadiness (deg K)

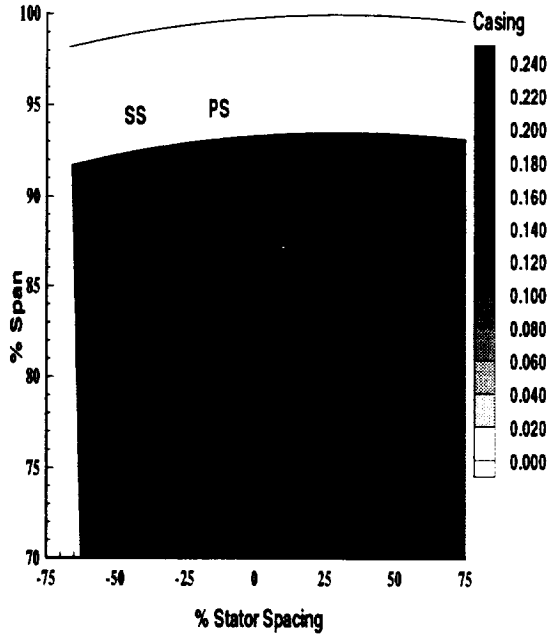

(f) RMS Revolution Periodic Unsteadiness (Cpt)

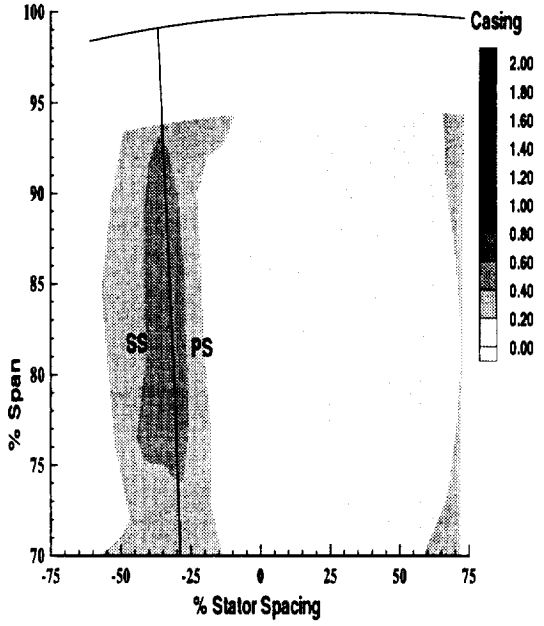

(g)RMS Revolution Aperiodic Unsteadiness (deg K)

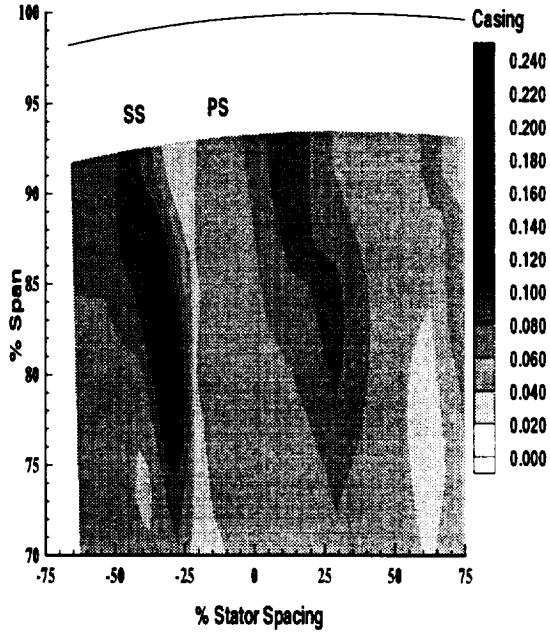

(h) RMS Revolution Aperiodic Unsteadiness (Cpt)

Figure 5.17. Contours of RMS unsteadiness in total temperature and total pressure near Tip (cont'd)

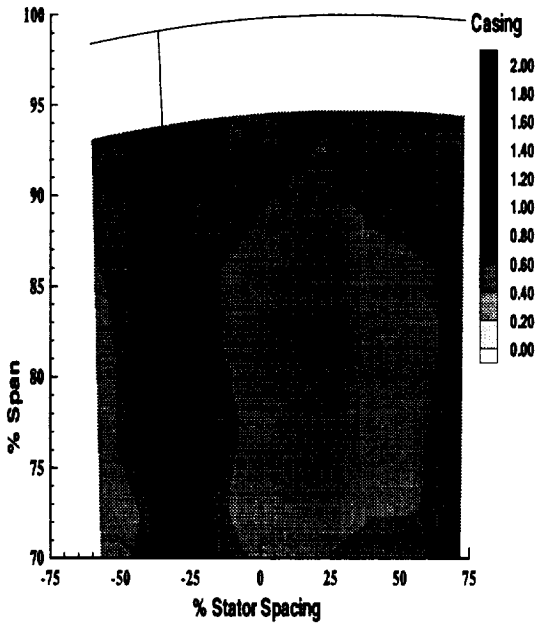

(a)RMS Revolution Periodic Unsteadiness (deg K)

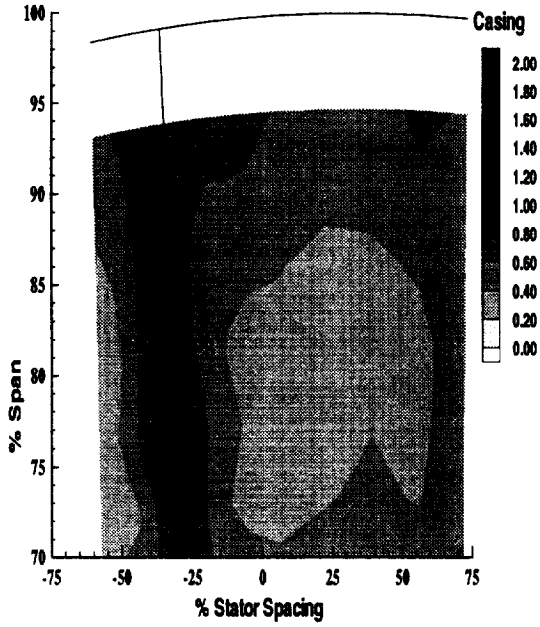

(b)RMS Blade Aperiodic Unsteadiness (deg K)

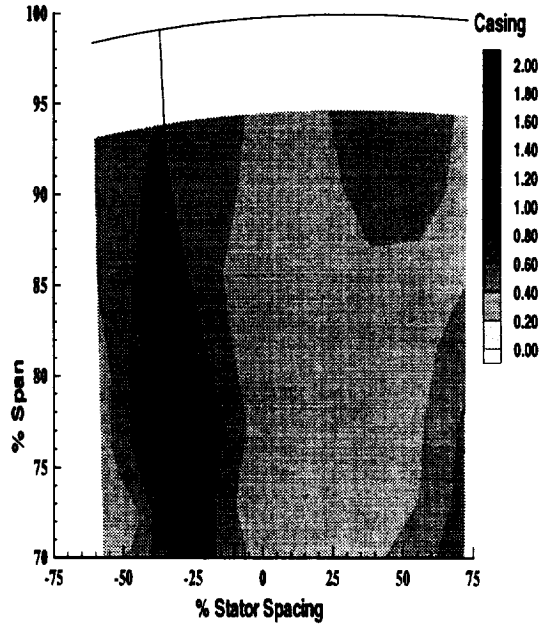

(c)RMS Blade Periodic Unsteadiness (deg K)

Figure 5.18. Contours of RMS Blade Aperiodic and Blade Periodic Unsteadiness in Total Temperature Near Tip

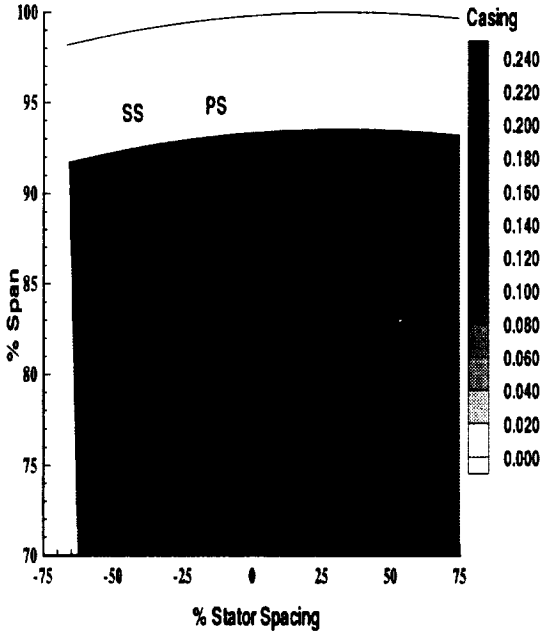

(a) RMS Revolution Periodic Unsteadiness (Cpt)

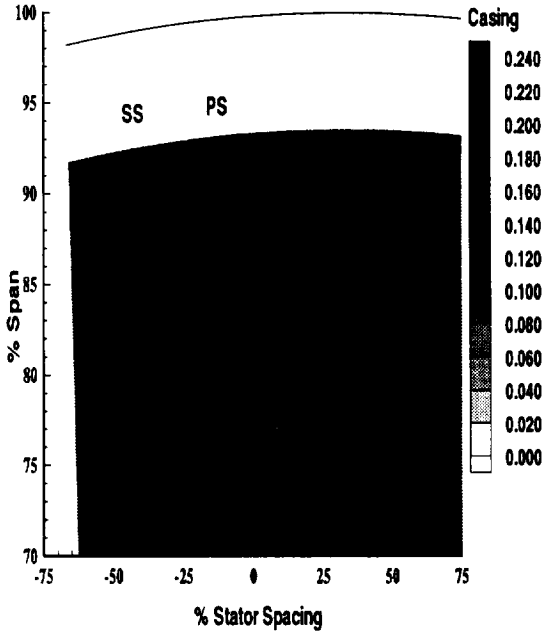

(b) RMS Blade Aperiodic Unsteadiness (Cpt)

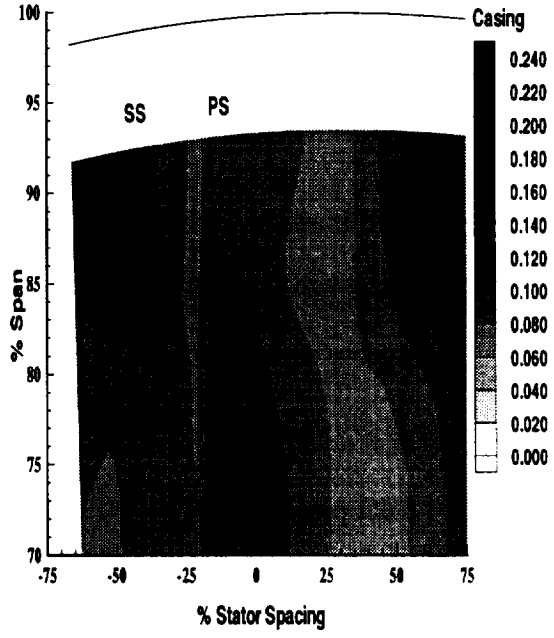

(c) RMS Blade Periodic Unsteadiness (Cpt)

Figure 5.19. Contours of RMS Blade Aperiodic and Blade Periodic Unsteadiness in Total Pressure Near Tip

is the same with respect to all locations in the stator passage [1] The discussion in focused on the following phenomena:

1. Behavior of the rotor wake
2. Behavior of the stator wake
3. Behavior of the hub endwall leakage flow region
4. Behavior of the casing endwall corner region (blade suction surface and casing endwall corner)
5. Behavior of the casing endwall region away from the blade surfaces

The temporal variation distribution is shown in Figures 5.20 through 5.26. In each of these figures the following information is plotted:

- The blade-to-blade distributions of the following total pressure rise coefficients at midspan: time averaged, ensemble averaged at that instant, time averaged RMS unresolved and the RMS unresolved unsteadiness at that instant in time.
- The blade-to-blade distributions of the following total temperature rise quantities at midspan: time averaged, ensemble averaged at that instant, time averaged RMS unresolved and the RMS unresolved unsteadiness at that instant in time.
- Hub-to-tip contours of the ensemble averaged and RMS unresolved unsteadiness in total pressure rise coefficient and total temperature rise at that instant, the location on the rotor revolution being indicated by the clock on the upper right hand corner of the plot.

[1] A video of this flowfield is available with Dr. B. Lakshminarayana, Evan Pugh Professor of Aerospace Engineering, Penn State University, University Park, PA 16802, (814) 865-5551

In addition, the blade-to-blade variations of ensemble averaged and RMS unresolved unsteadiness in total pressure rise coefficient and total temperature rise at various instants of time of the rotor revolution at various radial locations (near hub-7.86%, midspan-53.36%, 81.89% and near casing-90.44% span) is plotted in Figures 5.27 through 5.34. The blade count difference between rotor 2 and stator 2 is one. So slightly more than one rotor wake is found in the stator passage. Figures 5.36, 5.38 and 5.40 show the hub-to-tip variation of rotor 2 exit flow at the midpitch, suction and pressure surfaces respectively. Approximately seven blade passages of ensemble averaged total pressure and total temperature rise and RMS unresolved unsteadiness in total pressure and total temperature rise are shown plotted in each of the above figures. This perspective is used to interpret the passing of the rotor wake through the stator passage. The two stator blade passages are identified as *CB* and *KB* respectively and this is shown in Figures 5.20 through 5.26.

5.2.1 Behavior of the Rotor Wake

The rotor wake is identified by local increases in total pressure and temperature (both ensemble averaged and unresolved unsteadiness) above the time average. At the same instant of time, there is a phase lag between the ensemble averaged and unresolved unsteadiness in both pressure and temperature. There is also a time shift between the total temperature and total pressure distributions. The phase difference between the ensemble averaged and unresolved data is due to the reference frame where the measurement was conducted in. All the measurements conducted in this thesis are in the absolute frame of reference and also presented in the absolute frame of reference. The unresolved unsteadiness is the same irrespective of the frame of reference, whereas the ensemble averaged flow is dependent on the frame. This leads to a phase shift between the ensemble average and the unresolved unsteadiness. The time lag between the total pressure and

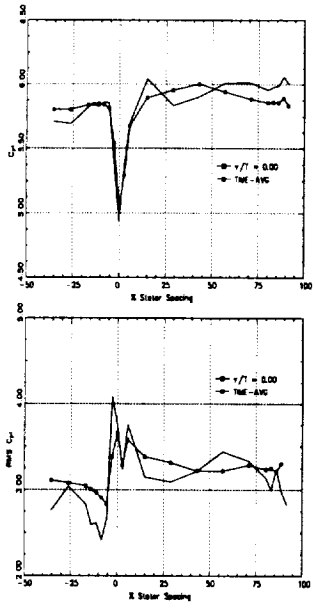

(a) Total Pressure

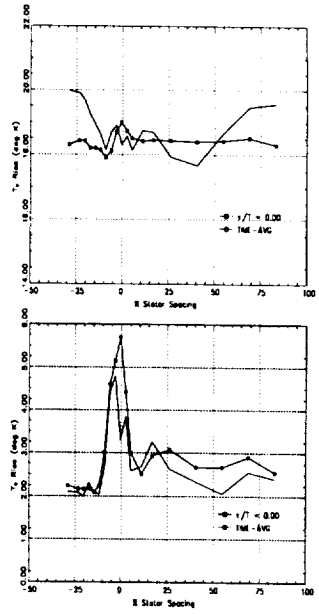

(b) Total Temperature

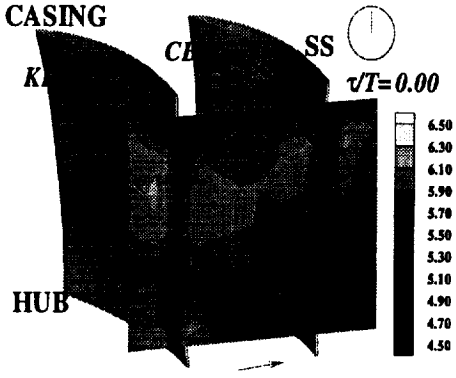

Ensemble Averaged Cpt

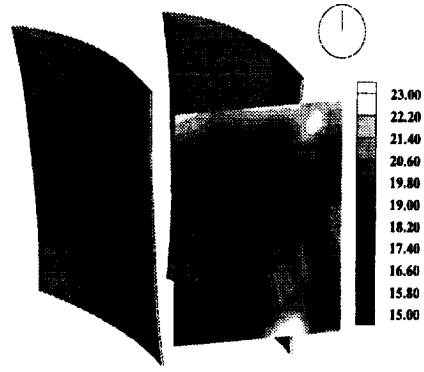

Ensemble Averaged ΔT_0 (Deg K)

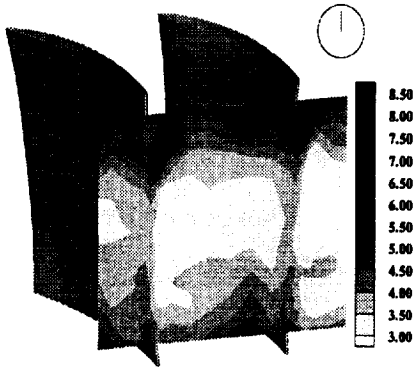

Unresolved Unsteadiness in Cpt (%)

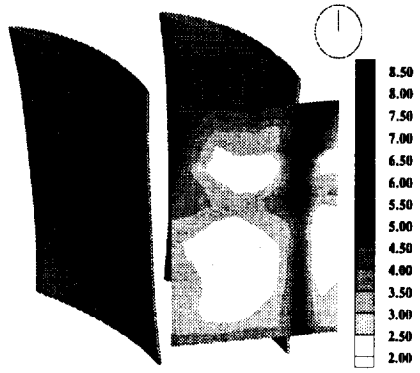

Unresolved Unsteadiness in ΔT_0 (Deg K)

Figure 5.20. Temporal Variation of Stator Exit Flow: Contours of Ensemble averaged and RMS unresolved unsteadiness - Time τ/T=0.00

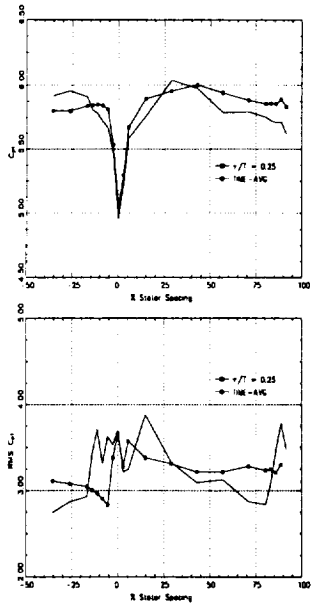

(a) Total Pressure

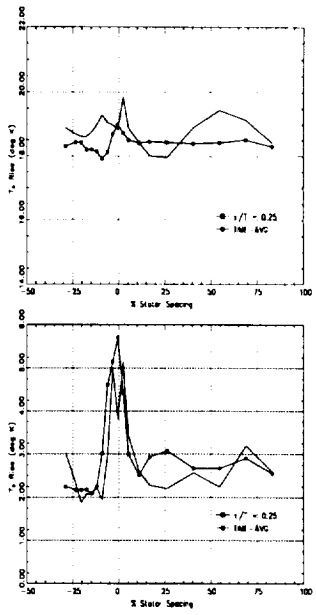

(b) Total Temperature

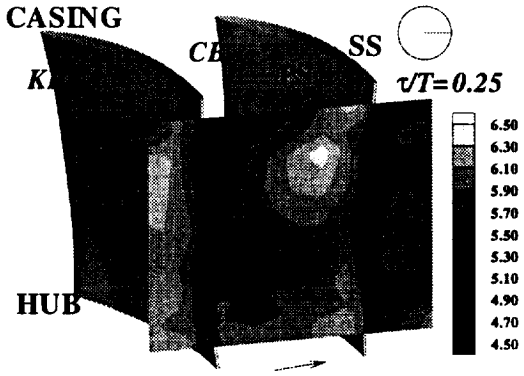

Ensemble Averaged Cpt

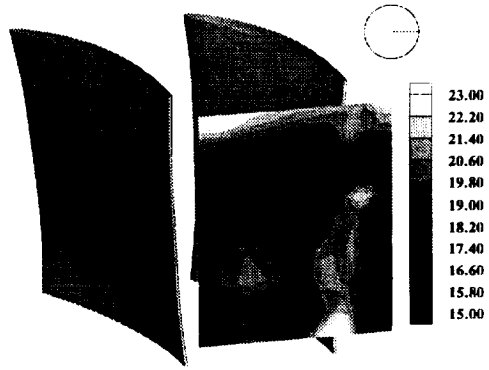

Ensemble Averaged ΔT_o (Deg K)

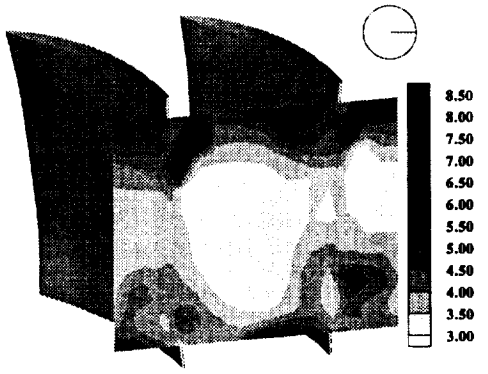

Unresolved Unsteadiness in Cpt (%)

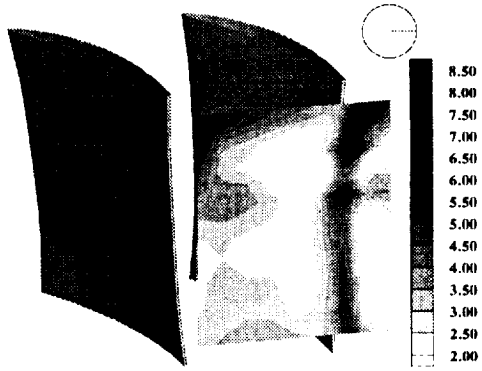

Unresolved Unsteadiness in ΔT_o (Deg K)

Figure 5.21. Temporal Variation of Stator Exit Flow: Contours of Ensemble averaged and RMS unresolved unsteadiness - Time τ/T=0.25

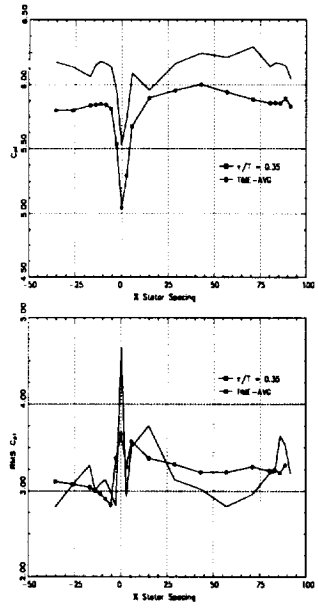

(a) Total Pressure

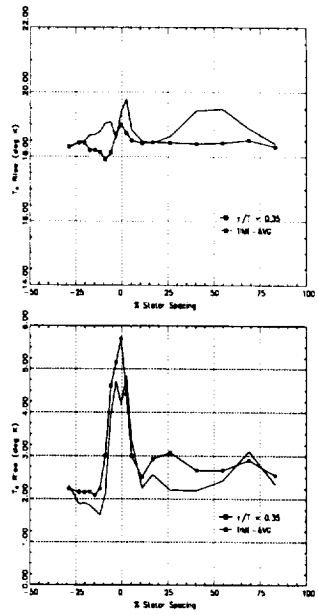

(b) Total Temperature

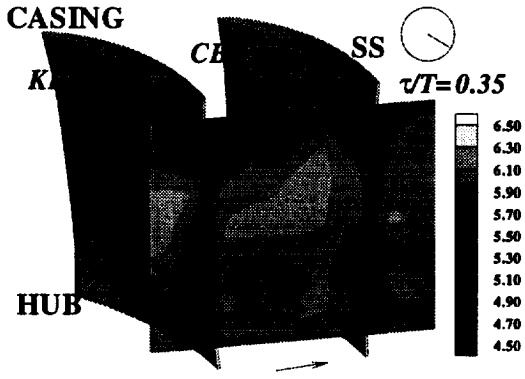

Ensemble Averaged Cpt

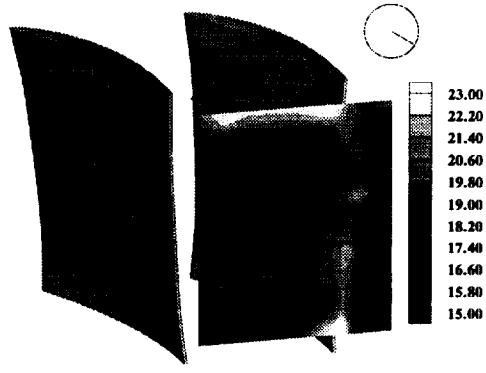

Ensemble Averaged ΔT_0 (Deg K)

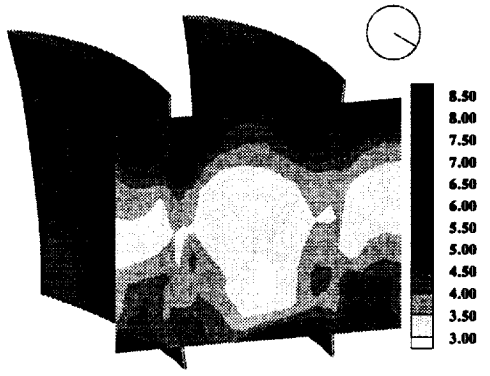

Unresolved Unsteadiness in Cpt (%)

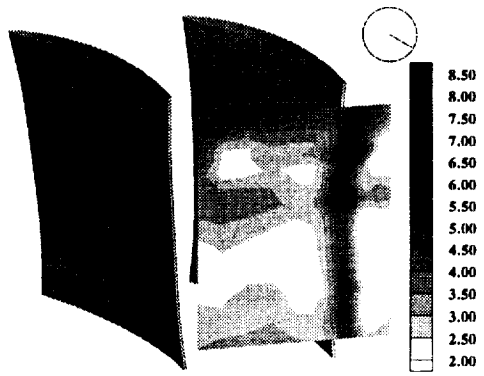

Unresolved Unsteadiness in ΔT_0 (Deg K)

Figure 5.22. Temporal Variation of Stator Exit Flow: Contours of Ensemble averaged and RMS unresolved unsteadiness - Time τ/T=0.35

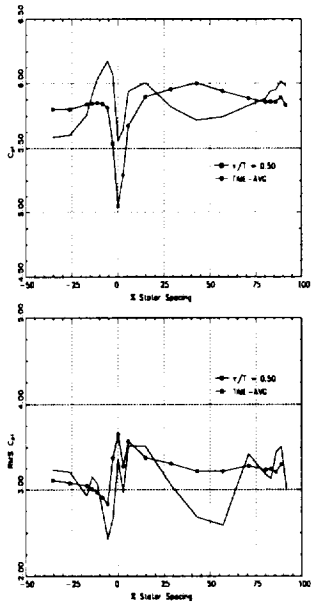

(a) Total Pressure

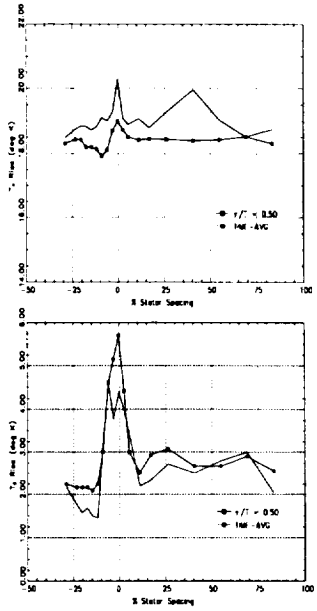

(b) Total Temperature

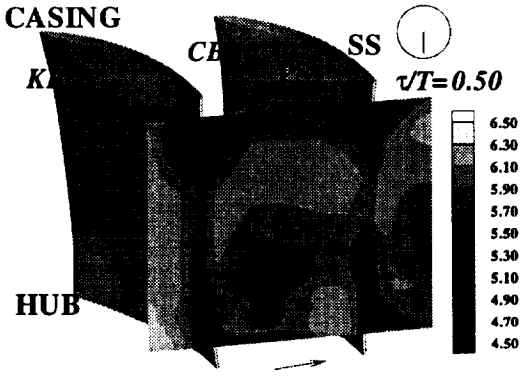

Ensemble Averaged Cpt

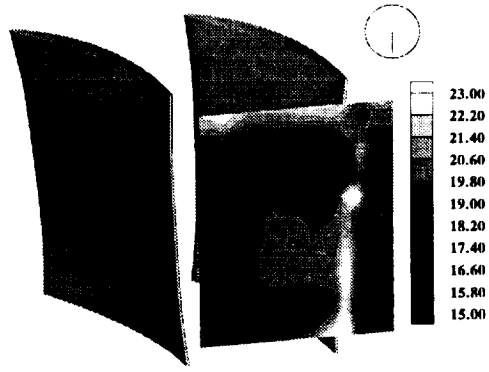

Ensemble Averaged ΔT_o (Deg K)

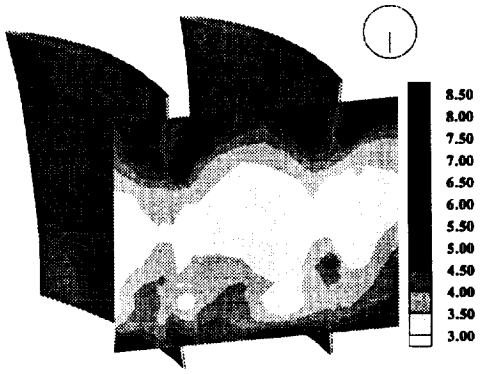

Unresolved Unsteadiness in Cpt (%)

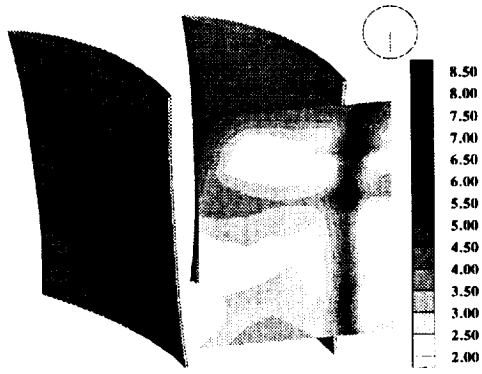

Unresolved Unsteadiness in ΔT_o (Deg K)

Figure 5.23. Temporal Variation of Stator Exit Flow: Contours of Ensemble averaged and RMS unresolved unsteadiness - Time τ/T=0.50

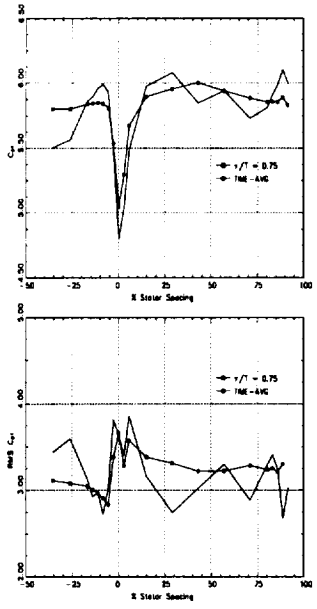

(a) Total Pressure

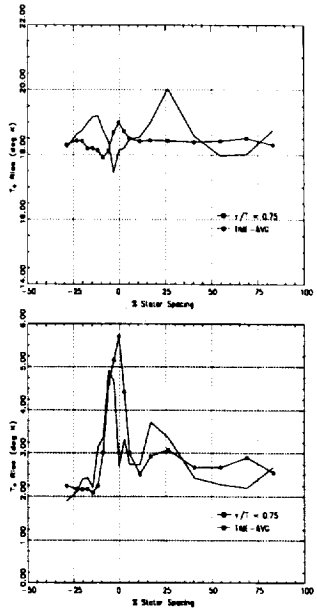

(b) Total Temperature

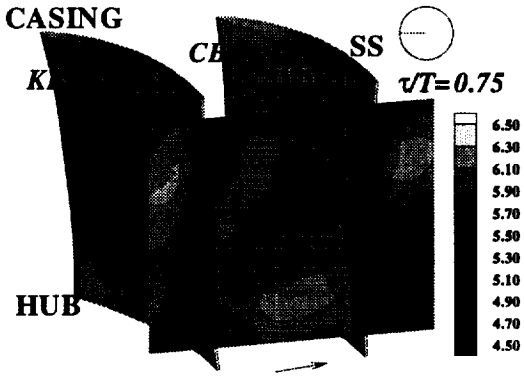

Ensemble Averaged Cpt

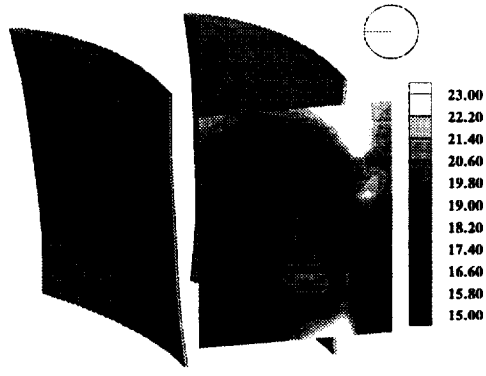

Ensemble Averaged ΔT_o (Deg K)

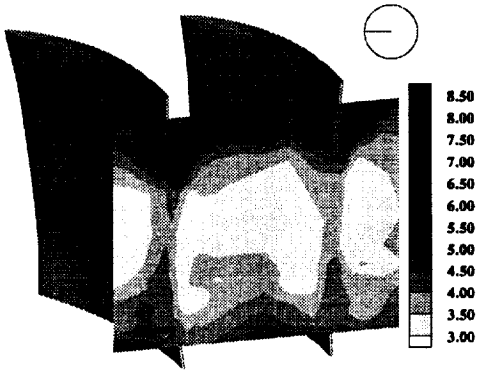

Unresolved Unsteadiness in Cpt (%)

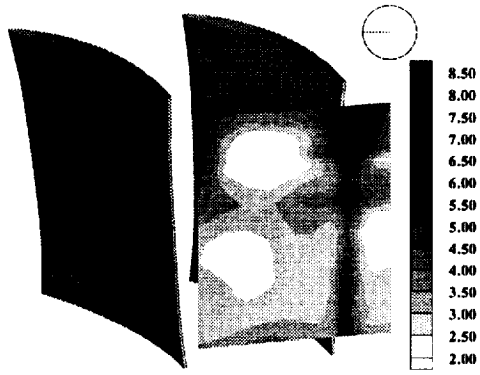

Unresolved Unsteadiness in ΔT_o (Deg K)

Figure 5.24. Temporal Variation of Stator Exit Flow: Contours of Ensemble averaged and RMS unresolved unsteadiness - Time τ/T=0.75

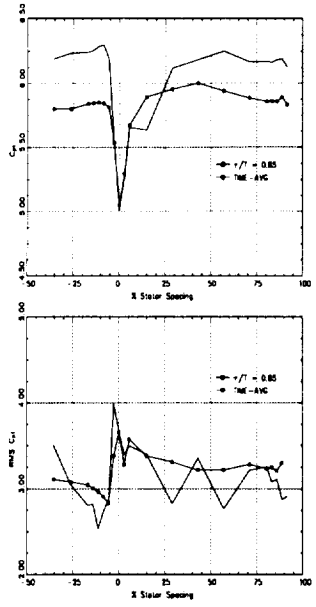

(a) Total Pressure

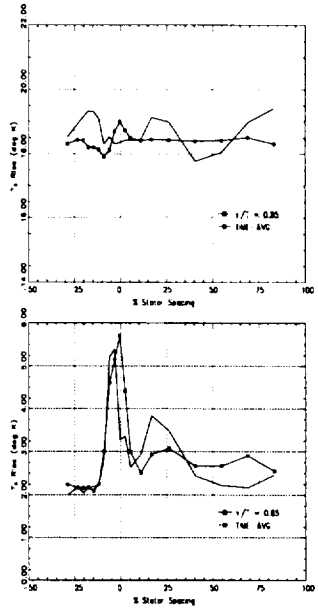

(b) Total Temperature

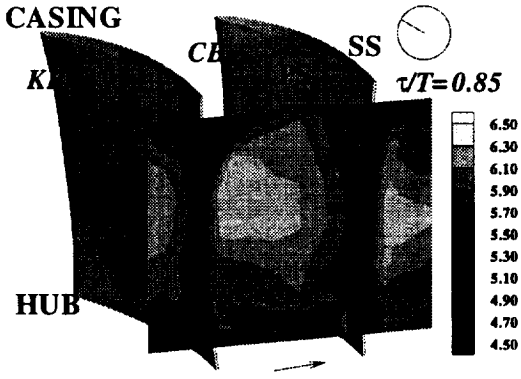

Ensemble Averaged Cpt

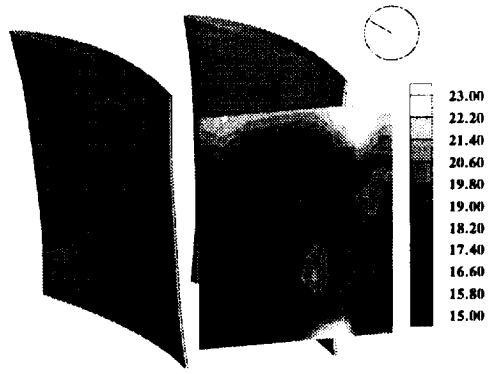

Ensemble Averaged ΔT_o (Deg K)

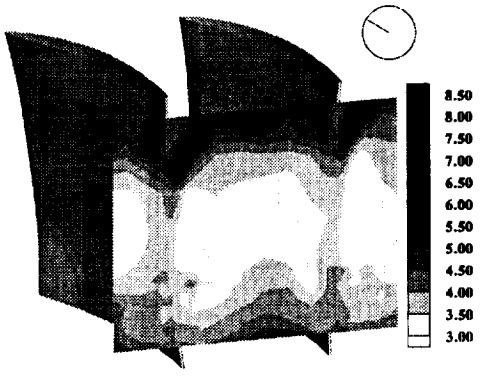

Unresolved Unsteadiness in Cpt (%)

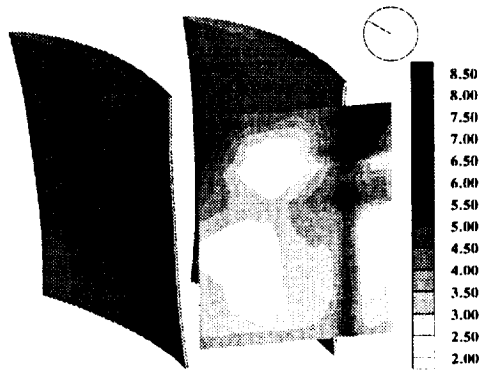

Unresolved Unsteadiness in ΔT_o (Deg K)

Figure 5.25. Temporal Variation of Stator Exit Flow: Contours of Ensemble averaged and RMS unresolved unsteadiness - Time τ/T=0.85

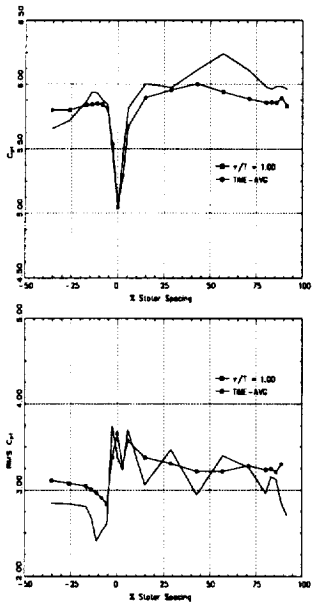

(a) Total Pressure

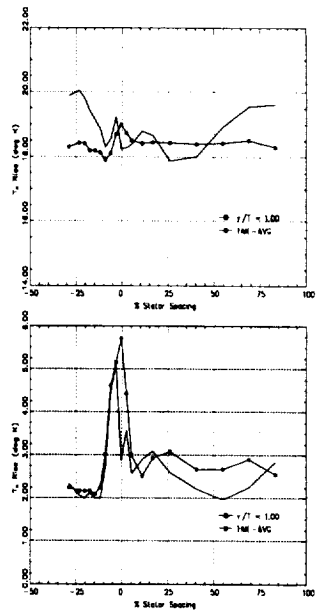

(b) Total Temperature

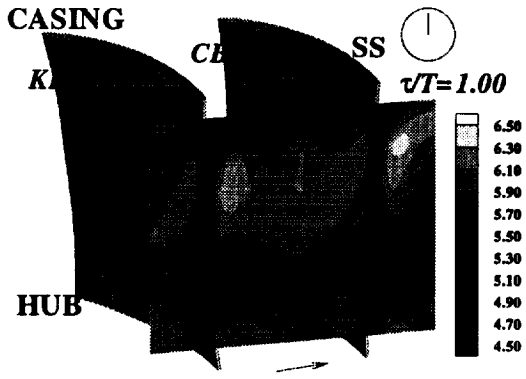

Ensemble Averaged Cpt

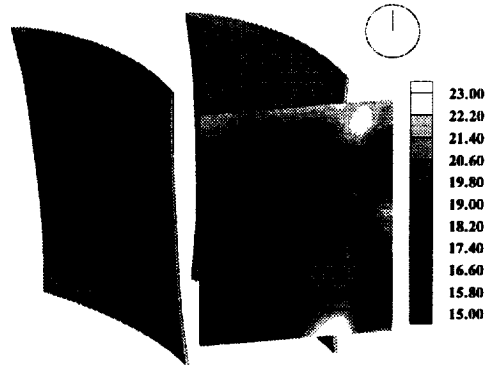

Ensemble Averaged ΔT_o (Deg K)

Unresolved Unsteadiness in Cpt (%)

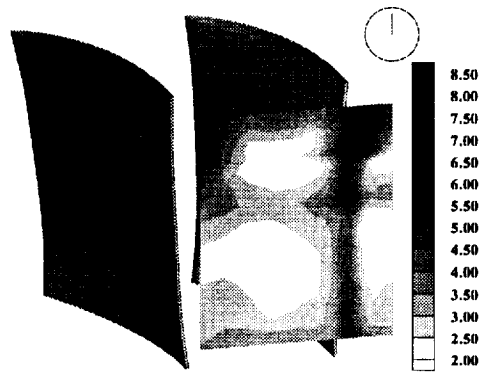

Unresolved Unsteadiness in ΔT_o (Deg K)

Figure 5.26. Temporal Variation of Stator Exit Flow: Contours of Ensemble averaged and RMS unresolved unsteadiness - Time τ/T=1.00

total temperature data is probably due to the differential wake decay rates of the total temperature and total pressure wakes and the convection rates inside the stator passage.

From figures 5.36, 5.40 and 5.38, it is observed that the rotor wake flow is quite different in each of these locations. In the regions away from the endwalls, a continuous rotor wake is only seen at the midpitch location. At the suction and pressure surface locations, the wakes are quite distorted and discontinuous in the pitchwise direction. This is due to the chopping of the rotor wake by the stator blade. In the endwall regions, the wakes are distorted due to a combination of various regions: (a) the hub endwall leakage flow interaction with the rotor wake fluid at midpitch, (b) the casing endwall suction surface corner region interaction with the rotor wake fluid on the suction surface near the casing endwall and (c) the interaction between the rotor wake and the casing endwall fluid away from the blade surfaces. These interactions are studied in subsequent sections with more focus on the behavior of the individual phenomena. So in order to study, the effect of the passing rotor wake the midspan data is used. The passing of the rotor wake is best explained by the total pressure data than by the total temperature data at midspan. The midspan distributions are also used to explain the minimum and maximum interaction regions as pertaining to the rotor wake.

Closer examination of the rotor wake as it crosses the stator passage reveals that it becomes discontinuous either side of the stator wake. Starting with non-dimensional time τ/T=0.0 (Figure 5.20(a)), one leg of the deterministic content of the rotor wake is seen on the suction side of stator and the other leg is seen approaching the pressure surface of the stator. This is because of higher convection speeds of the rotor wake on the suction surface of the downstream stator than on the pressure side. This is more noticeable as the chopped rotor wake progress up the stator wake and the difference between the arrival times of the wake segments either side of the stator wake becomes more significant (Figures 5.20(a) and 5.21(a)). As the rotor sweeps across the stator passage, the rotor wake is observed

to be at various locations in the core flow region of the compressor until time approaches τ/T=0.35, where the wake approaches the next stator blade wake on the suction side. It is between times 0.35 and 0.5, that the next rotor wake makes its appearance on the suction side of the stator blade *CB*. Since the blade count difference between rotor 2 and stator 2 is 1, part of the wake of first rotor blade is still in the stator passage when the next rotor wake makes its appearance. From the video animation, at time τ/T=0.40, both the rotor wakes are observed distinctly in the stator passage and this accounts for the maximum interaction between the stator and the rotor flow.

5.2.2 Behavior of the stator wake regions

As the rotor passes across the stator passage, the stator wakes show changes in their behavior. Different behaviors are observed at different radii. Reference is made to Figures 5.27 through 5.34 to interpret this region. Near the hub (7.86% span) (Figure 5.27 and 5.28), the width and depth of the total pressure wake remains almost constant (both ensemble average and unresolved unsteadiness) with rotor passing whereas the ensemble averaged total temperature wake width changes with blade passing. The total temperature wake is widest at τ/T=0.75 and the thinnest at τ/T=0.25. However, the depth of the wake does not change with blade passing. The increase of the wake width on the pressure side of the stator is indicative of the rotor wake arrival at the measurement station. Since in the hub endwall region, there is entrainment of fluid from the suction side into the hub leakage flow due to the pressure gradient which exists from the pressure to suction side, there is no change in the wake width on the suction side.

At mid-span (53.36% span)(Figures 5.29 and 5.30), both pressure and temperature wakes show changes in wake width. In contrast to the situation at the hub, the wake depths do change with blade passing. The total temperature wake is quite jumbled up at this location so the interpretation is based on the total pressure data. The ensemble

averaged wake is widest at τ/T=0.35 and the thinnest at τ/T=0.75, whereas the unresolved unsteadiness distributions do not show too much of a change. It may be recalled here that at τ/T=0.35, the rotor wake was observed approaching the suction side of the stator.

The 81.89% spanwise location (Figures 5.31 and 5.32) is in the core of the casing vortex region. The width of the wake and its depth changes with rotor passage. The wake width is the largest at τ/T=0.85 and the smallest at τ/T=1.00 for the total pressure data. The corresponding times for the total temperature data are τ/T=0.75 and τ/T=0.50 respectively even though the change in wake width is not as pronounced as in the total pressure data. The wake depth change is not as high as in the midspan region for both the data sets. The unresolved unsteadiness distributions do not show a very pronounced change as the ensemble averaged data sets. Both the pressure and suction sides of the wake show widening at this spanwise location, compared with the hub and midspan locations where the widening is predominantly on the pressure side of the stator.

At the 90.44% spanwise location, bulk of the changes occur outside the wake. There is very little change in the wake depth and width with blade passing on the suction side of the wake in both the pressure and temperature data sets. On the pressure side of the wake, the total pressure wake is the widest at τ/T=0.85 and thinnest at τ/T=0.25. The corresponding times for the total temperature wake are τ/T=0.75 and τ/T=0.25. Once again the change in wake depth is not as pronounced as it is at midspan. These interaction times are for the ensemble averaged data and once again the unresolved unsteadiness distributions do not show significant changes in width and depth. The influence of the rotor wake passing is felt much more strongly outside the wake both on the suction and pressure surfaces and was explained in the previous section.

From the above discussion it can be concluded that the stator wake is adversely affected by the rotor wake passage. There is an almost periodic pulsing motion of the wake brought about by wake passing. This can be clearly seen in the video animation

However, this pulsing occurs at different times at various radial locations. This is most certainly due to differential wake decay and skewing of the rotor wake as it passes through the stator passage. The pulsing was the highest at around 81% span in the suction surface corner and the lowest near the hub. There is certainly an influence of the downstream rotor which would affect the stator wake behavior through the potential influence, though it is difficult to quantify. The maximum potential interaction is expected to occur near the hub due to much tighter axial spacing compared to the casing endwall. It is possible that this potential field acts to nullify the pulsing motion somewhat. The other reason for a lack of pulsing near the hub could be due to the transport of the rotor wake away from the stator wake region by the hub wall leakage flow.

5.2.3 Behavior of the hub endwall flow region

This region can be best explained using both the unresolved unsteadiness and the ensemble averaged distributions (Figures 5.27 and 5.28). Slightly higher levels of unsteadiness observed in between the stator blades very close to the hub is indicative of this region. At $\tau/T = 0.0$, the region is spread out almost across the entire passage and as the rotor moves across the stator blade, the clearance flow grows in size in the spanwise direction while shrinking in the circumferential direction and starts moving across the passage transporting some of the hub endwall boundary layer flow towards the pressure surface of the stator blade. This can be verified by the appearance of higher levels of unsteadiness on the pressure surface of the blade with the passage of time. This is a clear indication of the scraping of the hubwall boundary layer and a presence of scraping vortex (see section on time averaged results earlier in this chapter). The appearance of high unsteadiness on the pressure surface away from the hub substantiates this notion. And as the rotor blade continues further, the hub clearance region starts decreasing in size in the spanwise direction and starts spreading across the stator passage. The core of this

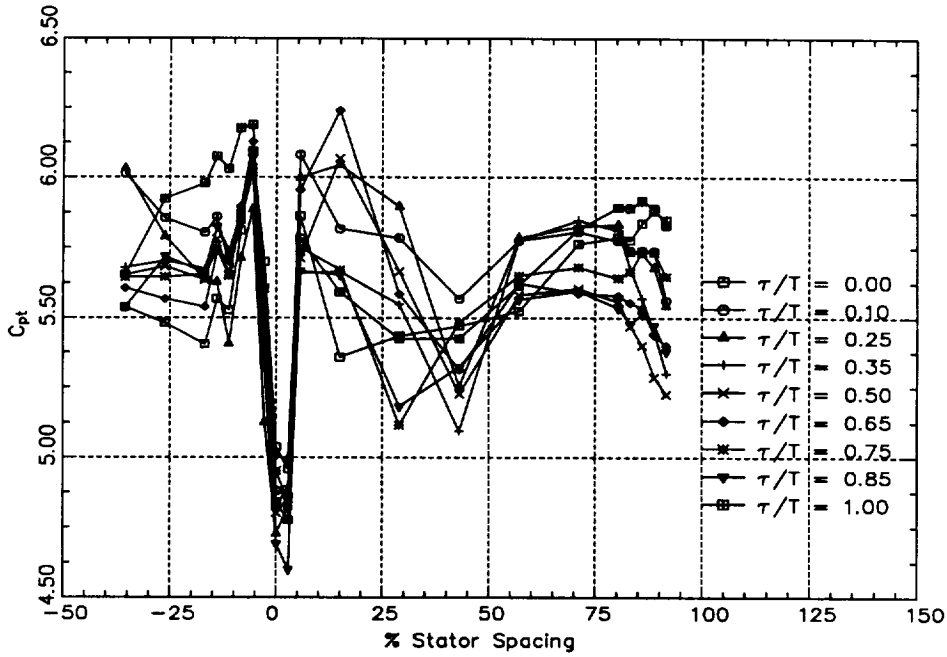

(a) Ensemble Average

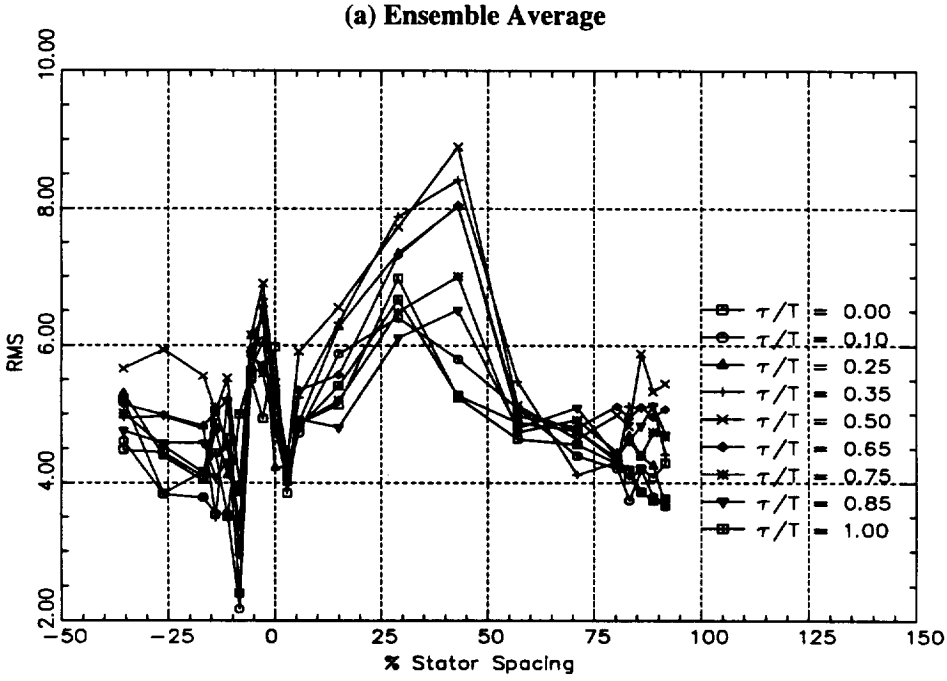

(b) Unresolved Unsteadiness (%)

Figure 5.27. Temporal Variation of Stator Exit Flow: Blade-to-blade Distribution of Total Pressure at 7.86% Span

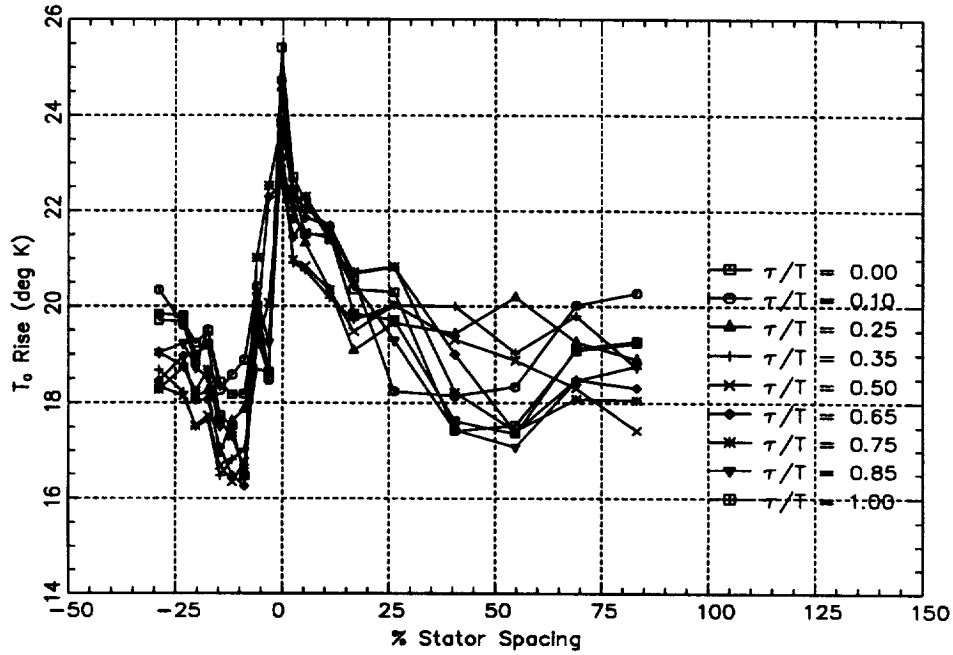

(a) Ensemble Average

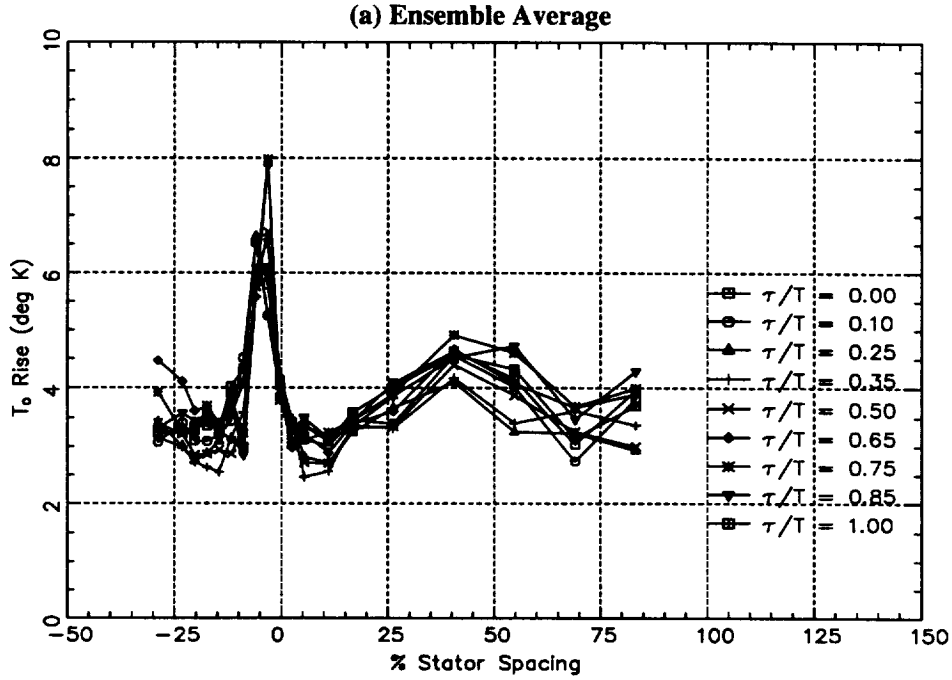

(b) Unresolved Unsteadiness (Deg K)

Figure 5.28. Temporal Variation of Stator Exit Flow: Blade-to-blade Distribution of Total Temperature at 7.86% Span

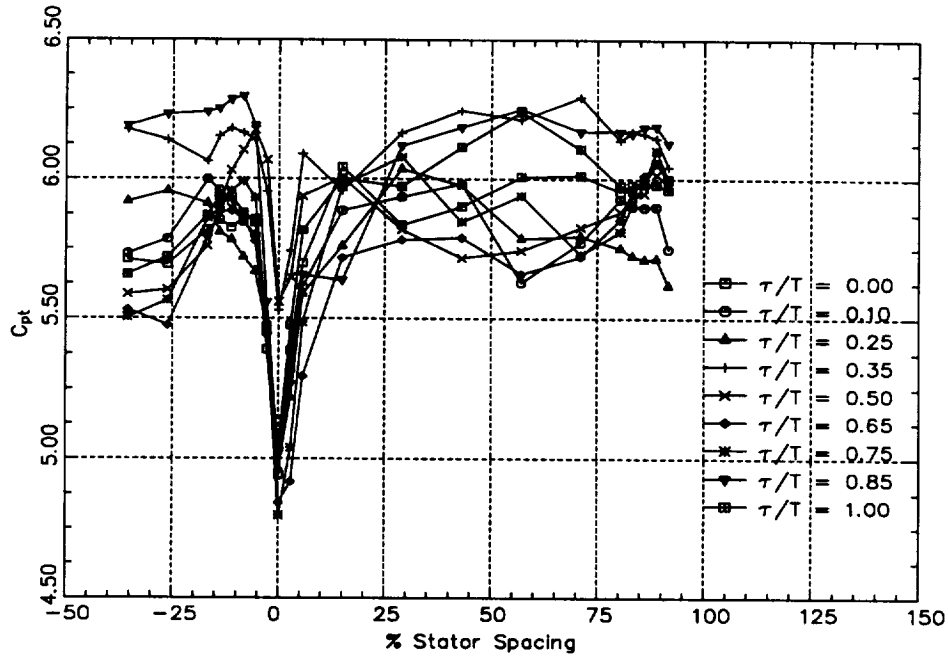

(a) Ensemble Average

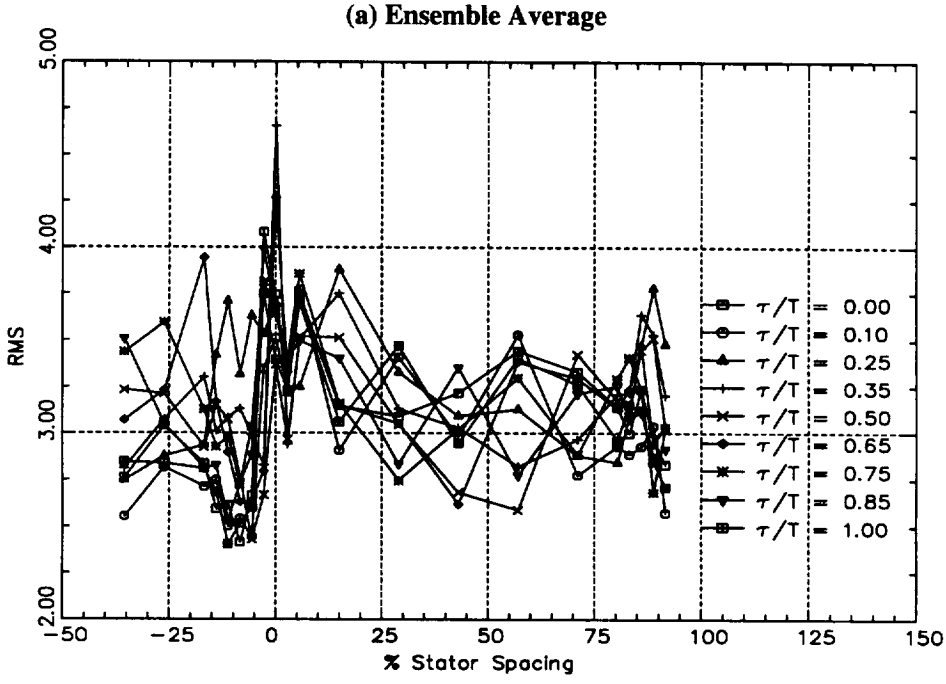

(b) Unresolved Unsteadiness (%)

Figure 5.29. Temporal Variation of Stator Exit Flow: Blade-to-blade Distribution of Total Pressure at 53.36% Span

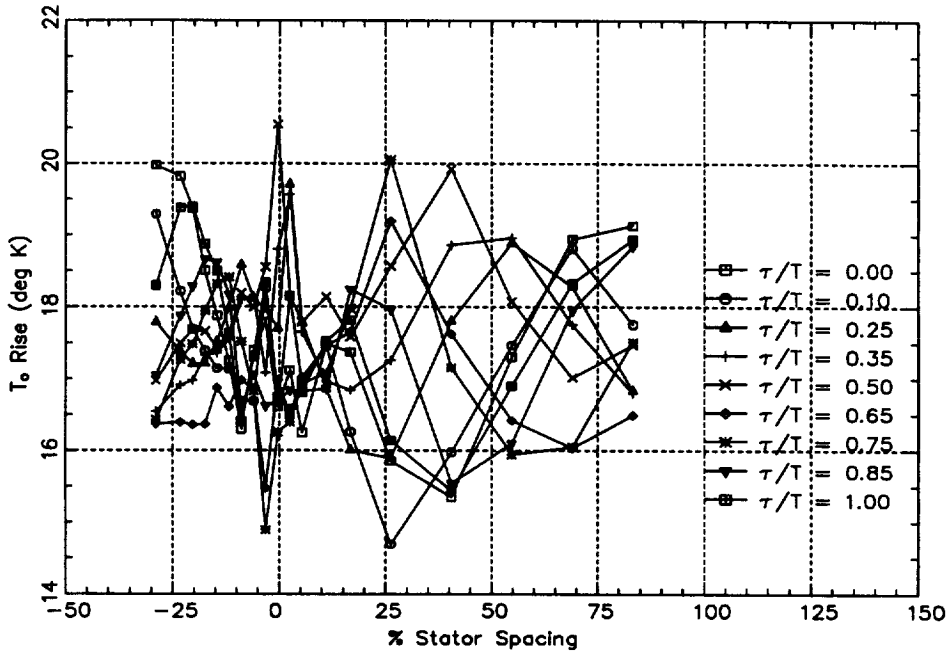

(a) Ensemble Average

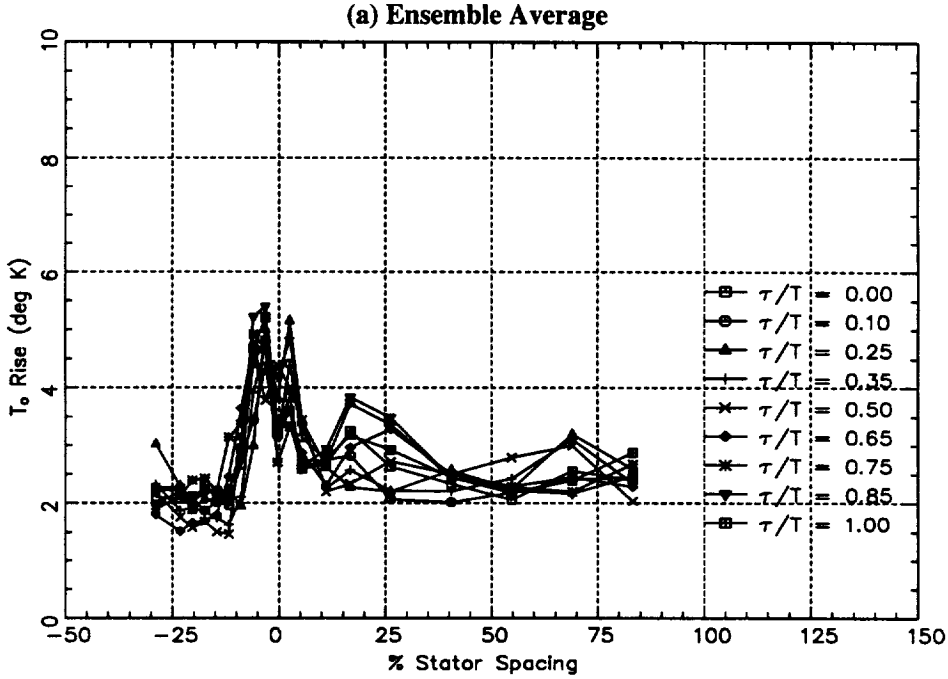

(b) Unresolved Unsteadiness (Deg K)

Figure 5.30. Temporal Variation of Stator Exit Flow: Blade-to-blade Distribution of Total Temperature at 53.36% Span

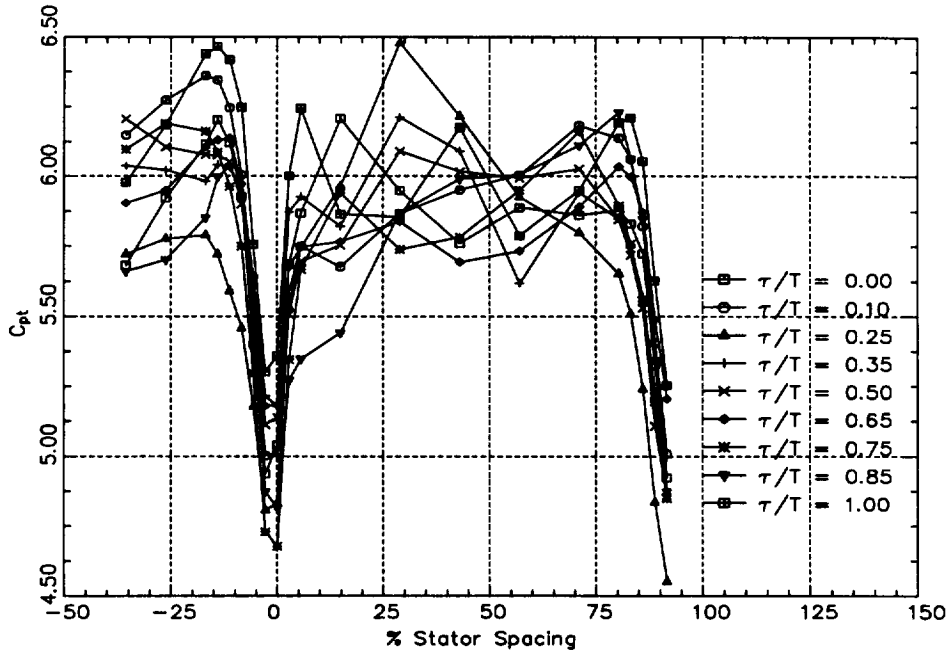

(a) Ensemble Average

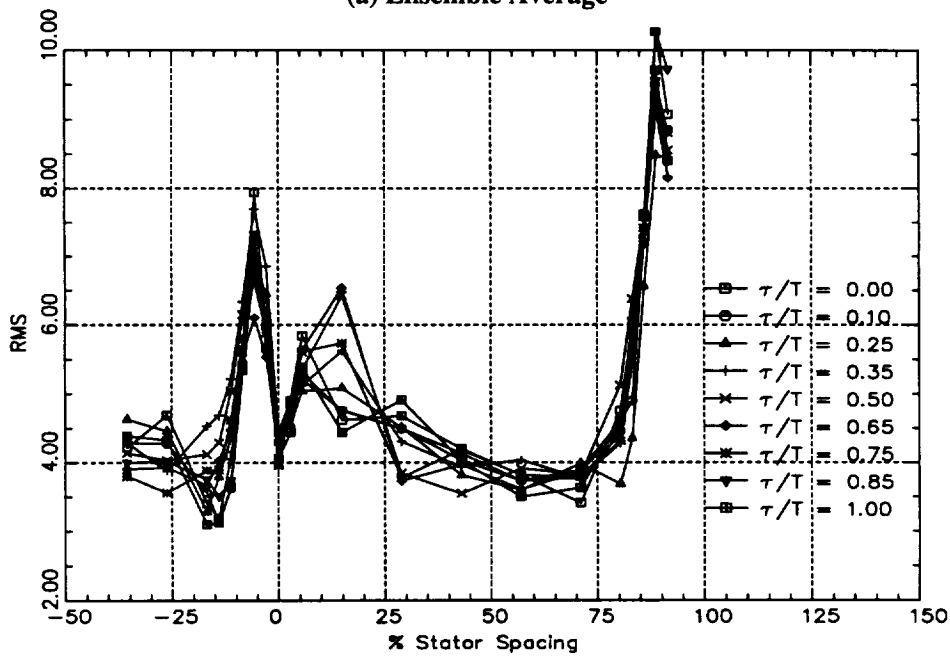

(b) Unresolved Unsteadiness (%)

Figure 5.31. Temporal Variation of Stator Exit Flow: Blade-to-blade Distribution of Total Pressure at 81.89% Span

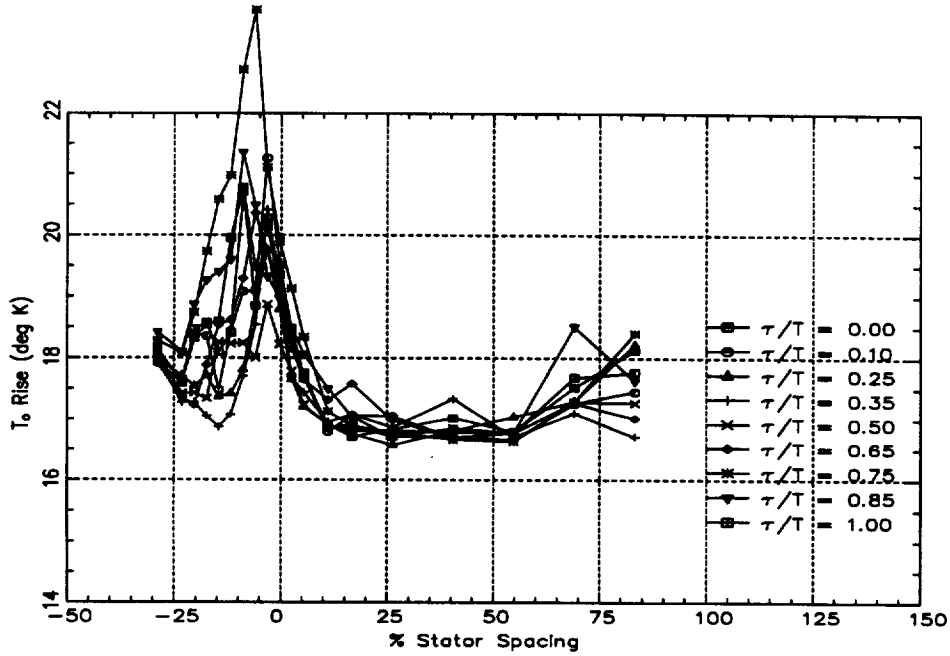

(a) Ensemble Average

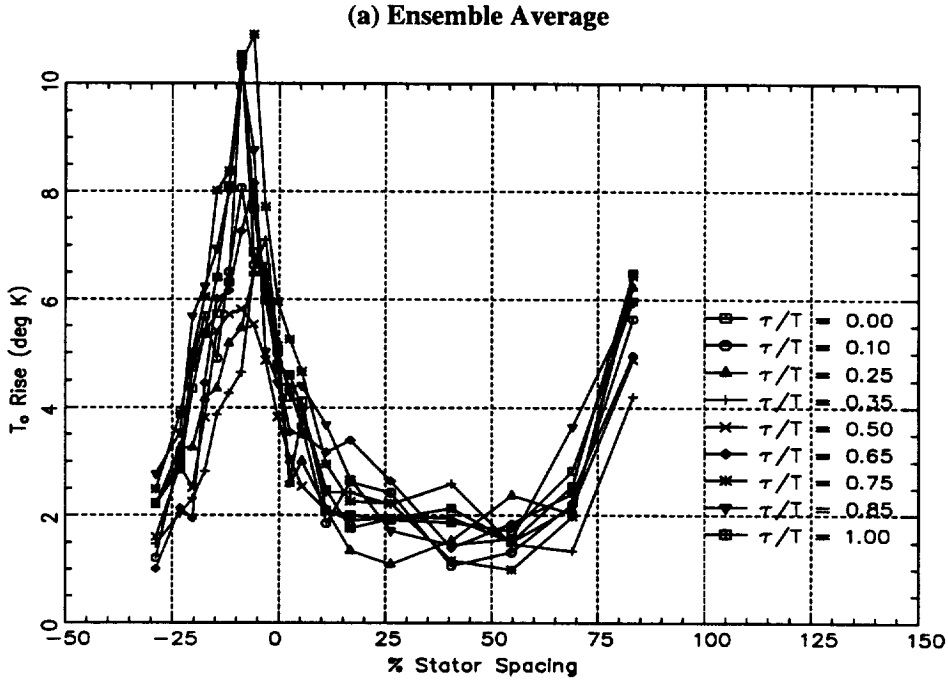

(b) Unresolved Unsteadiness (Deg K)

Figure 5.32. Temporal Variation of Stator Exit Flow: Blade-to-blade Distribution of Total Temperature at 81.89% Span

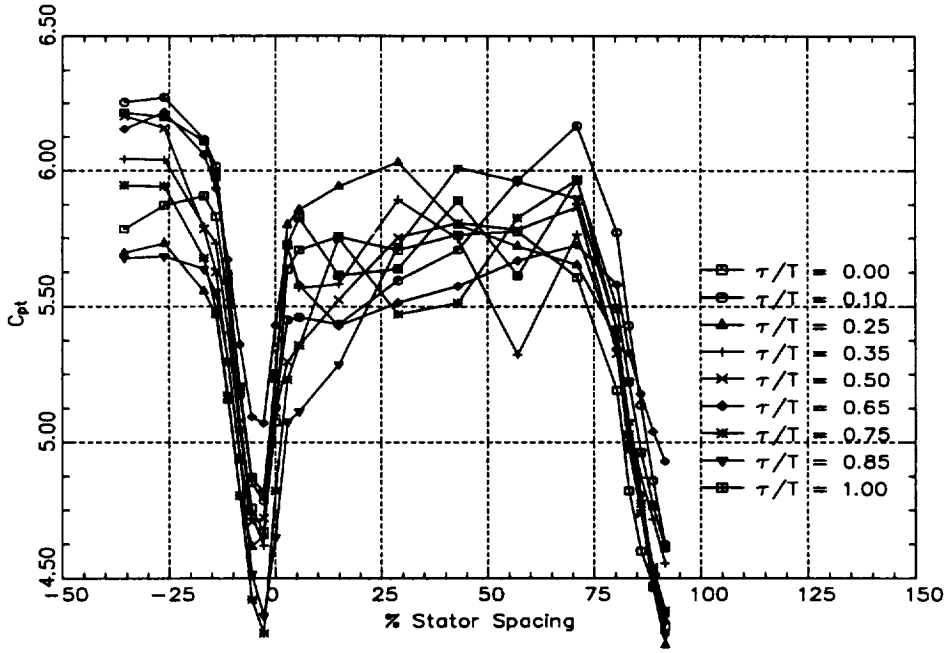

(a) Ensemble Average

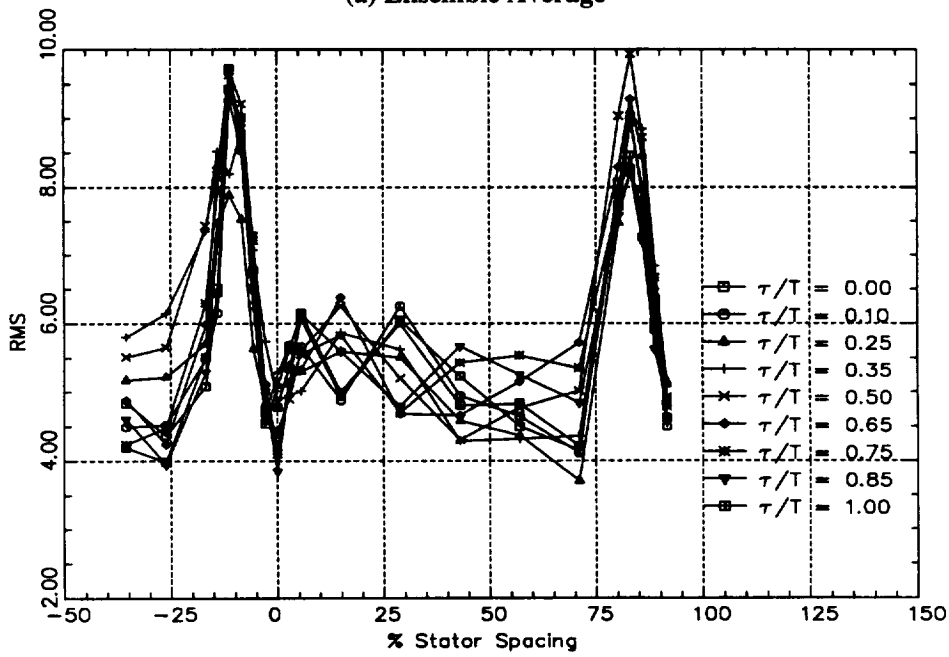

(b) Unresolved Unsteadiness (%)

Figure 5.33. Temporal Variation of Stator Exit Flow: Blade-to-blade Distribution of Total Pressure at 90.44% Span

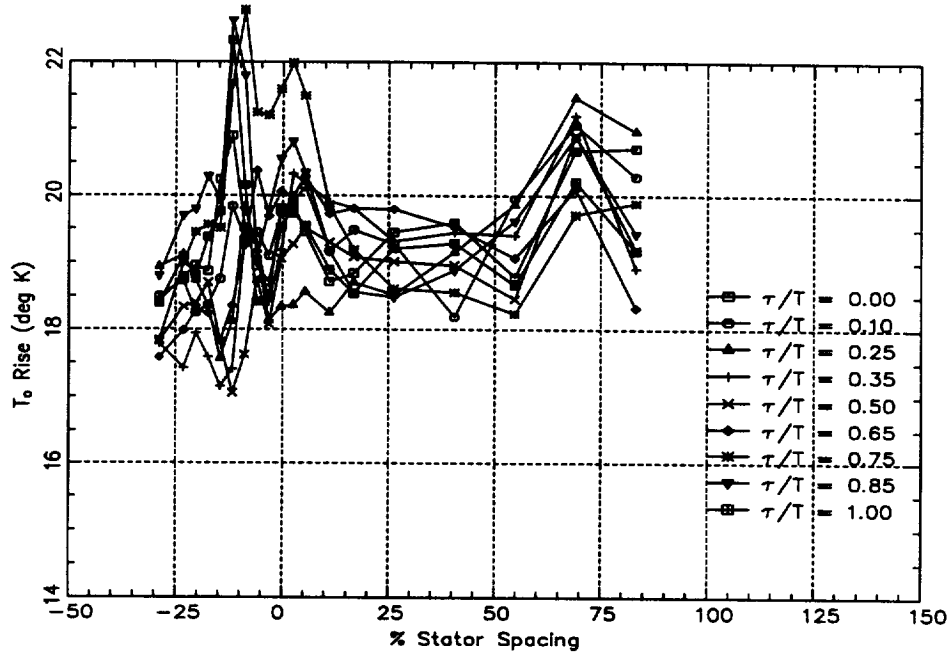

(a) Ensemble Average

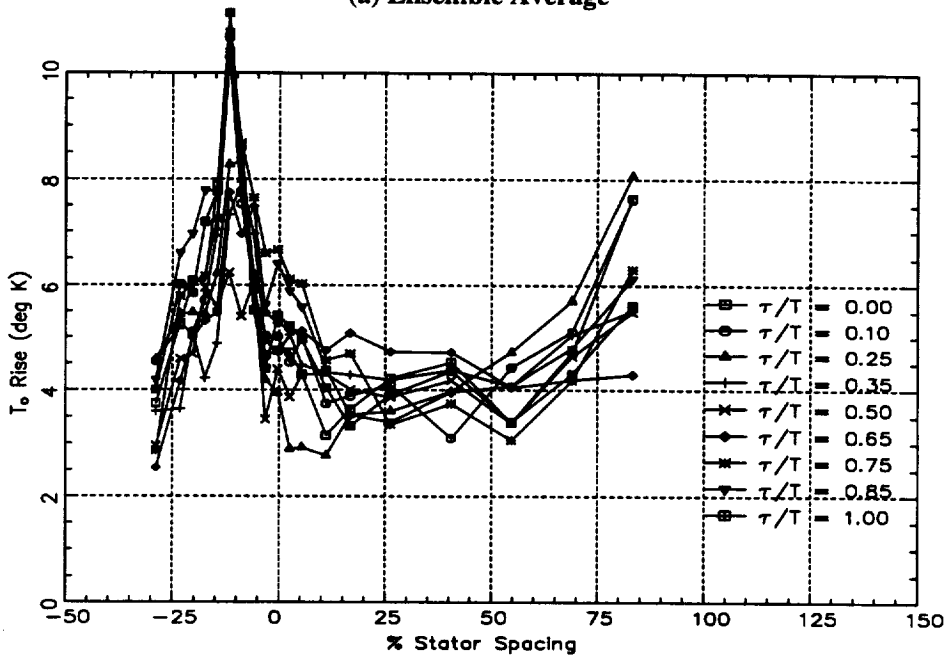

(b) Unresolved Unsteadiness (Deg K)

Figure 5.34. Temporal Variation of Stator Exit Flow: Blade-to-blade Distribution of Total Temperature at 90.44% Span

region remains approximately at the same position with respect to the stator pitch. From Figure 5.27, it is observed that the magnitude of the pressure at the core of the leakage flow is the lowest at τ/T=0.75 and highest at τ/T=0.25 and from the unsteadiness distribution, the corresponding values are 0.0 and 0.5 respectively. It was observed earlier that the wake showed very little effect of the rotor passing even though there appears to be a circumferential transport of the flow as seen from the animation. The rotor passing has indeed triggered this type of behavior and certainly needs to be modeled for accurate prediction of the stator exit flow fields in a multistage compressor.

5.2.4 Behavior of the casing endwall suction surface corner region

Like the wake region, this region also changes significantly with rotor passing. Reference is made to Figures 5.20- 5.26 and Figures 5.31 and 5.32 to explain this region very carefully. This region pulses (increases and decreases in size) as the rotor passes. Similar behavior was observed by Cherrett et al. (1994) in the hub corner flow region downstream of a stator of a single stage transonic fan. The region starts decreasing in size as the time increases from $\tau/T = 0.0$ and is the smallest at $\tau/T = 0.35$ and then starts increasing rapidly reaching a maximum at the $\tau/T = 0.85$. As time further increases, the region starts decreasing once again in size. This is true for both the ensemble average as well as the unresolved unsteadiness (both pressure and temperature). Cherrett et al. (1994) theorize that this is due to the rotor moving across the stator leading edge. The stator wake as was observed earlier was the thickest at τ/T = 0.85. As the corner flow region grows in size from τ/T = 0.35 to 0.85, the region is no longer confined to the suction surface region. It slowly spreads to the pressure surface and at the maximum interaction time, the region is almost the same size on either of side of the stator blade. It is also interesting to see that the corner region is observed to be "feeding" the flow in the casing region away from the endwalls as the blade passes by. This is observed very clearly

in the unresolved unsteadiness distribution but not so clearly in the ensemble averaged plots. This was a region of intense secondary flow activity as seen in the time averaged flow field features seen earlier. So there is radial and circumferential transportation from both secondary flow as well as rotor wake related unsteadiness.

5.2.5 Behavior of the casing endwall region away from the blade surfaces

The flow in this region is best explained by the use of both the ensemble and unresolved unsteadiness plots. The ensemble average values in the casing wall region, away from the suction surface corner vary significantly. This is caused by rotor leakage flow and endwall flow interacting with the stator flow.The upstream rotor clearance flow (low pressures and higher levels of unsteadiness away from the corner regions) seems to have been smeared across the stator passage. As time progresses from 0.0, the high unsteadiness in the midpitch region (unresolved unsteadiness in total pressure), starts reducing in size circumferentially and very slightly increasing in size in the spanwise direction until time reaches $\tau/T = 0.40$. Afterwards, the region starts spreading in size in the circumferential direction as time approaches $\tau/T = 0.85$. At this time it is almost spread across the passage with feeding into this flow from the suction surface casing corner region as well. As already observed, the rotor wakes do have different wake widths and depths not only in the same revolution, but also in successive revolutions. Coupled to the fact that the wake location in the stator passage oscillates with time, tends to give the impression of smearing. As observed in the unresolved unsteadiness plots, as the rotor passes by, the clearance flow seems to be transported to the pressure surface of the stator. This shows that the rotor clearance flow is being transported through the stator passage and being deposited on the pressure surface of the stator as well.

5.3 Rotor 2 Exit Field

In this section, the rotor 2 field at the exit of the stator at three locations (suction surface, pressure surface and midpitch) are analyzed and discussed. The ensemble averaged and unresolved unsteadiness data acquired at these locations from the area traverse is used to interpret this flow field. A complete revolution plot (72 blade passages) of ensemble averaged and unresolved unsteadiness in total pressure data at midpitch shown in Figure 5.35, reveals a typical 2 nodes per revolution pattern consistent with the difference in blade count between rotors 2 and 1 and 3 and 2. This 2 nodes per revolution pattern is identified by the symmetry of the flow field across any sectional plane. This is a due to a combination of the viscous interaction between rotors 1 and 2 and the potential interaction between rotors 2 and 3. This pattern in seen in both the deterministic and unresolved pressure distributions. The effect of the viscous interaction can be removed by decomposing the ensemble average into components and subtracting the revolution aperiodic unsteadiness. However, the effect of the potential interaction which is not small due to the proximity of the rotor 3 blade to the measurement location and the small axial gaps between stages cannot be eliminated by averaging. The only possible method of eliminating this is by acquiring data triggered to the rotor 3 shaft frequency. So at this time no remarks can be made on the strength of the potential interaction compared with the viscous interaction and will not be discussed further. This twice per revolution nodal distribution is found at the other locations as well, even though the intensity are much higher at the suction surface locations near the hub and casing endwalls compared with the pressure surface and midpitch locations. On the suction side of the stator, the levels of revolution aperiodic unsteadiness were quite high compared to the other locations. This is further evidence to show that the revolution aperiodic unsteadiness levels reflect the amount of rotor-rotor interaction downstream of stator 2.

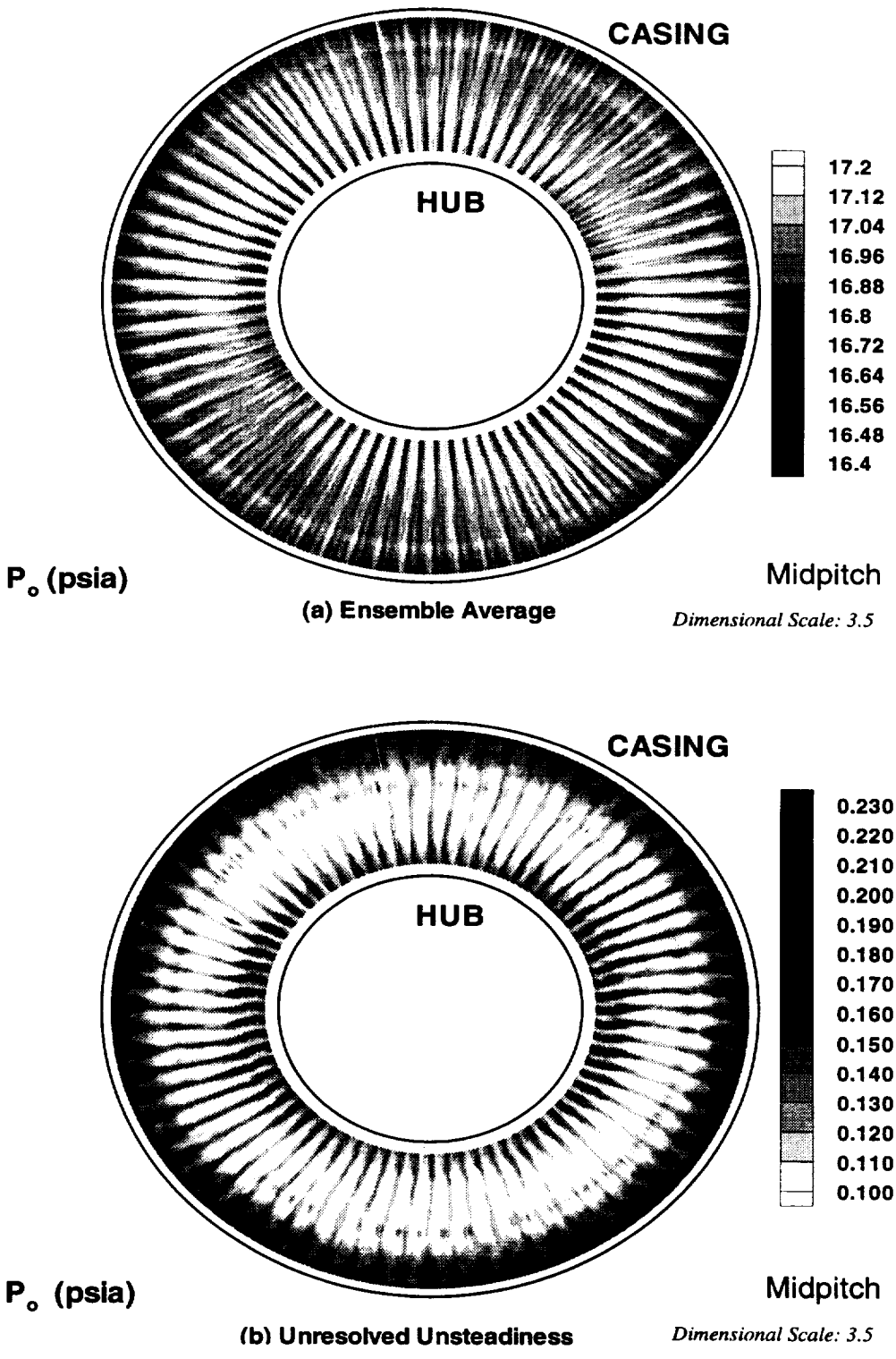

Figure 5.35. Rotor 2 Exit Flow at Midpitch: Complete Revolution Plot - Ensemble averaged and Unresolved Distribution of Total Pressure

Contour plots of the ensemble averaged and unresolved unsteadiness in total temperature and total pressure is shown in Figures 5.36(a) - (d), 5.38(a) - (d) and 5.40(a) - (d) for the midpitch, suction surface and pressure surface respectively. Six blade passages are shown in each plot and the same blade passages are shown in all the plots. The blade periodic components of total pressure and total temperature are plotted in Figures 5.37, 5.39 and 5.40 for the midpitch, suction surface and pressure surface respectively. For each of these plots, the rotor wake location is identified by the higher total temperature and pressure as well as by the higher unresolved unsteadiness. There is a phase shift between the pressure and temperature wakes. The time lag between the total pressure and total temperature data is probably due to the differential wake decay rates of the total temperature and total pressure wakes and the convection rates inside the stator passage.

5.3.1 Mid-Pitch Location

The ensemble averaged results shown in Figure 5.36 indicate that both total temperature and total pressure wakes are present at this axial location. At midpitch the interaction of the rotor 2 wake with the stator is minimal. Consequently a very clear wake is observed all the way from hub to tip and is not very distorted except near the casing endwall. The flow is also fairly periodic from blade to blade. This can be observed by comparing the ensemble averaged values with the respective blade periodic values shown in Figure 5.37. Much larger core regions (low total pressure, low total temperature and low unsteadiness) are seen in the unresolved data than in the ensemble averaged distributions. Near the hub endwall, there is a region of very high pressure and very low total temperature. The extent of this region varies both circumferentially and radially in the total pressure data compared with the total temperature data. This is further clarified by the averaged out pattern seen in the blade periodic pressure data compared with the blade periodic total temperatures. This is probably due to the upstream rotor hub flow corner region interaction which has

higher pressures and low temperatures. Detailed velocity measurements may shed some light on this matter. The wakes are the thickest (as evidenced by the ensemble averaged data) at approximately 25% span from the hub, possibly due to radial inward transport of the rotor wake by the stator flow field due to imbalance between the centrifugal forces and the pressure gradient as well as radial outward flow generated by the rotation of the hub. An interesting phenomena is that the total temperature wake in the casing endwall region is almost non existent. This could be due to the rapid decay of the total temperature and its mixing with the flow field. The results of this mixing is seen in the relative higher levels of the unresolved unsteadiness in total temperature in the casing region compared with the pressure distribution. This could also be due to an ensemble averaging problem with the total temperature rotor wakes not being periodic in this region. The rotor wake width is lowest in the tip, increasing to very high values near the hub. The rotor wake is distorted as it passes through the stator passage due to differing convection velocity. Higher levels of unresolved unsteadiness in the casing endwall region is probably a manifestation of the rotor clearance flow. These are seen on the suction side of the rotor wake only in the total pressure distribution and they seem to be smeared out in the total temperature distribution. Coupled with the fact that low total pressure are seen on the suction side of the rotor wake in the casing endwall region, this tends to indicate that this low pressure-high unsteadiness region is the rotor clearance flow. This low pressure region in seen quite clearly in the blade periodic distribution on the suction side of the rotor wake. This indicates that mixing of the clearance flow has not yet taken place and will be a factor in the incidence distribution to the downstream rotor stage. The unsteadiness associated with the clearance flow is the dominant one at this location and needs to be taken into account during design and analysis. On the suction side of the rotor wake near the hub, low pressures are seen both in the ensemble average and blade periodic data. This is probably due to possible separation of flow on the rotor hub on the suction side. However, the CFD simulation

does not show any such separation. However, the unsteadiness associated with this low pressure region is smaller than that associated with the clearance flow region.

5.3.2 Suction Surface Location

At the suction surface location (Figure 5.38), the wakes are much more distorted than that at the midpitch location. The wake regions shows a distinctive double leg from hub to about 65% span. This is due to the chopping of the rotor wake by the stator blade surface. This is seen quite clearly in the pressure distribution compared with the temperature distribution. The ensemble averaged distribution shows a clearer wake as opposed to the unresolved unsteadiness. Also in the casing endwall region, the suction surface corner flow has either decayed out or smeared out the rotor wake almost completely leaving a band of low levels in the ensemble averaged pressure. From the ensemble averaged temperatures, spots of high temperature are found in this banded region near the casing endwall region. Even though the wakes are distorted fairly good periodicity of flow exists as can be observed by comparing Figures 5.38 and 5.39. The measurement location passes through the suction surface casing corner region, which was observed earlier to have the highest levels of mixing as evidenced by high levels of unresolved unsteadiness as well as large secondary flow features. It is this mixing that has probably decayed the rotor wake considerably. The wakes are thicker at this location than that at the midpitch location and the core regions of the rotor exit flow (represented by low temperatures, low pressures and low levels of unresolved unsteadiness) are very thin. Higher levels of unsteadiness are observed quite close to the hub both in the pressure and temperature. This is due to interaction of the rotor wake flow and the hub endwall fluid that is being transported away from the suction surface of the stator. Just as in the midpitch location, the dominant unsteadiness is in the casing endwall region associated partly with the mixing of the rotor clearance flow and partly with the suction surface casing endwall corner region.

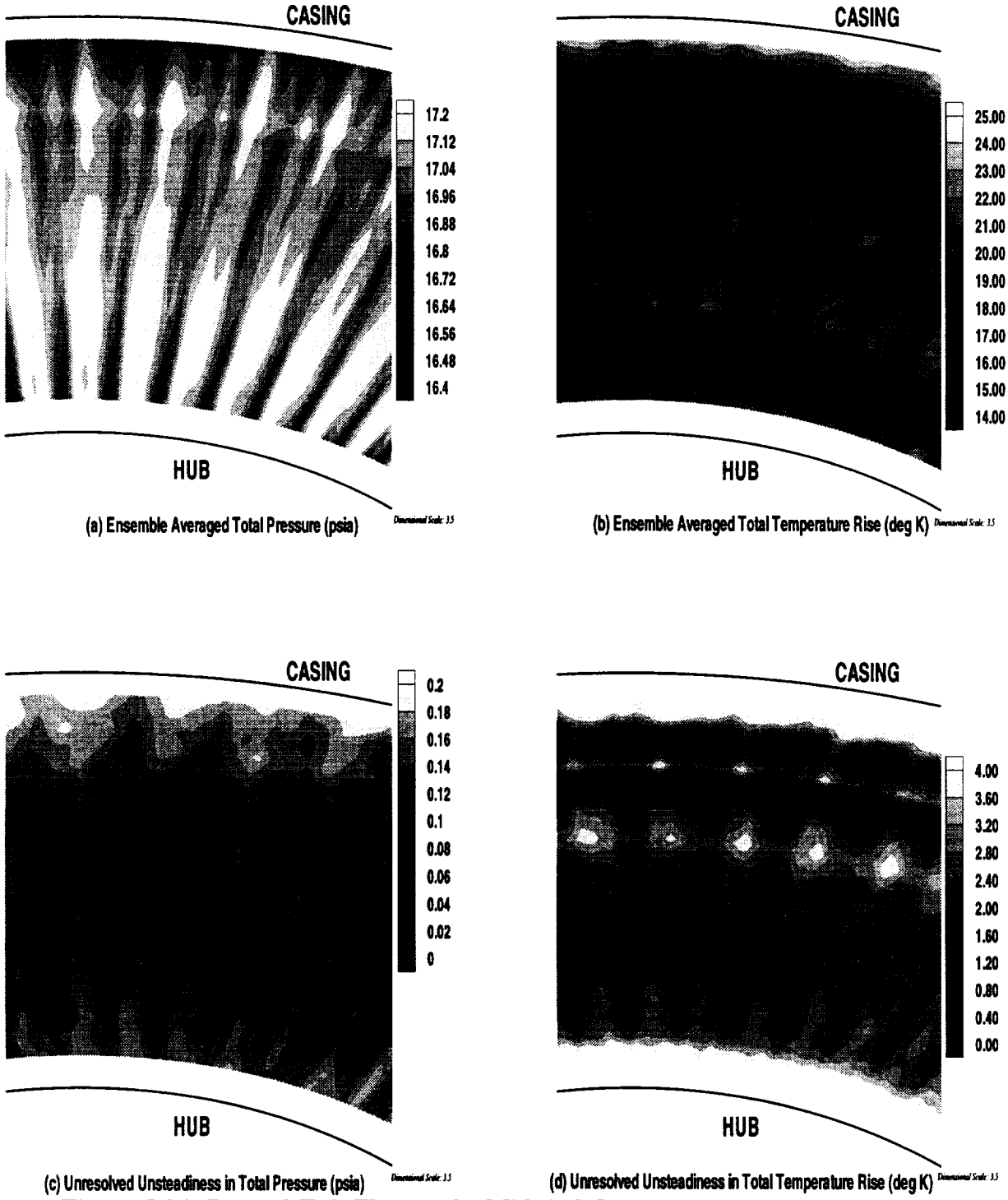

Figure 5.36. Rotor 2 Exit Flow at the Midpitch Location: - Ensemble averaged and Unresolved Distribution of Total Pressure and Total Temperature

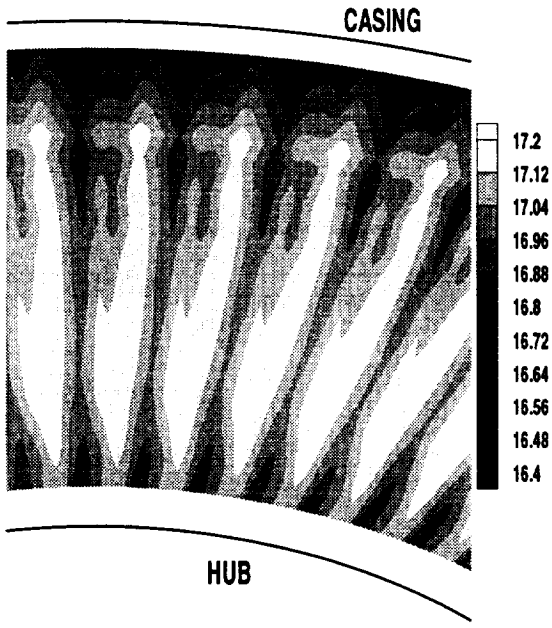

(a) Blade Periodic Total Pressure (psia)

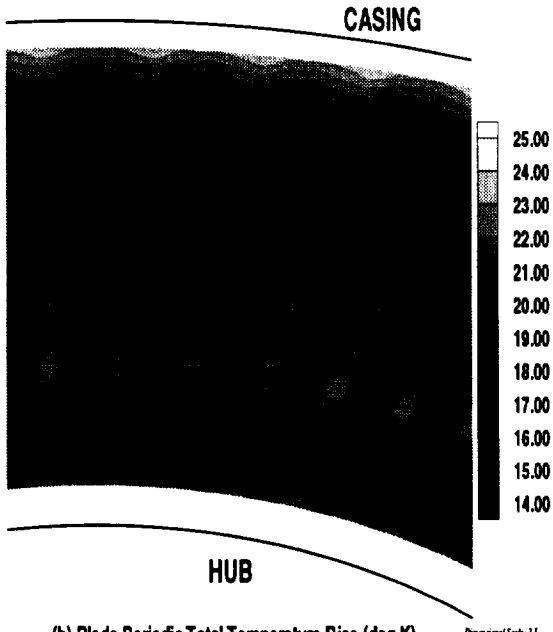

(b) Blade Periodic Total Temperature Rise (deg K)

Figure 5.37. Rotor 2 Exit Flow at the Midpitch Location: - Blade Periodic Distribution of Total Pressure and Total Temperature

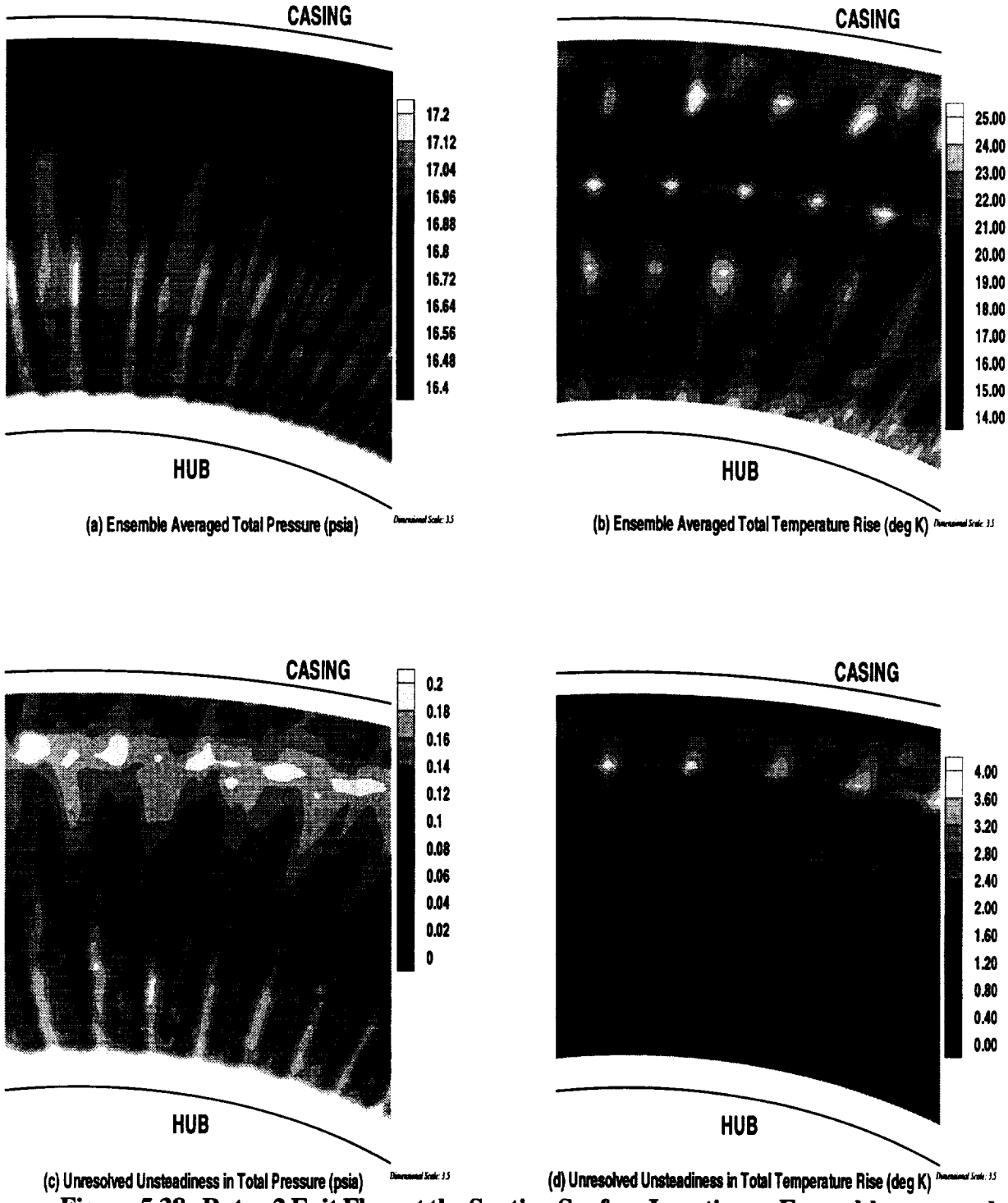

Figure 5.38. Rotor 2 Exit Flow at the Suction Surface Location: - Ensemble averaged and Unresolved Distribution of Total Pressure and Total Temperature

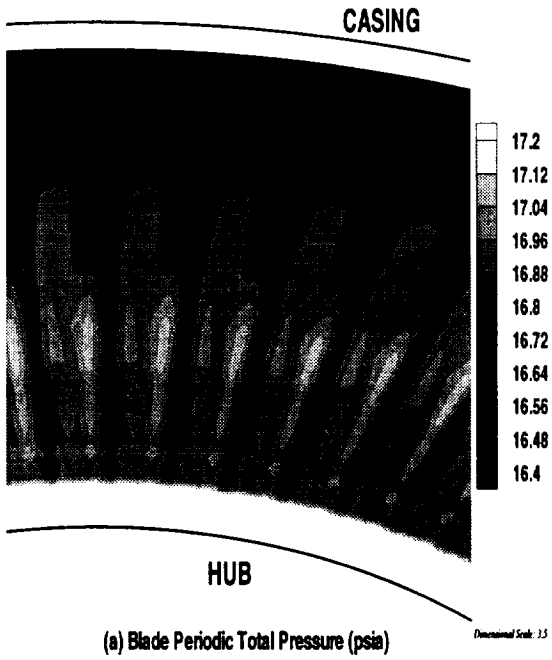

(a) Blade Periodic Total Pressure (psia)

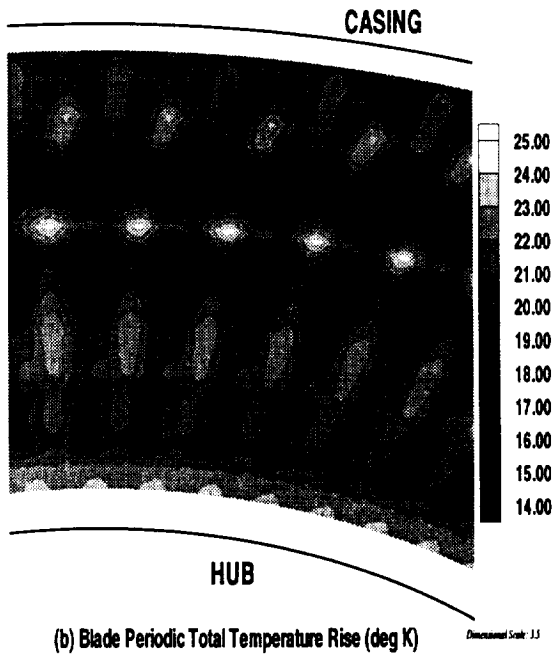

(b) Blade Periodic Total Temperature Rise (deg K)

Figure 5.39. Rotor 2 Exit Flow at the Suction Surface Location: - Blade Periodic Distribution of Total Pressure and Total Temperature

5.3.3 Pressure Surface Location

At the pressure surface location (Figure 5.40) too the wakes are highly distorted from hub to tip. A double leg wake is observed at this location too, unlike the one on the suction surface, the smearing out of the flow occurs close to the hub endwall in this case. This double leg is certainly due to the chopping of the wake by the stator blade. Due to different convection velocities that exist on the suction and pressure surfaces of the stator blades as well as the different lengths the rotor flow has to pass to get to the measurement location, the decay rates of the rotor flow are different on either sides of the stator blade. And this is very clearly observed in the midspan region from Figures 5.38 and 5.40 respectively where the wake on the pressure side is much more deeper than the one on the suction surface. From hub to about 30% span, very low pressures and temperatures and higher levels of unsteadiness are observed with very little evidence of any wakes or core flow distinction. This pitchwise location passes through the region where there is accumulation of stator hub leakage flow as observed in both the time averaged and the temporal variation of stator exit flow. This is a region of intense mixing and this seems to have decayed out the rotor wake considerably. The thickness of the wakes in the mid-span region is the highest at the pressure surface location and the thinnest at midpitch. The highest levels of unsteadiness in pressure occur in the casing, whereas the highest levels of unsteadiness in temperature occur in the rotor wakes and in casing endwall region. All this points to an increase in the overall unsteadiness level on the pressure side of the stator brought about by transport of the rotor exit flow. From the above discussion, it is quite clear that future analysis and prediction methods should take into account the clocking of the stator with the downstream rotor for achieving accurate results.

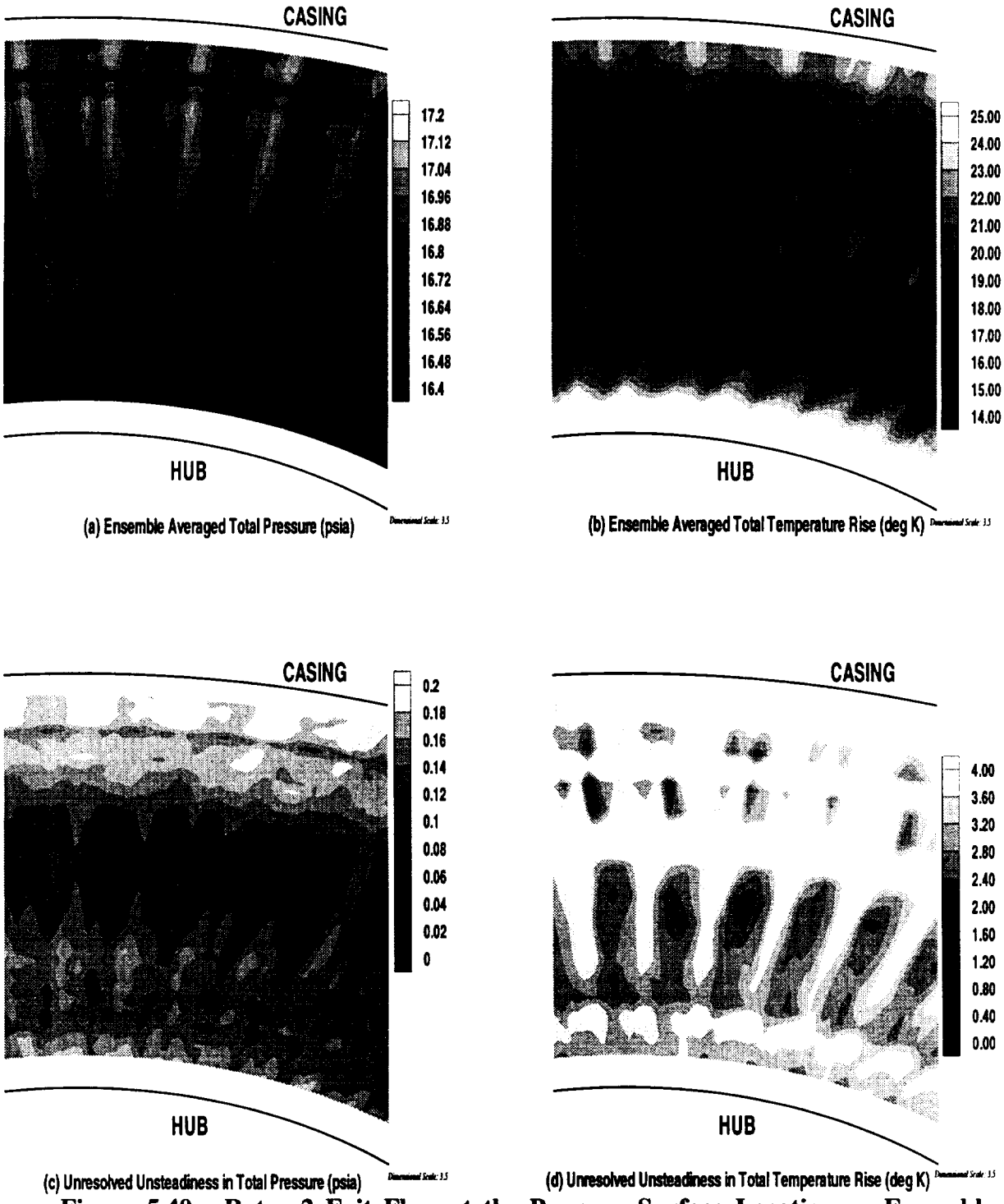

Figure 5.40. Rotor 2 Exit Flow at the Pressure Surface Location: - Ensemble averaged and Unresolved Distribution of Total Pressure and Total Temperature

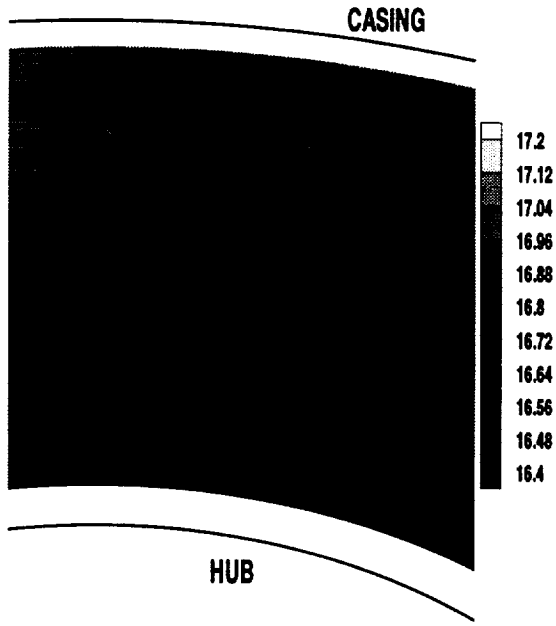

(a) Blade Periodic Total Pressure (psia)

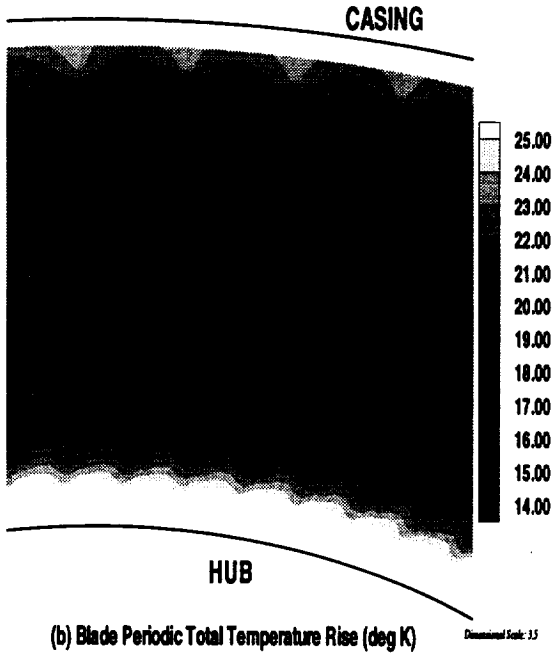

(b) Blade Periodic Total Temperature Rise (deg K)

Figure 5.41. Rotor 2 Exit Flow at the Pressure Surface Location: - Blade Periodic Distribution of Total Pressure and Total Temperature

5.4 Composite Flow Field at Mid-Span, Mid-Pitch

An attempt was made to evaluate the composite rotor exit flow field downstream of stator 2 at the mid-pitch location by correlating the total temperature rise distribution with the total pressure data acquired using the kulite probe and the unsteady velocity distributions acquired using the slanted hot-film probe with four rotations. Only ensemble averaged quantities can be compared since they are rotor locked. Blade-to-blade distributions of ensemble averaged total pressure, total temperature rise and the three velocity components at various radii (near hub, midspan, 81.89% span and near casing endwall) are shown in Figures 5.42 through 5.45 for the midpitch location. Also shown on these plots are the ensemble averaged RMS unresolved unsteadiness in total pressure and total temperature rise and the unresolved unsteadiness (RMS V_{eff1}) derived from one position of the slanted hot-film measurement. Six blade passages of an ensemble averaged revolution are shown for the ensemble average and unresolved unsteadiness distribution in each of these plots.

For the rotor exit flow in the absolute frame of reference, the rotor wake is characterized as the region which has lower axial velocity, higher absolute tangential velocity and higher radial velocity. Depending upon the velocity triangles, the total pressure and total temperature could be higher or lower in the wake. At this location the velocity triangles indicate that the total pressure and total temperature should be higher in the wake. Since the data is acquired with respect to the trigger on the compressor shaft, it is expected that the ensemble average does indeed show the same wake location. There seem to be small discrepancies in the location of the wake (within 5% of the blade passage) between the velocity, pressure and temperature data. This seems acceptable considering the data has been acquired at different times and the pitchwise resolution of each of these probes is different (hot-film has the best resolution whereas the kulite has the worst). The axial

location of measurement is 130% chord downstream of the rotor. Hence, it is reasonable to expect that the rotor wake has decayed and widened considerably. Larger inter passage oscillations are found in the total pressure data than in the either the velocity or temperature data sets. This is possibly due to a much higher frequency response of the kulite probe compared with the aspirating and hot-film probes and differing measuring techniques.

Rotor wakes are clearly seen from hub to about midspan locations. At the 81.89% and 90.44% span locations, the wakes are quite distorted. All components of the rotor wake (low axial velocity, high tangential velocity, high temperatures and pressures) are seen at hub and midspan locations, but in the casing endwall locations the flow picture is quite distorted. Similar wake widths are observed in all three measurements (temperature, velocity and pressure) in both the hub endwall and midspan region. The velocity wake defects indicate almost 20% defect in the axial velocity at midspan, midpitch. This is much higher than that observed in single stage compressor data (Prato and Lakshminarayana, 1993). This is probably due to slower wake decay rates observed in adverse pressure gradients (Hill et al. (1963)). Very similar features are observed in all the data sets with respect to the wake widths and shapes. This indicates that the velocity and temperature data can be correlated to derive the various terms of the average passage equation system. In the casing endwall region (81 and 90% span) low total pressure, low axial velocity and high tangential velocity regions are seen indicating some sort of a leakage flow structure. This is more clearly seen in the 81% spanwise location than at 90.44% span. The unresolved unsteadiness in both total pressure and temperature show two peaks in each blade passage consistent with appearance of another structure of high unsteadiness which is most probably the rotor tip leakage vortex. However, it is expected that the leakage vortex would have decayed under the influence of very high levels of freestream turbulence but it does not seem to be the case. Further detailed measurements using casing static kulite measurements are probably needed to quantify this feature.

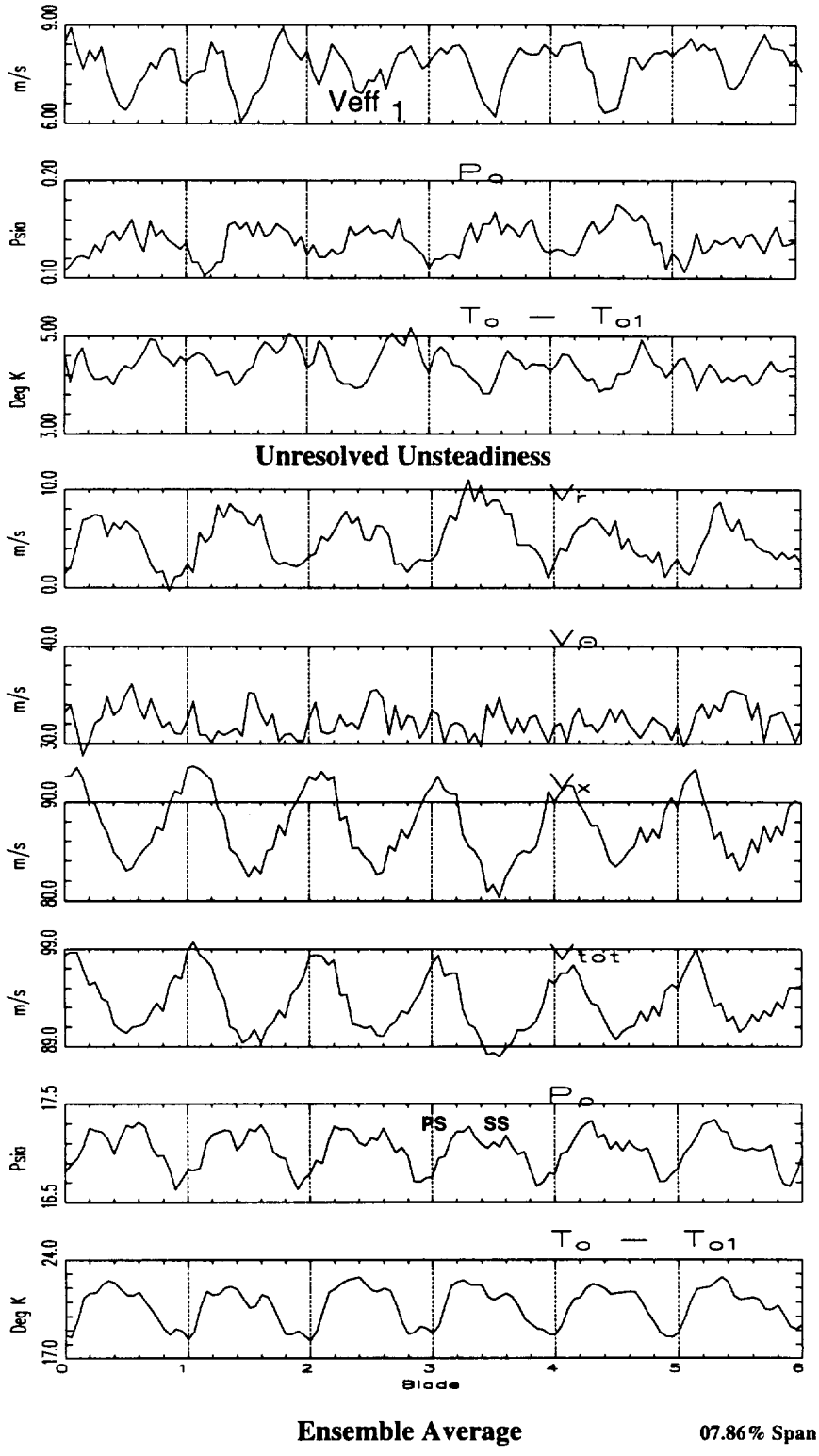

Figure 5.42. Blade-to-blade Distribution of the Composite flow field: Mid-pitch, 07.86% Span

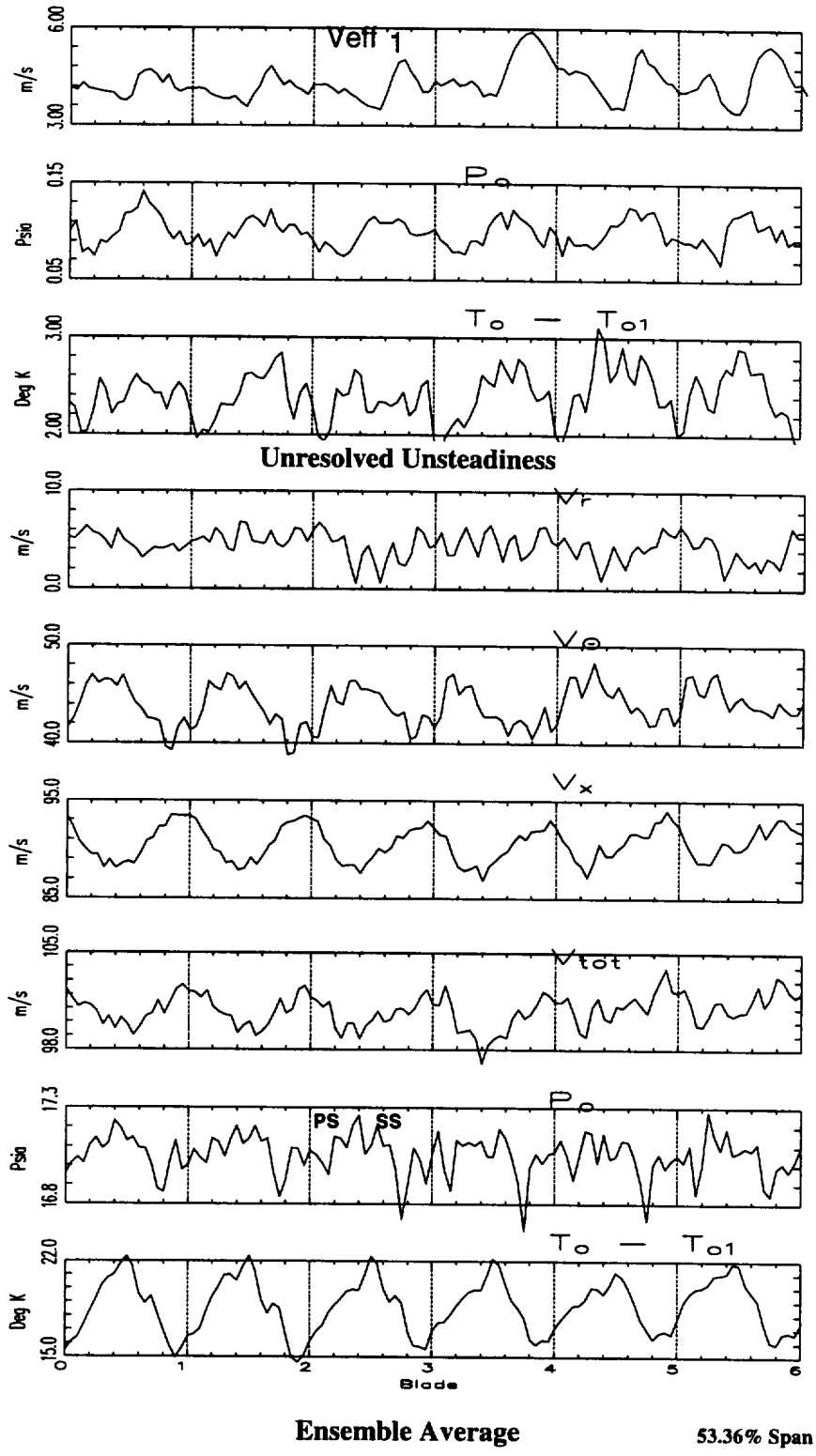

Figure 5.43. Blade-to-blade Distribution of the Composite flow field: Mid-pitch, 53.36% Span

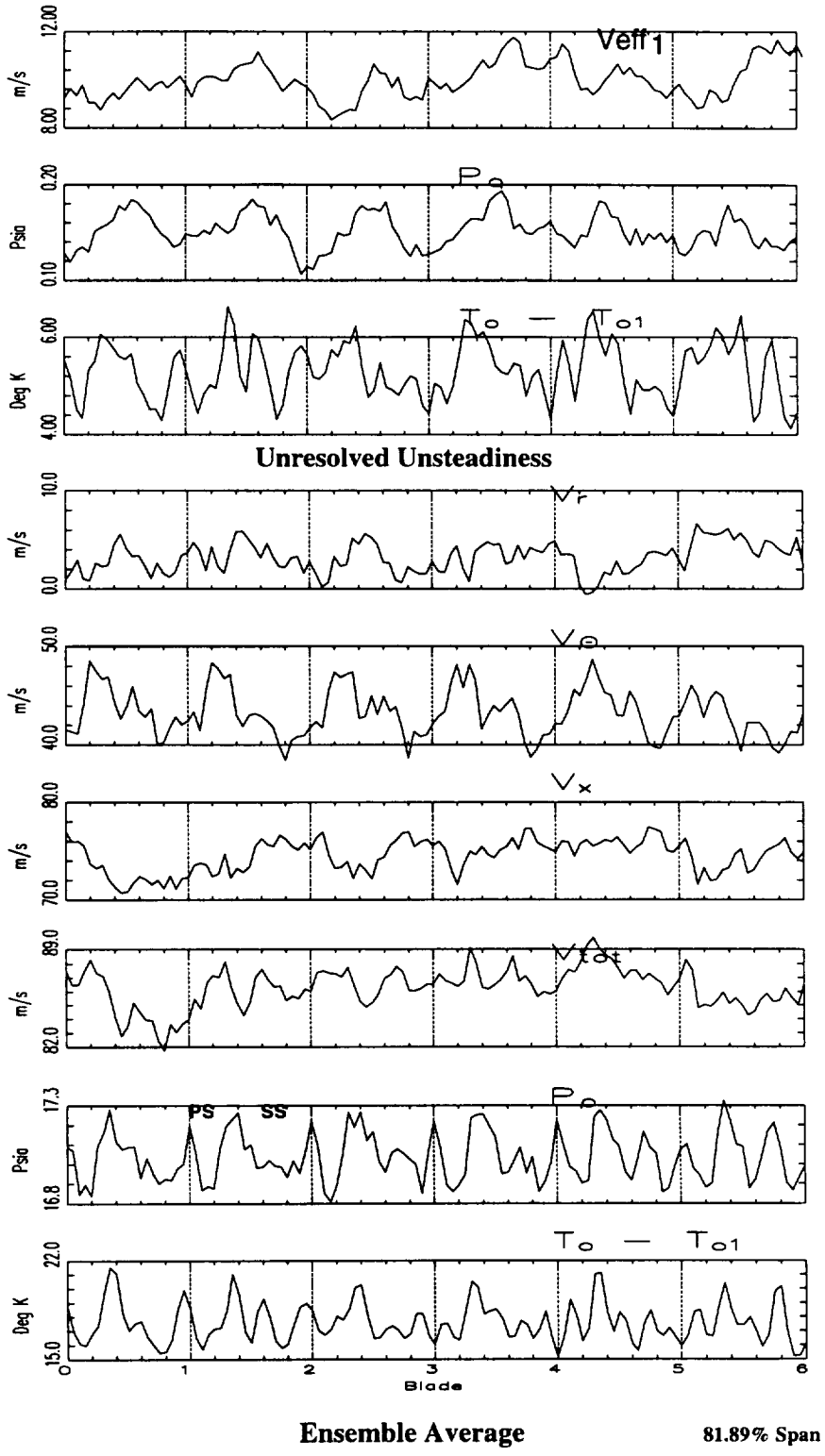

Figure 5.44. Blade-to-blade Distribution of the Composite flow field: Mid-pitch, 81.89% Span

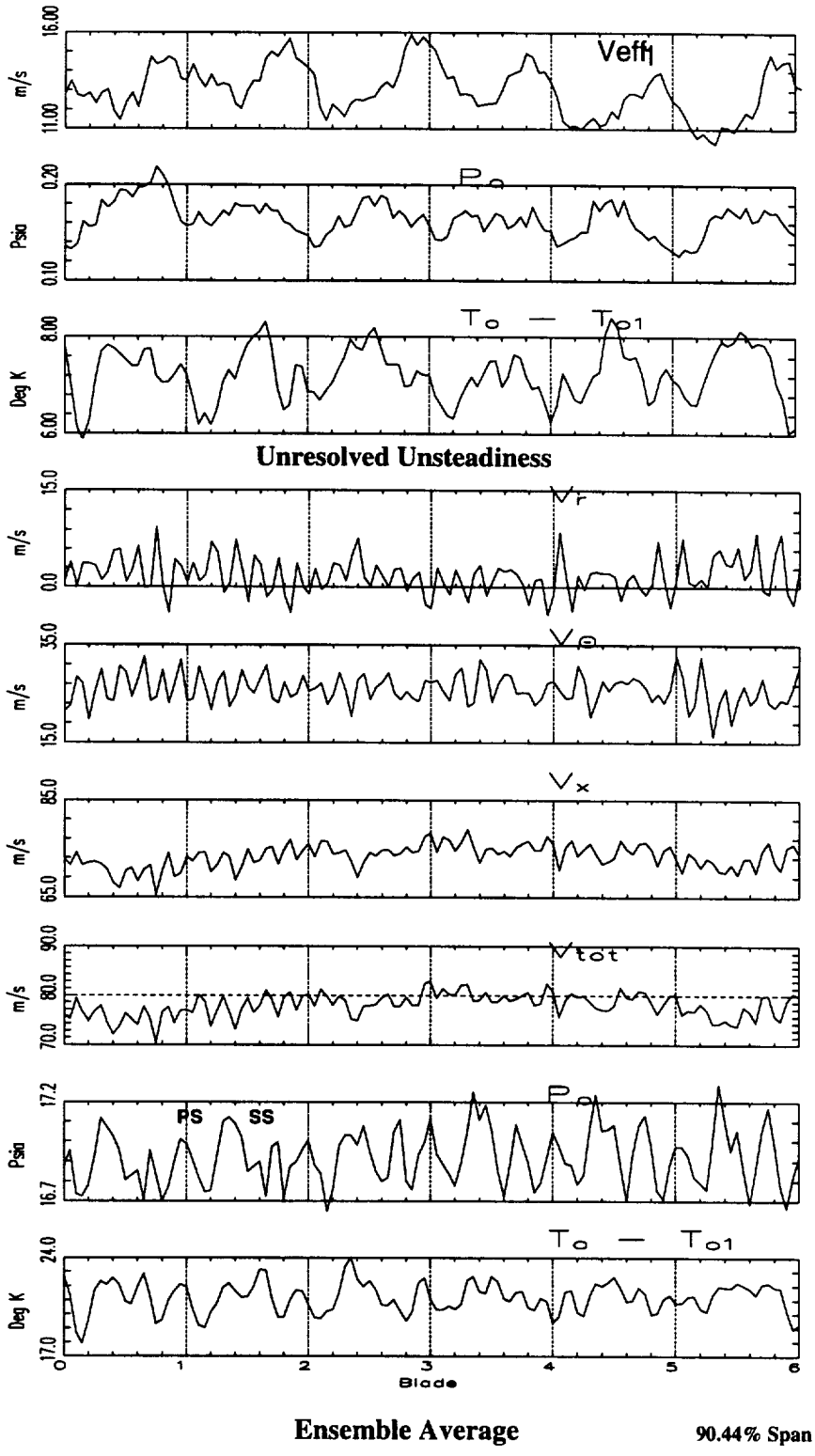

Figure 5.45. Blade-to-blade Distribution of the Composite flow field: Mid-pitch, 90.44% Span

5.5 Isentropic Efficiency Distribution

Isentropic efficiency has been calculated using equation 4.3 for the ensemble averaged pressure and temperature distribution (one rotor revolution each) at the midpitch location. This is the location away from the blade surfaces downstream of the stator which has the least influence on the rotor flow. Instantaneous efficiency cannot be calculated since the pressure and temperature measurements have been made at different times. It has to be remembered here that the efficiency calculated in this section is for two stages and is not calculated on a streamline. As a result, the efficiency numbers could be higher than 100%. The overall efficiency calculated using the mass averaged total temperature and pressure downstream of stator 2 referenced to the compressor inlet conditions is 89.5% compared with the overall isentropic efficiency of 89.3%. The uncertainty in the computed efficiency is about $\pm 0.25\%$. An algebraically averaged (across the passage) efficiency (at each radial location) was calculated for each blade passage in the revolution and Figure 5.46(a) shows the radial variation of this average efficiency for each blade passage. This figure depicts the bandwidth of efficiency variation across the rotor revolution. There is significant variation in the efficiency of each of the rotor blades. The average bandwidth is about 5% with the maximum variation being around 10%. The possible reasons for the change in efficiency across the rotor revolution are: different incidences, loading changes, influence of the aperiodicity brought about by the differing blade count (observed in the complete rotor revolution contours) etc. From the designer's viewpoint, it would be desirable to have all the blades perform with the same efficiency. By radially averaging the efficiency for each blade passage, it is possible to look at the best, worst and average blade. The radial variation of efficiency for the best, worst and average blade is shown in Figure. 5.46(b). The efficiency of the best blade is better than the average blade at almost all radial locations except close to the endwalls where the efficiencies are almost

the same. The highest efficiency is seen at about 20% span. This was the region which had the highest pressure levels in the wake as seen in the hub-to-tip contours of the ensemble averaged pressures (Figure 5.36). This high pressure is probably due to rotor wake migration away from the endwalls and the change in temperature is not significant. As a result the efficiency levels are high at this region.

Blade to blade distributions of ensemble averaged and blade periodic isentropic efficiency calculated from the temperature and pressure distributions at the midpitch circumferential location is shown in Figure. 5.47(a) and (b) respectively. For both the distributions, 3 radial locations are shown and at each location 4 blade passages are shown for the ensemble average and 1 blade passage for the blade periodic efficiency, respectively. The locations of the rotor wake can be easily identified as those that have low efficiency. The efficiency distributions are fairly periodic from blade to blade but they do change substantially in the radial direction. The efficiency is very low near the casing. This is partly due to the use of a mass averaged total pressure and total temperature at the inlet and partly due to the large flow mixing that is occurring in the casing endwall region due to the rotor clearance flow.

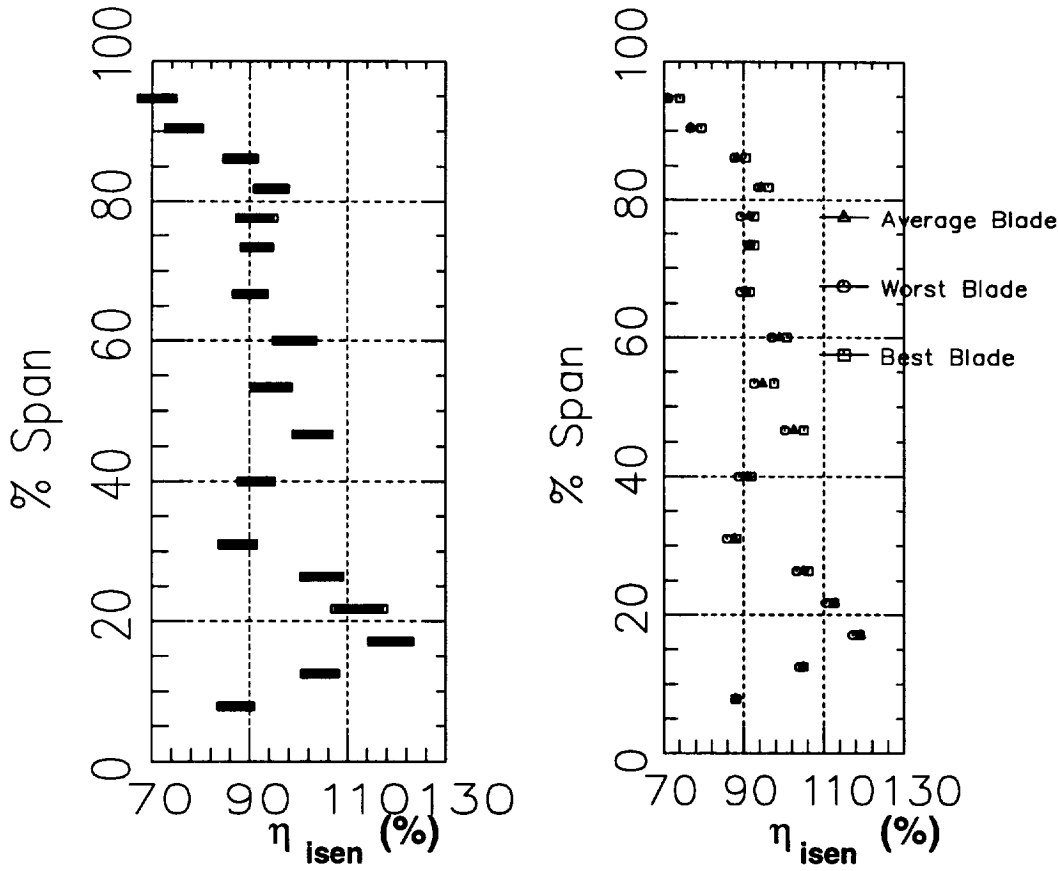

(a) Bandwidth of Efficiency

(b) Best, Worst and Average Blade

Figure 5.46. Hub to Tip Distribution of Isentropic efficiency distribution at midpitch

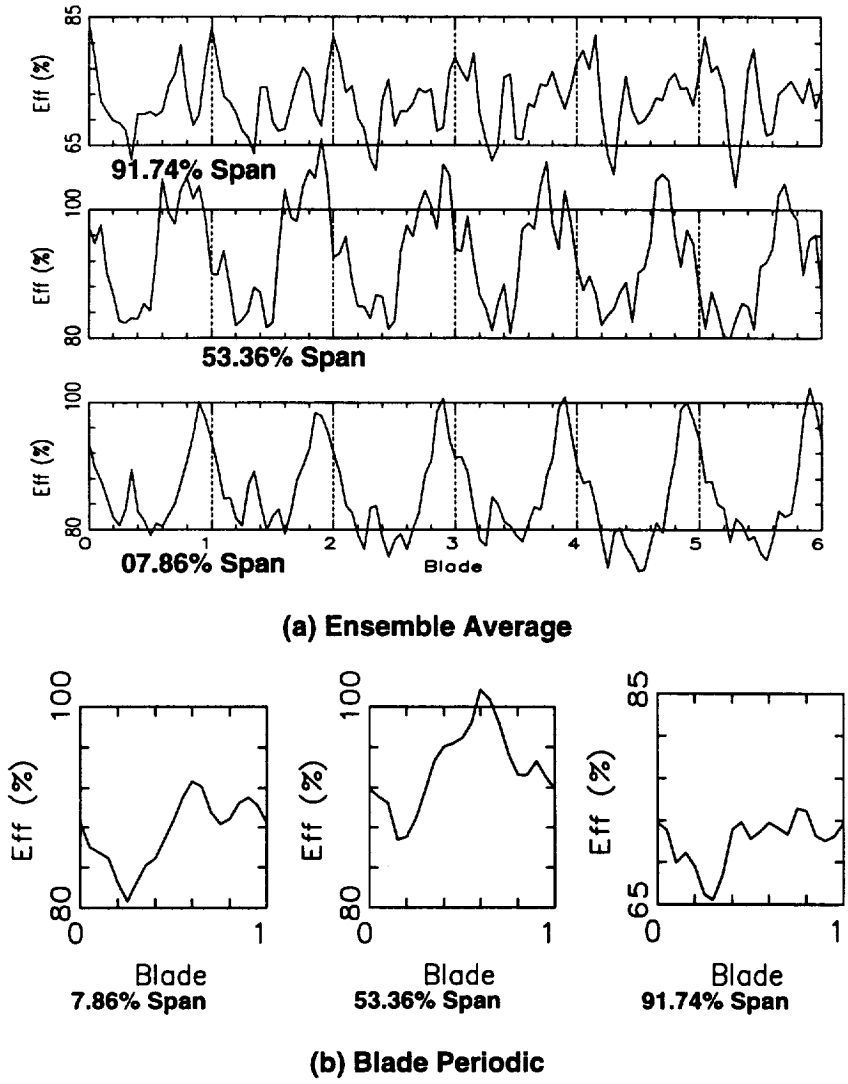

Figure 5.47. Blade-to-Blade Distribution of Isentropic efficiency at midpitch: Ensemble Average and Blade Periodic

Chapter 6

DETERMINISTIC MIXING HEAT-FLUX TERMS AND THE TERMS IN THE AVERAGE PASSAGE EQUATION SYSTEM

There have been tremendous advances over the past decade in the capabilities of computational fluid dynamics (CFD) methods to solve the steady state Navier-Stokes equations for subsonic and transonic flows. This gives the turbomachinery component designer new tools with the potential capability to accurately model the detailed structures of the flow field resulting in improved predictions of the component performance. Several researchers have also developed multistage turbomachinery analysis techniques based on the concept of coupling multiple isolated blade row analyses through through specialized boundary conditions. These so-called "mixing-plane" approaches yield relatively rapid solutions for the complex multistage turbomachinery flow problems (Adamczyk (1986) and Hall (1996)). Without the simplification of a tangential averaging procedure (a mixing plane), CFD analyses based on the Reynolds-averaged Navier-Stokes equations must employ a time-accurate solution strategy to account for the aerodynamic interactions resulting from relative blade motion in multistage turbomachinery which is very prohibitive.

For a single stage machine, the time-averaged Navier-Stokes equations are an acceptable model for the turbomachinery design approach. However, for multistage machines, this fails to adequately model the flow field. One of the approaches to solve this problem is due to Adamczyk (1985). In this approach, further decomposition and averaging must be applied to the Reynolds averaged Navier-Stokes equations. Adamczyk identified various sources of unsteadiness due to rotor-rotor and rotor-stator interactions, unequal number of blades etc. and represented various sources of unsteadiness described in Chapter 3. An averaging procedure is invoked to determine the "average-passage" of the time-averaged

flow field. The resulting equation system is the "average-passage" equation system.

This averaging procedure results in additional terms which appear as "stresses" in the equation system. These terms are called "deterministic stresses" somewhat analogous to the "Reynolds stresses" which are still present in the resulting equation system. These "deterministic stresses" are either modeled using conventional turbulence modeling techniques or entirely neglected (Adamczyk et al. (1986)). The physics that is associated with these terms is fundamentally different from turbulent fluctuations that result in the Reynolds stress terms. These terms result from deterministic features of the flow field such as blade wakes, shed vortices, leakage vortex and secondary flow which are known to be dominant features in turbomachinery fields. It is not surprising that the treatment of the "deterministic" tensors for turbomachinery fields based solely on the random processes of turbulence is not adequate to accurately model turbomachinery component flow fields. Similar "heat-flux" terms arise from the energy equation and need to be modeled.

Adequate data to support this modeling effort is not available and the acquisition and analysis of unsteady temperature, pressure and velocity measurements in a high speed multistage compressor constitutes significant part of this program. The Penn State research program has been focused on filling this void. This chapter attempts to derive the various deterministic velocity-velocity and velocity-temperature correlation terms and to then obtain the non-dimensional values of all the possible terms of the average-passage equation system (momentum and energy) with the objective of evaluating which of these terms are important in the mixing process and which terms need to be modeled.

6.1 Average Passage Equation System

The complete mathematical details of formulating the average-passage equation system from the un-averaged Navier-Stokes equations are beyond the scope of this thesis; however, it may be useful to list an outline of the equation development process. The development of the tangential momentum equation in the average-passage system for a stationary vane is given in Appendix D for reference. The remaining momentum, energy, and continuity equations and the equations pertaining to rotating blades can be developed in a similar manner (for complete details, see Adamczyk(1985)).

1. The development is begun with the particular equation in cylindrical coordinates.

2. This equation is then density weighted ensemble averaged. The averaging procedure is begun by decomposing the velocity field, pressure and temperature (as the case may be) defined in the absolute frame of reference into a density weighted ensemble average component plus an unresolved variable. The additional terms which appear as a result of the ensemble averaging are referred to as "*Reynolds stresses*" (for the momentum equation) and "*unresolved heat-fluxes*" (for the energy equation).

3. The next step in the development process is to time-average the ensemble-averaged equation. This results in the further decomposition of the ensemble averaged quantity into a revolution periodic component. The additional terms that arise from this averaging represent the mixing stress and heat-flux attributed to the revolution periodic field.

4. This equation is then passage-to-passage averaged to yield the average passage equation system. This then results in further mixing stress and heat-flux terms attributed to the revolution aperiodic field.

5. Now for the experimental data taken in this program, the density was assumed to be constant since the mach numbers encountered in this flow field are very low subsonic. And also the various time averaging parameters can be combined into a common time average since the overall time period for the data acquired is one rotor revolution (because of ensemble average). The viscous body forces and the energy sources can be neglected since they go to zero outside the blade row. Incorporating these simplifications, the average-passage equation system is given by:

Continuity equation:

$$\underbrace{\frac{\partial}{\partial t}(\overline{\rho})}_{C1} + \underbrace{\frac{\partial}{\partial r}(r\overline{\rho V_r})}_{C2} + \underbrace{\frac{\partial}{\partial \theta}(\overline{\rho V_\theta})}_{C3} + \underbrace{\frac{\partial}{\partial z}(\overline{\rho V_z})}_{C4} = 0 \tag{6.1}$$

Axial momentum equation:

$$\underbrace{\frac{\partial}{\partial t}(r\overline{\rho}\,\overline{V_z})}_{AM1} + \underbrace{\frac{\partial}{\partial r}(r\overline{\rho}\,\overline{V_r}\,\overline{V_z})}_{AM2} + \underbrace{\frac{\partial}{\partial \theta}(r\overline{\rho}\,\overline{V_\theta}\,\overline{V_z})}_{AM3} + \underbrace{\frac{\partial}{\partial z}(r\overline{\rho}\,\overline{V_z}\,\overline{V_z} + r\overline{p})}_{AM4} =$$

$$\frac{\partial}{\partial r}\left(\underbrace{r\overline{\tau_{rz}}}_{AM5} - \underbrace{r\overline{\rho V_{rRA} V_{zRA}}}_{AM6} - \underbrace{r\overline{\rho V_{rRP} V_{zRP}}}_{AM78} - \underbrace{r\overline{\rho V_r' V_z'}}_{AM9}\right)$$

$$+\frac{\partial}{\partial \theta}\left(\underbrace{\overline{\tau_{\theta z}}}_{AM10} - \underbrace{\overline{\rho V_{\theta RA} V_{zRA}}}_{AM11} - \underbrace{\overline{\rho V_{\theta RP} V_{zRP}}}_{AM1213} - \underbrace{\overline{\rho V_\theta' V_z'}}_{AM14}\right)$$

$$+\frac{\partial}{\partial z}\left(\underbrace{r\overline{\tau_{zz}}}_{AM15} - \underbrace{r\overline{\rho V_{zRA} V_{zRA}}}_{AM16} - \underbrace{r\overline{\rho V_{zRP} V_{zRP}}}_{AM1718} - \underbrace{r\overline{\rho V_z' V_z'}}_{AM19}\right) \tag{6.2}$$

Tangential momentum equation:

$$\underbrace{\frac{\partial}{\partial t}(r\overline{\rho}\,\overline{V_\theta})}_{TM1} + \underbrace{\frac{\partial}{\partial r}(r\overline{\rho}\,\overline{V_r}\,\overline{V_\theta})}_{TM2} + \underbrace{\frac{\partial}{\partial \theta}(r\overline{\rho}\,\overline{V_\theta}\,\overline{V_\theta} + \overline{p})}_{TM3} + \underbrace{\frac{\partial}{\partial z}(r\overline{\rho}\,\overline{V_z}\,\overline{V_\theta})}_{TM4} =$$

$$-\left(\underbrace{\overline{\rho}\,\overline{V_r}\,\overline{V_\theta}}_{TM5}\right)$$

$$+\left(\underbrace{\overline{\tau_{r\theta}}}_{TM6}-\underbrace{\overline{\rho V_{rRA}V_{\theta RA}}}_{TM7}+\underbrace{\overline{\rho V_{rRP}V_{\theta RP}}}_{TM89}+\underbrace{\overline{\rho V_r'V_\theta'}}_{TM10}\right)$$

$$+\frac{\partial}{\partial r}\left(\underbrace{r\overline{\tau_{r\theta}}}_{TM11}-\underbrace{r\overline{\rho V_{rRA}V_{\theta RA}}}_{TM12}-\underbrace{r\overline{\rho V_{rRP}V_{\theta RP}}}_{TM1314}-\underbrace{r\overline{\rho V_r'V_\theta'}}_{TM15}\right)$$

$$+\frac{\partial}{\partial \theta}\left(\underbrace{r\overline{\tau_{\theta\theta}}}_{TM16}-\underbrace{\overline{\rho V_{\theta RA}V_{\theta RA}}}_{TM17}-\underbrace{\overline{\rho V_{\theta RP}V_{\theta RP}}}_{TM1819}-\underbrace{\overline{\rho V_\theta'V_\theta'}}_{TM20}\right)$$

$$+\frac{\partial}{\partial z}\left(\underbrace{r\overline{\tau_{z\theta}}}_{TM21}-\underbrace{\overline{\rho V_{zRA}V_{\theta RA}}}_{TM22}-\underbrace{\overline{\rho V_{zRP}V_{\theta RP}}}_{TM2324}-\underbrace{\overline{\rho V_z'V_\theta'}}_{TM25}\right) \tag{6.3}$$

Radial momentum equation:

$$\underbrace{\frac{\partial}{\partial t}(r\overline{\rho V_r})}_{RM1}+\underbrace{\frac{\partial}{\partial r}(r\overline{\rho V_r}\,\overline{V_r}+\overline{p})}_{RM2}+\underbrace{\frac{\partial}{\partial \theta}(r\overline{\rho V_\theta}\,\overline{V_r})}_{RM3}+\underbrace{\frac{\partial}{\partial z}(r\overline{\rho V_z}\,\overline{V_r})}_{RM4}=$$

$$\left(\underbrace{\overline{p}+\overline{\rho V_\theta^2}-\overline{\tau_{\theta\theta}}}_{RM5}\right)$$

$$+\overline{\rho}\left(\underbrace{\overline{V_{\theta RA}V_{\theta RA}}}_{RM6}+\underbrace{\overline{V_{\theta RP}V_{\theta RP}}}_{RM78}+\underbrace{\overline{V_\theta'V_\theta'}}_{RM9}\right)$$

$$+\frac{\partial}{\partial r}\left(\underbrace{r\overline{\tau_{rr}}}_{RM10}-\underbrace{r\overline{\rho V_{rRA}V_{rRA}}}_{RM11}-\underbrace{r\overline{\rho V_{rRP}V_{rRP}}}_{RM1213}-\underbrace{r\overline{\rho V_r'V_r'}}_{RM14}\right)$$

$$+\frac{\partial}{\partial \theta}\left(\underbrace{r\overline{\tau_{\theta r}}}_{RM15}-\underbrace{\overline{\rho V_{\theta RA}V_{rRA}}}_{RM16}-\underbrace{\overline{\rho V_{\theta RP}V_{rRP}}}_{RM1718}-\underbrace{\overline{\rho V_\theta'V_r'}}_{RM19}\right)$$

$$+\frac{\partial}{\partial z}\left(\underbrace{r\overline{\tau_{zr}}}_{RM20}-\underbrace{\overline{\rho V_{zRA}V_{rRA}}}_{RM21}-\underbrace{\overline{\rho V_{zRP}V_{rRP}}}_{RM2223}-\underbrace{\overline{\rho V_z'V_r'}}_{RM24}\right) \tag{6.4}$$

and the Energy Equation:

$$\underbrace{\frac{\partial}{\partial t}(r\overline{\rho e_o})}_{E1}+\underbrace{\frac{\partial}{\partial r}(r\overline{\rho V_r H_o})}_{E2}+\underbrace{\frac{\partial}{\partial \theta}(r\overline{\rho V_\theta H_o})}_{E3}+\underbrace{\frac{\partial}{\partial z}(r\overline{\rho V_z H_o})}_{E4}=$$

$$\frac{\partial}{\partial r}r\left(\underbrace{\overline{V_r\tau_{rr}}}_{E5}+\underbrace{\overline{V_\theta\tau_{r\theta}}}_{E6}+\underbrace{\overline{V_z\tau_{rz}}}_{E7}\right)$$

$$+\frac{\partial}{\partial\theta}\left(\underbrace{\overline{V_r}\,\overline{\tau_{\theta r}}}_{E8}+\underbrace{\overline{V_\theta}\,\overline{\tau_{\theta\theta}}}_{E9}+\underbrace{\overline{V_z}\,\overline{\tau_{\theta z}}}_{E10}\right)$$

$$+\frac{\partial}{\partial z}r\left(\underbrace{\overline{V_r}\,\overline{\tau_{zr}}}_{E11}+\underbrace{\overline{V_\theta}\,\overline{\tau_{z\theta}}}_{E12}+\underbrace{\overline{V_z}\,\overline{\tau_{zz}}}_{E13}\right)$$

$$+\underbrace{\frac{\partial}{\partial r}r\left(\overline{k}\frac{\overline{\partial T}}{\partial r}\right)}_{E14}+\underbrace{\frac{\partial}{\partial\theta}\left(\frac{\overline{k}}{r}\frac{\overline{\partial T}}{\partial\theta}\right)}_{E15}+\underbrace{\frac{\partial}{\partial z}r\left(\overline{k}\frac{\overline{\partial T}}{\partial z}\right)}_{E16}$$

$$-\frac{\partial}{\partial r}r\left(\underbrace{\overline{\rho}\,\overline{V_{rRA}}\,\overline{H_{oRA}}}_{E17}+\underbrace{\overline{\rho}\,\overline{V_{rRP}H_{oRP}}}_{E1819}+\underbrace{\overline{\rho}\,\overline{V_r'H_o'}}_{E20}\right)$$

$$-\frac{\partial}{\partial\theta}\left(\underbrace{\overline{\rho}\,\overline{V_{\theta RA}}\,\overline{H_{oRA}}}_{E21}+\underbrace{\overline{\rho}\,\overline{V_{\theta RP}H_{oRP}}}_{E2223}+\underbrace{\overline{\rho}\,\overline{V_\theta'H_o'}}_{E24}\right)$$

$$-\frac{\partial}{\partial z}r\left(\underbrace{\overline{\rho}\,\overline{V_{zRA}}\,\overline{H_{oRA}}}_{E25}+\underbrace{\overline{\rho}\,\overline{V_{zRP}H_{oRP}}}_{E2627}+\underbrace{\overline{\rho}\,\overline{V_z'H_o'}}_{E28}\right)$$

$$+\frac{\partial}{\partial r}r\left(\underbrace{\overline{V_{rRA}\tau_{rrRA}}}_{E29}+\underbrace{\overline{V_{rRP}\tau_{rrRP}}}_{E3031}+\underbrace{\overline{V_r'\tau_{rr}'}}_{E32}\right.$$
$$\left.+\underbrace{\overline{V_{\theta RA}\tau_{r\theta RA}}}_{E33}+\underbrace{\overline{V_{\theta RP}\tau_{r\theta RP}}}_{E3435}+\underbrace{\overline{V_\theta'\tau_{r\theta}'}}_{E36}\right.$$
$$\left.+\underbrace{\overline{V_{zRA}\tau_{rzRA}}}_{E37}+\underbrace{\overline{V_{zRP}\tau_{rzRP}}}_{E3839}+\underbrace{\overline{V_z'\tau_{rz}'}}_{E40}\right)$$

$$+\frac{\partial}{\partial\theta}\left(\underbrace{\overline{V_{rRA}\tau_{\theta rRA}}}_{E41}+\underbrace{\overline{V_{rRP}\tau_{\theta rRP}}}_{E4243}+\underbrace{\overline{V_r'\tau_{\theta r}'}}_{E44}\right.$$
$$\left.+\underbrace{\overline{V_{\theta RA}\tau_{\theta\theta RA}}}_{E45}+\underbrace{\overline{V_{\theta RP}\tau_{\theta\theta RP}}}_{E4647}+\underbrace{\overline{V_\theta'\tau_{\theta\theta}'}}_{E48}\right.$$
$$\left.+\underbrace{\overline{V_{zRA}\tau_{\theta zRA}}}_{E49}+\underbrace{\overline{V_{zRP}\tau_{\theta zRP}}}_{E5051}+\underbrace{\overline{V_z'\tau_{\theta z}'}}_{E52}\right)$$

$$+\frac{\partial}{\partial z}r\left(\underbrace{\overline{V_{rRA}\tau_{zrRA}}}_{E53}+\underbrace{\overline{V_{rRP}\tau_{zrRP}}}_{E5455}+\underbrace{\overline{V_r'\tau_{zr}'}}_{E56}\right.$$

$$+\underbrace{\overline{V_{\theta RA}\tau_{\theta zRA}}}_{E57}+\underbrace{\overline{V_{\theta RP}\tau_{\theta zRP}}}_{E5859}+\underbrace{\overline{V'_{\theta}\tau'_{\theta z}}}_{E60}$$

$$+\underbrace{\overline{V_{zRA}\tau_{zzRA}}}_{E61}+\underbrace{\overline{V_{zRP}\tau_{zzRP}}}_{E6263}+\underbrace{\overline{V'_{z}\tau'_{zz}}}_{E64}\Bigg) \tag{6.5}$$

where $\overline{V_r}$, $\overline{V_\theta}$, $\overline{V_z}$ are the components of time averaged velocity, $\overline{\rho}$ the time averaged density, $\overline{p}$ the static pressure, T the static temperature, H_o the stagnation enthalpy and τ the stress components (normal and shear). Since the experimental data was acquired only at one axial station downstream of the second stator, none of the axial gradient terms including those in the shear-stress terms can be computed. However, by comparing the relative weights of all the other terms, definite conclusions can be drawn towards explaining the relative importance of the terms that can be computed with respect to the other terms that can be computed. Table 6.1 gives a list of all the terms that can be calculated from the data reported in Parts 1 and 2 of this paper and Suryavamshi et al. (1996). The total stress resulting from the average-passage equations may be expressed as:

$$\underbrace{R_{ij}}_{Total\ Stress} = \underbrace{\overline{\overline{\rho}V_{iRA}V_{jRA}}}_{Revolution\ Aperiodic\ Stress} + \underbrace{\overline{\overline{\rho}V_{iRP}V_{jRP}}}_{Revolution\ Periodic\ Stress} + \underbrace{\overline{\overline{\rho}V'_{i}V'_{j}}}_{Reynolds\ Stress} \tag{6.6}$$

and the total heat-flux terms are expressed as:

$$\underbrace{\Gamma_j}_{Total\ Heat-Flux} = \underbrace{\overline{\overline{\rho}V_{jRA}H_{oRA}}}_{Revolution\ Aperiodic\ Heat-Flux} + \underbrace{\overline{\overline{\rho}V_{jRP}H_{oRP}}}_{Revolution\ Periodic\ Heat-Flux} + \underbrace{\overline{\overline{\rho}V'_{j}H'_{o}}}_{Turbulent\ Heat-Flux} \tag{6.7}$$

Adequate progress has been made and is being made to adequately simulate (at least for the present purposes) through well-developed turbulence modeling procedures the Reynolds Stress and Turbulent Heat-Flux terms. The problem remaining in effecting a

Table 6.1. Computable Terms in the Average-Passage Equation System

Equation	Eq. No	Computable Terms
1. Continuity	6.1	C2, C3
2. Axial Momentum	6.2	AM2, AM3, AM6, AM78, AM11, AM1213
3. Tangential Momentum	6.3	TM2, TM3, TM5, TM6, TM7, TM89, TM11, TM12, TM1314, TM17, TM1819
4. Radial Momentum	6.4	RM2, RM3, RM5, RM6, RM78, RM11 RM1213, RM15, RM16, RM1718
5. Energy	6.5	E2, E3, E5, E6, E8, E9, E14, E15, E17, E1819, E21, E2223, E33, E3435, E41, E4243

numerical solution of the average-passage system of equations, referred to as the closure problem, is to effectively model the body force, energy source, and deterministic mixing stress and heat-flux terms for a multiple blade row turbomachinery environment. In this thesis an attempt will be made to evaluate a gradient diffusion type model for the deterministic heat-flux terms.

6.1.1 Procedure for Calculation of Various Terms

Auto- and cross-correlation methods were used to calculate the various terms listed in Table 6.1. Since the data has been acquired and triggered with respect to the same trigger, cross correlation between the various velocity components is the average of the product of the various components. For example the term $\overline{\overline{\rho} V_{zRP} V_{\theta RP}}$ is given by:

$$\overline{\overline{\rho} V_{zRP} V_{\theta RP}} = \frac{1}{N_b \times N_{pb}} \sum_{j=1}^{N_b} \sum_{k=1}^{N_{pb}} \overline{\rho} (V_{zRP})_{jk} \, (V_{\theta RP})_{jk} \tag{6.8}$$

where, N_b and N_{pb} stand for the number of blades and points per blade. In the velocity-enthalpy correlation, however, the location of the trigger pulse with respect to the data is very important. First of all in the enthalpy computation, it is assumed that the specific heat for constant pressure is constant over the temperature range being dealt with in this experiment. So as a result, enthalpy is just a product of total temperature and specific heat for constant pressure. The correlation term $\overline{\overline{\rho} V_{zRP} H_{oRP}}$ is then given by:

$$\overline{\overline{\rho} V_{zRP} H_{oRP}} = \frac{1}{N_b \times N_{pb}} \sum_{j=1}^{N_b} \sum_{k=1}^{N_{pb}} \overline{\rho}(V_{zRP})_{jk} \, (H_{oRP})_{jk+\Delta k} \tag{6.9}$$

where Δk is the time shift to be applied to the enthalpy data in order to correlate the two signals. The maximum shift can be one blade passage (20 points). The value of the cross-correlation corresponding to the highest cross correlation coefficient is the value of the correlation between the velocity component and stagnation enthalpy at that location. The steps involved are as follows:

1. The time-averaged deterministic stress and heat-flux terms are calculated using auto- and cross-correlation methods and time averaging the results.

2. The stress, heat-flux and the steady flow field parameters are spline-fit and interpolated onto a very fine grid (101X101) within the overall boundaries of the measurement mesh. The spline-fit and interpolation technique is done using cubic splines. Care is taken to ensure no spurious gradients are introduced into the flow field due to spline fitting.

3. Then the various terms of the equation are calculated and then their gradients are determined. Second order accurate finite difference formulations are used to evaluate the derivatives. Central differencing is used for the central nodes and forward and backward differencing schemes are used to evaluate the end nodes respectively.

4. Contour plots and blade-to-blade distribution of the various terms are generated and these are used in the interpretation and analysis of the flow field.

The equations used to calculate the various molecular stresses are:

$$\begin{aligned}
\tau_{rr} &= \mu\left[\frac{2\partial V_r}{\partial t} - \frac{2}{3}(\nabla \bullet \vec{V})\right] \\
\tau_{rr} &= \mu\left[2(\frac{1}{r}\frac{\partial V_\theta}{\partial \theta} + \frac{V_r}{r}) - \frac{2}{3}(\nabla \bullet \vec{V})\right] \\
\tau_{zz} &= \mu\left[\frac{2\partial V_z}{\partial t} - \frac{2}{3}(\nabla \bullet \vec{V})\right] \\
\tau_{r\theta} = \tau_{\theta r} &= \mu\left[r\frac{\partial}{\partial r}(\frac{V_\theta}{r}) + \frac{1}{r}\frac{\partial V_r}{\partial \theta}\right] \\
\tau_{\theta z} = \tau_{z\theta} &= \mu\left[\frac{\partial V_\theta}{\partial z} + \frac{1}{r}\frac{\partial V_z}{\partial \theta}\right] \\
\tau_{rz} = \tau_{zr} &= \mu\left[\frac{\partial V_z}{\partial r} + \frac{\partial V_r}{\partial z}\right]
\end{aligned} \tag{6.10}$$

6.2 Distribution of Deterministic Heat-Flux Downstream of the Stator

In this section, the blade-to-blade and hub-to-casing distributions of the various deterministic heat-flux terms are presented and analyzed. The deterministic heat-flux terms were calculated using the cross-correlation methods described earlier and are non-dimensionalized by the average heat-flux at the inlet to the compressor ($\overline{\rho_{in} c_p V_{z_{in}} T_{o_{in}}}$). In this section the hub-to-tip contour and the blade-to-blade distributions of revolution periodic components of axial ($q_{z_{RP}}$), tangential ($q_{\theta_{RP}}$) and radial ($q_{r_{RP}}$) heat-flux are presented and analyzed. The axial, tangential and radial components of heat-flux are given by:

$$\begin{aligned}
q_{z_{RP}} &= \frac{\overline{\bar{\rho} V_{z_{RP}} H_{o_{RP}}})}{(\overline{\rho_{in}} c_p V_{z_{in}} T_{o_{in}})} \\
q_{\theta_{RP}} &= \frac{\overline{\bar{\rho} V_{\theta_{RP}} H_{o_{RP}}})}{(\overline{\rho_{in}} c_p V_{z_{in}} T_{o_{in}})} \\
q_{r_{RP}} &= \frac{\overline{\bar{\rho} V_{r_{RP}} H_{o_{RP}}})}{(\overline{\rho_{in}} c_p V_{z_{in}} T_{o_{in}})}
\end{aligned} \tag{6.11}$$

Table 6.2. Uncertainty of Various Derived Quantities: Deterministic Heat-Flux

Quantity	Uncertainty (%)	Figures
q_{zRP}	±20.21%	6.1, 6.2, 6.3
$q_{\theta RP}$	±14.15%	6.1, 6.2, 6.4
q_{rRP}	±40.532%	6.1, 6.2, 6.5

The uncertainties of the various heat-flux variables are given in Table 6.2. Uncertainty analysis principles given in Appendix A is used to calculate the uncertainties of these quantities. The table shows that the uncertainty in q_{rRP} is the highest and is probably the least reliable measurement.

Blade-to-blade distributions at 5 radial locations (near hub, 21.76% span, midspan, 81.89% span and near the casing) is shown in Figures 6.1 and 6.2 and the contour plots are shown in Figures 6.3, 6.4 and 6.5. In general all three components of deterministic heat-flux have similar levels in the core flow and show changes mainly in the wake, suction surface casing endwall corner region and in the hub endwall region. Once again it should be emphasized here that only periodic velocity-temperature correlations are shown and the non-deterministic fluctuations cannot be determined due to different probe used for velocity and temperature measurement.

On the suction side of the wake near the hub at 7.86% span from the hub (Figures 6.1 and 6.3), the levels of deterministic heat-flux terms are almost zero. This indicates that there is very little transport of stagnation enthalpy associated with the deterministic unsteadiness on the suction side near the hub. On the pressure side of the stator wake, levels of heat-flux higher than that found on the suction side are observed. All three deterministic heat-flux terms have almost the same levels. The flow on the pressure side of the stator near the hub is quite complex. There is interaction between the wakes shed

from the stator blade, possible leakage flow vortical structures, possible scraping of the hubwall viscous layer and its accumulation on the pressure side due to the hub rotation and the deterministic unsteadiness associated with the rotor wakes. This interaction induces mixing and heat-transfer and consequently higher levels of the deterministic heat-flux terms due to all three velocity components are observed on the pressure side compared to the suction side. However, the levels on the pressure side are much lower than that found in the midpitch region at the hub. The presence of a hub leakage vortex in the midpitch region (as explained in Chapter 4) is characterized by high levels of all three components of deterministic heat-flux. The pitchwise extent of this region is approximately 35% of the pitch and is of the same order of magnitude as the extent of the region of low momentum observed in the time averaged contour plots (Part 2 of this paper) at this location. This may be caused by fluctuating hub leakage flow/vortex due to the unsteady rotor hub exit flow. This indicates that deterministic unsteadiness contributes significantly to the energy redistribution. Presence of very high levels of unresolved unsteadiness (compared to the deterministic unsteadiness) in this region as observed in contour plots of unresolved total temperature and total pressure (Chapter 5) shows that mixing due to unresolved unsteadiness is also probably very high.

At the 21.76% spanwise region (Figures 6.1 and 6.3), high levels of deterministic heat-flux are observed in the wake and on the pressure side of the stator. The contour plots show a decrease in the extent as well as magnitude of the deterministic heat flux in the midpitch region as this spanwise location. On the suction side of the wake as in the hub, there is very little mixing and this is reflected in the levels of deterministic heat-flux which are almost zero. The time-averaged total temperature, pressure and secondary flow distributions show a region of intense mixing on the pressure side around 21.76% span which probably is due to accumulation of the hub endwall fluid being transported by the hub rotation as well as interaction with the rotor wake fluid which has been transported

to the pressure side of the downstream stator was observed. This region has high positive levels of heat-flux due to axial velocity and appreciable negative levels of heat-flux due to radial and tangential velocities (Figures 6.1 and 6.3). This reflects the radial and tangential transport of enthalpy fluctuations.

In the midspan region (Figures 6.1 and 6.3), the highest levels of deterministic heat-flux are observed in the wake region where contributions from heat-flux in the axial and tangential components are quite high. The radial velocity fluctuations are quite small in this region and is reflected in the heat-flux due to the fluctuating radial velocity being very small. Positive levels of heat-flux due to tangential velocity fluctuations and negative levels of heat-flux due to the axial velocity fluctuations in the wake, is indicative of tangential and axial transport of heat. On the pressure side of the stator, there is appreciable levels of heat flux due to all three velocity components which is mainly due to the rotor wake impingement on the pressure side of the stator.

In the casing endwall region (81 and 90% span, Figures 6.1, 6.3(a), 6.3(b) and 6.3(c)) , the focus once again shifts to the suction side of the stator wake and the stator wake itself. This is the region of high losses and also of high levels of unresolved unsteadiness possibly caused by casing stall as observed in Part 1 of this paper. High levels of mixing associated with momentum and heat-transfer is expected in this region. Around 81% span, high levels of heat-flux due to all three velocity components are observed on the suction side. Away from the blade surface, high negative values of heat-flux due to the axial velocity fluctuations and positive levels of heat-flux due to the radial velocity fluctuations indicates intense heat transfer in this region. Close to the blade surface on the suction side, high +ve and -ve values of heat-flux due to all three components of velocity are observed also indicating intense heat transfer in this region. Experiments indicate that non-deterministic (including unresolved) unsteadiness in total temperature and velocity are very high, but could not be correlated due to different measurement techniques. Very high levels of

unresolved unsteadiness in total pressure and total temperature and velocity components leads to high levels of heat-transfer from this region by the unresolved velocity. Detailed measurements wherein the unresolved velocity-temperature can be correlated is needed to quantify the levels of heat-transfer due to deterministic and unresolved heat-fluxes. Close to the casing endwall (90% span), the levels of deterministic heat-flux are very small compared to the other location. This is because of very low levels of deterministic unsteadiness in total velocity and total temperature present at this location.

6.3 Distribution of the Various Terms of the Average Passage Equation System

In this section an attempt will be made to evaluate the relative magnitudes of the various terms presented in Table 6.1 in order to determine which of these terms are important and which terms can be neglected in the equation system for stator and rotor flow computation and design. The gradients are calculated using the non-dimensional values of each of the terms. The velocities are non-dimensionalized by the mass averaged axial velocity at the inlet to the compressor ($\overline{V_{z_{in}}}$), the stagnation enthalpies by the stagnation enthalpy at the inlet ($\overline{\rho C_p V_{z_{in}} H_{o_{in}}}$), density by the static density at the inlet (ρ_{in}), the static pressure by the inlet static pressure ($\overline{p_{in}}$), the deterministic stress terms by the square of the inlet axial velocity and the deterministic heat-flux terms by a product of the inlet axial velocity and inlet stagnation enthalpy. The following procedure is used to calculate the various terms:

1. The ensemble averaged velocity data and the ensemble averaged total temperature data are correlated to evaluate all the deterministic normal, shear and heat-flux terms. These are then appropriately normalized to derive the non-dimensional form of these terms.

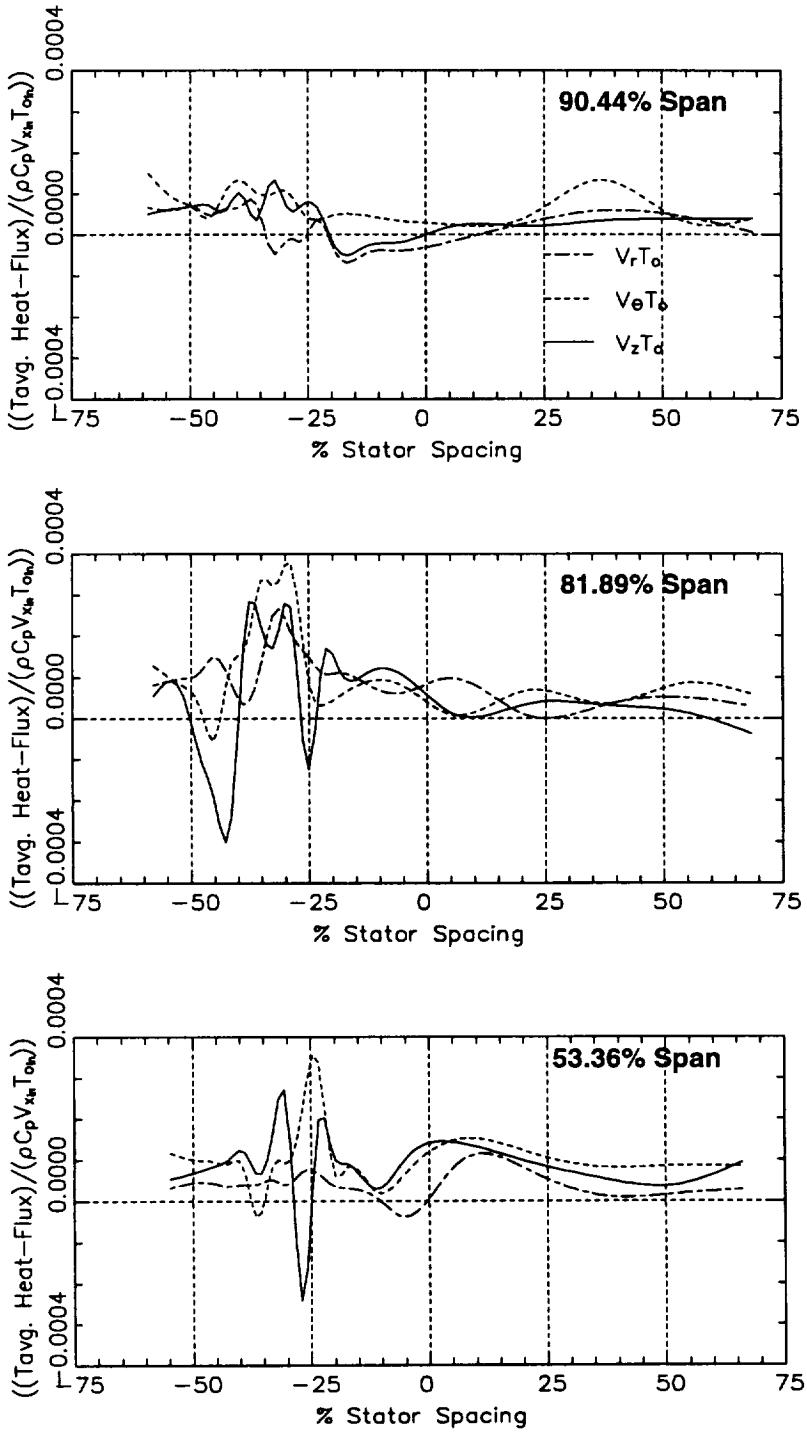

Figure 6.1. Blade-to-blade Distribution of Time Averaged Deterministic Heat-Flux Components at Various Radial Locations

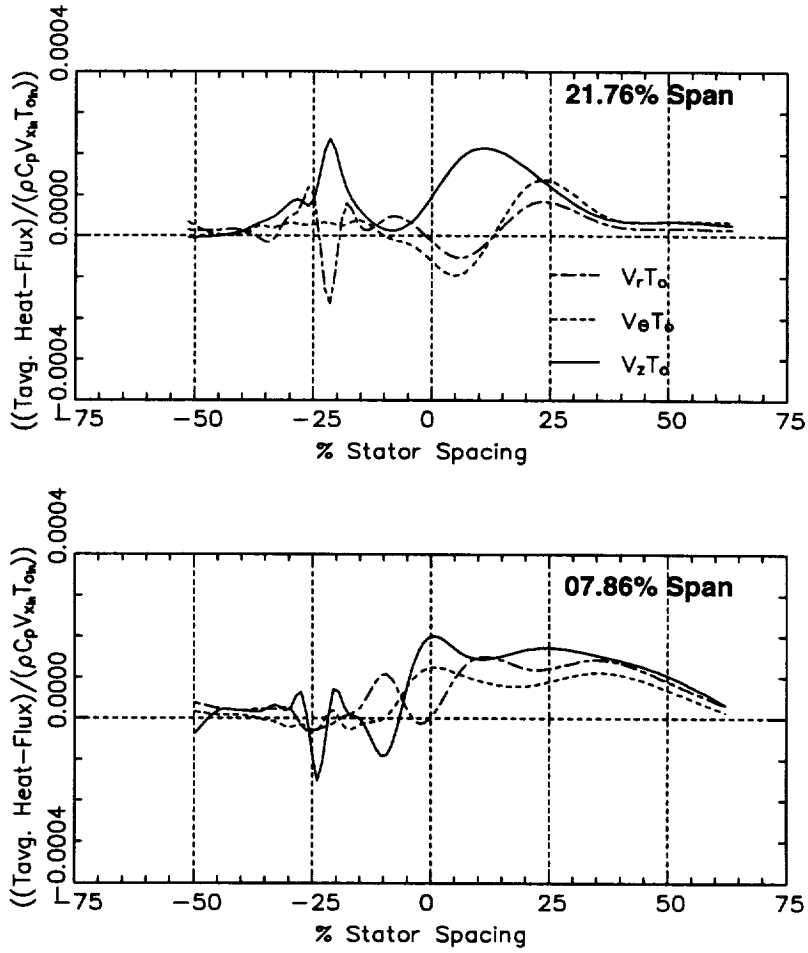

Figure 6.2. Blade-to-blade Distribution of Time Averaged Deterministic Heat-Flux Components at Various Radial Locations (cont'd)

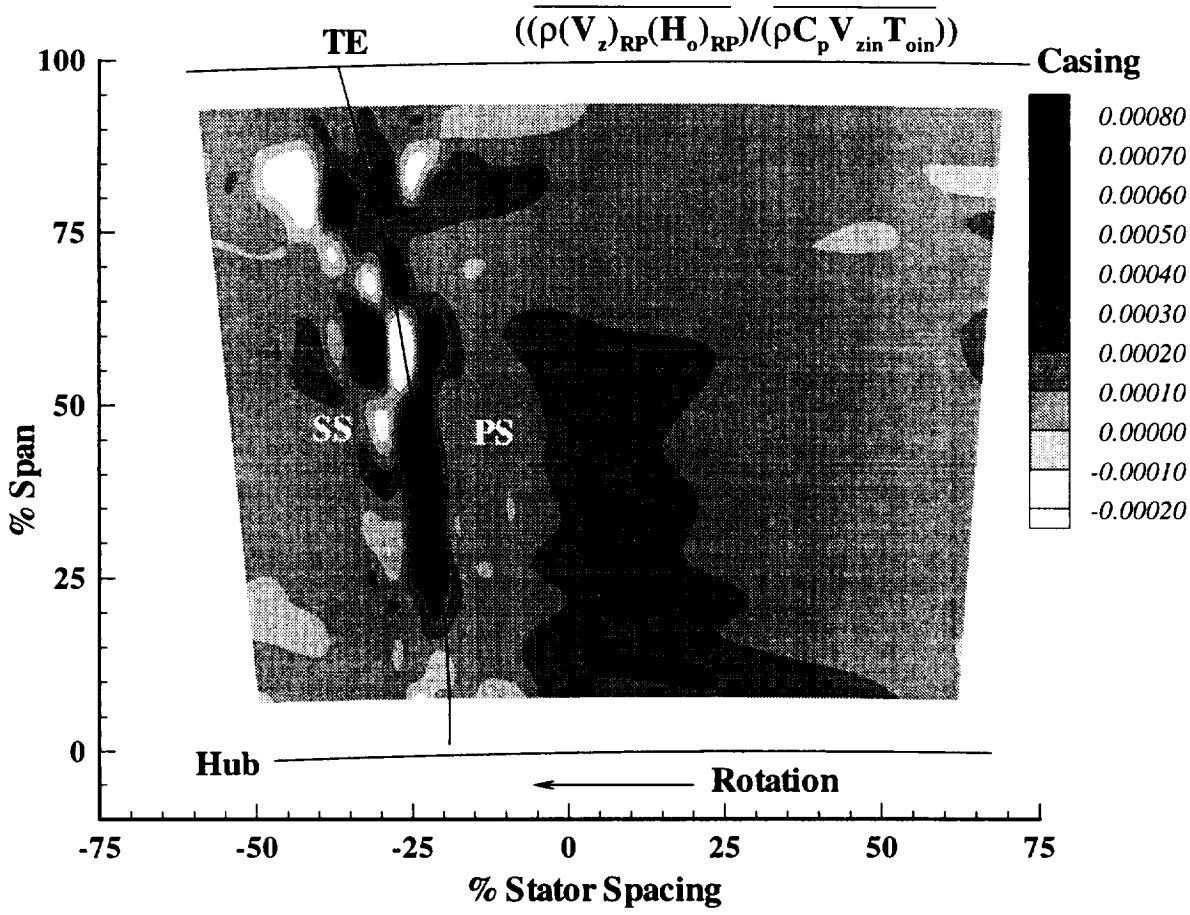

Figure 6.3. Contour Plot of the Axial Component of Deterministic Heat-Flux

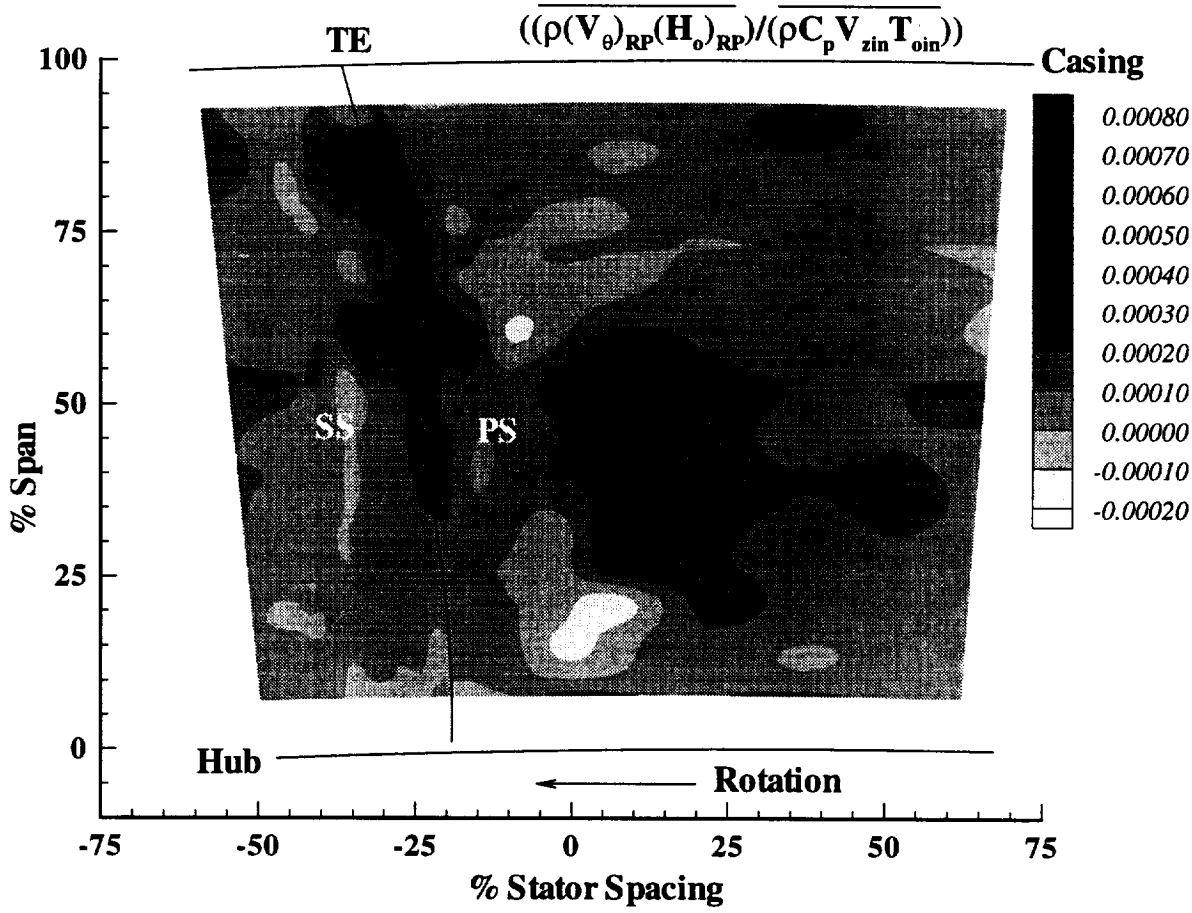

Figure 6.4. Contour Plot of the Tangential Component of Deterministic Heat-Flux

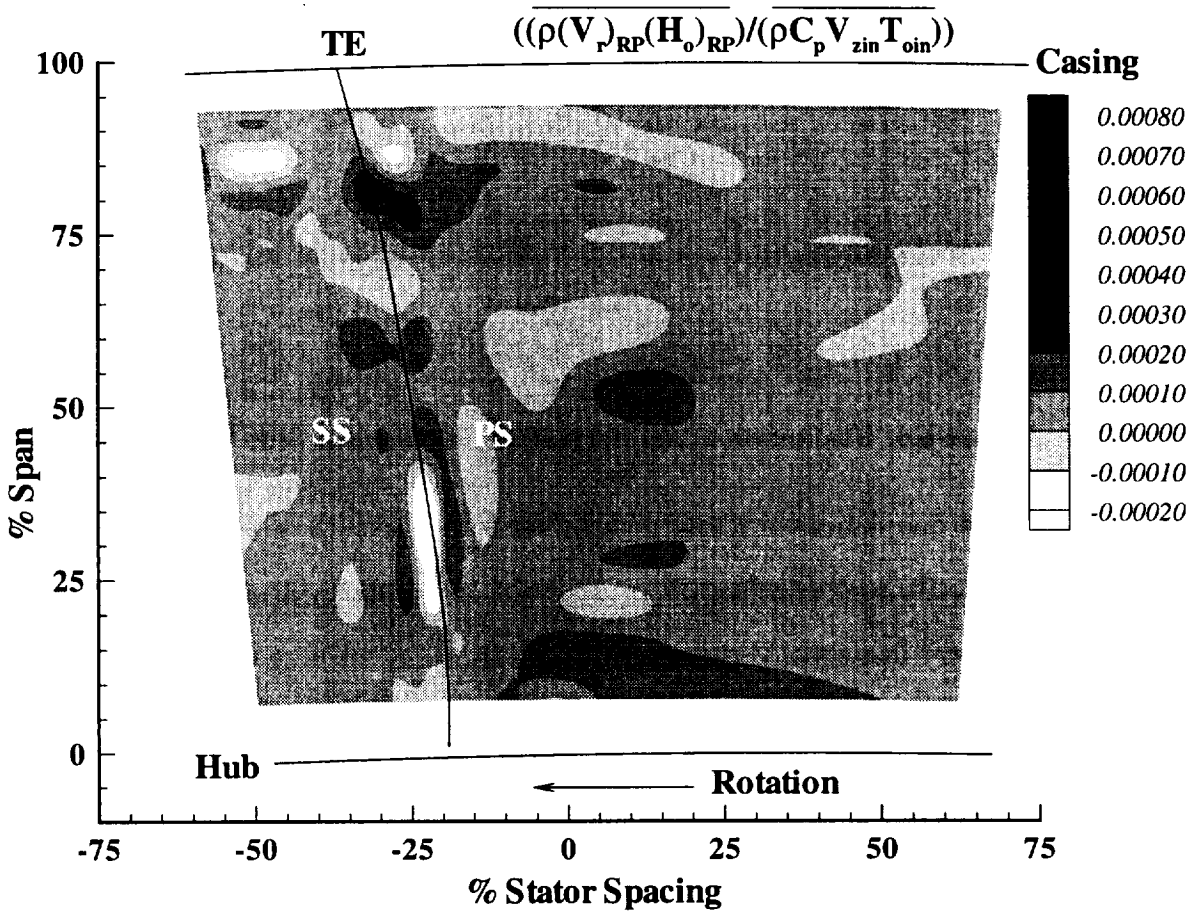

Figure 6.5. Contour Plot of the Radial Component of Deterministic Heat-Flux

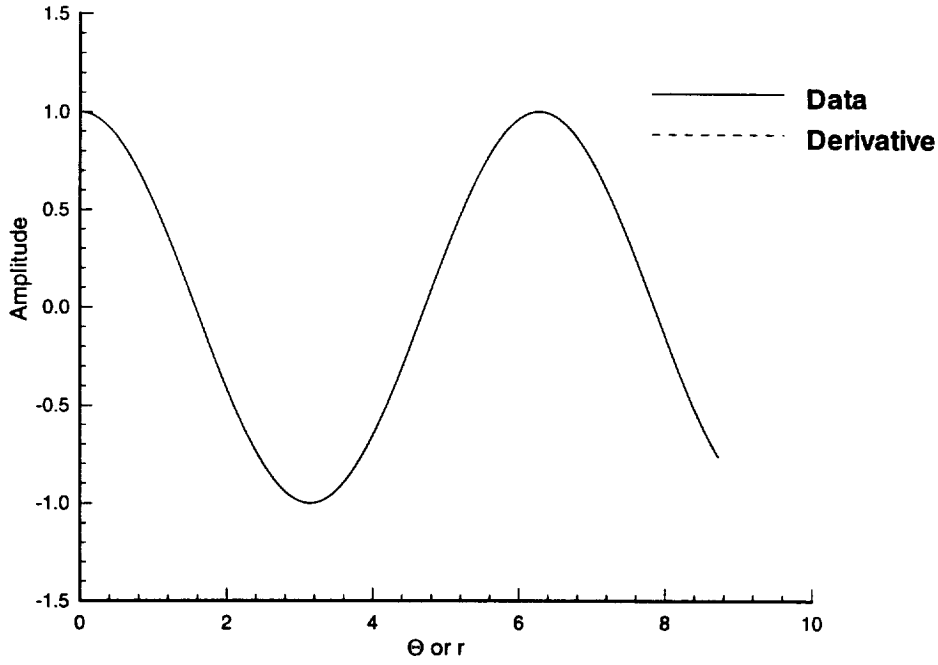

Figure 6.6. Evaluation of the Derivative Calculation: Sine Wave Distribution

2. The non-dimensional deterministic normal, shear and heat-flux terms, time averaged velocity components, static pressure and total enthalpy terms are then spline fit onto a very fine equally spaced grid with care being taken to ensure that the resulting distributions faithfully follow the original data.

3. The gradients of the various terms are calculated using this fine grid. Finite difference formulations (of second order error) are used to evaluate the gradients.

In order to ensure that the various derivatives were calculated correctly, a check was conducted with a sine wave distribution. The results are shown in Figure 6.6. The agreement between the data and the derivative is very good. After establishing this fact the various terms from the axial, tangential and radial momentum and the energy equation were calculated.

The uncertainties of the various terms of the average passage equation system are given in Tables 6.3 and 6.4. Uncertainty analysis principles given in Appendix A is used

to calculate the uncertainties of these quantities. The table shows that the uncertainty in terms related to radial velocity and gradients in the radial direction have the highest values and is probably the least reliable quantity.

6.3.1 Axial Momentum equation

Figures 6.7 and 6.8 show the contour plots of the distribution of terms AM2, AM3, AM78 and AM1213 respectively of the axial momentum equation (equation 6.2). Terms AM2 and AM3 represent the advection terms (i.e. the transport by mean flow velocity) whereas terms AM78 and AM1213 represent the deterministic transport rate in the radial and tangential direction.

Comparing terms AM2 and AM3, it is clear that AM3 is the dominant term in the wake. This indicates that the dominant transport term in the axial momentum equation in the stator wake region is due to the tangential gradients in the time averaged tangential velocity. The term AM4 is probably of the same order of magnitude as AM3 since the gradients in axial velocity decay rates are of the same order of magnitude as the tangential velocity decay rates at this axial location downstream of the stator (Lakshminarayana and Davino, 1980). Consistent with the decrease and increase of the axial and tangential velocity on the suction and pressure sides of the stator wake, both AM2 and AM3 distributions show negative and positive signs for the gradient respectively. Outside the stator wakes, the values of these terms are very small indicating that bulk of the action is taking place in the stator wake regions. In the casing endwall region away from the blade surfaces as well, the gradients in both the terms are quite small. In the suction surface casing endwall corner region, the gradients in the tangential advection terms (AM3) are much higher than the term AM2. This is probably due to the intense secondary flow features as well as possible accumulation of rotor tip leakage flow on the suction side of the stator. Hence lateral mixing is dominated by secondary flow in the endwall region and wake spreading

Table 6.3. Uncertainty of Various Terms of the Average-Passage Equation System

Quantity	Uncertainty (%)	Figures
Term AM2	±7.5%	6.7
Term AM3	±5.0%	6.7
Term AM78	±15.0%	6.8
Term AM1213	±12.0%	6.8
Term TM2	±7.5%	6.9
Term TM3	±5.0%	6.9
Term TM5	±3.54%	6.10
Term TM6	±5.0%	6.11
Term TM89	±3.54%	6.11
Term TM11	±7.5%	6.12
Term TM1314	±6.0%	6.12
Term TM16	±6.5%	6.13
Term TM1819	±6.0%	6.13
Term RM2	±10.0%	6.14
Term RM3	±8.5%	6.14
Term RM5	±6.0%	6.15
Term RM78	±3.54%	6.15
Term RM10	±15.0%	6.16
Term RM1213	±10.0%	6.16
Term RM15	±10.0%	6.17
Term RM1718	±10.0%	6.17

Table 6.4. Uncertainty of Various Terms of the Average-Passage Equation System (Contd)

Quantity	Uncertainty (%)	Figures
Term E2	±7.5%	6.18
Term E3	±5.0%	6.18
Term E5	±15.0%	6.19
Term E6	±12.5%	6.19
Term E8	±10.0%	6.19
Term E9	±8.5%	6.19
Term E14	±10.0%	6.20
Term E15	±8.0%	6.20
Term E1819	±45.0%	6.21
Term E2223	±25.0%	6.21

away from the endwalls. Without a knowledge of the term (AM4) it is very difficult to speculate on which is the most dominant mechanism of advection. Based on some single stage data, it appears as though the values of the axial gradient are very similar to the tangential gradients in the wake and free-stream.

Attention is now focused on the two deterministic stress terms that can be calculated (AM78 and AM1213). AM78 is a measure of the axial momentum change due to correlation of revolution periodic fluctuations in the radial velocity and revolution periodic fluctuations in the axial velocity and AM1213 is a measure of the tangential gradient of the correlation between the revolution periodic fluctuations in tangential velocity and revolution periodic fluctuations of the axial velocity component. It has to be mentioned here that terms AM6 and AM11 which represent the transport rates due to the revolution aperiodic terms are very small compared with AM78 and AM1213 respectively and can for the most part be neglected for modeling stator exit flows. It can be observed from figure 6.7 that the highest levels of these terms occur in the stator wake particularly on the pressure side of the stator especially for the term AM1213. Even though the term AM1213 shows higher levels than the term AM78, the distributions show that neither term can be neglected from the equation system. High negative values of the term AM1213 on the pressure side of the stator wake is indicative of the transport caused by the deterministic fluctuations away from the wake. AM78 also shows some gradients in the casing endwall region away from the blade surfaces which is smeared across the entire passage.

6.3.2 Tangential Momentum Equation

Figures 6.9, 6.10, 6.11, 6.12 and 6.13 show the contour plots of the distribution of terms TM2, TM3, TM5, TM6, TM89, TM11, TM1314, TM16 and TM1819 of the tangential momentum equation (equation 6.3). Terms TM2 and TM3 represent the advection terms, terms TM5 and TM89 are a result of the cylindrical co-ordinate system used, TM6

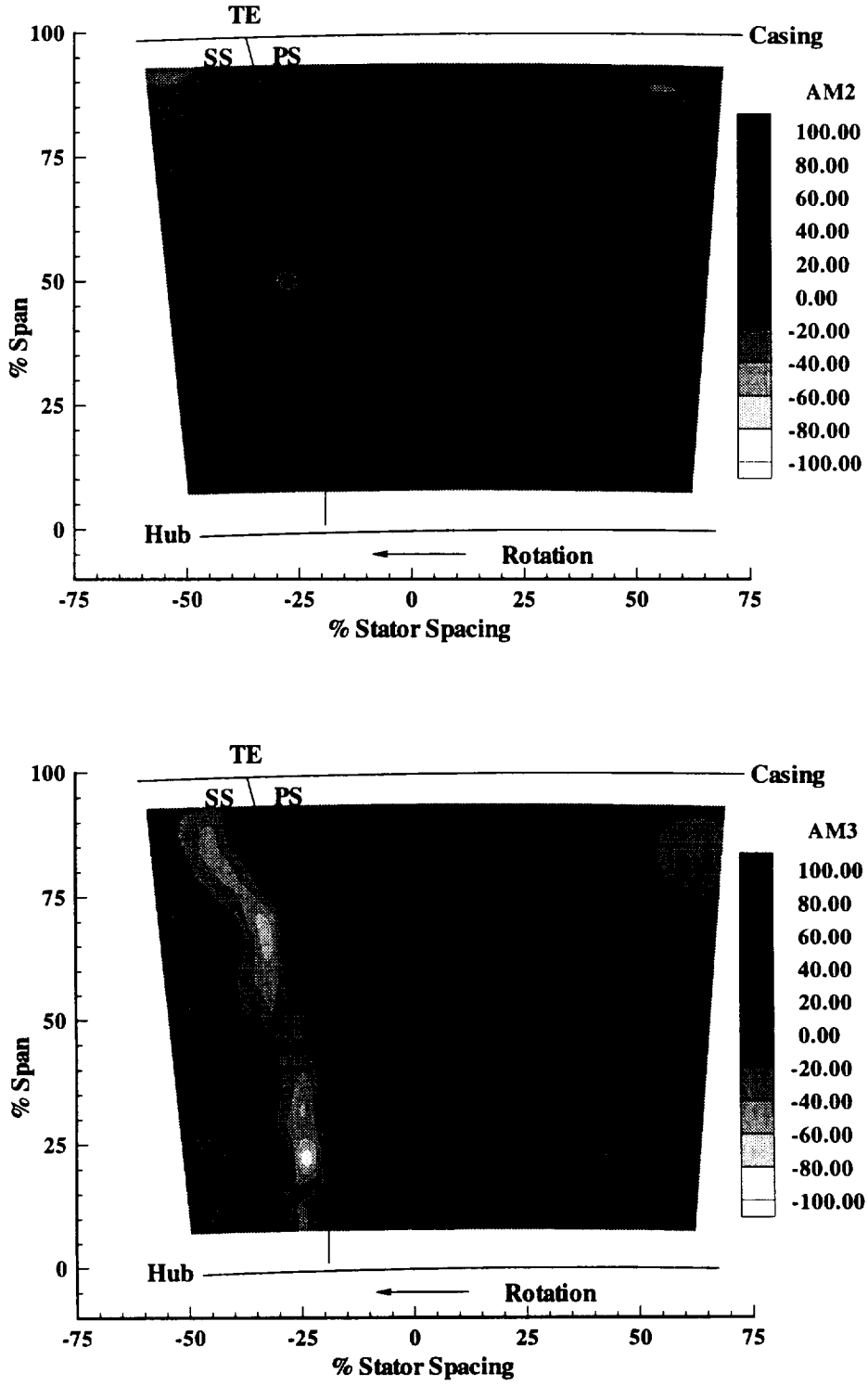

Figure 6.7. Contour Plots of Terms (a) AM2 and (b) AM3 of the Axial Momentum Average Passage Equation

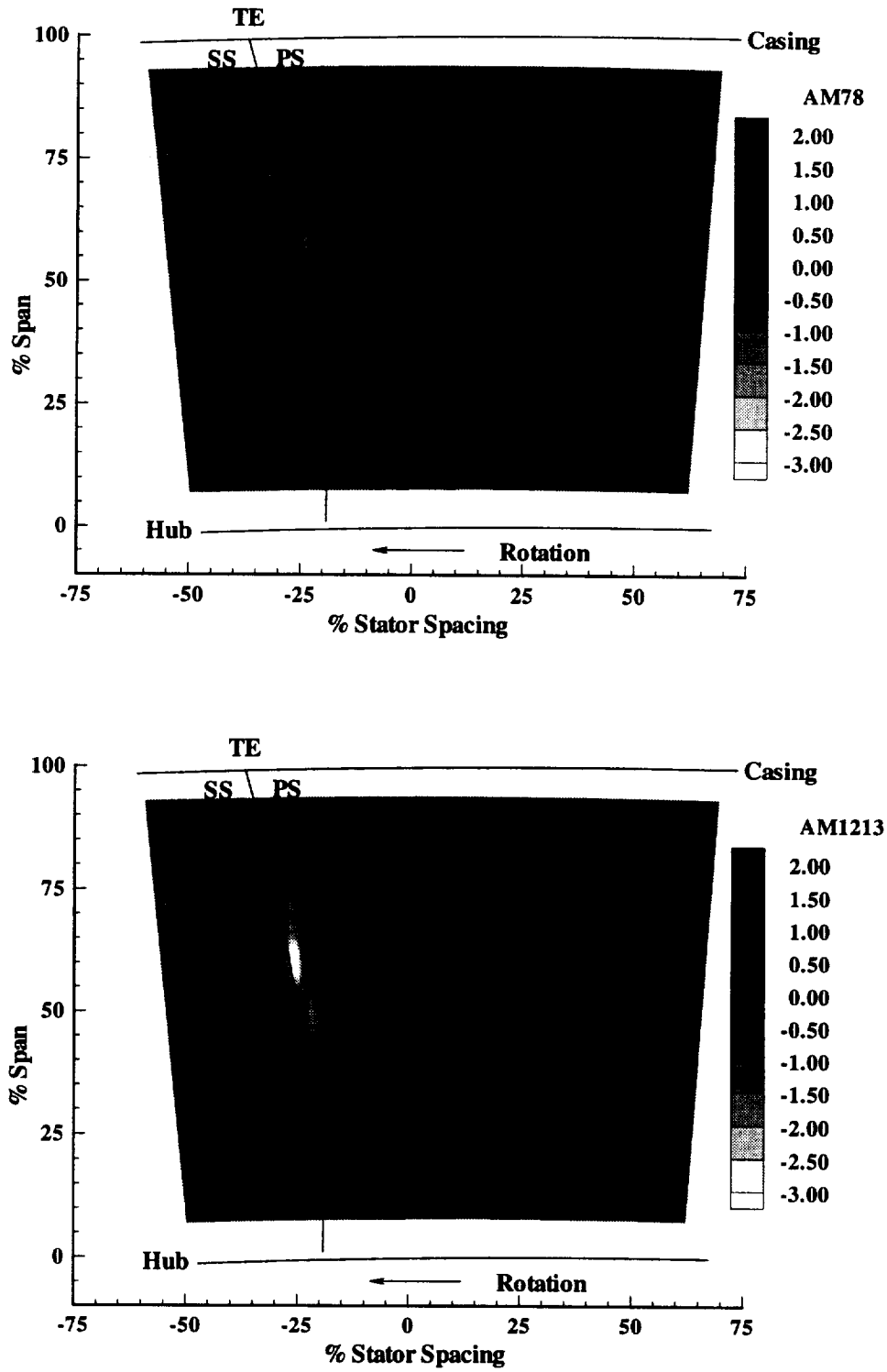

Figure 6.8. Contour Plots of Terms (a) AM78 and (b) AM1213 of the Axial Momentum Average Passage Equation

the viscous shear stress in the $r - \theta$ direction, terms TM1314 and TM1819 represent the deterministic transport rate in the radial and tangential direction and terms TM11, TM16 represent the molecular transport rate in the radial and tangential directions respectively.

Comparing terms TM2 and TM3, it is clear that TM3 is the dominant term in the wake. Term TM3 includes the static pressure as well. This indicates that the dominant transport term in the tangential momentum equation in the wake region is due to the tangential velocity and its gradient in the tangential direction. Very little information is available on the gradients in the axial direction (Term TM4) but it is expected to be similar in magnitude to term TM3 due to the high decay rates of the stator wake expected to be present at this axial location. The gradients (TM3) are higher on the pressure side of the stator than on the suction surface. This is due probably to the transport of rotor exit flow towards the pressure surface of the downstream stator. This increases the magnitude and gradients in tangential velocity. This also leads to higher total temperatures observed on the pressure surface location. Outside the stator wakes, the values of these terms are very small indicating that bulk of the mixing takes place in the stator wake regions. In the casing endwall region away from the blade surfaces as well, the gradients in both the terms are quite small. In the suction surface casing endwall corner region, a small region of high values of terms TM3 is observed. This is probably due to the intense secondary flow features as well as possible accumulation of rotor tip leakage vortex with large tangential velocities on the suction side of the stator. Hence it is safe to reiterate that advection due to tangential velocity is more dominant than advection due to radial velocity at this location. However, without knowing the value of the axial term (TM4) it is very difficult to speculate on which is the most dominant mechanism of advection. Based on some single stage data, it appears as though the values of the axial gradient (TM4) are very similar to the tangential gradients (TM3) in the wake and free-stream.

Term TM5 and TM89 are not gradient terms so they do not change the transport

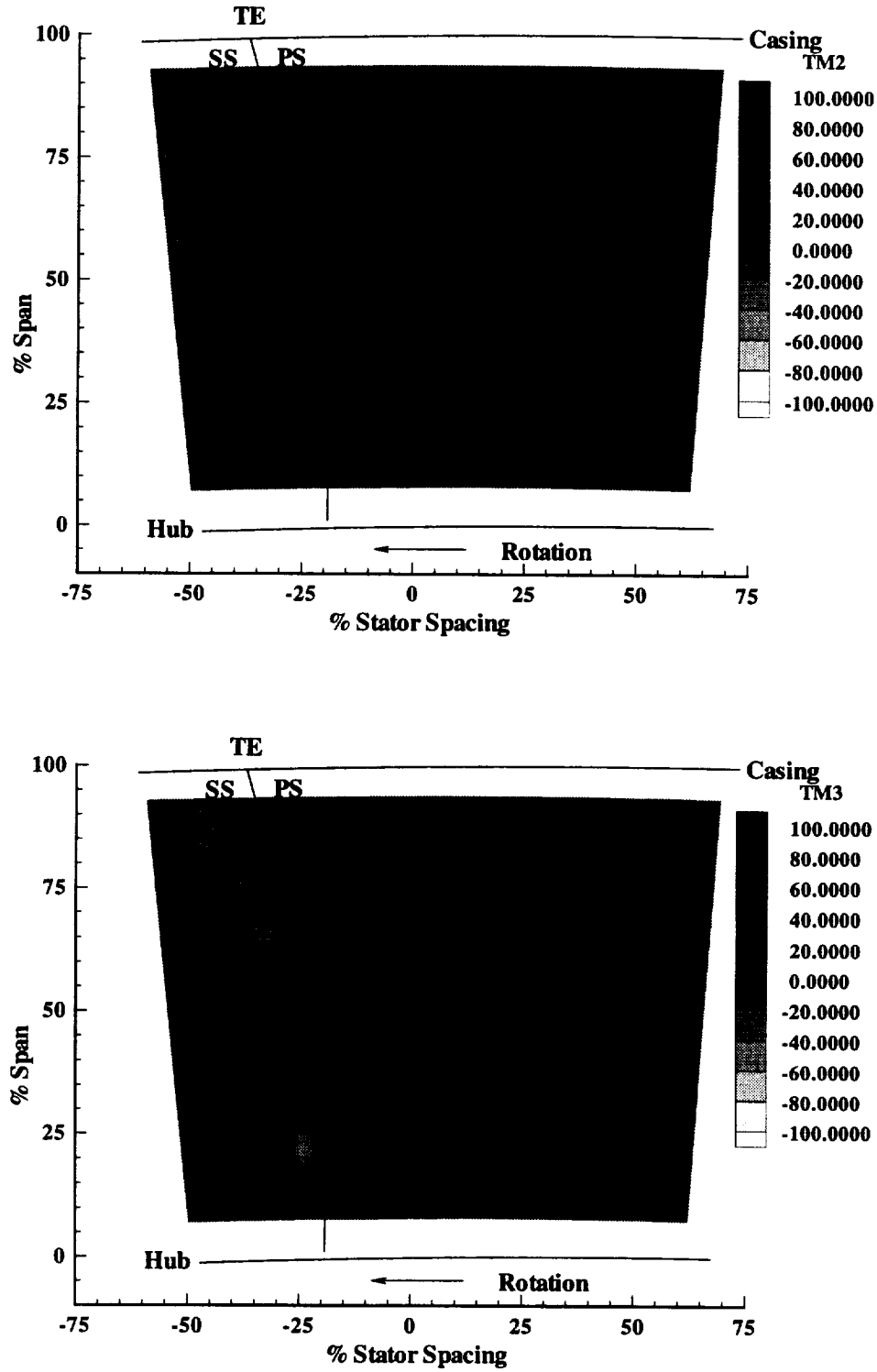

Figure 6.9. Contour Plots of Terms (a) TM2 and (b) TM3 of the Tangential Momentum Average Passage Equation

characteristics of the flow. They are like source terms and contribute towards the overall balance of tangential momentum. Term TM5 represents the product of the tangential and radial velocity and term TM89 represents the product of the deterministic unsteadiness in radial velocity and tangential velocity. The highest levels of TM5 occur on the suction side near the casing endwall corner and in the hub endwall flow. This is consistent with the highest levels of secondary and leakage flow distributions observed in these locations respectively. Term TM6 represents the viscous shear stress (molecular) in the $r - \theta$ direction. Figure 6.11 shows a comparison between the viscous shear stress and the apparent mixing stress in the $r - \theta$ direction (TM89). At first glance it is clear that the relative magnitudes of each of these terms is of the same order of magnitude. Also the regions of high levels of these terms are quite common to both the terms. High levels are seen in the wake, suction surface casing endwall corner and casing endwall region away from the blade surfaces. Since they are of the same order of magnitude the net contribution to the tangential momentum distribution is almost negligible and may be neglected for modeling of stator exit flows fields.

Figure 6.12 shows the distribution of terms TM11 and TM1314 of the tangential momentum equation. TM1314 is a measure of the radial gradient of revolution periodic shear stress and TM11 represents the radial transport due to viscous or molecular shear. It has to be mentioned here that term TM12 which represents the transport rate of the revolution aperiodic term is very small compared with TM1314 and can for the most part be neglected for modeling stator exit flows. The distributions show that for the most part except for small patches in the flow field both these terms are quite small. Now it remains to check whether these terms can be neglected with respect to the tangential transport terms (TM16 and TM1819).

Contour plots of terms TM16 and TM1819 are shown in Figure 6.9. TM16 is a measure of the tangential transport due to viscous normal stress (molecular) and TM1819

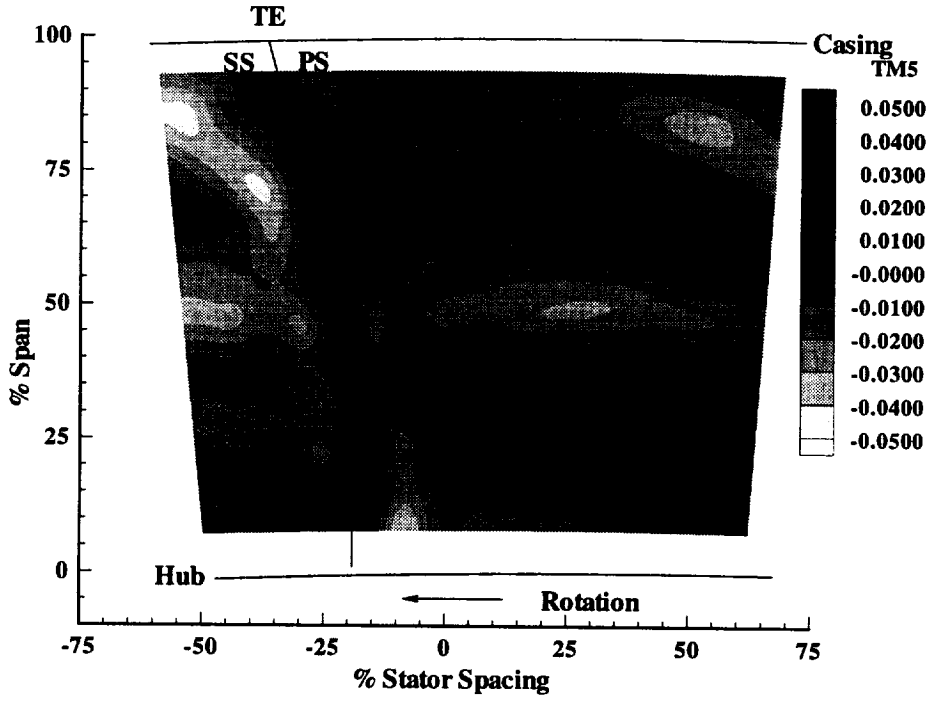

Figure 6.10. Contour Plot of Term TM5 of the Tangential Momentum Average Passage Equation

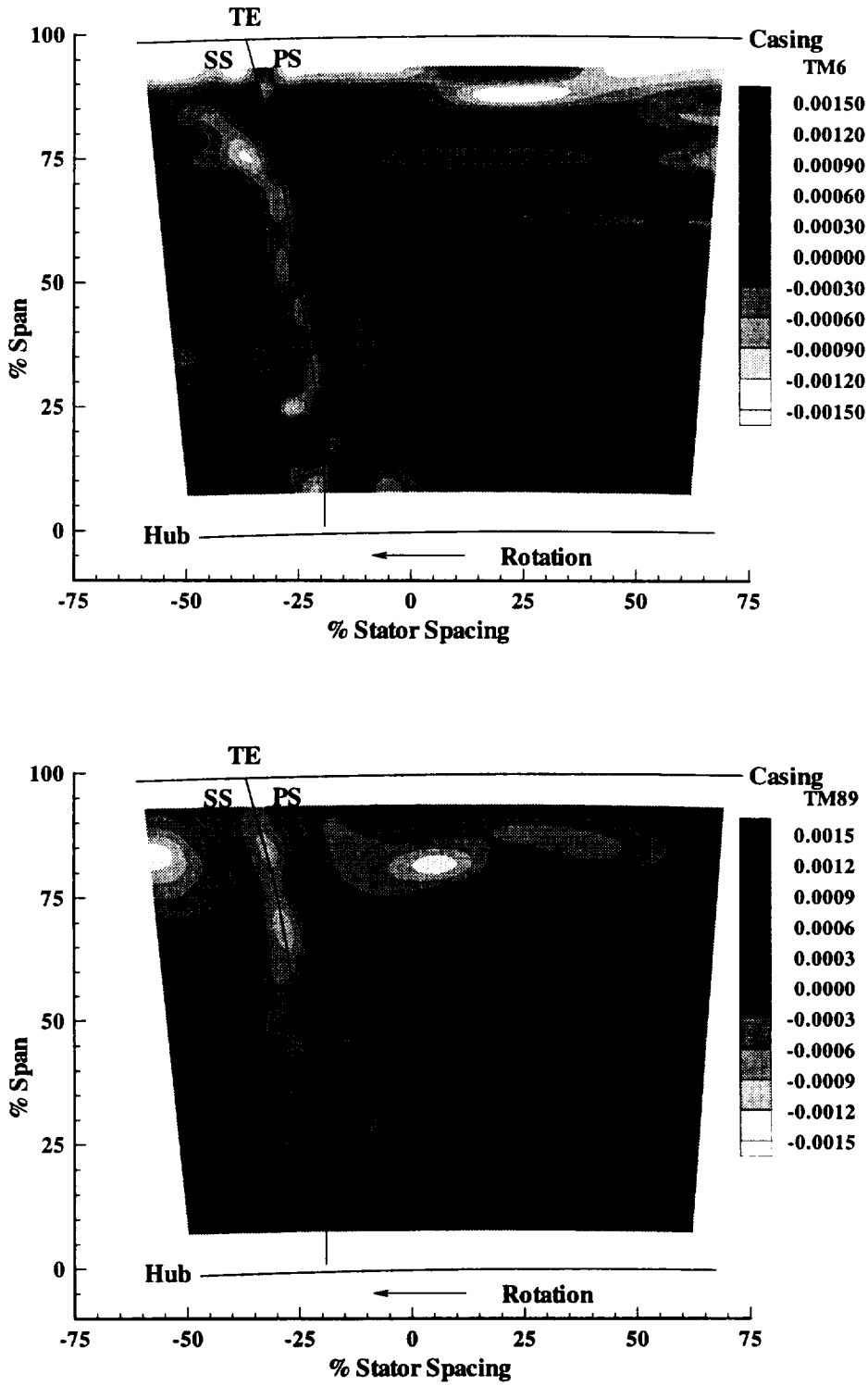

Figure 6.11. Contour Plots of Terms (a) TM6 and (b) TM89 of the Tangential Momentum Average Passage Equation

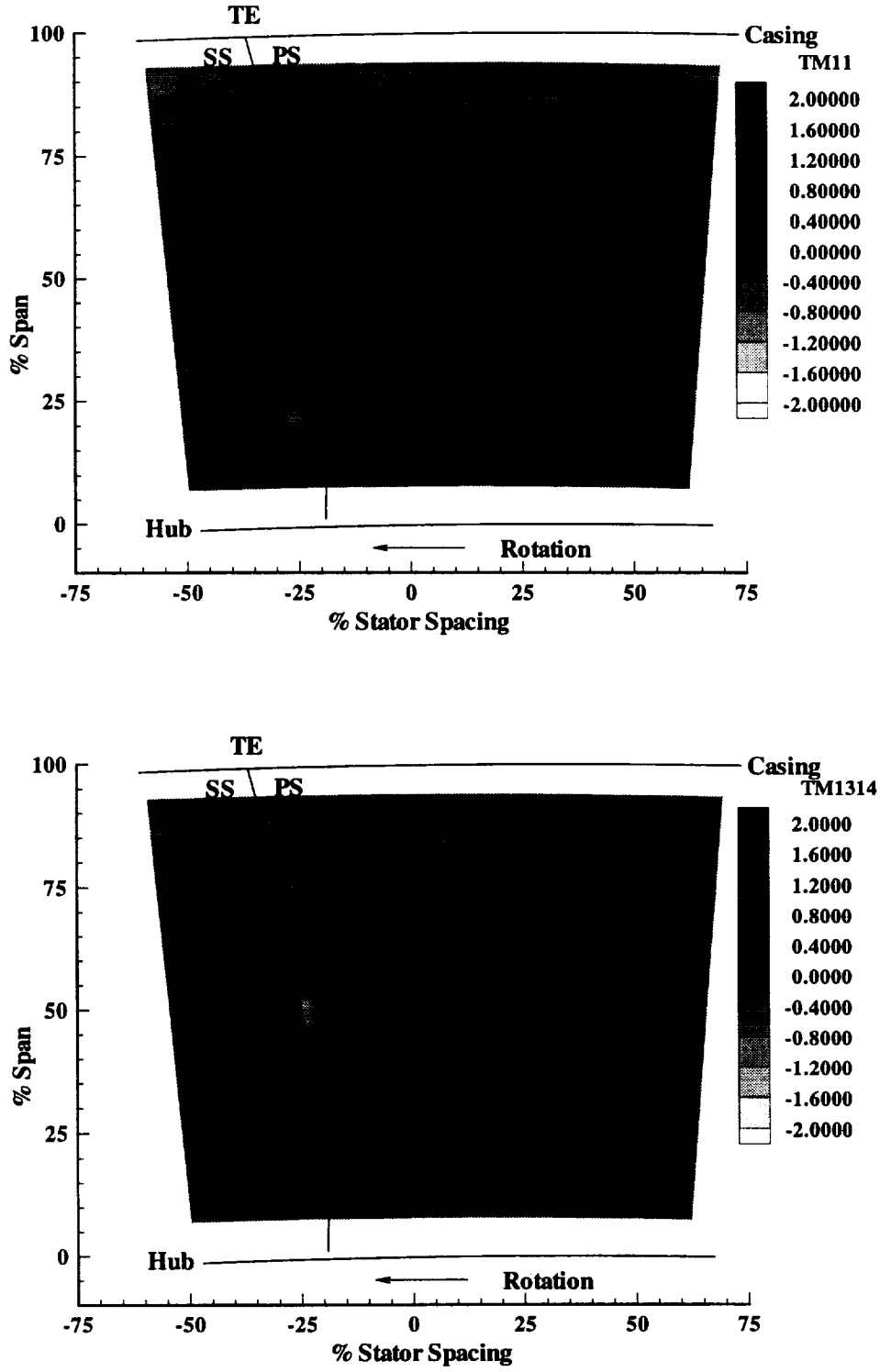

Figure 6.12. Contour Plots of Terms (a) TM11 and (b) TM1314 of the Tangential Momentum Average Passage Equation

represents the tangential transport due to revolution periodic fluctuations in the tangential velocity (deterministic normal stress). The highest levels of both these terms occur in the stator wake and also are of the same order of magnitude. And compared to terms TM11 and TM1314, terms TM16 and TM1819 were found to be much higher in magnitude and hence terms TM11 and TM1314 can be neglected. However, no information is available on the magnitudes of terms TM10, TM15 and TM20 as well as the gradients in the axial direction (TM21, TM22, TM2324 and TM25). As a result, no final decision can be made with regard to neglecting deterministic terms in the equation system.

6.3.3 Radial Momentum Equation

Figures 6.14, 6.15, 6.16 and 6.17 show the contour plots of the distribution of terms RM2, RM3, RM5, RM78, RM10, RM1213, RM15 and RM1718 of the radial momentum equation (equation 6.4). Terms RM2 and RM3 represent the advection terms, terms RM5 and RM78 are a result of the cylindrical co-ordinate system used, terms RM1213 and RM1718 represent the deterministic transport rate in the radial and tangential direction and terms RM10, RM15 represent the molecular transport rate in the radial and tangential directions respectively.

Comparing terms RM2 and RM3, it is clear that RM3 is the dominant term in the wake. This indicates that the dominant transport in the wake is caused by the advection terms due to the tangential velocity. The radial gradients in radial velocity are small due to the very small levels of radial flow found in the stator exit flow compared to the tangential velocity. Very little information is available on the gradients in the axial direction but it is expected to be small since the radial velocity is quite low. Outside the stator wakes, the values of these terms are very small indicating that bulk of the action takes place in the stator wake regions just as in the axial and tangential momentum equations. In the casing endwall region away from the blade surfaces as well, the gradients in both the terms are

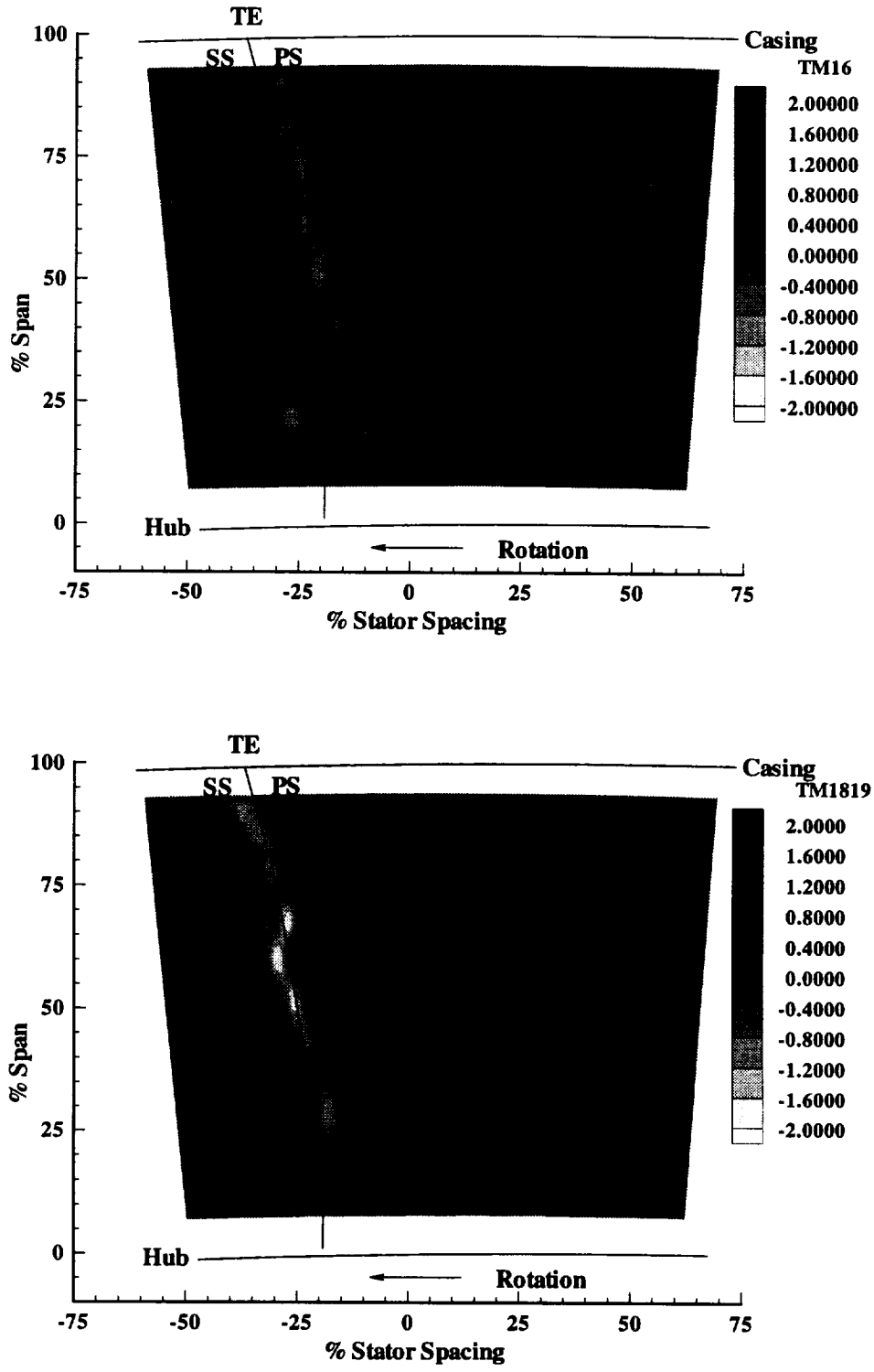

Figure 6.13. Contour Plots of Terms (a) TM16 and (b) TM1819 of the Tangential Momentum Average Passage Equation

quite small. In the suction surface casing endwall corner region, a small region of high values of terms RM3 is observed. This is probably due to the intense secondary flow features found in this region as seen in Chapter 4.

Figure 6.15 shows the term RM5, which in essence behaves as a source term in the radial momentum equation. From an order of magnitude analysis it is of the same order of magnitude as RM2. The term RM78 represents the distribution of the deterministic revolution periodic normal stress due to periodic tangential velocity fluctuations. This also behaves as a source term on the right hand side of the radial momentum equation. Highest values are seen on the pressure side of the wake from about 35% span to the casing, but the order of magnitude of this term is much smaller than the term RM5 and can be neglected compared to the term RM5.

Figure 6.16 shows the distribution of terms RM10 and RM1213 of the radial momentum equation. RM10 is a measure of the transport due to viscous normal stress in the radial direction and RM1213 is a measure of the radial transport of revolution periodic fluctuations in the radial velocity due to revolution periodic fluctuations in the radial velocity (deterministic normal stress in radial velocity). Values of the term RM10 is much smaller than RM1213 and can for the most part be neglected. However, comparisons must be made to the tangential gradient terms RM15 and RM1718 which represent the transport due viscous shear stress and deterministic shear stress respectively. The contour plots of these terms are shown in Figure 6.17. The radial distribution shows that the term RM15 is continuous in the stator wake compared to the RM1718 which is only present at certain locations. However, the magnitudes of terms RM15, RM1718 and RM1213 are of the same order and hence cannot be neglected in the equation system. This leads to evaluation of strategies to model terms RM1213 and RM1718 of the radial momentum equation.

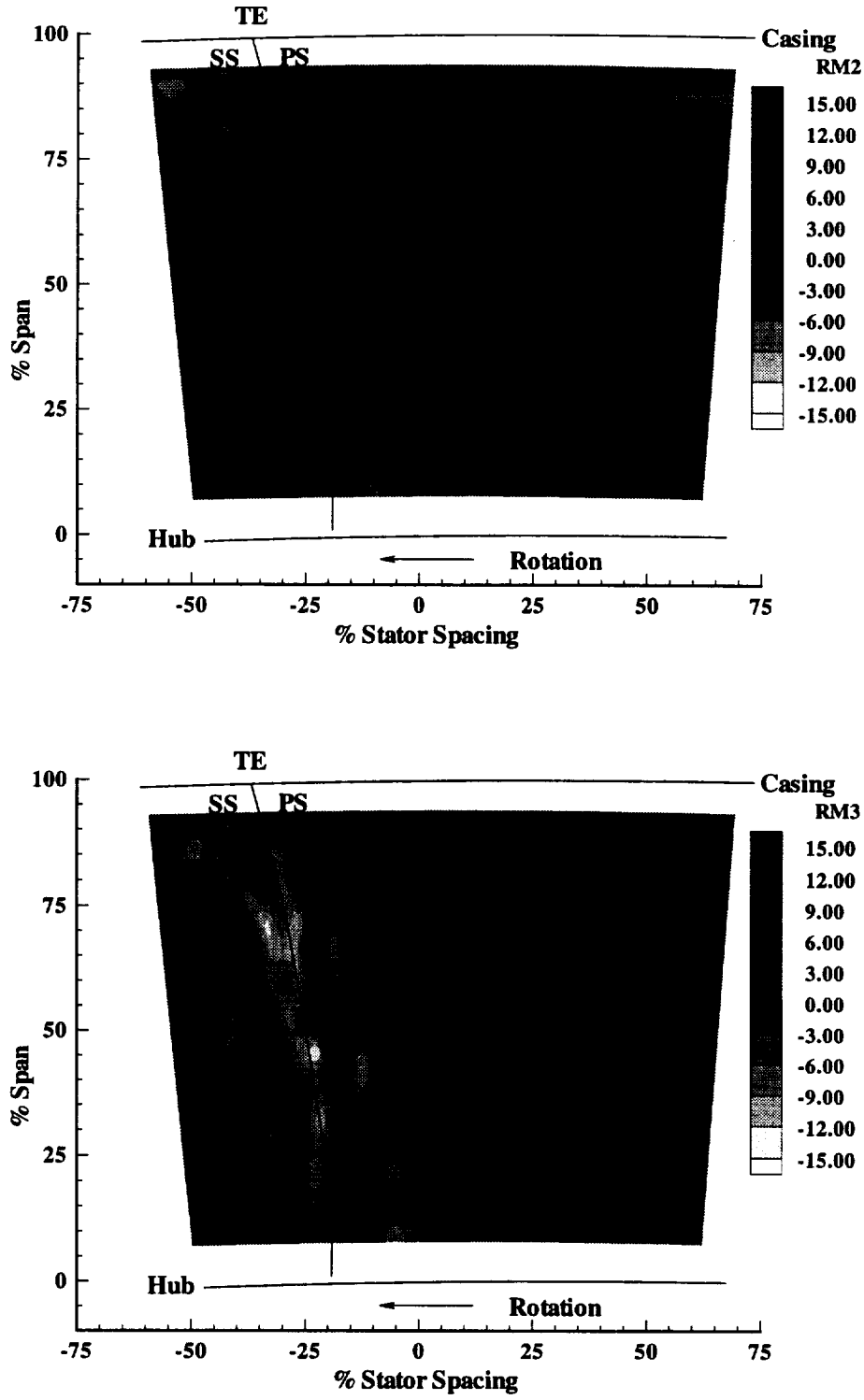

Figure 6.14. Contour Plots of Terms (a) RM2 and (b) RM3 of the Radial Momentum Average Passage Equation

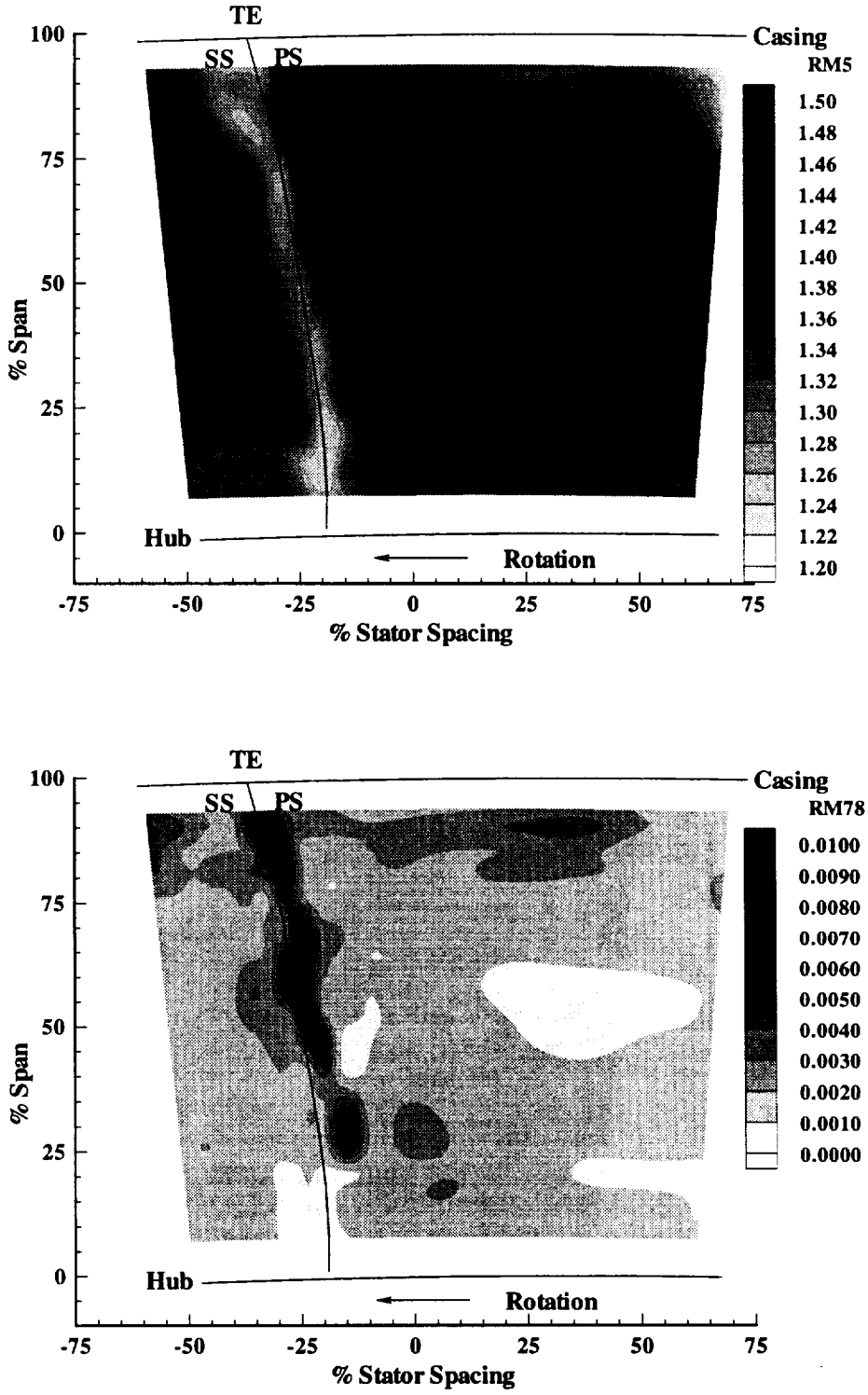

Figure 6.15. Contour Plots of Terms (a) RM5 and (b) RM78 of the Radial Momentum Average Passage Equation

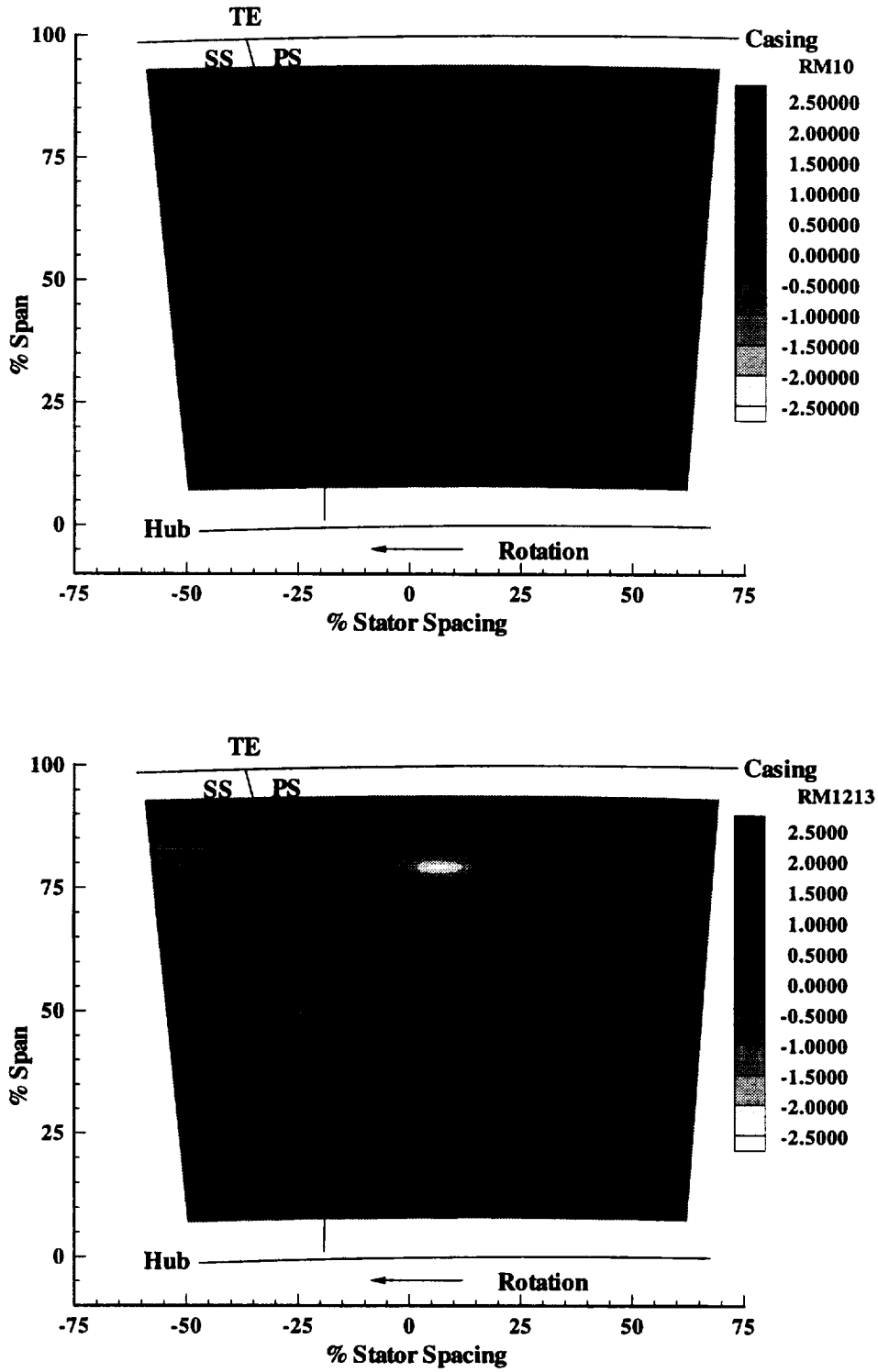

Figure 6.16. Contour Plots of Terms (a) RM10 and (b) RM1213 of the Radial Momentum Average Passage Equation

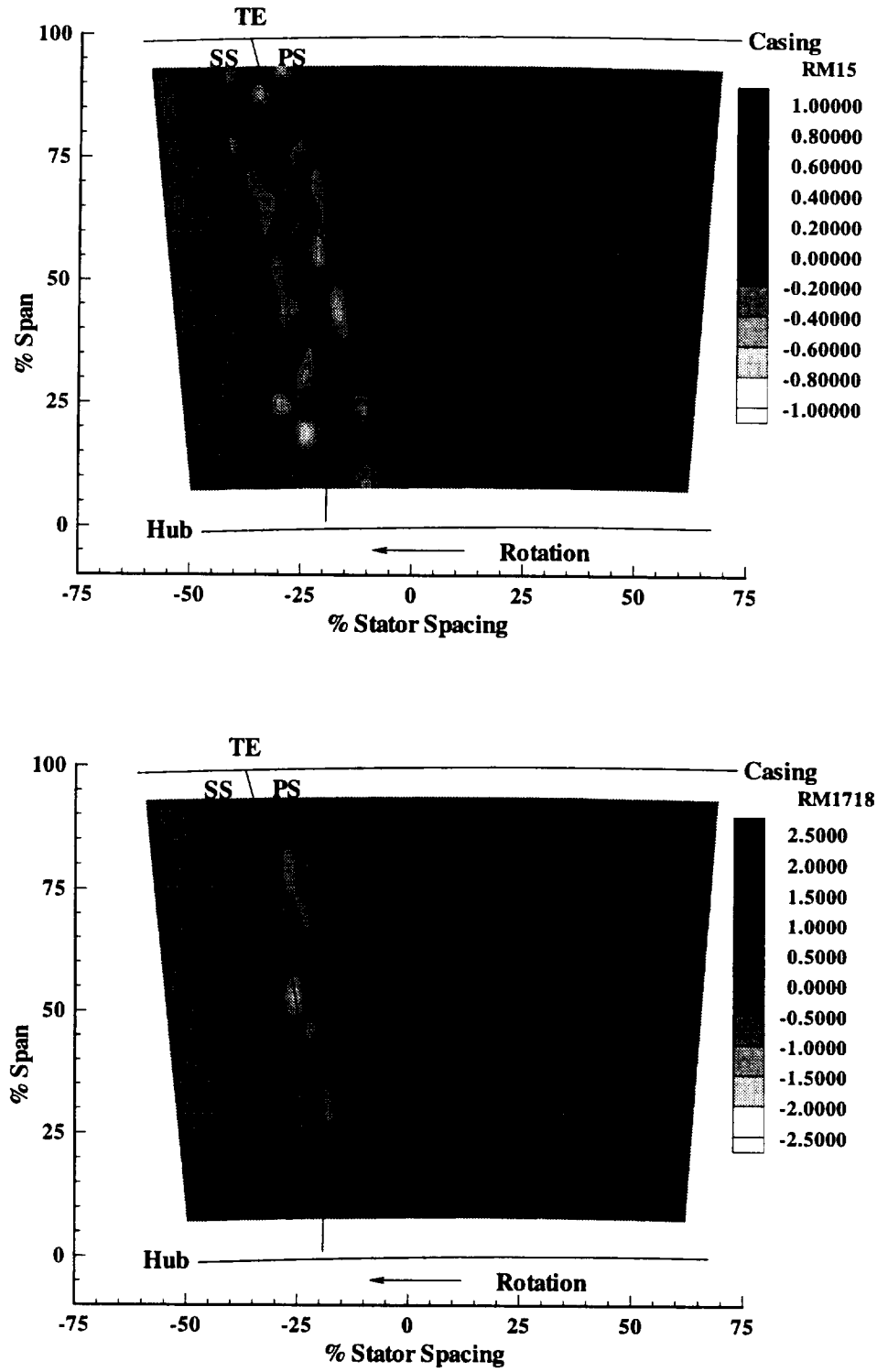

Figure 6.17. Contour Plots of Terms (a) RM15 and (b) RM1718 of the Radial Momentum Average Passage Equation

6.3.4 Energy Equation

Figures 6.18, 6.19, 6.20 and 6.21 show the contour plots of the distribution of terms E2, E3, E5+E6, E8+E9, E14, E15, E1819 and E2223 of the average passage energy equation (equation 6.5). Terms E2 and E3 represent the advection of stagnation enthalpy by the time averaged radial and tangential velocity components, E5, E6, E8 and E9 represent the work done by the normal and shear stresses (molecular), terms E14 and E15 represents the transport of thermal flux by the molecular thermal conductivity of the due to radial and tangential gradients respectively and terms E1819 and E2223 represent the change in stagnation enthalpy due to gradient of the revolution periodic heat-flux due to radial and tangential velocities. Unfortunately some of the terms such as the influence of the work done by viscous stress (both time averaged as well as periodic fluctuations) cannot be calculated due to the lack of the axial gradient of the respective velocity components.

Comparing terms E2 and E3, it was observed that E3 is almost an order of magnitude higher than E2 and the highest gradients occur in the stator wake. The distribution is continuous from hub to tip for term E3 and very discontinuous in the radial direction for term E2. Outside the wake, the value of the term E3 almost goes to zero. In the casing endwall region, there is a thickening of the wake and high levels of transport are seen. The advection is away from the blade surfaces on the suction side and is probably responsible for the lack of increase of total temperature in this region. Term E14 represents the transport of the thermal flux by the molecular thermal conductivity of the fluid and was found to be of the same order of magnitude as the advection terms in the wakes.

Terms E5, E6, E8 and E9 represent the work done by the normal and shear stresses (molecular) in the radial and tangential directions. These terms are shown in Figure 6.19. The highest levels of terms E8+E9 occur in the wake region and E5+E6 occur in the casing endwall region. Both these terms are of the same order of magnitude and hence all these

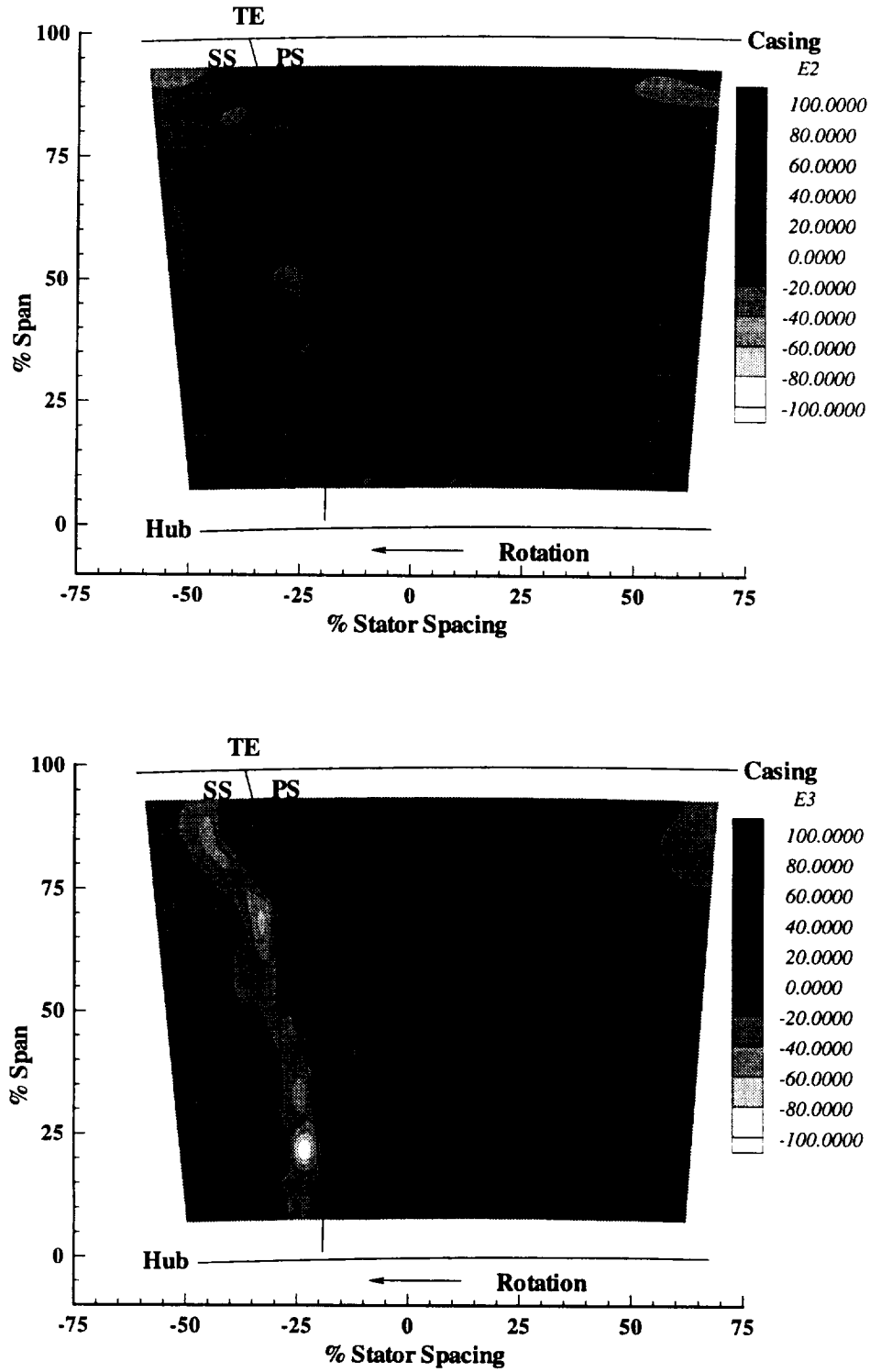

Figure 6.18. Contour Plots of Terms (a) E2 and (b) E3 of the Energy Average Passage Equation

terms are needed in the energy equation. These terms can be easily calculated as they only involve the mean velocity components.

Terms E14 and E15 represent the transport of the thermal flux by the molecular thermal conductivity of the fluid and Figure 6.20 shows that the tangential gradient is an order of magnitude higher than the radial gradient inside the wakes. Outside the wakes, both the terms have similar magnitude. In the casing endwall region, the radial transport term is much higher compared with the tangential transport. So both terms are necessary for the solution of the energy equation.

Figure 6.21 shows the distribution of terms E1819 and E2223 of the energy equation. E1819 and E2224 represent the change in stagnation enthalpy due to gradient of the revolution periodic heat-flux due to radial and tangential velocities respectively. It has to be mentioned here that terms E17 and E21 which represent the transport rates by the revolution aperiodic terms are very small compared with E1819 and E2223 respectively and can for the most part be neglected for modeling stator exit flows. The highest levels of these terms occur in the stator wake and in the casing endwall region. A core of high value of term E1819 is seen in the casing endwall suction surface corner region. This shows that high levels of mixing occur in this region due to the transport of stagnation enthalpy by the radial velocity in the casing corner flow. Outside the wake in the core flow there are no significant gradients in E2223 except in the hub endwall region at mid-pitch. It can be concluded that the leakage flow near the hub has dominant influence on transport by the mean velocity, transport by the deterministic radial velocity fluctuation and possibly transport by the unresolved component.

Based upon the results of traverses in the multistage compressor facility at medium speed and at the peak efficiency condition, it can be generally concluded that there is a need to model some of the deterministic stress and heat-flux terms for the accurate prediction of stator exit flows. These terms are: $\overline{\rho V_{\theta RP} V_{zRP}}$, $\overline{\rho V_{\theta RP} V_{\theta RP}}$, $\overline{\rho V_{\theta RP} V_{rRP}}$, $\overline{\rho V_{rRP} H_{oRP}}$

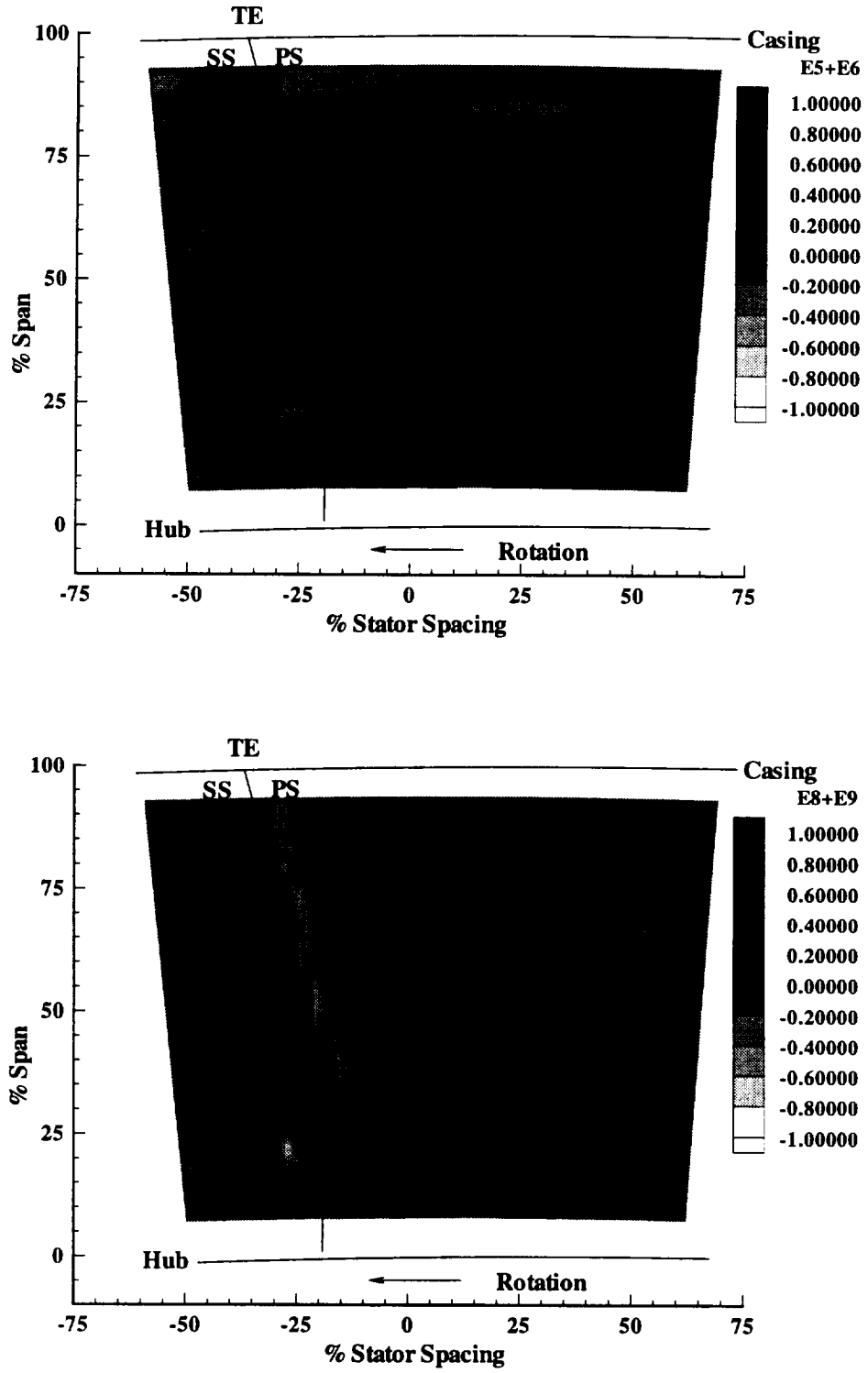

Figure 6.19. Contour Plots of Terms (a) E5+E6 and (b) E8+E9 of the Energy Average Passage Equation

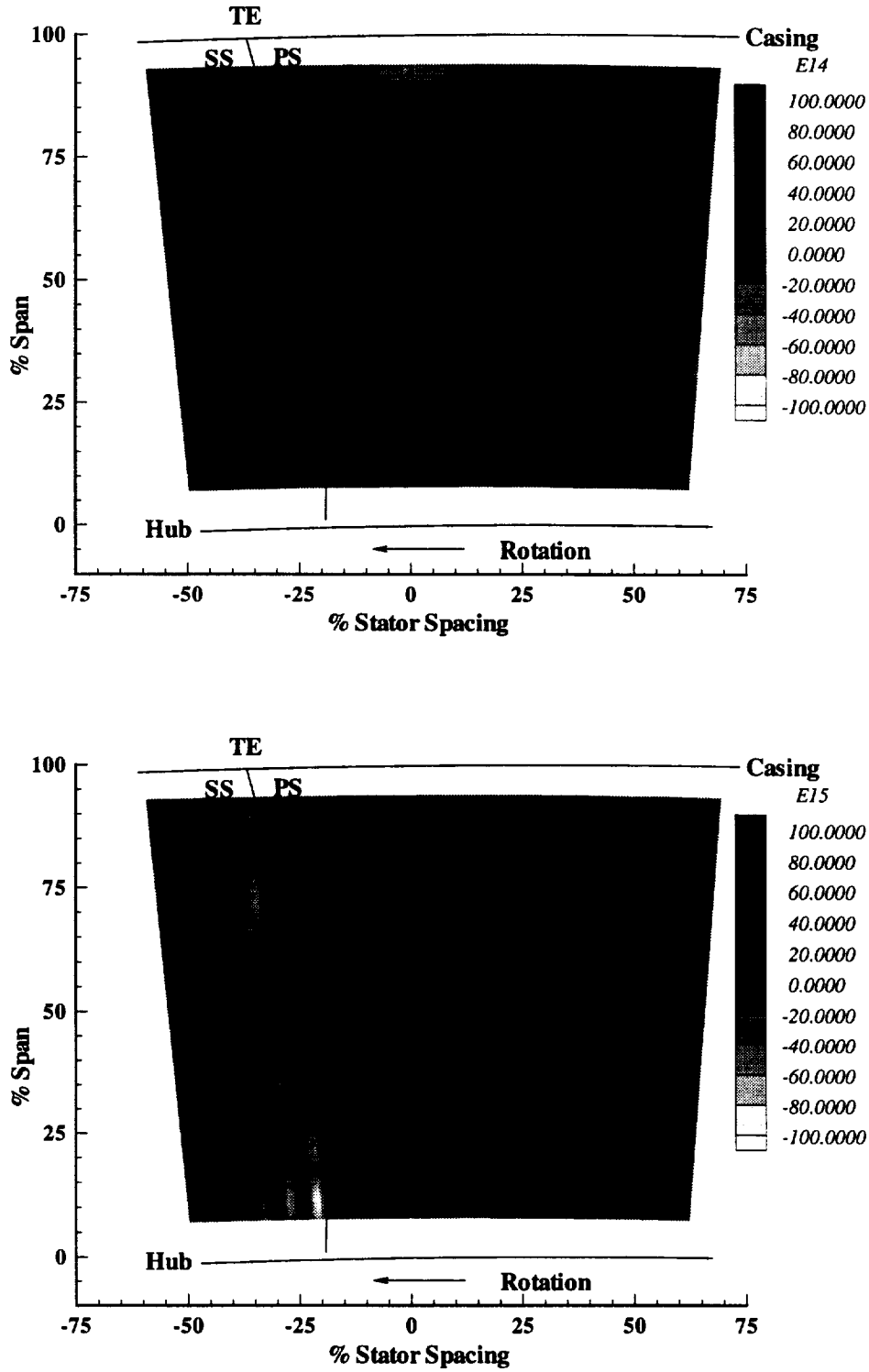

Figure 6.20. Contour Plots of Terms (a) E14 and (b) E15 of the Energy Average Passage Equation

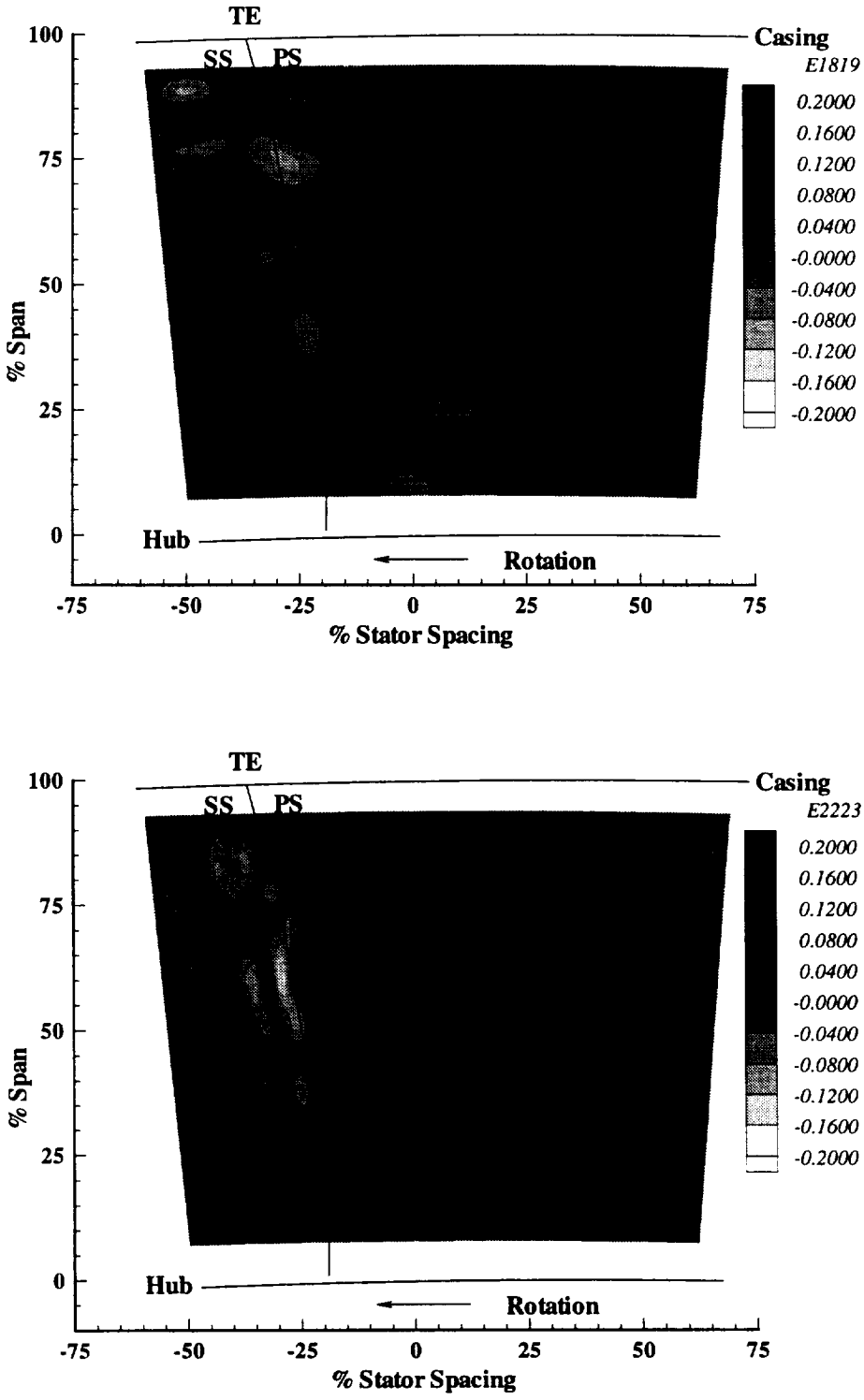

Figure 6.21. Contour Plots of Terms (a) E1819 and (b) E2223 of the Energy Average Passage Equation

and $\overline{\overline{\rho}\overline{V_{\theta RP}}\overline{H_{oRP}}}$. Since the emphasis on this thesis has been on the temperature and pressure fields, possible modeling strategies for only the deterministic heat-flux terms will be explored in the next section.

6.4 Modeling of the Deterministic Heat-Flux Distribution

From the previous sections it can be recognized that the terms $\overline{\overline{\rho}\overline{V_{rRP}}\overline{H_{oRP}}}$ and $\overline{\overline{\rho}\overline{V_{\theta RP}}\overline{H_{oRP}}}$ mainly occur in the wakes, in the casing endwall regions on the suction side and in the hub endwall at midpitch (Figures 6.3(a), 6.3(b) and 6.3(c)). These are also regions of the highest gradients in total temperature. So it may be possible to correlate the gradients in total temperature with the corresponding heat-fluxes as in a gradient diffusion model and this is explored in this section. It should be cautioned here that the magnitudes of the deterministic heat-fluxes are small in the endwall regions due to the averaging procedures employed. High levels of unresolved components of heat-flux are expected in the endwall region since high levels of unresolved velocities and temperatures were also observed in this region. Since the unresolved fluctuations in velocity and total temperature are measured independently no attempt is made to correlate these terms in this paper. Using concepts analogous to the eddy diffusivities of heat for turbulent flow an attempt is made to determine the eddy diffusivity of heat (ϵ_{D_θ}).

$$-\overline{\overline{\rho}\overline{V_{\theta RP}}\overline{H_{oRP}}} = \epsilon_{D_\theta}\left(\frac{1}{r}\frac{\partial \overline{H}_o}{\partial \theta}\right) \tag{6.12}$$

6.4.1 Distribution of Deterministic Eddy Diffusivities of Heat

Figure 6.22 shows the contour plot of the deterministic eddy diffusivity of heat ($\epsilon_{D\theta}$) normalized by the thermal diffusivity of heat (α) downstream of the second stator. Since the gradients in the total enthalpy as well as the numerical value of the velocity-enthalpy correlation terms are almost zero outside the wake and endwall regions, the numerical

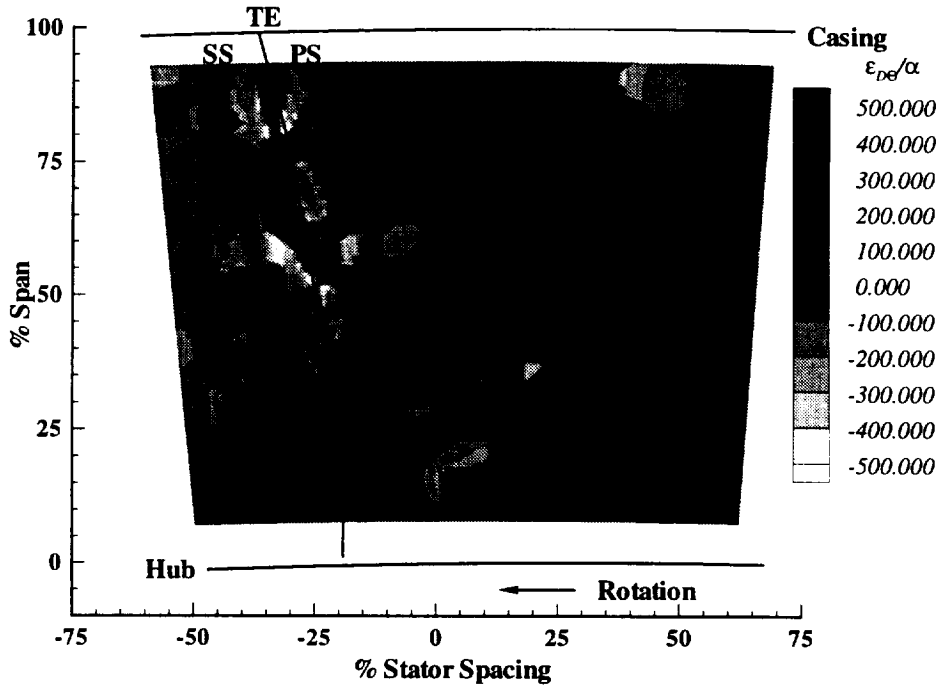

Figure 6.22. Contour Plot of the Deterministic Diffusivity of Heat Normalized by the Thermal Diffusivity

value of the eddy diffusivity is forced to be equal to zero in order to eliminate any numerical singularities.

There was wide variation in the value of $\epsilon_{D\theta}$ in the stator wake region it was concluded that the modeling based on eddy diffusivities is not adequate to represent the deterministic heat flux $\overline{\overline{\rho} V_{\theta RP} H_{oRP}}$ and this approach was abandoned.

Chapter 7

SUMMARY AND CONCLUSIONS

The flow field in a multistage compressor is three-dimensional, unsteady, and turbulent with substantial viscous effects. Some of the specific phenomena that has eluded designers include the effects of rotor-stator and rotor-rotor interactions and the physics of mixing of velocity, pressure and temperature fields. An attempt will be made, to resolve experimentally, the unsteady pressure, temperature and velocity fields downstream of the second stator of a multistage axial flow compressor which will provide information on rotor-stator interaction effects and the nature of spanwise mixing in an embedded stator of a three stage axial flow compressor.

The major objectives of the thesis were:

1. To understand the nature of the steady and unsteady three-dimensional pressure and temperature field in an embedded stator of a multi-stage axial flow compressor with a view of identifying sources and magnitudes of unsteadiness and losses.

2. To understand the physics of rotor-stator interaction and their effects on the unsteady total pressure and temperature field downstream of an embedded stator.

3. To correlate the periodic, aperiodic and unresolved components of velocity and total temperature (velocity-temperature correlation) to evaluate the phenomena of thermal energy transport in a multistage compressor.

4. To evaluate the magnitude and nature of the various terms of the average-passage equation system, their gradients in the radial and circumferential direction and their relative weights so as to provide guidance to CFD specialists and compressor designers.

5. To evaluate the magnitude of the uncertainty in various measurement variables including velocity-temperature correlations.

6. To provide benchmark quality data to validate various flow models and solvers for multistage compressor flow field analysis and prediction.

In order to accomplish the above objectives, an experimental investigation of the steady and the unsteady flow downstream of the second stator of a three stage axial flow compressor representative of the aft stages of a high pressure core compressor was undertaken. Detailed area traverse measurements using pneumatic five hole probe, thermocouple probe, semi-conductor total pressure probe (Kulite) and an aspirating probe downstream of the second stator were conducted at the peak efficiency operating condition. The unsteady data was then reduced through an ensemble averaging technique which splits the signal into deterministic and unresolved components. Various analysis methods like surface contour plots, passage average distributions, blade-to-blade distributions, temporal distribution and hub-to-tip distributions of the rotor exit flow along with spectral information was used to analyze the flow behaviour. Auto and cross correlation techniques were used to correlate the fluctuating total temperature and fluctuating velocity components (acquired using a slanted hot-film probe at the same measurement locations) and the gradients, distributions and relative weights of each of the terms of the average passage equation were then determined.

Some of the important conclusions that can be drawn based on the results of the present investigation as well as the velocity measurements by Prato (1996) are presented below.

7.1 Time Averaged Flow Field

1. Thin stator wakes are consistently observed in all data sets near the midspan regions.

2. In the hub endwall region the wake width increases both on the pressure side and on the suction side of the stator due to interaction between the stator wake flow and the hub clearance flow as well as an increase in the blade loading brought about by high incidences from the rotor exit low momentum flow region upstream.

3. In the casing endwall region, the thickening of the stator wake is mainly on the suction side. This is due in large to the presence of a corner interaction with the endwall flow on the suction side.

4. Accumulation of high temperature wake fluid from the upstream rotor causes and increase in the total temperature on the pressure side of the stator away from the endwalls.

5. A region of low momentum, high losses and high levels of axial vorticity near the hub is caused by the leakage flow generated due to the clearance between the stator tip and the rotating hub. The extent of this leakage flow region is around 60% in the pitchwise and nearly 10% in the spanwise directions. As a result, this endwall phenomena generates more blockage than that generated by endwall viscous fluid on the hub endwall.

6. The phenomena of scraping on the hub endwall is probably responsible for the radially outward transport of flow on the pressure side of the stator from the hub upto 35% span.

7. Near the suction side of the stator wake close to the hub, low temperatures, moderate pressure rise and high efficiency is observed. This is probably caused by leakage flow from the hub region augmented by hub rotation washing away the corner separation region.

8. The suction surface casing endwall corner region is characterized by low axial velocity, very low tangential velocity and high levels of inward radial velocity. This is also a region of low efficiency and high unresolved unsteadiness as well as high total pressure loss.

9. Interaction between the secondary flow and the stator wake on the suction side casing endwall corner generates high levels of vorticity close to the blade surface.

10. Cascade loss correlations which are mainly used in the preliminary design stages of compressor design tend to over-predict the overall stator loss coefficient by as much as 77% (ζ=0.1735 for the correlations compared with ζ=0.09802 for the experiment). It is clear that major improvements are required in the development of the loss correlations for multistage compressors.

7.2 RMS Unsteady Flow Field

1. The spectral distribution of hot-wire and kulite voltages shows that at least eight harmonics of all three rotor blade passing frequencies are present at this measurement location.

2. Significant levels of potential flow field interactions from all three rotors are felt both at the inlet and the exit of the compressor.

3. Appreciable levels of total unsteadiness in both pressure and temperature are observed in the core region away from the blade surfaces and the hub and casing endwalls.

4. In the core region of the flow, values of deterministic (revolution periodic and revolution aperiodic) unsteadiness is of the same order of magnitude as the unresolved unsteadiness.

5. Close to the endwalls, bulk of the total unsteadiness is unresolved in nature.

6. The revolution aperiodic unsteadiness is quite small compared to the revolution periodic unsteadiness almost everywhere except in the suction surface casing endwall corner region and the hub endwall region suction surface corner.

7. Fairly good periodicity in the rotor wake flow away from the endwalls is indicated by the presence of similar levels of both blade periodic unsteadiness and blade aperiodic unsteadiness.

8. In the stator wake region, values of the shaft resolved unsteadiness (revolution periodic and revolution aperiodic) and unresolved unsteadiness are of the same order of magnitude in the mid-span regions and shaft resolved unsteadiness is much lower than the unresolved unsteadiness in both the hub and casing endwall regions.

9. The thickness of the wake based on the RMS unsteadiness compares favorably with the thickness of the wake based on the time averaged values.

10. Migration of rotor wake flow onto the pressure side of the stator is confirmed by higher levels of both the revolution periodic and unresolved unsteadiness than the corresponding values on the suction side of the stator.

11. The influence of rotor-rotor interaction (both potential and viscous) is seen very clearly in the two node per revolution pattern on the rotor ensemble averaged data. The degree of amplitude of this node is a measure of the interaction between the rotors. This is different in various regions of the flow.

12. The hub endwall region has significant levels of both revolution periodic and unresolved unsteadiness in both total temperature and pressure.

13. High levels of unresolved unsteadiness found in the hub region is due to decay of the hub leakage vortex. The revolution periodic unsteadiness is the rotor hub wake fluid which is transported by the leakage flow and its subsequent interaction with the leakage flow.

14. Slightly away from the hub leakage flow region on the suction side of the blade, a region of comparable levels of revolution periodic and revolution aperiodic unsteadiness is observed. It is probably due to the transport of low momentum rotor fluid on the suction side close to the hub.

15. On the pressure side of the stator near the hub, a thickening of the wake is seen in the total unsteadiness distribution all the way upto 15% span from the hub in total pressure and about 12% in total temperature. This is mainly unresolved in nature both for the temperature and pressure. This is surmised to be due to accumulation of the hub leakage fluid on the pressure side of the stator due to the hub rotation.

16. In the casing endwall region, the dominant source of unsteadiness is in the suction surface corner region and bulk of this unsteadiness is unresolved in nature.

17. The center of the core of high unresolved unsteadiness in the casing corner region is at approximately the same location as the total pressure loss and high vorticity region. This shows that mixing in this region generates significant amount of unresolved unsteadiness.

18. There is also significant level of revolution periodic unsteadiness on the suction side of the stator close to the blade surface. This is probably due to the transport of the rotor exit flow to the suction side of the stator passage by the rotor tip clearance flow.

19. Away from the blade surfaces in the casing endwall region, the levels of unresolved unsteadiness are higher than that observed in the core flow region, consistent with the increase in vorticity and associated turbulence production in the endwall viscous fluid.

7.3 Temporal Variation of Stator Exit Flow

Significant changes occur to the stator exit flow features with passage of the rotor upstream of the stator. Different regions of the flow are affected in different fashions. Some of the important conclusions that can be drawn from this study are given below.

1. *Behaviour of rotor wake in the stator passage:* Closer examination of the rotor wake as it crosses the stator passage reveals that it becomes discontinuous either side of the stator wake. Starting with non-dimensional time τ/T=0.0, one leg of the deterministic content of the rotor wake is seen on the suction side of stator and the other leg is seen approaching the pressure surface of the stator. This is because of higher convection speeds of the rotor wake on the suction surface of the downstream stator than on the pressure side. This is more noticeable as the chopped rotor wake progress up the stator passage and the difference between the arrival times of the wake segments either side of the stator wake becomes more significant. Since the blade count difference between rotor 2 and stator 2 is 1, part of the wake of first rotor wake is still in the stator passage when the next rotor wake makes its appearance on the suction side. From the video animation, at time τ/T=0.40, both the rotor wakes are observed distinctly in the stator passage and this accounts for the maximum interaction between the stator and the rotor flow. This time is labeled the *maximum interaction time for rotor wake*. However, the maximum interaction times for the total pressure and total temperature wakes are different. The corresponding

maximum interaction times for the total temperature data is τ/T=0.75.

2. *Behavior of the stator wake regions:* The stator wake flow is adversely affected temporally by the rotor passage. There is an almost periodic pulsing motion of the wake brought about by wake passing. However, this pulsing occurs at different times at various radial locations. This is most certainly due to differential wake decay and skewing of the rotor wake as it passes through the stator passage. The pulsing was the highest at around 81% span in the suction surface corner and the lowest near the hub. There is certainly an influence of the downstream rotor which would affect the stator wake behavior through the potential influence, though it is difficult to quantify. The maximum potential interaction is expected to occur near the hub due to much tighter axial spacing compared to the casing endwall. It is possible that this potential field acts to affect the pulsing motion somewhat. The other reason for a lack of pulsing near the hub could be due to the transport of the rotor wake away from the stator wake region by the hub wall leakage flow.

3. *Behavior of the hub endwall flow region:* At $\tau/T = 0.0$, the region is spread out almost across the entire passage and as the rotor moves across the stator blade, the clearance flow grows in size in the spanwise direction while shrinking in the circumferential direction and starts moving across the passage transporting some of the hub endwall boundary layer flow towards the pressure surface of the stator blade. As the rotor blade continues further, the hub clearance region starts decreasing in size in the spanwise direction and starts spreading across the stator passage. The core of this region remains approximately at the same position with respect to the stator pitch. It is observed that the magnitude of the pressure at the core of the leakage flow is the lowest at τ/T=0.75 and highest at τ/T=0.25 and from the unsteadiness distribution, the corresponding values are 0.0 and 0.5 respectively.

4. *Behavior of the casing endwall suction surface corner region:* Like the wake region, this region also changes significantly with rotor passing. This region pulses (increases and decreases in size) as the rotor passes. The region starts decreasing in size as the time increases from $\tau/T = 0.0$ and is the smallest at the minimum interaction time and then starts increasing rapidly reaching a maximum at the maximum interaction time. As time further increases, the region starts decreasing once again in size. This is true for both the ensemble average as well as the unresolved unsteadiness (both pressure and temperature). As the corner flow region grows in size from τ/T = 0.35 to 0.85, the region is no longer confined to the suction surface region. It slowly spreads to the pressure surface and at the maximum interaction time, the region is almost the same size on either of side of the stator blade. It is also interesting to see that the corner region is observed to be "feeding" the flow in the casing region away from the endwalls as the blade passes by. So there is radial and circumferential transportation from both secondary flow as well as rotor wake related unsteadiness.

5. *Behavior of the casing endwall region away from the blade surfaces:* The ensemble average values in the casing wall region, away from the suction surface corner vary significantly. This is caused by rotor leakage flow and endwall flow interacting with the stator endwall flow. The upstream rotor clearance flow (low pressures and higher levels of unsteadiness away from the corner regions) seems to have been smeared across the stator passage. As time progresses from τ/T=0.0, the high unsteadiness in the midpitch region (unresolved unsteadiness in total pressure), starts reducing in size circumferentially and very slightly increasing in size in the spanwise direction until time reaches the minimum interaction position. Afterwards, the region starts spreading in size in the circumferential direction as time approaches the maximum

interaction point. At this time it is almost spread across the passage with feeding into this flow from the suction surface casing corner region as well.

7.4 Rotor Exit Flow Field

1. At midpitch, the interaction of the rotor 2 wake with the stator is minimal. Consequently a very clear rotor wake is observed all the way from hub to tip and is not very distorted (but skewed) except near the casing endwall. The flow is also fairly periodic from blade to blade.

2. Near the hub endwall, there is a region of very high pressure and very low total temperature. The extent of this region varies both circumferentially and radially in the total pressure data compared with the total temperature data. This is probably due to probable acceleration of rotor exit flow around the hub clearance fluid which is rolling up into a vortex.

3. The rotor wakes are the thickest (as evidenced by the ensemble averaged data) at approximately 25% span from the hub, possibly due to radial inward transport of the rotor wake by the stator flow field due to imbalance between the centrifugal forces and the pressure gradient as well as radial outward flow generated by the rotation of the hub.

4. Near the stator suction surface location, the rotor wakes are much more distorted than that at the midpitch location. The wake regions shows a distinctive double leg from hub to about 65% span. This is due to the chopping of the rotor wake by the stator blade surface.

5. Also in the casing endwall region, the suction surface corner flow has either decayed out or smeared out the rotor wake almost completely leaving a band of low levels

in the ensemble averaged pressure and spots of high temperature. Even though the wakes are distorted, fairly good periodicity of flow exists.

6. The wakes are thicker near the suction surface location than that at the midpitch location probably due to a faster decay brought about by the suction surface boundary layers on the blade. The dominant unsteadiness is in the casing endwall region associated partly with the mixing of the rotor clearance flow and partly with the suction surface casing endwall corner region.

7. Near the stator pressure surface location, the rotor wakes are highly distorted from hub to tip. The wakes on the pressure side are deeper than the wake on the suction side and this is due to different decay rates on the suction and pressure surface.

8. From hub to about 30% span, very low pressures and temperatures and higher levels of unsteadiness are observed with very little evidence of any wakes or core flow distinction. This is a region of intense mixing brought about by accumulation of hub endwall fluid on the pressure side of the stator by the hub rotation and this seems to have decayed out the rotor wake considerably.

9. Away from the endwalls, the thickness of the rotor wakes is the highest at the pressure surface location and the thinnest at midpitch. It is quite clear that future analysis and prediction methods should take into account the clocking of the stator with the downstream rotor for achieving accurate results.

10. The composite rotor exit flow field downstream of stator 2 at the mid-pitch location shows that the wakes are clearly seen from hub to about midspan. Near the casing endwall region, the wakes are quite distorted.

11. Similar wake widths are observed in all three measurements (temperature, velocity and pressure) in both the hub endwall and midspan region.

12. In the casing endwall region (81 and 90% span) on the suction side of the wakes, low total pressure, low axial velocity and high tangential velocity regions are seen indicating some sort of a leakage flow structure. This could be the rotor tip leakage flow as it has progressed through the stator blade row.

7.5 Deterministic Heat-Flux Distribution and Terms in the Average Passage Equation

1. Significant levels of deterministic heat flux quantities were found downstream of the second stator in the stator wakes, hub leakage flow region and the casing endwall suction surface corner region. Away from the endwall region, the highest levels of deterministic heat-flux are observed in the wake region where the fluctuations in axial and tangential velocity and total temperature are quite high. On the pressure side of the stator, appreciable levels of deterministic heat flux are observed, this is mainly due to the rotor wake impingement on the pressure side of the stator.

2. The deterministic stress terms due to the revolution aperiodic fluctuations in velocity in the momentum equation were found to be very small downstream of the present stator and can be neglected. However, the stress terms due to the revolution periodic components in velocity is quite significant at this axial location downstream of the stator.

3. The dominant transport term in the axial momentum equation in the stator wake region is due to secondary flow in the endwall region and wake spreading away from the endwalls. The dominant transport term in the tangential momentum equation in the wake region is due to the tangential velocity and its gradient in the tangential direction. Outside the wakes, the transport is almost zero. The tangential transport due to viscous normal stress (molecular) in the tangential momentum equation was

found to be of the same order of magnitude as the transport due to revolution periodic fluctuations in the tangential velocity.

4. In the radial momentum equation, the dominant transport in the wake is caused by the advection terms due to the tangential velocity. Intense secondary flows in the casing endwall suction surface corner region increase the radial transport in this region. The transport due to viscous normal stress (molecular) was found to be much smaller than caused by the radial transport due to revolution periodic fluctuations in the radial velocity component.

5. In the energy equation, transport of stagnation enthalpy due to the tangential and radial velocities was found to be of similar orders in magnitude. in the hub endwall region, the flux due to deterministic radial velocity fluctuations are found to be quite significant.

6. Attempts to derive a correlation for the deterministic heat flux $\overline{\bar{\rho} V_{\theta RP} H_{oRP}}$ using the eddy diffusivity concept was not successful and this approach was abandoned.

Chapter 8

RECOMMENDATIONS FOR FUTURE RESEARCH

The present investigation has provided a good understanding of an embedded stator exit flow field. However, there are many unanswered questions. The first question is regarding the influence of the rotor 3 potential flow field on the stator exit flow. This can be resolved by filtering out the rotor 3 blade passing frequency and its harmonics from the existing data and ensemble averaging the filtered data set and comparing the results with the existing results.

Attempts should be made to measure the temperature-velocity correlation directly probably by piggy-backing a hot-wire sensor on the aspirating probe. However, care should be taken to ensure that the gradients of the flow are taken into account while piggy-backing and efforts should be made to reduce the excessive flow blockage due to the probe.

Efforts can be directed at improving the aspirating probe by reducing the size of the probe in order to reduce flow blockage. The calibration of the aspirating probe can be improved by a better control of the total temperature of calibration. From the uncertainty analysis it is clear that the major error arises from the uncertainty of the total temperature measurement. Efforts should be made to improving the uncertainty of the thermocouple measurement.

The axial variation of the various flow properties can be documented by conducting the traverse at a couple of axial stations downstream of the present location. This will also provide necessary information to determine the dominant terms of the average-passage equation system that is presently open ended.

The next investigation could concentrate on the measurement of the hub endwall

and the casing endwall flow regions with a fine grid resolution to document the flow characteristics in better detail.

It would be very useful to measure the flow properties upstream of the second stator. This would not only provide the inlet conditions for conducting a good CFD simulation of the stator flow, it would also provide a basis of comparing the rotor exit distributions at the rotor and stator exit locations. This would answer a lot of questions like possible separation of flow near the rotor hub, the location and strength of the rotor tip leakage flow and its propagation through the stator passage, whether the deterministic stresses are decaying faster than the unresolved stresses or not and so on. Casing static and hub static kulite measurements as well as blade static pressures would help augment this understanding.

Detailed area traverse downstream of the third rotor of the various unsteady measurements will help document the flow features downstream of the rotor as well as correlate these measurements with those acquired downstream of the second stator to quantify the influence of the stator on the rotor flow field.

In order to make the measurements complete, the above measurements could be repeated at various off-design conditions like choke flow, near peak pressure ratio, near stall conditions and also at other rotor speeds.

REFERENCES

Adamczyk, J. J., 1985, "Model Equation for Simulating Flows in Multistage Turbomachinery," ASME Paper No. 85-GT-226.

Adamczyk, J. J., Mulac, R. A., and Celestina, M. L., 1986, "A Model for Closing the Inviscid Form of the Average Passage Equation System," ASME Paper No. 86-GT-227.

Adkins, G. G., Jr., and Smith, L. H., Jr., 1982, "Spanwise Mixing in Axial FLow Turbomachines," *ASME Journal of Engineering for Power*, Vol. 104, pp. 97–110.

Behlke, R. F., Bursdall, E. A., Canal, E. Jr., and Korm, N. D., 1979, "Core Compressor Exit Stage Study: Part II–Final Report," NASA CR-159812.

Binder, A., Förster, W., Kruse, H., and Rogge, H., 1985, "An Experimental Investigation Into the Effect of Wakes on the Unsteady Turbine Rotor Flow," *ASME Journal of Engineering for Gas Turbines and Power*, Vol. 107, pp. 458–466.

Calvert, W. J., Ginder, R. B., McKenzie, I. R., and Way, D. J., 1989, "Performance of a Highly-Loaded HP Compressor," ASME Paper No. 89-GT-24.

Capece, V. R., and Fleeter, S., 1987, "Unsteady Aerodynamic Interactions in a Multistage Compressor," ASME Paper No. 87-GT-171.

Cherrett, M. A., Bryce, J. D., and Ginder, R. B., 1994, "Unsteady 3D Flow in a Single-Stage Transonic Fan. Part II: Unsteady Stator Exit Flow Field," ASME Paper No. 94-GT-224.

Cherrett, M. A., and Bryce, J. D., 1992, "Unsteady Viscous Flow in a High Speed Core Compressor," *ASME Journal of Turbomachinery*, Vol. 114, pp. 287–294.

Christianson, M. C., 1991 Private Communication.

Coleman, H. W., and Steele, W. G., 1989, *Experimentation and Uncertainty Analysis for Engineers*. John Wiley & Sons, Inc., New York.

Collis, D. C., and Williamson, M. J., 1959, "Two-Dimensional Convection from Heated Wires at Low Reynolds Numbers," *Journal of Fluid Mechanics*, Vol. 6, pp. 357–363.

Das, D. K., and Jiang, H. K., 1984, "An Experimental Study of Rotating Stall in a Multistage Axial-FLow Compressor," *ASME Journal of Engineering for Gas Turbines and Power*, Vol. 106, pp. 542 – 551.

Dawes, W. N., 1992, "Towards Improved Throughflow Capability: The Use of Three-Dimensional Viscous Flow Solvers in a Multistage Environment," *ASME Journal of Turbomachinery*, Vol. 114, pp. 8–17.

De Ruyck, J., and Hirsch, C., 1988, "A Radial Mixing Computation Method," ASME Paper No. 88-GT-68.

Denton, J. D., 1992, "Time Marching Methods for Turbomachinery Calculations," *Application of Numerical Methods to Flow Calculations in Turbomachines*, VKI Lecture Series LS-07.

Dransfield, D. C., and Calvert, W. J., 1976, "Detailed Flow Measurements in a Four Stage Axial Compressor," ASME Paper No. 76-GT-46.

Dring, R. P., and Joslyn, H. D., 1986, "Throughflow Analysis of a Multistage Compressor: Part I - Aerodynamic Input," ASME Paper No. 86-GT-13.

Dring, R. P., and Joslyn, H. D., 1986, "Throughflow Analysis of a Multistage Compressor: Part II - Analytical-Experimental Comparisons," ASME Paper No. 86-GT-14.

Dunham, J., 1992, "Analysis of High Speed Multistage Compressor Throughflow Using Spanwise Mixing," ASME Paper No. 92-GT-13.

Erdos, J. I., Alzner, E., McNally, W., 1977, "Numerical Solution of Periodic Transonic Flow Through a Fan Stage," *AIAA Journal*, Vol. 15, pp. 1559–1568.

Fagan, J. R., Jr., 1991, "Results from the Allison Axi-Symmetric Design Code," Private Communication.

Falchetti, F., 1992, "Advanced CFD Simulation and Testing of Blading in the Multistage Environment," AIAA Paper No. 92-3040.

Gallimore, S. J., 1986, "Spanwise Mixing in Multistage Axial Flow Compressors: Part II - Throughflow Calculations Including Mixing," *ASME Journal of Turbomachinery*, Vol. 108, pp. 9–16.

Gallimore, S. J., and Cumpsty, N. A., 1986, "Spanwise Mixing in Multistage Axial Flow Compressors: Part I - Experimental Investigation," *ASME Journal of Turbomachinery*, Vol. 108, pp. 2–9.

Goto, A., 1992, "Three-Dimensional Flow and Mixing in an Axial Flow Compressor With Different Rotor Tip Clearances," *ASME Journal of Turboamchinery*, Vol. 114, pp. 675–685.

Grant, H. L., Hughes, B. A., Vogel, W. M., and Moilliet, A., 1968, "Spectrum of Temperature Fluctuations in Turbulent Flow," *Journal of Fluid Mechanics*, Vol. 34, pp. 423–442.

Gundy-Burlet, K. L., and Rai, M. M., 1989, "Two-Dimensional Computations of Multi-Stage Compressor Flows Using a Zonal Approach," AIAA Paper No. 89-2452.

Hall, E. J., 1996, "Improved Modeling for Multistage Compressors - Progress Report No. 1," Allison Engine Company, Engineering Data Report No. 17762, prepared for Penn State University Under Subcontract CURF-TPSU-AEC-SR036-1132.

Hall, E. J., Topp, D. A., Heidegger, N. J., and Delaney, R. A., 1995, "Investigation of Advanced Blade Configuration Concepts for High Speed Turboprop Systems: Task VII - Endwall Treatment Inlet Flow Distortion Analysis Final Report," NASA Contract NAS3-25270, NASA CR-195468.

Hill, P. G., Schaub, U. W., and Senoo, Y., 1963, "Turbulent Wakes in Pressure Gradients," *ASME Journal of Applied Mechanics*, Vol. 1, pp. 518–524.

Hinze, J. O., 1975, *Turbulence*. McGraw Hill Publishing Company, New York.

Howard, M. A., Ivey, P. C., Barton, J. P., and Young, K. F., 1993, "Endwall Effects at Two Tip Clearances in a Multi-stage Axial Flow Compressor with Control Diffusion Blading," ASME Paper No. 93-GT-299.

Howard, M. A., and Gallimore, S. J., 1992, "Viscous Throughflow Modelling for Multi-stage Compressor Design," ASME Paper No. 92-GT-302.

Jung, M., and Eikelmann, J., 1995, "Stator Exit Flow Fields in the Multistage Environment of an Axial Compressor," ASME Paper No. 95-GT-165.

Kerrebrock, J. L., and Mikolajczak, A. A., 1970, "Intra-Stator Transport of Rotor Wakes and Its Effect on Compressor Performance," *ASME Journal of Engineering for Power*, pp. 359–368.

Kiousis, P., Chaviaropolous, P., Papailiou, K. D., 1992, "Meridional Flow Calculation Using Advanced CFD Techniques," ASME Paper 92-GT-325.

Kuroumaru, M., Inoue, M., Higaki, T., Abd-Elkhalek, F., and Ikui, T., 1982, "Measurement of Three-Dimensional Flow Field Behind an Impeller by Means of Periodic Multi-sampling Technique," *JSME*, Vol. 25, No. 209, pp. 1674–1681.

Lakshminarayana, B., 1987, "A Discussion to Paper Secondary Flow, Turbulent Diffusion, and Mixing in Axial Flow Compressors, *ASME Journal of Turbomachninery*," Vol. 109, pp. 475–477.

Lakshminarayana, B., 1996, *Fluid Dynamics and Heat Transfer of Turbomachinery*. John Wiley and Sons.

Lakshminarayana, B., and Davino, R., 1980, "Mean Velocity and Decay Characteristics of the Guidevane and Stator Blade Wake of an Axial FLow Compressor," *Journal of Engineering for Power*, Vol. 102, pp. 50–60.

Lakshminarayana, B., and Hall, E. J., 1996, "Semi-Annual Progress Report on Improved Techniques for Turbomachinery Flow Fields," PSU Turbo 9602, Submitted to South Carolina Energy Research and Development Center.

Lakshminarayana, B., Zaccaria, M., Marathe, B., 1995, "Structure of Tip Clearance Flow in Axial Compressors," *ASME Journal of Turbomachinery*, Vol. 115, p. 336.

Leylek, J. H., and Wisler, D. C., 1991, "Mixing in Axial Flow Compressors: Conclusions Drawn from 3-D Navier-Stokes Analyses and Experiments," *ASME Journal of Turbomachinery*, Vol. 113, No. 2, pp. 139–160.

Li, S. M. and Chen, M. Z., 1992, "A Simple and Unified Model for Spanwise Mixing in Multistage Axial Flow Compressors," *Journal of Thermal Science*, Vol. 1, No. 2, pp. 98–107.

Rai. M. M., 1987, "Navier-Stokes Simulations of Rotor/Stator Interactions Using Patched and Overlaid Grids," *Journal of Propulsion and Power*, Vol. 3, No. 5, pp. 387–396.

Ng, W. F., 1990 Private Communication.

Ng, W. F., and Epstein, A. H., 1983, "High Frequency Temperature and Pressure Probe for Unsteady Compressible Flows," *Review of Scientific Instruments*, Vol. 54, No.12, pp. 113–124.

Ng, W. F., and Epstein, A. H., 1985, "Unsteady Losses in Transonic Compressors," *ASME Journal of Engineering for Gas Turbines and Power*, Vol. 107, pp. 113–124.

Norton, J. M., Hobbs, D. E., Williams, M. C., House, R. D., and Harvey, W. B., 1989, "Energy Efficient Engine Hollow Fan Blade Technology, Volume I - Shroudless High Aspect Ratio Fan Rig, Part 2 - Laser Doppler Velocimeter Test," NASA CR-182221.

Prato, J. P., 1996, *Steady and Unsteady Flow in an Embedded Stator Stage of a Multistage Axial Flow Compressor.* PhD thesis, The Pennsylvania State University.

Prato, J. P., and Lakshminarayana, B., 1993, "Investigation of the Compressor Rotor Wake Structure at Peak Pressure Rise Coefficient and the Effects of Loading," *ASME Journal of Turbomachinery*, Vol. 115, pp. 487–500.

Raj, R., and Lakshminarayana, B., 1973, "On the Investigation of Cascade and Turbomachinery Rotor Wake Characterisitics," *Journal of Fluid Mechanics*, Vol. 61, Part. 4, pp. 676–690.

Ravindranath, A., and Lakshminarayana, B., 1980, "Mean Velocity and Decay Characteristics of the Near- and Far-Wake of a Compressor Rotor Blade of Moderate Loading," *Journal of Engineering for Power*, Vol. 102, No. 3, pp. 535–540.

Robinson, C. J., 1992, "Endwall Flows and Blading Design for Axial FLow Compressors," Axial Flow Compressors, von Karman Institute for Fluid Dynamics Lecture Series 1992-02 (Also Ph.D Thesis, Cranfield Institute of Technology, May 1991).

Sharma, O. P., Butler, T. L., Pratt & Whitney Aircraft; and Joslyn, H. D., and Dring, R. P., United Technologies Research Center, 1983, "An Experimental Investigation of the Three-Dimensional Unsteady Flow in an Axial Flow Turbine," AIAA Paper No. 83-1170.

Smith, L. H. Jr., 1970, *Casing Boundary Layers in Multistage Axial Flow Compressors in Flow Research On Blading*. Edited By L. S. Dzung, Elsevier Publishing Company.

Stauter, R. C., Dring, R. P., and Carta, F. O., 1991, "Temporally and Spatially Resolved Flow in a Two-Stage Axial Compressor Part 1 - Experiment," *ASME Journal of Turbomachinery*, Vol. 113, pp. 219–226.

Stauter, R. C., 1992, "Measurement of the Three-Dimensional Tip Region Flowfield in an Axial Compressor," ASME Paper No. 92-GT-211.

Suder, K. L., et al., 1987, "Measurements of the Unsteady Flow Fields Within the Stator Row of a Transonic Axial Flow Fan, Part I: Measurement and Analysis Technique," ASME Paper No. 87-GT-226.

Suryavamshi, N., Lakshminarayana, B., and Prato, J.,, 1996, "Aspirating Probe Measurements of the Unsteady Total Temperature Downstream of An Embedded Stator in a Multistage Axial Flow Compressor," ASME Paper No. 96-GT-543, Accepted for Publication in the ASME *Journal of Turbomachinery*.

Suryavamshi, N., Lakshminarayana, B., Prato, J., and Fagan, J., 1994, "Unsteady Total Pressure Field Downstream of An Embedded Stator in a Multistage Axial Flow Compressor," Presented at the Winter Annual Meeting of the ASME - ASME AD-Vol. 40 Unsteady Flows in Aeropropulsion, pp. 61–76.

Van Zante, D. E., Suder, K. L., Strazisar, A. J., and Okiishi, T.H., 1994, "An Improved Aspirating Probe for Total Temperature and Total Pressure Measurements in Compressor Flows," ASME Paper No. 94-GT-222.

Wennerstrom, A. J., 1991, "A Review of Predictive Efforts for Transport Phenomena in Axial Flow Compressors," *ASME Journal of Turbomachinery*, Vol. 113, pp. 175–179.

Whitfield, C. W., and Keith, J. S., 1985, "Spanwise Redistribution of Energy and Loss in an Axial Flow Compressor by Wake Centrifugation," Final Report, Air Force Wright Aeronautical Laboratories, AFWAL-TR-84-2109.

Wisler, D. C., Bauer, R. C., and Okiishi, T. H., 1987, "Secondary Flow, Turbulent Diffusion, and Mixing in Axial Flow Compressors," *ASME Journal of Turbomachinery*, Vol. 109, pp. 455–482.

Wisler, D. C., 1984, "Loss Reduction in Axial Flow Compressors Through Low Speed Model Testing," ASME Paper No. 84-GT-184.

Yavuzkurt, S., 1984, "A Guide to Uncertainty Analysis of Hot-Wire Data," *ASME Journal of Fluids Engineering*, Vol. 106, pp. 181–186.

Appendix A

GENERAL UNCERTAINTY ANALYSIS

There is no such thing as a perfect measurement. All measurements of a variable contain inaccuracies. Because it is important to have an understanding of these inaccuracies if we are to perform experiments or if we are simply to use values that have been experimentally determined, we must carefully quantify the uncertainty of various variables and calculate the overall uncertainty of the measurement variable.

Here the word *accuracy* refers to the closeness of agreement between a measured value and the true value. The degree of inaccuracy or the total measurement error (δ) is the difference between the measured value and the true value. The *total error* is the sum of the bias error and the *precision error*. The bias error (β) is the fixed, systematic or constant component of the total error and is sometimes referred to simply as bias. The precision error (ϵ) is the random component of the total error and is sometimes called the repeatability or repeatability error. Since the precision error is a random error, it will have different value for each measurement. It then follows that the total error in each measurement will be different, since

$$\delta_i = \beta + \epsilon_i \tag{A.1}$$

So, for N measurements of a variable X, more than likely as N approached infinity, the data band would behave as a *Gaussian distribution*. Then the bias would be given by the difference between the average value of the N readings, μ, and the true value of X (based on some precalibrated standard), whereas the precision errors would cause the frequency of occuraence of the readings to be distributed about the mean value. The above concepts are illustrated in Figure A.1.

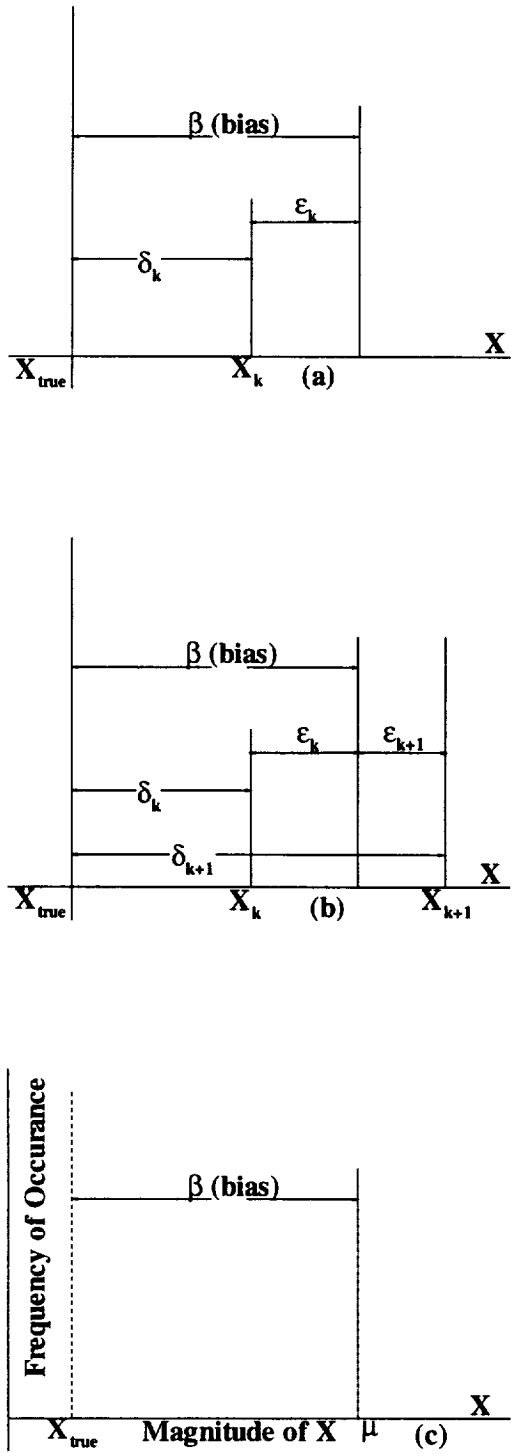

Figure A.1. Errors in the Measurement of a Variable X: (a) Single Reading; (b) Two Readings; (c) Infinite Number of Readings

It has to be mentioned here that certain bias errors can be eliminated by calibration, but only to the limit of the bias error associated with the standard used in the calibration procedure.

The precision error S, is the random part of the total error which for N measurements ($X_{ii=1,N}$) of the parameter X, is

$$S = \sqrt{\frac{\sum_{i=1}^{N}(X_i - \overline{X})^2}{N-1}} \qquad (A.2)$$

where $\overline{X}$, the average value of X_i is

$$\overline{X} = \frac{1}{N}\sum_{i=1}^{N} X_i \qquad (A.3)$$

The precision index of the sample mean $\overline{X}$ can be also be found from

$$S_{\overline{x}} = \frac{S}{\sqrt{N}} \qquad (A.4)$$

To obtain the precision error of a given parameter, the root mean square method is used to combine the precision errors from the different k sources of error as

$$S = [S_1^2 + S_2^2 + S_3^2 + \cdots + S_k^2] \qquad (A.5)$$

Similarly the bias of a given parameter can be found as

$$B = [B_1^2 + B_2^2 + B_3^2 + \cdots + B_k^2] \qquad (A.5)$$

The total uncertainty U is obtained for a 95% confidence level by using the *Root Mean Square (RSS)* method

$$U = [B^2 + S^2]^{\frac{1}{2}} \qquad (A.6)$$

where $P = tS_{\bar{x}}$. For a large number of samples (>30), t=2.0. If a data reduction equation is used to determine the uncertainty (as it is in the present case) then the following procedure is used.

The basis behind the general uncertainty analysis, is to determine how the uncertainties in various variables propagate through a data reduction equation into the result. The following procedure is as described by Coleman and Steele (1989).

Consider a general case in which and experimental result, r is a function of j variables X_j

$$r = r(X_1, X_2, X_3, \cdots, X_j) \tag{A.7}$$

The above equation is the data reduction equation used for determining r from the measured values of the variables X_j. Then the uncertainty in the result is given by

$$U_r = \left[\left(\frac{\partial r}{\partial X_1} U_{x_1} \right)^2 + \left(\frac{\partial r}{\partial X_2} U_{x_2} \right)^2 + \cdots + \left(\frac{\partial r}{\partial X_j} U_{x_j} \right)^2 \right]^{\frac{1}{2}} \tag{A.8}$$

where the U_{x_j} are the uncertainties in the measured variables X_j for a 95% confidence interval.

Appendix B

UNCERTAINTY ANALYSIS FOR PERFORMANCE MEASUREMENT

In this appendix a general uncertainty analysis on the performance data of the multi-stage compressor facility is reported. The general uncertainty analysis procedure is based on the techniques described by Coleman and Steele (1989) and expounded in Appendix A.

B.1. Data Reduction Equations for Performance Evaluation

The data reduction equations for performance evaluation are given in detail in Chapter 2. They are reproduced below for the sake of completeness.

1. *Mass flow:*

   Segmental mass flow W_i is given by:

$$W_i = P_s \sqrt{\frac{\left(\frac{P_{oi}}{P_s}\right)^{\frac{\gamma-1}{\gamma}} \left[\left(\frac{P_{oi}}{P_s}\right)^{\frac{\gamma-1}{\gamma}} - 1\right]}{T_{oi}}} \qquad (B.1)$$

   where the subscript i stands for the radial location of the total pressure and temperature measurement.

$$m_{uncor} = \left[\sum_{i=1}^{7} \frac{W_i \Delta A_i}{C}\right] \qquad (B.2)$$

   where ΔA_i is the incremental area and C is defined by

$$C = \sqrt{\frac{R}{\gamma}\left(\frac{\gamma - 1}{2}\right)} \qquad (B.3)$$

   In this analysis values of γ and R are assumed to be 1.4 and 1716 ft.lb/slug.°R.

   Corrected mass flow m_{cor} is given by:

$$m_{cor} = m_{uncor} \frac{\sqrt{\theta}}{\delta} \qquad (B.4)$$

where θ is the ratio of the absolute stagnation temperature at the inlet to rotor 1 to the absolute static temperature at sea level condition and δ is the ratio of the absolute stagnation pressure at the inlet to rotor 1 to the absolute static pressure at sea level.

2. *Mass Averaged Total Pressure Ratio:*

Since the tests were intended to reproduce conditions which would be present in the latter stages of a core compressor, the overall performance is presented from upstream of the first rotor (Station 2) to the exit station (station 9). The overall pressure ratio based on the inlet to the first rotor was calculated as follows: (This procedure is the same as that used by P&W. All emperical correlations are based on Behlke et al., (1979)).

$$\overline{P}_r = \frac{\overline{P}_{o9}}{\overline{P}_{o2}} \qquad (B.5)$$

where

$$\overline{P}_{o2} = \overline{P}_{o1} \times \overline{P}_{r,IGV} \times \overline{P}_{r,pole} \times \overline{P}_{r,strut} \qquad (B.6)$$

and

$\overline{P}_{o9}$ = exit station mass averaged total pressure

$\overline{P}_{o2}$ = first rotor inlet mass averaged total pressure

$\overline{P}_{o1}$ = inlet station mass averaged total pressure

$\overline{P}_{r,IGV}$ = total pressure ratio across the inlet guide vane

$\overline{P}_{r,pole}$ = total pressure ratio due to losses of flow station pole rakes

$\overline{P}_{r,strut}$ = total pressure ratio due to inlet strut losses

All the inlet loss pressures were calculated as a function of the inlet dynamic pressure

calculated as a function of flow by:

$$\left(\frac{P_o - P}{P_o}\right) = 1.682842 \times 10^{-2} + m_{cor}(4.28655 \times 10^{-4} m_{cor} - 6.602824 \times 10^{-4}) \tag{B.7}$$

where m_{cor} is the corrected weight flow in lbm/s. The coefficients in the above correlation provided by P&W are dimensional.

$$\overline{P}_{r,IGV} = 1.0 - 0.0153400\left(\frac{P_o - P}{P_o}\right) \tag{B.8}$$

$$\overline{P}_{r,pole} = 1.0 - 0.0105285\left(\frac{P_o - P}{P_o}\right) \tag{B.9}$$

$$\overline{P}_{r,strut} = 1.0 - 0.0014550\left(\frac{P_o - P}{P_o}\right) \tag{B.10}$$

Here mass averaged total pressure is calculated as follows:

$$\overline{P}_o = \frac{\Sigma(W_i P_{oi} \Delta A_i)}{\Sigma(W_i \Delta A_i)} \tag{B.11}$$

3. *Mass Averaged Temperature Ratio:*

Since no work is done ahead of the first rotor and heat loss through the casing is estimated to be negligible, the total temperature ratio from inlet of strut to the exit of IGV is unchanged. Hence, $T_{o0} = T_{o1} = T_{o2}$.

$$\overline{T}_r = \frac{\overline{T}_{o9}}{\overline{T}_{o1}} \tag{B.12}$$

where the mass averaged total temperature is given by:

$$\overline{T}_o = \frac{\Sigma(W_i T_{oi} \Delta A_i)}{\Sigma(W_i \Delta A_i)} \tag{B.13}$$

4. *Temperature and Torque Based Efficiencies:*

The mass averaged adiabatic (temperature ratio based) and the torque based efficiencies are given by:

$$\eta_{temp} = \frac{\left(\overline{P}_r^{\left(\frac{\gamma-1}{\gamma}\right)} - 1\right)}{\left(\overline{T}_r - 1\right)} \qquad (B.14)$$

$$\eta_{torque} = \frac{\left(\overline{P}_r^{\left(\frac{\gamma-1}{\gamma}\right)} - 1\right)\overline{T}_{o1} m_{uncor} C_p}{2\pi N T_{net}} \qquad (B.15)$$

B.2. Uncertainty in Various Measurement Variables

The measurement variables considered in this analysis are: pressure measurement (total and static), temperature measurement, measurement of compressor input torque and compressor shaft speed. The uncertainties are based on the accuracies stated by the manufacturer for various transducers and data acquisition and readout systems and are calculated by the RSS method. The gas constants γ and R and the incremental area ΔA_i are assumed to be constant.

1. *Uncertainty in pressure:*

   Uncertainty in the validyne transducer = ±0.25% FS = ±0.025 psi

   Uncertainty in the demodulator unit = ±0.1% FS = ±0.01 psi

   Uncertainty in the DAS-20 A/D board = ±1 LSB= ±4.88E-07 psi

   Therefore overall uncertainty in pressure measurement = ±0.0269 psi.

2. *Uncertainty in temperature:*

   Uncertainty in the Omega C-J Compensation Unit = ±0.75°K

   Uncertainty in the Omega Amplifier = ±0.07° K

Uncertainty in Calibration = $\pm 0.4839°$ K

Overall uncertainty in temperature = $\pm 0.8953°$K = $\pm 1.61°$R

3. *Uncertainty in torque measurement:*

   Due to the drift of the torque meter the overall uncertainty in the torquemeter is estimated as ± 10 lb-in.

4. *Uncertainty in speed measurements:*

   Overall uncertainty is estimated as ± 1 rpm.

B.3 Uncertainty Estimate

The uncertainty in the determination of mass flow, total pressure ratio, total temperature ratio, torque and temperature ratio based efficiencies are estimated in this section.

1. *Uncertainty in mass flow:*

   The segmental mass flow is given by:

$$W_i = P_s \sqrt{\frac{\left(\frac{P_{oi}}{P_s}\right)^{\frac{\gamma-1}{\gamma}}\left[\left(\frac{P_{oi}}{P_s}\right)^{\frac{\gamma-1}{\gamma}} - 1\right]}{T_{o=oi}}} \qquad (B.16)$$

   The uncertainty in segmental mass flow is given by:

$$U_{wi} = \sqrt{\left(\frac{\partial W_i}{\partial P_s} U_{Ps}\right)^2 + \left(\frac{\partial W_i}{\partial P_o} U_{Po}\right)^2 + \left(\frac{\partial W_i}{\partial T_o} U_{To}\right)^2} \qquad (B.17)$$

   where the partial derivatives are:

$$\frac{\partial W_i}{\partial P_s} = \frac{1}{2\gamma W_i T_o}\left[\left(2P_o^{\frac{2\gamma-2}{\gamma}} P_s^{\frac{2-\gamma}{\gamma}}\right) - \left((\gamma+1)P_o^{\frac{\gamma-1}{\gamma}} P_s^{\frac{1}{\gamma}}\right)\right] \qquad (B.18)$$

$$\frac{\partial W_i}{\partial P_o} = \frac{1}{2\gamma W_i T_o}\left[\left((2\gamma-2)P_o^{\frac{\gamma-2}{\gamma}} P_s^{\frac{2}{\gamma}}\right) - \left((\gamma-1)P_o^{\frac{-1}{\gamma}} P_s^{\frac{\gamma+1}{\gamma}}\right)\right] \qquad (B.19)$$

$$\frac{\partial W_i}{\partial T_o} = \frac{1}{2W_i T_o^2}\left[\left(P_s^{\frac{\gamma+1}{\gamma}} P_o^{\frac{\gamma-1}{\gamma}}\right) - \left(P_s^{\frac{2}{\gamma}} P_o^{\frac{2\gamma-2}{\gamma}}\right)\right] \qquad (B.20)$$

The overall uncertainty in mass flow is the average of the segmental uncertainties.

2. *Uncertainty in* $\overline{P}_r$*:*

In this analysis we consider the total pressure ratio based on upstream inlet total pressure (excluding the losses due to struts, IGV and pole rakes).

The pressure ratio is given by:

$$\overline{P}_r = \frac{\overline{P}_{o9}}{\overline{P}_{o1}} \qquad (B.21)$$

Now the uncertainty in $\overline{P}_r$: is:

$$U_{\overline{P}_r} = \sqrt{\left(\frac{\partial \overline{P}_r}{\partial \overline{P}_{o1}} U_{\overline{P}_{o1}}\right)^2 + \left(\frac{\partial \overline{P}_r}{\partial \overline{P}_{o9}} U_{\overline{P}_{o9}}\right)^2} \qquad (B.21)$$

where the partial derivatives are:

$$\frac{\partial \overline{P}_r}{\partial \overline{P}_{o1}} = \frac{-\overline{P}_{o9}}{\overline{P}_{o1}^2} \qquad (B.22)$$

$$\frac{\partial \overline{P}_r}{\partial \overline{P}_{o9}} = \frac{1}{\overline{P}_{o1}} \qquad (B.23)$$

3. *Uncertainty in* $\overline{T}_r$*:*

The temperature ratio is given by:

$$\overline{T}_r = \frac{\overline{T}_{o9}}{\overline{T}_{o1}} \qquad (B.24)$$

Now the uncertainty in $\overline{T}_r$: is:

$$U_{\overline{T}_r} = \sqrt{\left(\frac{\partial \overline{T}_r}{\partial \overline{T}_{o1}} U_{\overline{T}_{o1}}\right)^2 + \left(\frac{\partial \overline{T}_r}{\partial \overline{T}_{o9}} U_{\overline{T}_{o9}}\right)^2} \qquad (B.25)$$

where the partial derivatives are:

$$\frac{\partial \overline{T}_r}{\partial \overline{T}_{o1}} = \frac{-\overline{T}_{o9}}{\overline{T}_{o1}^{\,2}} \tag{B.26}$$

$$\frac{\partial \overline{T}_r}{\partial \overline{T}_{o9}} = \frac{1}{\overline{T}_{o1}} \tag{B.27}$$

4. *Uncertainty in temperature Efficiencies:*

Temperature efficiency is given by

$$\eta_{temp} = \frac{\left(\overline{P}_r^{\left(\frac{\gamma-1}{\gamma}\right)} - 1\right)}{\left(\overline{T}_r - 1\right)} \tag{B.28}$$

Now the uncertainty in the temperature efficiency is

$$U_{\eta_{temp}} = \sqrt{\left(\frac{\partial \eta_{temp}}{\partial \overline{P}_r} U_{\overline{P}_r}\right)^2 + \left(\frac{\partial \eta_{temp}}{\partial \overline{T}_r} U_{\overline{T}_r}\right)^2} \tag{B.29}$$

where the partial derivatives are:

$$\frac{\partial \eta_{temp}}{\partial \overline{P}_r} = \frac{\left(\frac{\gamma-1}{\gamma}\right)\overline{P}_r^{\frac{-1}{\gamma}}}{\overline{T}_r - 1} \tag{B.30}$$

$$\frac{\partial \eta_{temp}}{\partial \overline{T}_r} = -\frac{\left(\overline{P}_r^{\frac{\gamma-1}{\gamma}} - 1\right)}{\left(\overline{T}_r - 1\right)^2} \tag{B.31}$$

5. *Uncertainty in torque efficiency*

Torque efficiency is given by:

$$\eta_{torque} = \frac{\left(\overline{P}_r^{\left(\frac{\gamma-1}{\gamma}\right)} - 1\right)\overline{T}_{o1} m_{uncor} C_p}{2\pi N T_{net}} \tag{B.32}$$

The uncertainty in torque efficiency is given by:

$$U_{\eta_{tor}} = \sqrt{\left(A\, U_{\overline{P}_r}\right)^2 + \left(B\, U_{\overline{T}_{o1}}\right)^2 + \left(C\, U_{m_{uncor}}\right)^2 + \left(D\, U_N\right)^2 + \left(D\, U_{T_{net}}\right)^2} \tag{B.33}$$

where

$$A = \frac{\partial \eta_{tor}}{\partial \overline{P}_r} = \frac{\overline{T}_{o1} m_{uncor} C_p}{2\pi N T_{net}} \left(\frac{\gamma - 1}{\gamma}\right) \tag{B.34}$$

$$B = \frac{\partial \eta_{tor}}{\partial \overline{T}_{o1}} = \frac{\left(\overline{P}_r^{\left(\frac{\gamma-1}{\gamma}\right)} - 1\right) m_{uncor} C_p}{2\pi N T_{net}} \tag{B.35}$$

$$C = \frac{\partial \eta_{tor}}{\partial m_{uncor}} = \frac{\left(\overline{P}_r^{\left(\frac{\gamma-1}{\gamma}\right)} - 1\right) \overline{T}_{o1} C_p}{2\pi N T_{net}} \tag{B.36}$$

$$D = \frac{\partial \eta_{tor}}{\partial N} = \frac{-\left(\overline{P}_r^{\left(\frac{\gamma-1}{\gamma}\right)} - 1\right) m_{uncor} \overline{T}_{o1} C_p}{2\pi N^2 T_{net}} \tag{B.37}$$

$$E = \frac{\partial \eta_{tor}}{\partial T_{net}} = \frac{-\left(\overline{P}_r^{\left(\frac{\gamma-1}{\gamma}\right)} - 1\right) m_{uncor} \overline{T}_{o1} C_p}{2\pi N T_{net}^2} \tag{B.38}$$

B.4. Results and Discussion

The above equations were programmed into the computer and the uncertainty calculation was conducted on the data acquired during performance run 4 at 100% corrected speed. At the peak efficiency (design) operating point of 20.83 lbm/s (corrected mass flow), 1.354 (total pressure ratio), 1.102 (total temperature ratio), 90.512% (torque based efficiency) and 89.150% (temperature based efficiency), the respective uncertainty bands

are: ±0.091 lbm/s, ±0.003, ±0.005, ±0.9069%, and ±4.043%. These numbers translate to uncertainty levels of ±0.44% in mass flow, ±0.22% in total pressure ratio, ±0.453% in total temperature ratio, ±1.0% in torque efficiency and ±4.54% in temperature based efficiency. All these numbers except the uncertainty bands in temperature ratio, temperature and torque based efficiencies are within acceptable levels.

B.5. Parametric Evaluation of Factors Affecting Uncertainty

In order to establish which factors influence the uncertainty in mass flow, torque and temperature based efficiencies, a parametric study was conducted with various uncertainty levels of pressure, temperature, torque and speed measurements. This study was done for the peak efficiency condition at 100% corrected speed. From this table it was clear that the maximum reduction in temperature based efficiency came from the reduction in the uncertainty in temperature measurement and the maximum reduction in the uncertainty in corrected mass flow and torque based efficiency is in the reduction in uncertainty in the pressure measurement.

Appendix C

UNCERTAINTY ANALYSIS FOR ASPIRATING PROBE TOTAL TEMPERATURE MEASUREMENT

In this appendix a general uncertainty analysis is conducted on the aspirating probe data reduction equation system to evaluate the overall uncertainty of temperature measurement. The uncertainty analysis procedure is based on the techniques expounded in Appendix A.

C.1. Data Reduction Equation

The data reduction equation for total temperature measurement based on the 2-wire technique is given by equation 3.10 and is reproduced below:

$$\left[\frac{V_1^2\, T_o^{\frac{n_{1,T}}{2}}}{C_{1,T}(T_{w1} - rT_o)}\right]^{\frac{1}{n_{1,T}}} = \left[\frac{V_2^2\, T_o^{\frac{n_{2,T}}{2}}}{C_{2,T}(T_{w2} - rT_o)}\right]^{\frac{1}{n_{2,T}}} \qquad (C.1)$$

C.2. Uncertainty Equation

The uncertainty in total temperature is given by:

$$\begin{aligned} U_{T_o} = \Big[&\Big(\frac{\partial T_o}{\partial V_1} U_{V_1}\Big)^2 + \Big(\frac{\partial T_o}{\partial V_2} U_{V_2}\Big)^2 + \Big(\frac{\partial T_o}{\partial C_1} U_{C_1}\Big)^2 \\ &+ \Big(\frac{\partial T_o}{\partial C_2} U_{C_2}\Big)^2 + \Big(\frac{\partial T_o}{\partial n_1} U_{n_1}\Big)^2 + \Big(\frac{\partial T_o}{\partial n_2} U_{n_2}\Big)^2 \\ &+ \Big(\frac{\partial T_o}{\partial T_{w1}} U_{T_{w1}}\Big)^2 + \Big(\frac{\partial T_o}{\partial T_w 2} U_{T_{w2}}\Big)^2\Big]^{\frac{1}{2}} \end{aligned} \qquad (C.2)$$

where the partial derivatives are:

$$\frac{\partial T_o}{\partial V_1} = \frac{-2n_2(T_{w1} - rT_o)(T_{w2} - rT_o)}{V_1 r N_2(T_{w2} - rT_o) - V_1 r N_1(T_{w1} - rT_o)} \qquad (C.3)$$

$$\frac{\partial T_o}{\partial V_2} = \frac{-2n_1(T_{w1} - rT_o)(T_{w2} - rT_o)}{V_2 r N_2(T_{w2} - rT_o) - V_2 r N_1(T_{w1} - rT_o)} \qquad (C.4)$$

$$\frac{\partial T_o}{\partial C_1} = \frac{n_2(T_{w1} - rT_o)(T_{w2} - rT_o)}{C_1 r N_2(T_{w2} - rT_o) - C_1 r N_1(T_{w1} - rT_o)} \tag{C.5}$$

$$\frac{\partial T_o}{\partial C_2} = \frac{-n_1(T_{w1} - rT_o)(T_{w2} - rT_o)}{C_2 r N_2(T_{w2} - rT_o) - C_2 r N_1(T_{w1} - rT_o)} \tag{C.6}$$

$$\frac{\partial T_o}{\partial n_1} = \frac{-n_2(T_{w1} - rT_o)(T_{w2} - rT_o)\left[2lnV_1 - lnC_1 - ln(T_{w1} - rT_o)\right]}{rN_1{}^2(T_{w1} - rT_o) - rN_1N_2(T_{w2} - rT_o)} \tag{C.7}$$

$$\frac{\partial T_o}{\partial n_2} = \frac{-n_1(T_{w1} - rT_o)(T_{w2} - rT_o)\left[2lnV_2 - lnC_2 - ln(T_{w2} - rT_o)\right]}{rN_2{}^2(T_{w2} - rT_o) - rN_1N_2(T_{w1} - rT_o)} \tag{C.8}$$

$$\frac{\partial T_o}{\partial T_{w1}} = \frac{n_2(T_{w2} - rT_o)}{rN_2(T_{w2} - rT_o) - rN_1(T_{w1} - rT_o)} \tag{C.9}$$

$$\frac{\partial T_o}{\partial T_{w2}} = \frac{n_1(T_{w1} - rT_o)}{rN_1(T_{w1} - rT_o) - rN_2(T_{w2} - rT_o)} \tag{C.10}$$

C.3. Uncertainty in Various Measurement Variables

The uncertainties are based on the accuracies stated by the manufacturer for various transducers and data acquisition and readout systems and are calculated by the RSS method. The hot-wire recovery factor r is assumed to be constant. The uncertainty in various measurements are given below:

1. *Uncertainty in Voltage:* The uncertainty of voltage is a combination of the bridge voltage and the data acquisition uncertainties. The overall Uncertainty in voltage measurement = $\pm 0.0024496\ V$

2. *Uncertainty in Total Pressure Measurement in calibration* = $\pm 0.012\ psia$

3. *Uncertainty in Total Temperature Measurement in calibration* = $\pm 0.895\ Deg\ C$

4. *Uncertainty in Wire Temperature* (T_{wi})*:* The wire temperature is given by:

$$T_{wi} = T_o + \frac{\frac{R_{wi}}{R_o} - 1}{\alpha} \qquad (C.11)$$

The uncertainty in wire temperature is given by:

$$U_{T_{wi}} = \sqrt{\left(\frac{\partial T_{wi}}{\partial R_{wi}} U_{R_{wi}}\right)^2 + \left(\frac{\partial T_{wi}}{\partial R_o} U_{R_o}\right)^2 + \left(\frac{\partial T_{wi}}{\partial T_{oc}} U_{T_{oc}}\right)^2 + \left(\frac{\partial T_{wi}}{\partial \alpha} U_\alpha\right)^2} \qquad (C.12)$$

Evaluating the various partial derivatives, the overall uncertainty estimate of $T_{w1} = \pm 1.31\ Deg\ C$ and of $T_{w2} = \pm 1.42\ Deg\ C$.

5. *Uncertainty in Calibration Constant* C_i*:* The uncertainty estimate in C_i is given by:

$$U_{C_i} = \sqrt{\left(\frac{\partial C_i}{\partial V_i} U_{V_i}\right)^2 + \left(\frac{\partial C_i}{\partial T_{wi}} U_{T_{wi}}\right)^2 + \left(\frac{\partial C_i}{\partial T_o} U_{T_o}\right)^2 + \left(\frac{\partial C_i}{\partial P_o} U_{P_o}\right)^2} \qquad (C.13)$$

where, the partial derivatives are:

$$\frac{\partial C_i}{\partial V_i} = \frac{2C_i}{V_i} \qquad (C.14.i)$$

$$\frac{\partial C_i}{\partial T_{wi}} = \frac{-C_i}{T_{wi} - rT_o} \qquad (C.14.ii)$$

$$\frac{\partial C_i}{\partial T_o} = \frac{rC_i}{T_{wi} - rT_o} \qquad (C.14.iii)$$

$$\frac{\partial C_i}{\partial P_o} = \frac{n_i C_i \sqrt{T_o}}{P_o} \qquad (C.14.iv)$$

So the overall uncertainty estimates of $C_1 = \pm 0.0024$ and $C_2 = \pm 0.00252$.

6. *Uncertainty in Calibration Constant* n_i*:* The uncertainty estimate of n_i is given by:

$$U_{n_i} = \sqrt{\left(\frac{\partial n_i}{\partial V_i} U_{V_i}\right)^2 + \left(\frac{\partial n_i}{\partial T_{wi}} U_{T_{wi}}\right)^2 + \left(\frac{\partial n_i}{\partial T_o} U_{T_o}\right)^2 + \left(\frac{\partial n_i}{\partial P_o} U_{P_o}\right)^2} \qquad (C.15)$$

where, the partial derivatives are:

$$\frac{\partial n_i}{\partial V_i} = \frac{2}{V_i ln(\frac{P_o}{\sqrt{T_o}})} \qquad (C.16.i)$$

$$\frac{\partial n_i}{\partial T_{wi}} = \frac{-1}{(T_{wi} - rT_o) ln(\frac{P_o}{\sqrt{T_o}})} \qquad (C.16.ii)$$

$$\frac{\partial n_i}{\partial T_o} = \left(\frac{r}{(T_{wi} - rT_o)} + \frac{1}{2T_o^2}\right) \frac{1}{ln(\frac{P_o}{\sqrt{T_o}})} \qquad (C.16.iii)$$

$$\frac{\partial n_i}{\partial P_o} = \frac{n_i}{P_o ln(\frac{P_o}{\sqrt{T_o}})} \qquad (C.16.iv)$$

So the overall uncertainty estimates of $n_1 = \pm 0.0002$ and $n_2 = \pm 0.00031$.

Now substituting all these quantities into the uncertainty equation, the overall uncertainty in total temperature measurement is $\pm 1.438\ Deg\ C$. This value holds good for both the time averaged as well as the RMS value of total temperature (Yavuzkurt, 1984). This estimate is a very conservative one and it is very likely that the actual uncertainty may be much lower than this number.

Appendix D

DEVELOPMENT OF THE AVERAGE PASSAGE EQUATION SYSTEM

In this appendix details of the development of the average passage equation system is discussed. Just the basic steps are discussed here. For full details of this system the reader is refered to Adamczyk (1985).

The development is begun with the circumferential momentum equation from the Navier-Stokes equations in cylindrical coordinates for a non-rotating blade as:

$$\frac{\partial}{\partial t}(\rho r V_\theta) + \frac{\partial}{\partial r}(\rho r V_r V_\theta) + \frac{\partial}{\partial \theta}(\rho V_\theta V_\theta) + \frac{\partial}{\partial z}(\rho r V_z V_\theta) + \rho V_r V_\theta = -\frac{\partial p}{\partial \theta} + \frac{\partial}{\partial r}(r\tau_{r\theta}) + \frac{\partial}{\partial \theta}(\tau_{\theta\theta}) + \frac{\partial}{\partial z}(r\tau_{z\theta}) + \tau_{r\theta} \qquad (D.1)$$

Here, t is time, z, r, θ are the axial, radial, and circumferential coordinate directions, respectively, ρ is the fluid density, V_z, V_r, V_θ are the velocity components in the axial, radial, and circumferential coordinate directions, respectively, p is pressure, and $\tau_{z\theta}, \tau_{\theta\theta}, \tau_{r\theta}$ are components of the viscous shear stress. The density-weighted ensemble-average of the variable f_i is defined for compressible flows as:

$$\tilde{f} = \lim_{N\to\infty} \frac{1}{\bar{\rho} N} \sum_{1}^{N} \rho_i f_i \qquad (D.2)$$

In each case, f_i is the i^{th} sample of the function of interest, and the average is taken over a large number of samples (N).

To begin, the velocity field (defined in the absolute frame of reference) is decomposed into a density weighted ensemble average component plus an unresolved variable. The radial velocity component, for example, becomes:

$$V_r = \tilde{V}_r + V_r' \qquad (D.3)$$

It is immediately obvious that the density-weighted ensemble average of the unresolved variable V_r' is zero. Substituting this velocity decomposition into the circumferential

momentum equation, and utilizing a similar non-density-weighted decomposition for the remaining flow variables, and ensemble-averaging the result:

$$\frac{\partial}{\partial t}(\bar{\rho} r \tilde{V}_\theta) + \frac{\partial}{\partial r}(\bar{\rho} r \tilde{V}_r \tilde{V}_\theta) + \frac{\partial}{\partial \theta}(\bar{\rho} \tilde{V}_\theta \tilde{V}_\theta) + \frac{\partial}{\partial z}(\bar{\rho} r \tilde{V}_z \tilde{V}_\theta) + \bar{\rho} \tilde{V}_r \tilde{V}_\theta =$$

$$-\frac{\partial \bar{p}}{\partial \theta} + \frac{\partial}{\partial r}(r\bar{\tau}_{r\theta} - r\underline{\underline{\overline{\rho V_r' V_\theta'}}}) + \frac{\partial}{\partial \theta}(\bar{\tau}_{\theta\theta} - \underline{\underline{\overline{\rho V_\theta' V_\theta'}}}) + \frac{\partial}{\partial z}(r\bar{\tau}_{z\theta}) + \bar{\tau}_{r\theta} - r\underline{\underline{\overline{\rho V_z' V_\theta'}}} - \underline{\underline{\overline{\rho V_r' V_\theta'}}} \quad (D.4)$$

The similarity between this equation and the original equation is obvious. The additional terms which appear as a result of the ensemble averaging are referred to as Reynolds stresses (here the underscored terms represent three of the nine components of the Reynolds stress tensor). It is these stress terms which are typically represented through the use of turbulence models in detailed numerical solutions for turbulent viscous flows.

The next step in the development process is to time-average the ensemble-averaged equation. The density-weighted time-averaging operator is defined as:

$$\bar{\bar{f}} = \frac{\Omega}{2\pi \lambda_R \bar{\bar{\rho}}} \int_{t_1}^{t_1 + \frac{2\pi}{\Omega}} \bar{\rho} H(t) \bar{f}(t) dt \quad (D.5)$$

Here $H(t)$ represents a gate function which equals 1 outside of a blade and equals zero inside a blade. This function effectively prohibits including the blade region during the time average (as the rotor passes through the region downstream of a vane, for example). The term λ_R is a representation of the blockage imposed by the neighboring rotor row. This results from the gate function in the time-average operator.

Applying the density-weighted time-averaging to the ensemble-averaged velocity the decomposition is defined as:

$$\tilde{V}_r = \tilde{\bar{V}}_r + V_{rRP} \quad (D.6)$$

where V_{rRP} denotes the unsteady component of the ensemble-averaged velocity (revolution periodic unsteadiness defined in Chapter 3). By definition, then, the time average of V_{rRP} is identically zero. Introducing this decomposition for the velocities into the ensemble-averaged equation and time-averaging the result yields:

$$\frac{\partial}{\partial t_1}(\overline{\overline{\rho}} r \lambda_R \tilde{\tilde{V}}_\theta) + \frac{\partial}{\partial r}(\overline{\overline{\rho}} r \lambda_R \tilde{\tilde{V}}_r \tilde{\tilde{V}}_\theta) + \frac{\partial}{\partial \theta}\lambda_R(\overline{\overline{\rho}} \tilde{\tilde{V}}_\theta \tilde{\tilde{V}}_\theta + \overline{\overline{p}}) + \frac{\partial}{\partial z}(\overline{\overline{\rho}} r \lambda_R \tilde{\tilde{V}}_z \tilde{\tilde{V}}_\theta) + \lambda_R \overline{\overline{p}} \tilde{\tilde{V}}_r \tilde{\tilde{V}}_\theta =$$

$$\frac{\partial}{\partial r} r \lambda_R (\overline{\overline{\tau}}_{r\theta} - \underline{\underline{\overline{\overline{\rho} V_{rRP} V_{\theta RP}}}} - \overline{\overline{\rho V_r' V_\theta'}}) + \frac{\partial}{\partial \theta}\lambda_R(\overline{\overline{\tau}}_{\theta\theta} - \underline{\underline{\overline{\overline{\rho} V_{\theta RP} V_{\theta RP}}}} - \overline{\overline{\rho V_\theta' V_\theta'}}) +$$

$$\frac{\partial}{\partial z} r \lambda_R (\overline{\overline{\tau}}_{z\theta} - \underline{\underline{\overline{\overline{\rho} V_{zRP} V_{\theta RP}}}} - \overline{\overline{\rho V_z' V_\theta'}}) + \lambda_R (\overline{\overline{\tau}}_{r\theta} - \underline{\underline{\overline{\overline{\rho} V_{rRP} V_{\theta RP}}}} - \overline{\overline{\rho V_r' V_\theta'}}) + F_{IN}^{\theta R} + F_V^{\theta R} \quad (D.7)$$

It should be mentioned that the algebra required to obtain this result is rather complex, and requires specific rules governing interchanging time averaging and differentiation (see Adamczyk (1985) for details). The underscored terms represent the mixing stress attributed to the unsteady coherent (ensemble-averaged) velocity field. The body forces $F_{IN}^{\theta R}$ and $F_V^{\theta R}$ are associated with the inviscid and viscous forces imparted by rotating blades. These forces are axisymmetric and vanish outside of a blade row.

The density-weighted passage-to-passage average of a variable f is defined with respect to a reference blade row as:

$$\overline{\overline{f}} = \frac{1}{\overline{\overline{\rho}} \lambda_S M} \sum_{m=0}^{M-1} G(r, \theta + \frac{2\pi}{M}, z) \overline{\overline{\rho}} \overline{\overline{f}}(r, \theta + \frac{2\pi}{M}, z, t_1) \quad (D.8)$$

Here, M represents the number of airfoils in the reference blade row. The function G acts as a gate function for the remaining non-rotating blade rows, to avoid applying the average inside an airfoil, which effectively introduces the blockage factor λ_S for these rows.

Finally, the passage-to-passage averaging operator is approached in much the same manner by defining a density-weighted decomposition of the time-averaged ensemble average velocity as:

$$\tilde{\tilde{V}}_r = \overline{V_r} + V_{rRAP} \quad (D.9)$$

Here V_{rRAP} represents the aperiodic component of the time-averaged ensemble-averaged velocity. By definition, then, the passage-to-passage average of this aperiodic

component is identically zero. This is equivalent to the revolution aperiodic unsteadiness as defined in Chapter 3. Substitution of this decomposition into the time-averaged, ensemble-averaged momentum equation, and application of the passage-to-passage averaging operator yields:

$$\frac{\partial}{\partial t_1}(r\lambda_j\overline{\overline{\rho}\overline{V_r}}) + \frac{\partial}{\partial r}(r\lambda_j\overline{\overline{\rho}\overline{V_r V_\theta}}) + \frac{\partial}{\partial \theta}(r\lambda_j\overline{\overline{\rho}\overline{V_\theta V_\theta}} + \lambda_j\overline{\overline{p}}) + \frac{\partial}{\partial z}(r\lambda_j\overline{\overline{\rho}\overline{V_z V_\theta}}) + \lambda_j\overline{\overline{\rho}\overline{V_r V_\theta}} =$$

$$\frac{\partial}{\partial r}r\lambda_j(\overline{\overline{\tau}}_{r\theta} - \underline{\underline{\overline{\overline{\rho}V_{rRAP}V_{\theta RAP}}}} - \overline{\overline{\rho V_{rRP}V_{\theta RP}}} - \overline{\overline{\rho V_r'V_\theta'}}) +$$

$$\frac{\partial}{\partial \theta}\lambda_j(\overline{\overline{\tau}}_{\theta\theta} - \underline{\underline{\overline{\overline{\rho}V_{\theta RAP}V_{\theta RAP}}}} - \overline{\overline{\rho V_{\theta RP}V_{\theta RP}}} - \overline{\overline{\rho V_\theta'V_\theta'}}) +$$

$$\frac{\partial}{\partial z}r\lambda_j(\overline{\overline{\tau}}_{z\theta} - \underline{\underline{\overline{\overline{\rho}V_{zRAP}V_{\theta RAP}}}} - \overline{\overline{\rho V_{zRP}V_{\theta RP}}} - \overline{\overline{\rho V_z'V_\theta'}}) +$$

$$\lambda_j(\overline{\overline{\tau}}_{r\theta} - \underline{\underline{\overline{\overline{\rho}V_{rRAP}V_{\theta RAP}}}} - \overline{\overline{\rho V_{\theta RP}V_{\theta RP}}} - \overline{\overline{\rho V_r'V_\theta'}}) +$$

$$F_{IN}^{(\theta R)} + F_V^{(\theta R)} + F_{IN}^{(\theta S)} + F_V^{(\theta S)} \qquad (D.10)$$

The variables $F_{IN}^{(\theta S)}$ and $F_V^{(\theta S)}$ represent the inviscid and viscous body force contributions by the neighboring non-rotating blade rows. The underscored terms represent the mixing stress generated by by the aperiodic component of the steady velocity field.

Now for the experimental data taken in this program, the density was assumed to be constant since the mach numbers encountered in this flow field are very low subsonic. And also the various time averaging parameters can be combined into a common time average since the overall time period for the data acquired is one rotor revolution (because of ensemble average). The viscous body forces and the energy sources can be neglected since they go to zero outside the blade row. Incorporating these simplifications into equation D.10, the average-passage equation system for the circumferential momentum equation is given by:

$$\underbrace{\frac{\partial}{\partial t}(r\lambda_j\overline{\rho}\overline{V_\theta})}_{TM1} + \underbrace{\frac{\partial}{\partial r}(r\lambda_j\overline{\rho}\overline{V_r V_\theta})}_{TM2} + \underbrace{\frac{\partial}{\partial \theta}(r\lambda_j\overline{\rho}\overline{V_\theta V_\theta} + \overline{p})}_{TM3} + \underbrace{\frac{\partial}{\partial z}(r\lambda_j\overline{\rho}\overline{V_z V_\theta})}_{TM4} =$$

$$
\begin{aligned}
&- \left(\underbrace{\lambda_j \overline{\rho V_r V_\theta}}_{TM5} \right) \\
&+\lambda_j \left(\underbrace{\overline{\tau_{r\theta}}}_{TM6} - \underbrace{\overline{\rho V_{rRAP} V_{\theta RAP}}}_{TM7} + \underbrace{\overline{\rho V_{rRP} V_{\theta RP}}}_{TM89} + \underbrace{\overline{\rho V_r' V_\theta'}}_{TM10} \right) \\
&+\frac{\partial}{\partial r}\lambda_j \left(\underbrace{r\overline{\tau_{r\theta}}}_{TM11} - \underbrace{r\overline{\rho V_{rRAP} V_{\theta RAP}}}_{TM12} - \underbrace{r\overline{\rho V_{rRP} V_{\theta RP}}}_{TM1314} - \underbrace{r\overline{\rho V_r' V_\theta'}}_{TM15} \right) \\
&+\frac{\partial}{\partial \theta}\lambda_j \left(\underbrace{\overline{r\tau_{\theta\theta}}}_{TM16} - \underbrace{\overline{\rho V_{\theta RAP} V_{\theta RAP}}}_{TM17} - \underbrace{\overline{\rho V_{\theta RP} V_{\theta RP}}}_{TM1819} - \underbrace{\overline{\rho V_\theta' V_\theta'}}_{TM20} \right) \\
&+\frac{\partial}{\partial z}\lambda_j \left(\underbrace{r\overline{\tau_{z\theta}}}_{TM21} - \underbrace{\overline{\rho V_{zRAP} V_{\theta RAP}}}_{TM22} - \underbrace{\overline{\rho V_{zRP} V_{\theta RP}}}_{TM2324} - \underbrace{\overline{\rho V_z' V_\theta'}}_{TM25} \right) \qquad (D.11)
\end{aligned}
$$

The terms in the underbraces denote the count of each of these terms. When analyzing the blade-to-blade and contour description of the equation system, reference is made to these terms. Using the procedure described above, the average-passage equation system for the continuity, radial-momentum, axial-momentum and the energy equations are derived. The reader is referred to Adamczyk (1985) for details. Only the equations are given below.

Radial momentum equation:

$$
\begin{aligned}
&\underbrace{\frac{\partial}{\partial t}(r\lambda_j \overline{\rho V_r})}_{RM1} + \underbrace{\frac{\partial}{\partial r}(r\lambda_j \overline{\rho V_r V_r} + \overline{p})}_{RM2} + \underbrace{\frac{\partial}{\partial \theta}(r\lambda_j \overline{\rho V_\theta V_r})}_{RM3} + \underbrace{\frac{\partial}{\partial z}(r\lambda_j \overline{\rho V_z V_r})}_{RM4} = \\
&\left(\underbrace{\overline{p} + \overline{\rho V_\theta^2} - \overline{\tau_{\theta\theta}}}_{RM5} \right) \lambda_j \\
&+\overline{\rho}\lambda_j \left(\underbrace{\overline{V_{\theta RAP} V_{\theta RAP}}}_{RM6} + \underbrace{\overline{V_{\theta RP} V_{\theta RP}}}_{RM78} + \underbrace{\overline{V_\theta' V_\theta'}}_{RM9} \right) \\
&+\frac{\partial}{\partial r}\lambda_j \left(\underbrace{r\overline{\tau_{rr}}}_{RM10} - \underbrace{r\overline{\rho V_{rRAP} V_{rRAP}}}_{RM11} - \underbrace{r\overline{\rho V_{rRP} V_{rRP}}}_{RM1213} - \underbrace{r\overline{\rho V_r' V_r'}}_{RM14} \right) \\
&+\frac{\partial}{\partial \theta}\lambda_j \left(\underbrace{r\overline{\tau_{\theta r}}}_{RM15} - \underbrace{\overline{\rho V_{\theta RAP} V_{rRAP}}}_{RM16} - \underbrace{\overline{\rho V_{\theta RP} V_{rRP}}}_{RM1718} - \underbrace{\overline{\rho V_\theta' V_r'}}_{RM19} \right)
\end{aligned}
$$

$$+\frac{\partial}{\partial z}\lambda_j\left(\underbrace{r\overline{\tau_{zr}}}_{RM20} - \underbrace{\overline{\rho V_{zRAP}V_{rRAP}}}_{RM21} - \underbrace{\overline{\rho V_{zRP}V_{rRP}}}_{RM2223} - \underbrace{\overline{\rho V_z'V_r'}}_{RM24}\right) \qquad (D.12)$$

Axial momentum equation:

$$\underbrace{\frac{\partial}{\partial t}(r\lambda_j\overline{\rho V_z})}_{AM1} + \underbrace{\frac{\partial}{\partial r}(r\lambda_j\overline{\rho V_r V_z})}_{AM2} + \underbrace{\frac{\partial}{\partial \theta}(r\lambda_j\overline{\rho V_\theta V_z})}_{AM3} + \underbrace{\frac{\partial}{\partial z}(r\lambda_j\overline{\rho V_z V_z} + r\overline{p})}_{AM4} =$$

$$\frac{\partial}{\partial r}\lambda_j\left(\underbrace{r\overline{\tau_{rz}}}_{AM5} - \underbrace{r\overline{\rho V_{rRAP}V_{zRAP}}}_{AM6} - \underbrace{r\overline{\rho V_{rRP}V_{zRP}}}_{AM78} - \underbrace{r\overline{\rho V_r'V_z'}}_{AM9}\right)$$

$$+\frac{\partial}{\partial \theta}\lambda_j\left(\underbrace{\overline{\tau_{\theta z}}}_{AM10} - \underbrace{\overline{\rho V_{\theta RAP}V_{zRAP}}}_{AM11} - \underbrace{\overline{\rho V_{\theta RP}V_{zRP}}}_{AM1213} - \underbrace{\overline{\rho V_\theta'V_z'}}_{AM14}\right)$$

$$+\frac{\partial}{\partial z}\lambda_j\left(\underbrace{r\overline{\tau_{zz}}}_{AM15} - \underbrace{r\overline{\rho V_{zRAP}V_{zRAP}}}_{AM16} - \underbrace{r\overline{\rho V_{zRP}V_{zRP}}}_{AM1718} - \underbrace{r\overline{\rho V_z'V_z'}}_{AM19}\right) \qquad (D.13)$$

and the Energy Equation:

$$\underbrace{\frac{\partial}{\partial t}(r\lambda_j\overline{\rho e_o})}_{E1} + \underbrace{\frac{\partial}{\partial r}(r\lambda_j\overline{\rho V_r H_o})}_{E2} + \underbrace{\frac{\partial}{\partial \theta}(r\lambda_j\overline{\rho V_\theta H_o})}_{E3} + \underbrace{\frac{\partial}{\partial z}(r\lambda_j\overline{\rho V_z H_o})}_{E4} =$$

$$\frac{\partial}{\partial r}r\lambda_j\left(\underbrace{\overline{V_r\tau_{rr}}}_{E5} + \underbrace{\overline{V_\theta\tau_{r\theta}}}_{E6} + \underbrace{\overline{V_z\tau_{rz}}}_{E7}\right)$$

$$+\frac{\partial}{\partial \theta}\lambda_j\left(\underbrace{\overline{V_r\tau_{\theta r}}}_{E8} + \underbrace{\overline{V_\theta\tau_{\theta\theta}}}_{E9} + \underbrace{\overline{V_z\tau_{\theta z}}}_{E10}\right)$$

$$+\frac{\partial}{\partial z}r\lambda_j\left(\underbrace{\overline{V_r\tau_{zr}}}_{E11} + \underbrace{\overline{V_\theta\tau_{z\theta}}}_{E12} + \underbrace{\overline{V_z\tau_{zz}}}_{E13}\right)$$

$$+\underbrace{\frac{\partial}{\partial r}r\lambda_j\left(\overline{k\frac{\partial T}{\partial r}}\right)}_{E14} + \underbrace{\frac{\partial}{\partial \theta}\lambda_j\left(\overline{\frac{k}{r}\frac{\partial T}{\partial \theta}}\right)}_{E15} + \underbrace{\frac{\partial}{\partial z}r\lambda_j\left(\overline{k\frac{\partial T}{\partial z}}\right)}_{E16}$$

$$-\frac{\partial}{\partial r}r\lambda_j\left(\underbrace{\overline{\rho V_{rRAP}H_{oRAP}}}_{E17} + \underbrace{\overline{\rho V_{rRP}H_{oRP}}}_{E1819} + \underbrace{\overline{\rho V_r'H_o'}}_{E20}\right)$$

$$-\frac{\partial}{\partial \theta}\lambda_j\left(\underbrace{\overline{\rho V_{\theta RAP}H_{oRAP}}}_{E21} + \underbrace{\overline{\rho V_{\theta RP}H_{oRP}}}_{E2223} + \underbrace{\overline{\rho V_\theta'H_o'}}_{E24}\right)$$

$$
\begin{aligned}
&-\frac{\partial}{\partial z} r\lambda_j \left(\underbrace{\overline{\rho V_{zRAP} H_{oRAP}}}_{E25} + \underbrace{\overline{\rho V_{zRP} H_{oRP}}}_{E2627} + \underbrace{\overline{\rho V_z' H_o'}}_{E28} \right) \\
&+\frac{\partial}{\partial r} r\lambda_j \left(\underbrace{\overline{V_{rRAP} \tau_{rrRAP}}}_{E29} + \underbrace{\overline{V_{rRP} \tau_{rrRP}}}_{E3031} + \underbrace{\overline{V_r' \tau_{rr}'}}_{E32} \right. \\
&\quad + \underbrace{\overline{V_{\theta RAP} \tau_{r\theta RAP}}}_{E33} + \underbrace{\overline{V_{\theta RP} \tau_{r\theta RP}}}_{E3435} + \underbrace{\overline{V_\theta' \tau_{r\theta}'}}_{E36} \\
&\quad \left. + \underbrace{\overline{V_{zRAP} \tau_{rzRAP}}}_{E37} + \underbrace{\overline{V_{zRP} \tau_{rzRP}}}_{E3839} + \underbrace{\overline{V_z' \tau_{rz}'}}_{E40} \right) \\
&+\frac{\partial}{\partial \theta} \lambda_j \left(\underbrace{\overline{V_{rRAP} \tau_{\theta rRAP}}}_{E41} + \underbrace{\overline{V_{rRP} \tau_{\theta rRP}}}_{E4243} + \underbrace{\overline{V_r' \tau_{\theta r}'}}_{E44} \right. \\
&\quad + \underbrace{\overline{V_{\theta RAP} \tau_{\theta\theta RAP}}}_{E45} + \underbrace{\overline{V_{\theta RP} \tau_{\theta\theta RP}}}_{E4647} + \underbrace{\overline{V_\theta' \tau_{\theta\theta}'}}_{E48} \\
&\quad \left. + \underbrace{\overline{V_{zRAP} \tau_{\theta zRAP}}}_{E49} + \underbrace{\overline{V_{zRP} \tau_{\theta zRP}}}_{E5051} + \underbrace{\overline{V_z' \tau_{\theta z}'}}_{E52} \right) \\
&+\frac{\partial}{\partial z} r\lambda_j \left(\underbrace{\overline{V_{rRAP} \tau_{zrRAP}}}_{E53} + \underbrace{\overline{V_{rRP} \tau_{zrRP}}}_{E5455} + \underbrace{\overline{V_r' \tau_{zr}'}}_{E56} \right. \\
&\quad + \underbrace{\overline{V_{\theta RAP} \tau_{\theta zRAP}}}_{E57} + \underbrace{\overline{V_{\theta RP} \tau_{\theta zRP}}}_{E5859} + \underbrace{\overline{V_\theta' \tau_{\theta z}'}}_{E60} \\
&\quad \left. + \underbrace{\overline{V_{zRAP} \tau_{zzRAP}}}_{E61} + \underbrace{\overline{V_{zRP} \tau_{zzRP}}}_{E6263} + \underbrace{\overline{V_z' \tau_{zz}'}}_{E64} \right)
\end{aligned}
\qquad (D.14)
$$